DTIC File Copy

1

Environment Sensitive Fracture of Metals and Alloys

AD-A213 332

DTIC
S ELECTE D
OCT 1 2 1989
D

July 1987

DISTRIBUTION STATEMENT A
Approved for public release
Distribution Unlimited

Office of Naval Research
Arlington, Va.

89 10 11 083

Environment Sensitive Fracture of Metals and Alloys

July 1987

Proceedings of the Office of Naval Research Workshop on
Environment Sensitive Fracture of Metals and Alloys held at the
Naval Research Laboratory, Washington, D.C. on 3-4 June 1985

Accession For
TAB
per CS
A-1

Office of Naval Research
Arlington, Va.

CONTENTS

DEDICATION v

PREFACE vii

CORROSION FATIGUE

Mechanisms of Corrosion Fatigue of Aluminum Alloys 1
David J. Duquette
Materials Engineering Department, Rensselaer Polytechnic Institute

Modifications in Microstructure Deformation and Fatigue Behavior by Ion Implantation 17
K. V. Jata and Edgar A. Starke
University of Virginia

Environmental Alteration of Fatigue Crack Plasticity 33
David L. Davidson
Southwest Research Institute

Fatigue Crack Propagation in HY80 and HY130 Steels 47
Morris E. Fine
Department of Materials Science and Engineering, Northwestern University

Modeling of Environmentally Assisted Crack Growth 63
R. P. Wei and G. W. Simmons
Department of Mechanical Engineering and Mechanics
and Department of Chemistry, Lehigh University

STRESS CORROSION CRACKING AND HYDROGEN EMBRITTLEMENT

Hydrogen Embrittlement of Steel 79
John P. Hirth
Metallurgical Engineering Department, Ohio State University

The Role of Trapping on Hydrogen Effects in Ferrous Alloys 89
I. M. Bernstein
Department of Metallurgical Engineering and Materials Science
Carnegie-Mellon University

On the Mechanisms of Hydrogen Related Fracture in Metals 105
Howard K. Birnbaum
Department of Metallurgy and Mining Engineering, University of Illinois

Mechanisms of Stress-Corrosion Cracking in Al-Zn-Mg and Al-Mg Alloys 115
Joseph R. Pickens, T. J. Langan, and J. A. S. Green
Martin Marietta Laboratories

MODELING

Chemical Factors Important to Environmentally Sensitive Fracture 133
Jerome Kruger
Department of Materials Science and Engineering, The Johns Hopkins University

Effect of Grain Boundary Structure on Sensitization and Corrosion of Stainless Steel 149
Bradley W. Bennett and Howard W. Pickering
Department of Materials Science and Engineering, Pennsylvania State University

Positron Studies of Hydrogen Effects in Alloys 165
J. G. Byrne
Departments of Metallurgy and Materials Science and Engineering, University of Utah

APPENDIX — ONR Workshop on Environment-Sensitive Fracture of Metals and Alloys 181

DEDICATION

This volume of "Environment Sensitive Fracture of Metals and Alloys" is dedicated to Dr. Philip A. Clarkin on his retirement from the Office of Naval Research.

PREFACE

This volume on "Environment Sensitive Fracture of Metals and Alloys" is a collection of papers presented at the Office of Naval Research Workshop that was held at the Naval Research Laboratory in Washington, D.C. on 3-4 June 1985. The purpose of the Workshop was to review and assess the status of Navy sponsored basic research in the areas of corrosion fatigue, stress corrosion cracking and hydrogen embrittlement. The scope of the research reported at the Workshop provides a 15-year perspective on the subject.

The period since 1970 has been an especially productive one in defining the phenomenology and basic mechanisms of cracking processes associated with hydrogen. A particularly interesting advance has been the emerging recognition of the ability of hydrogen to facilitate dislocation motion in the crack-tip region. This effect of hydrogen to enhance ductility on a localized microscopic scale has broadened the spectrum of cracking processes associated with its presence. Other significant advances include the ascribing of hydrogen mechanisms to corrosion-fatigue processes in high-strength aluminum alloys, the modeling of stress corrosion and corrosion fatigue crack growth in gaseous environments in terms of the controlling chemical processes, and recognizing the sensitivity of certain types of environmental cracking to the mode of loading.

In the area of new technique development, excellent progress has been made in applying positron annihilation to identify the location of hydrogen within the microstructure, electron backscattering to identify grain orientations in sensitization studies, triboellipsometry to study film repair processes, and stereoimaging for determining crack-opening-displacement and local strain at the crack tip.

The research described in this volume was largely conducted for the Office of Naval Research under the direction of Dr. Philip A. Clarkin. Dr. Clarkin retired from the Office of Naval Research in December, 1984. His association with this research and with those who conducted these studies is fondly remembered.

The editors with to express their appreciation to Mrs. Shirley Simmons for her devotion and care in overcoming the shortfalls of the electronic media to put all of the manuscripts into final form for publication.

R. P. Wei, Lehigh University
D. J. Duquette, Rensselaer Polytechnic Institute
T. W. Crooker, Naval Research Laboratory
A. J. Sedriks, Office of Naval Research

CORROSION FATIGUE

MECHANISMS OF CORROSION FATIGUE OF ALUMINUM ALLOYS

D. J. Duquette
Materials Engineering Department
Rensselaer Polytechic Institute
Troy, New York 12181
USA

An overview of experimental variables which are considered critical to understanding the mechanisms of corrosion fatigue of high strength aluminum alloys is presented. Based on this overview, an examination of previously proposed mechanisms is attempted. These models include anodic dissolution, surface energy reduction, and hydrogen embrittlement. It is concluded that hydrogen embrittlement of process zones at alloy surfaces (for crack initiation) and at crack tips (for crack propagation) best explains observed results. A general model of corrosion fatigue of these alloys is proposed. This model suggests that the nature of the naturally formed oxide film on aluminum alloys may be a critical factor. Chemical or mechanical damage of the film allows hydrogen ingress. The presence of second phase particles which may act as sinks for dislocation transported hydrogen, may also be a necessary prerequisite to significant amount of reduction in fatigue resistance associated with corrosion.

Introduction

It is well known that high strength aluminum alloys are highly susceptible to environmental degradation in the presence of halide ions. In the unstressed state, this degradation may be manifested by localized corrosion such as pitting, crevice corrosion or exfoliation (grain boundary attack). However, under conditions of applied or residual stresses, these alloys may suffer from stress corrosion cracking (SCC) or, if cyclic loads are present, from corrosion fatigue. In some circumstances, these two phenomena may be additive and a form of "stress-corrosion fatigue" may be observed. In general, SCC is reported as time delayed failure of smooth or of notched specimens, often at applied stress levels below the nominal yield strength of the alloy. Alternatively if high aspect ratio flaws such as pre-cracks are present, measurable crack growth may be observed which generally increases with stress intensity (K) until a plateau value of crack growth rate (da/dt , v) is reached. Both types of data are schematically described in Fig. 1.

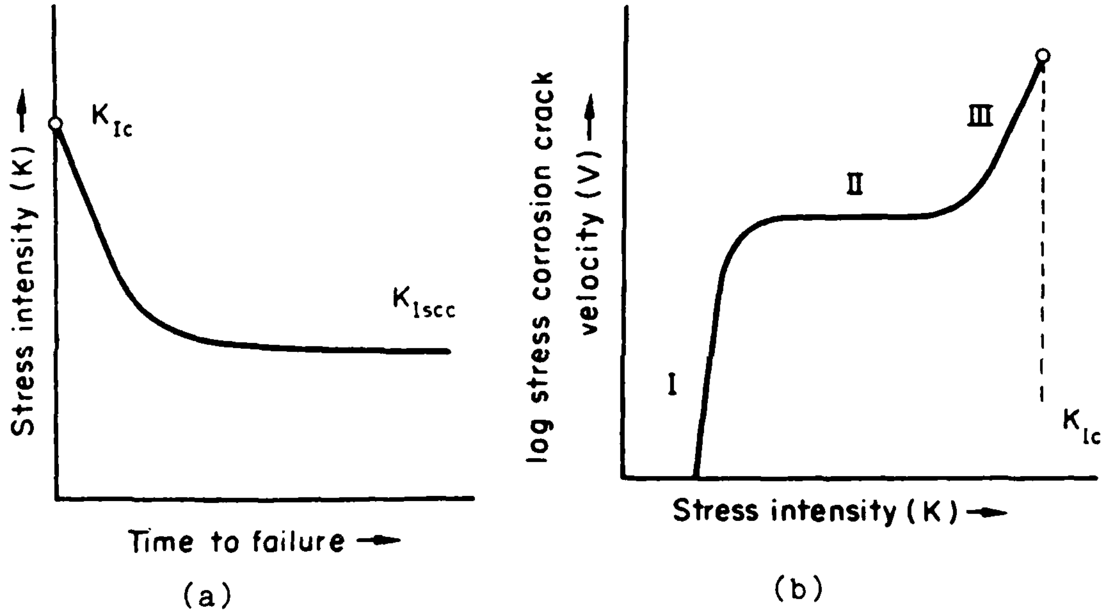

Fig. 1 - (a) Schematic diagram of stress intensity factor (K) versus time to failure in a stress corrosion environment. At K below K_{ISCC}, failure should not be observed. This type of data is also reported as stress versus time to failure for smooth specimens, and a threshold stress level is then determined, and (b) schematic diagram of crack velocity versus stress intensity factor for an alloy susceptible to SCC. K_{ISCC} is often described by the intersection of stage I cracking with the K axis. Stage III cracking is not always observed and K_{IC} is the fracture toughness of the alloy in the absence of environment.

Under cyclic loading conditions, similar trends are observed, except that the data which are obtained are generally described as stress (S or σ) versus numbers of cycles to failure (N_f) on semi-log plots for smooth or notched alloys. For the case of controlled, observable crack growth, the data are generally plotted as crack growth increment per cycle (da/dN) versus the range of stress intensity (ΔK) (Fig. 2). While halide has been shown to significantly increase crack propagation rates (and decrease time to failure) it

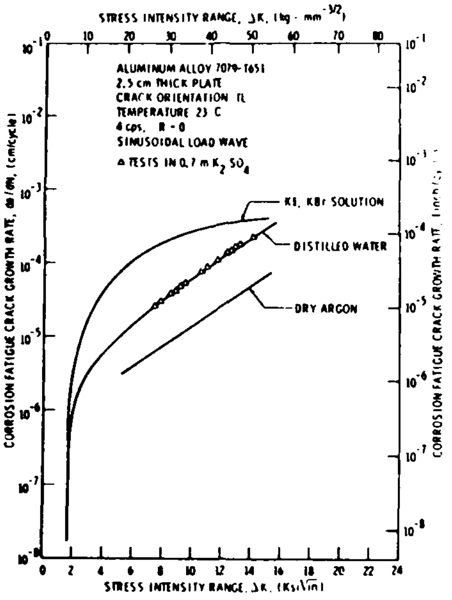

Fig. 2 - Typical fatigue crack propagation data for a precipitation hardened aluminum alloy. It should be noted that crack propagation rates in distilled water and in 0.7 m K_2SO_4 are identical and greater than in argon but that halides considerably increase crack propagation rates at virtually all ΔK values.

should be noted that distilled water, and even moist air have been shown to be very effective in inducing environmentally assisted cracking in several high strength aluminum alloys.

Aluminum Alloy Metallurgy

The aluminum alloys which are most seriously affected by environmental degradation of mechanical properties are precisely those of most interest for commercial application i.e. high strength/low density alloys. As a class, they are generally utilized in a precipitation hardened condition obtained by appropriate heat treatment. In general, the precipitates are intermetallic compounds which are formed and distributed as small particles by a solutionizing heat treatment, followed by a quench to maximize the vacancy concentration of the alloy. Aging temperatures and time determine the rate of nucleation and growth, and determine the size, distribution and morphology of the precipitates. The initial G.P. zones are considered to be coherent with the matrix and the final precipitates, η, maintain partial coherency with the matrix {111} plane [1,2], although as many as seven other matrix/precipitate coherencies have been reported [1,2]. In the peak aged condition slip is considered to be highly planar, while in the underaged or overaged condition slip is generally considered to be more diffuse.

General Fatigue Behavior of High Strength Al Alloys

The fatigue resistance of the more commonly used Al alloys such as 2024 (Al-4Cu) and 7075 (Al-5Zn-2Mg) is considered to be poor when the alloys are tested in the peak hardened condition. The 10^7 cycle fatigue limit in neutral environments is ≈ 0.3-0.35 of the UTS, and when cracks form, crack propagation rates are relatively rapid when compared with ferrous alloys. On smooth specimens in the high cycle fatigue regime, or in notched single crystals in inert atmospheres at relatively low stresses, cracks initiate in the stage I (crystallographic) mode and, as in many other alloy systems, convert to a stage II mode at some critical (but as yet undetermined) crack length (for a nominal applied stress below σ_{ys}). For precracked (fracture mechanics) specimens cracks are generally considered to grow only in the stage II mode. The specific process by which cracks initiate is still somewhat open to interpretation. Several models for crack initiation processes have been proposed and include resolution of ordered precipitates sheared by the slip process [3,4] or, alternatively, disordering of these precipitates thus creating a "soft" region along slip planes where stage I cracking initiates and grows [5]. However, at low applied stresses, approaching the endurance limit, evidence of precipitate by-pass resulting in sessile dislocation loops in the matrix of high purity Al-Zn-Mg alloys has been reported [6]. According to this model the sessile loops generate dilational stresses across slip planes leading to weak planes for crack initiation. It is possible that all of the models may be valid depending on combinations of applied stresses, precipitate morphologies, slip plane orientations, etc., and that no simple micro-process can explain all of the observed results.

Corrosion Fatigue Behavior of High Strength Al Alloys

A. Gaseous Environments

Corrosion fatigue of precipitation hardened Al alloys has been observed in environments as innocuous as damp laboratory air. In general, this environment has little or no effect on crack initiation processes, but reductions in the general $S\text{-}N_f$ behavior have been reported. Additionally, crack propagation experiments indicate significant increases in da/dN for a given ΔK [7,8] (Fig. 3). In order to observe a significant effect, water vapor must be present in the environment, oxygen alone having little or no effect on either fatigue lives or fatigue crack propagation rates [9]. In fact, virtually identical crack propagation rates have been observed for a 7075 type alloy in wet argon, wet oxygen and wet air [7]. While the presence of some

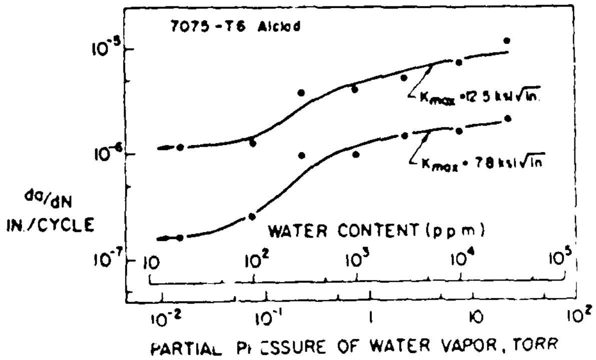

Fig. 3 - Typical crack propagation data for a precipitation hardened aluminum alloy as a function of the partial pressure of water vapor. Note that the behavior is similar for each K_{max} value, but that there is a marked increase in crack propagation rates at $pH_2O > 10^{-1}$ torr. With the exception of the transition zone between 10^{-1} and 10^0 torr da/dN is virtually constant.

water vapor is important, increases in water vapor concentrations in air do not increase crack propagation rates significantly when a critical concentration of water vapor has been exceeded [8]. The water vapor effect has been linked to a form of hydrogen embrittlement [9,10], although gaseous hydrogen does not appreciably affect fatigue resistance.

Water vapor has also been shown to affect crack paths in single crystals of an Al-Zn-Mg alloy. In dry air for a peak hardened alloy, conventional stage I cracking in {111} planes was observed, but exposure to moist air increased crack propagation rates and cracks grew in {100} planes [11, 12]. The effect is frequency sensitive and no appreciable effect is observed at 50 Hz, although a marked effect is noted at 5 Hz [12]. Also. a test started at 50 Hz but switched to 5 Hz alters the crack path out of the slip band; but a test begun at 5 Hz and switched to 50 Hz does not move the crack path back to the slip band (Fig. 4). These results indicate that the effect is time dependent and that the process is a bulk all y effect, rather than simply being strictly a surface related effect. In other experiments Wei and his co-workers have convincingly confirmed that the effect is in fact a bulk effect, but that the rate limiting step is not necessarily diffusion. Rather it appears to be related to a surface reaction of the water vapor on the aluminum alloy fracture surface which releases the damaging specie, presumed to be hydrogen [10,13].

The specific process by which hydrogen embrittles the alloy under cyclic deformation conditions is still open to question and most of the "classical" hydrogen cracking models have been invoked. These include high internal pressures at voids or defects in the alloy [14], surface energy reduction by the embrittling specie due to adsorption [15,17], effects of slip reversibility [18] and changes in the mechanical properties of the oxide film [19]. The high internal pressure theory suggests that hydrogen preferentially diffuses to regions of high hydrostatic stress ahead of a growing crack, precipitates, and increases the local tensile forces during the crack advance. Adsorption effects are thought to lower the surface energy required to create new crack surfaces, although the energy associated with crack tip plasticity is generally ignored. Hydrogen or other surface reactive species may also affect surface slip reversibility or alternatively crack tip plasticity resulting in less crack blunting as the crack surfaces are unloaded.

B. Aqueous Environments

While the previously cited results of the effects of gaseous environments are relatively recent, severe corrosion fatigue of Al alloys in aqueous, particularly saline, environments has been recognized for some time. Some of the earliest observations indicated that, for Al-Zn-Mg alloys, fracture surface appearance showed distinct differences when saline environments and dry air were compared [20,21]. Specifically, "ductile" striations (type "A") were observed in dry air, while "brittle" striations (type "B") were observed to occur in the saline solutions. Examples of these two morphologies are shown in Fig. 5. The type "A" striations were observed to be non-crystallographic and showed extensive shear, while type "B" striations were identified as occurring on or near {100} planes. It has also been observed that crack propagation rates were typically 3-10X more rapid in aqueous environments when compared to dry air [10,22]. Also, it has been reported that, the more aggressive is the solution toward general corrosion of the aluminum alloys, the lower is fatigue resistance when tested in those environments. Thus, increasing ionic concentration, particularly of halides, and both acid and basic solutions (where corrosion rates of aluminum increase) decrease fatigue resistance [23]. Lowering the corrosive nature of the solutions by adding inhibitors, such as nitrates, conversely increases the fatigue resistance

[17]. However, it has been shown that cathodic polarization of the alloy, (cathodic protection) may actually decrease fatigue resistance in nominally neutral solutions (Fig. 6). Anodic polarization, which invariably increases corrosion rates virtually always results in a degradation in fatigue resistance [23,24]. The general consensus of experiments utilizing polarization as a variable, are that small amounts of cathodic polarization slightly increase fatigue resistance but that large amounts of polarization lead to decreases in fatigue resistance. These results are by no means unequivocal, however. When significant amounts of cathodic polarization are applied, the evolution of hydrogen at the alloy surface results in a shift in the solution pH in the positive direction, and basic solutions are known to be corrosive to aluminum

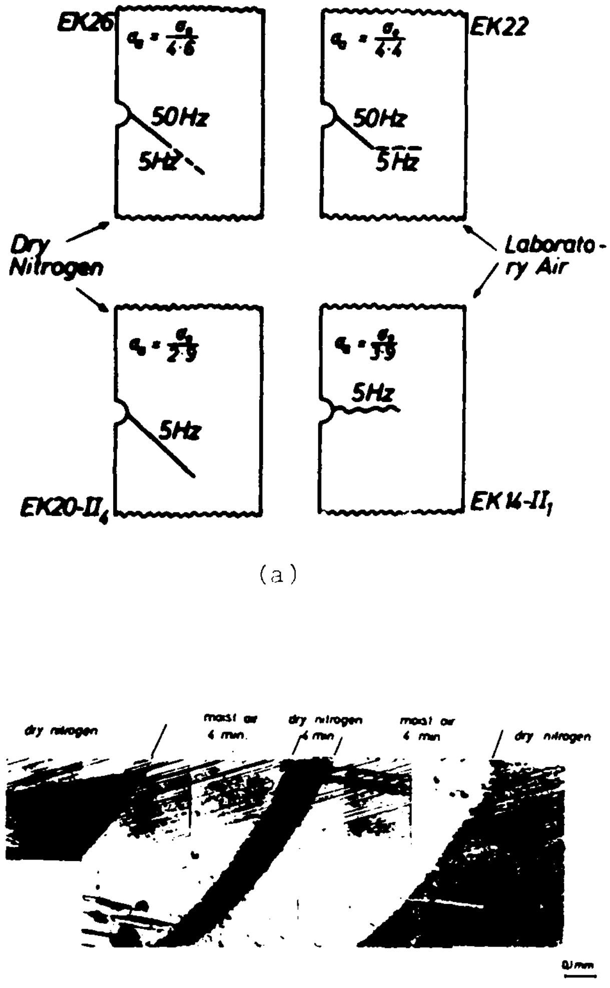
EK26
$a_0 = \frac{a_1}{4.6}$
50Hz
5Hz
EK22
$a_0 = \frac{a_1}{4.4}$
50Hz
5Hz
Dry Nitrogen
Laboratory Air
$a_0 = \frac{a_1}{2.9}$
5Hz
EK20-II$_4$
$a_0 = \frac{a_1}{3.9}$
5Hz
EK14-II$_1$
dry nitrogen
moist air 4 min.
dry nitrogen 4 min
moist air 4 min
dry nitrogen
0.1 mm

(a)

(b)

Fig. 4 - (a) Schematic diagram of crack propagation in high purity Al-Zn-Mg alloy single crystals exposed to dry N_2 and to laboratory air (with some unmeasured water vapor present) as a function of frequency. In N_2 cracks grow crystallographically independent of test frequency. However, in air, decreasing test frequency either causes the crack to deviate to a stage II mode or, if the test is begun at a low frequency, the stage I mode is not observed. These data suggest a time dependent reaction in laboratory air, and (b) Fracture surface of an Al-Zn-Mg single crystal showing that, at a constant frequency, crack propagation rates are considerably increased in moist air versus in dry N_2.

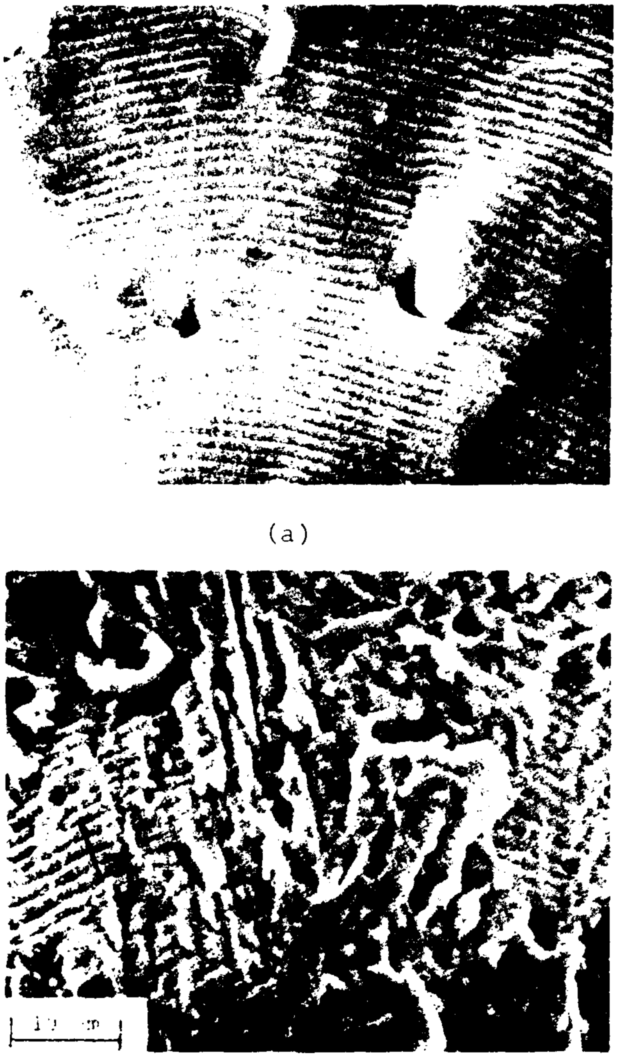

(a)

(b)

Fig. 5 - (a) Fatigue fracture surfaces of 7075 T6 tested in dry air showing ductile or type "A" striations, and (b) Fatigue fracture surfaces of 7075 T6 tested in 0.5 N NaCl showing brittle or type "B" striations. Tests of this alloy in distilled water or in 0.5 N Na_2SO_4 produce striations similar to type "A" but the application of cathodic potentials in Na_2SO_4 causes a change to type "B". Arrows indicate direction of crack growth and brackets indicate crack advance per cycle.

alloys. Additionally, the aqueous solution in growing cracks is quite different from the bulk solution and, in some cases, may be quite independent of surface polarization [25,26].

A recent experimental program in our laboratories has been specifically addressed toward understanding the mechanism of corrosion fatigue in a 7075 alloy and its high purity Al-Zn-Mg-Cu analogue. A summary of the results of this program follows:

1) It has been shown that Cl^- ion is not a prerequisite to induce lowered fatigue resistance in either alloy, particularly under conditions of cathodic polarization. Sulfate ion, while less damaging under free corrosion conditions, is equally aggressive at equivalent cathodic potentials. In chloride solutions under freely corroding conditions, surface pits dominate the crack nucleation event, but fatigue resistance in sulfate solutions where pitting is not observed is equivalent to that observed in distilled water (Figs. 2 and 7).

2) In distilled water or in sulfate solutions, under free corrosion conditions, only ductile situations are observed on the fracture surfaces, versus brittle situations invariably observed in chloride solutions. Under cathodic polarization conditions brittle situations are observed on all fracture surfaces.

3) Pre-corrosion experiments in NaCl followed by tests in laboratory air result in significant decreases in fatigue resistance. However, this effect is at least partially reversible. Post exposure heat treatments prior to fatigue testing increase fatigue resistance with larger increases observed as heat treatment times are extended (Table I).

4) In aggressive environments, the cyclic stress is the primary mechanical factor controlling the fatigue resistance. The magnitude of mean stress is only of secondary importance (Fig. 8).

5) Corrosion fatigue resistance of aluminum alloys is less sensitive to Mode III (torsional) loading than to Mode I (tensional) loading (Fig. 9).

6) Heat treatments which improve SCC resistance, (e.g., T73) have little or no effect on corrosion fatigue behavior in Cl^- solutions.

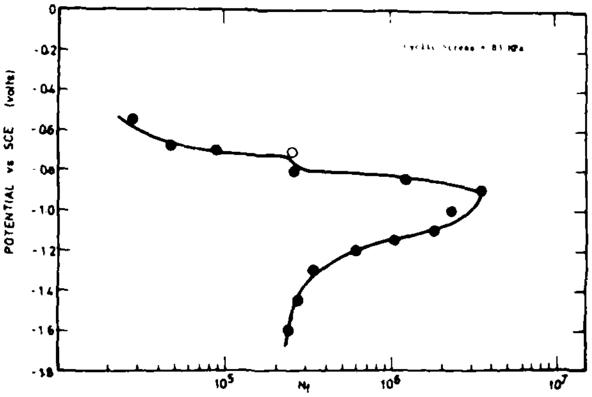

Fig. 6 - Fatigue life versus electrochemical potential for a 7075 T6 alloy in 0.5 N NaCl. The open circle corresponds to the corrosion potential. Small cathodic potentials increase fatigue lives, but larger deviations for the corrosion potential cause a decrease in fatigue resistance. Anodic polarization always decreases fatigue resistance.

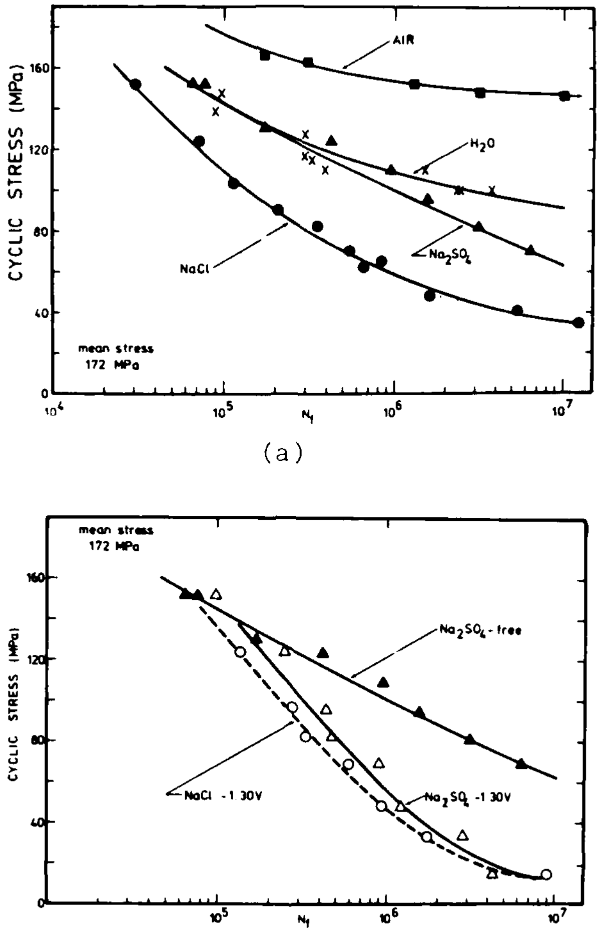

(a)

(b)

Fig. 7 - (a) Fatigue behavior of 7075 T6 exposed to air, H_2O and 0.5 N Na_2SO_4 and 0.5 N NaCl. H_2O and Na_2SO_4 solutions show similar behavior (see Fig. 2), and (b) Effect of cathodic polarization of 7075 T6 in 0.5 N NaCl and 0.5 N Na_2SO_4 showing essentially identical behavior for either anion.

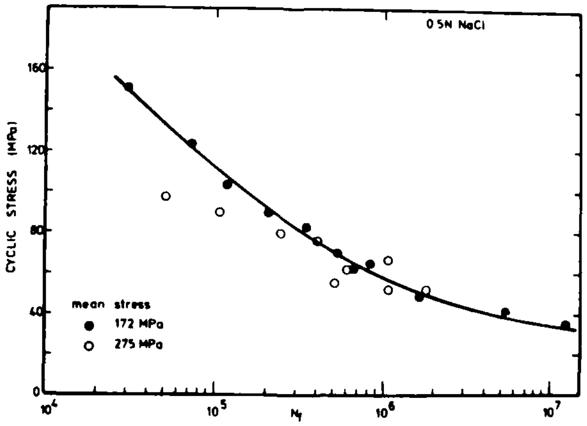

Fig. 8 - Effect of mean stress on the corrosion fatigue behavior of 7075 T6 in 0.5 N NaCl solution showing that, except at very large cyclic stresses (above σ_{ys}) mean stress has virtually no effect on fatigue resistance.

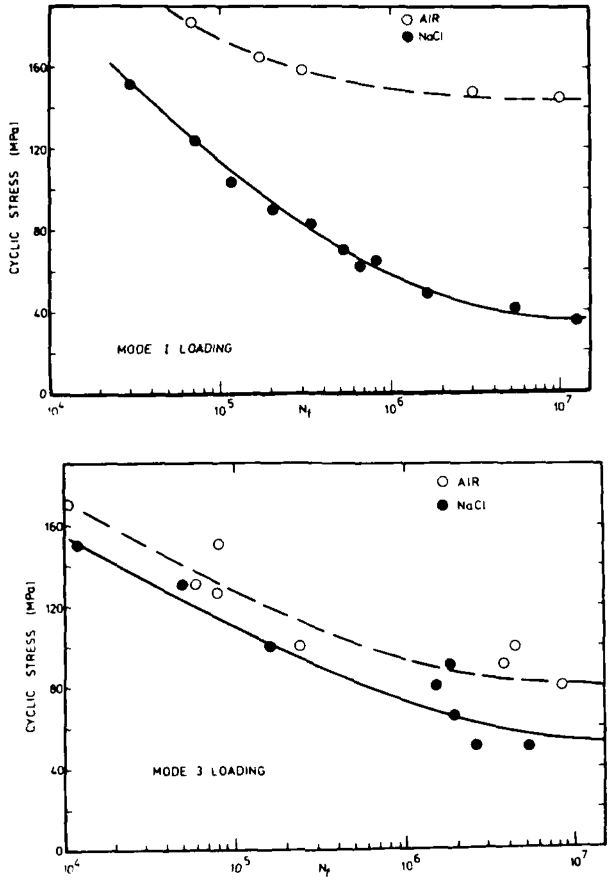

Fig. 9 - The effect of loading mode on fatigue resistance of 7075 T6 in 0.5 N NaCl solution. These data show that loading in shear has little effect on corrosion fatigue susceptibility when compared with tensile loading. The slight decrease in resistance which is observed in Mode III loading can probably be explained by the non-isotropic nature of the alloy.

Table I. The Effect of a Re-Heat Treatment Duration on Subsequent Fatigue Properties in Air

Pre-Corrosion: 24 hours in aerated 0.5 NaCl

Re-heat treat: Solutionize at 470°C for x hours
Age at 120°C for 24 hours

Fatigue in air: Mean stress 276 MPa, Cyclic stress ± 96 MPa

Time at 470°C	N_f
0 hours	30,000 cycles
3 hours	85,000 cycles
6 hours	101,000 cycles
24 hours	> 13,000,000 cycles

Specific Mechanisms of Corrosion Fatigue of Al Alloys

As already briefly mentioned, there are at least three principal mechanisms which have been suggested to explain the reduction of fatigue lives in Al alloys exposed to aggressive environments.

A. Strain Enhanced Dissolution

Older versions of this mechanism suggested that strained atomic bonds are more likely to lead to atomic dissolution (corrosion) than are unstrained bonds. Refinements to the mechanism include the role of plastic strain associated with dislocations intersecting the free surface of a metal or alloy during fatigue, resulting in preferential attack of emerging slip bands [27]. It has also been suggested that this preferential attack accelerates further slip processes in a kind of autocatalytic process. Evidence for such a model has been shown for mild steels and for copper alloys under controlled corrosion conditions [28-30]. It has also been shown that if corrosion rates are sufficiently low, fatigue resistance is unaffected by the environment. Another version of the strain assisted dissolution model is the film rupture theory. According to this mechanism, mechanical rupture of an otherwise protective film leads to rapid localized corrosion at the film rupture site, leading to crack initiation in emerging slip bands, and subsequently to corrosion assisted crack growth due to the high stress concentrations associated with crack tips [24,31-36].

While these mechanisms can be used to explain results observed for aluminum alloys exposed to liquid phase corrosive solutions, it is difficult to relate them to the significant decreases in fatigue resistance observed in water vapor or in deaerated distilled water. Additionally, the observation that the effects of pre-corrosion are at least partially reversible through conventional heat treatments suggests that this mechanism may be untenable even for aqueous corrosion fatigue. Thus, it may be considered that strain assisted dissolution processes cannot adequately explain either crack initiation processes or enhanced crack propagation process for these alloys.

B. Surface Energy Reductions

According to this theory, specific species which are strongly adsorbed at surfaces serve to lower the local bond energy and accordingly lead to increases in crack propagation rates. Some investigators have also suggested that reductions in surface energy may enhance plasticity and cause early crack initiation and propagation [37]. Still other investigators have suggested that surface energy reductions in growing cracks may reduce crack tip plasticity and thus induce brittleness [17]. Problems with acceptance of adsorption models have generally centered on the large amount of plastic energy associated with crack growth versus the relatively small amount of surface energy ($\approx 10^3:1$). Thus even large changes in surface energy should not appreciably affect cracking tendencies. Also, the observation that an appreciable effect on $SO_4^=$ ion is at least as damaging as Cl^- ion under cathodic charging conditions would tend to discount a specific species explanation.

C. Hydrogen Assisted Cracking

The possibility that aluminum alloys may suffer from hydrogen embrittlement was strongly suggested by experiments which showed that, for thin specimens, air borne water vapor caused totally brittle failures in Al-

Zn-Mg alloys [38,39]. In fact, brittle intergranular cracks were observed by high voltage transmission electron microscopy in thin foils of these alloys with no signs of anodic dissolution or plasticity. Further experiments indicated that, after exposure of this alloy to water vapor, voids were observed to grow from interactions with a focused electron beam. Also, fracture of these specimens in a mass spectrometer was accompanied with the release of clearly identifiable amounts of hydrogen [39]. Tensile experiments in an Al-Mg alloy (5086) charged with tritium also showed discontinuous yielding associated with tritium release [40]. It appears certain then, that Al alloys which contain hydrogen are accordingly embrittled and that there appears to be dislocation - hydrogen interactions.

Proposed Mechanism of Corrosion Fatigue of Al Alloys

On the basis of the results presented in this discussion, and on recently obtained, but yet unpublished results obtained at Rensselaer, it appears that this latter mechanism, that of hydrogen embrittlement, can successfully be applied to corrosion fatigue of high strength aluminum alloys. Table II summarizes some of the relevant arguments with support or lack of support for either a hydrogen embrittlement process or an anodic dissolution process. Perhaps the most significant observations are that water vapor alone can produce increases in crack propagation rates, which are equivalent to increases in rates obtained in distilled H_2O alone or with Na_2SO_4 additions. Also, the partial reversibility of damage when tested in air after exposure to pre-corrosion is strongly indicative of a dissolved species rather than an adsorbed species which is responsible for embrittlement. Other peripheral observations such as the effects of load mode (Mode I or tension being worse than Mode III or torsion) and the absence of mean stress effects permit the presentation of a qualitative model for corrosion fatigue of high strength Al alloys.

According to this model, hydrogen dissolved in the alloy, in the process zone at a crack tip, embrittles this region and causes increases in crack propagation rates. The specific process by which the embrittlement occurs remains elusive, although it may be significant that those alloys which have small, semi-coherent particles are the most susceptible to failure. Consideration that the non-coherent precipitate-matrix interface at grain boundaries in statically loaded specimens is the preferred crack path, suggests that hydrogen may collect at these interfaces to cause decohesion. Under cyclic loading conditions, the mobile dislocations may act as short circuit paths for hydrogen to precipitate at interfaces in the grain interiors in preference to grain boundary regions. Thus the fracture path is shifted to transgranular, since effective diffusion rates are enhanced still more than are grain boundary diffusion rates. It may be significant to note that, for alloys with equiaxed grains, low cyclic stresses and small amounts of cathodic charging result in intergranular crack initiation and early propagation even under cyclic loading conditions. As the cracks elongate, however, the local effective stress increases, dislocation densities and mobilities increase, and the cracks shift to a transgranular mode (Table III). The crack path shifts to {110} or {112} planes from the {111} slip planes (in non-aqueous environments) which has been reported may also be associated with a particular precipitate/matrix interfacial plane where hydrogen collects.

Since it has also been shown that sulfate is as effective as chloride in reducing fatigue resistance if external sources of hydrogen (cathodic charging) are applied, the specific role of chloride appears to be related to chemical damage of the otherwise protective film allowing the ingress of hydrogen to the alloy. In the absence of chemical damage to the film, mechanical damage by slip step intersection, first with the free surface for

Table II. A Summary of Experimental Observations on the Mechanisms of Corrosion Fatigue of Al Alloys

Experimental Observation	Hydrogen Embrittlement	Enhanced Anodic Dissolution
Sensitivity to water in both the liquid and vapor form.	Strong support for H.E.	Water vapor should have no effect when crack is not filled with a liquid phase.
Crack path shift reported from {111} to {100} in aggressive solutions.	Consistent with environmentally induced cleavage.	Not easily attributable.
Sensitivity to Anion Type and Concentration.	Affects the passivation rate and oxide film stability which control both mechanisms.	
Decreased fatigue resistance in both acid and basic Na_2SO_4.	Consistent if modifications in the oxide are more important than H^+ concentration of bulk solution.	Supportive because both make the oxide less stable and make dissolution easier.
Decreased fatigue resistance with cathodic polarization in NaCl.	Supportive, higher surface hydrogen concentration.	Some support, can be explained by changes in oxide film.
Decreased fatigue resistance with anodic polarization in NaCl.	Consistent with the non-protective nature of oxide and higher H^+ activity.	Supportive, increasing dissolution rate of cracking.
Decreased fatigue resistance in Na_2SO_4 with cathodic polarization.	Parallel behavior as in NaCl because there is increased hydrogen in both solutions.	Some support due to less protective oxide film.
Similarity between potential dependence for fatigue and hydrogen permeation in in NaCl.	Strong support.	Can be explained by modifications in oxide film behavior.
Fatigue in deaerated solutions.	Consistent with easier H entry.	Can be explained by resultant changes in the oxide film.
Pre-exposure effect and the partial reversibility upon reheat treatment.	Unambiguous support for H.E.	Cannot be explained.
Insensitivity of fatigue lives to mean stress in aggressive environments.	Consistent with idea of H transport by mobile dislocations which are produced by cyclic stress component.	Consistent with mechanism because the cyclic stress controls the slip step area exposed.
Insensitivity to aggressive environments under Mode III loading compared to Mode I loading.	Supportive, there is no hydrostatic stress component in Mode III to concentrate H in the crack tip region.	Not supportive unless effect is due to the inability of the solution to get to the crack tip region. This is considered unlikely in dynamic fatigue testing.

crack initiation, and subsequently with advancing fracture surfaces, allows hydrogen to enter the alloy, again presumably carried by dislocations. Thus non-chloride containing aqueous media (water vapor, distilled water, $SO_4^=$ solution, etc.) all behave in a similar manner. According to this model, only the process zone at the crack tip need contain hydrogen to cause accelerated crack growth. Thus the normally low bulk diffusion rates generally reported for hydrogen in aluminum alloys need not be rate controlling.

Table III. Effect of Cyclic Load on the Fracture Morphology of Al-5.5Zn-2.5Mg-1.5Cu in 0.5M NaCl Polarized to -1.75V versus SCE

Cyclic Stress MPa at σ_m = 207 MPa	% Intergranular Failure
76	0
69	0
55	0
41	10
28	26
17	35

A second aspect of the model is the requirement for a specific distribution and morphology of strengthening precipitates. Thus alloys such as 1100 Al (commercially pure) or 2024 (Al-Cu) would not necessarily be expected to be embrittled. Likewise, overaging or underaging heat treatments which alter precipitate/matrix relationships would be expected to alter the sensitivity of alloys to corrosion fatigue.

In summary, the key to the corrosion fatigue phenomenon in Al alloys may be related to the method by which hydrogen enters the alloy. Since the naturally formed film on the alloy appears to exhibit a low permeation to hydrogen, those mechanical or chemical events which weaken or damage the film may control the crack initiation/propagation process. This would then help to explain the effects of cyclic stress range and the lack of effect of mean stress level (mechanical factors) and the effects of such variables as chloride ion, high or low pH, applied potentials or currents, and solution chemistry in general.

Conclusions

In conclusion, a model for corrosion fatigue of high strength Al alloys is proposed which is dependent on surface film integrity. Chemical or mechanical damage to the film allows exposure of hydrogen of emerging dislocations (slip planes) which effectively "pump" hydrogen into the crack process zone. It is further suggested that the hydrogen collects at precipitate matrix interfaces and, through some still unknown specific mechanism, causes separation of the interfaces. The model is an extension of previous models proposed for stress corrosion cracking of these alloys, except that the cyclic nature of the dislocation motion creates a preferentially high diffusion path into the process zone rather than into the normal high diffusity zone of grain boundaries.

Acknowledgement

The support of the U.S. Office of Naval Research and the continued encouragement of Dr. P. A. Clarkin are gratefully acknowledged.

References

1. J. T. Staley, Met. Eng. Quarterly, 16 (1976) p. 52.
2. C. E. Lyman and J. B. VanderSande, Met. Trans. A, 7A (1976) p. 1211.
3. P.J.E. Forsyth, Acta Met., 11 (1963) p. 703.
4. C. A. Stubbington and P.J.E. Forsyth, J. Inst. Metals, 90 (1961) p. 374.
5. C. Calabrese and C. Laird, The Cyclic Stress-Strain Response of Metals and Alloys, Proc. 3rd Int. Conf. on Fracture, Munich, 6 (1973) V231; Cyclic Stress-Strain Response of Two-Phase Alloys, I. Microstructures Containing Particles Penetrable by Dislocations, II. Particles not Penetrable by Dislocations, Mater. Sci. Eng., 13 (1974) p. 141.
6. D. J. Duquette and R. R. Swann, Acta Met., 24 (1976) p. 241.
7. H. Hartman, Int. J. of Fract. Mech., 1 (1965) p. 167.
8. R. P. Wei, Eng. Fract. Mech., 1 (1970) p. 633.
9. T. Broom and A. Nicholson, J. Inst. of Metals, 89 (1960) p. 183.
10. R. P. Wei, Int. J. of Fract. Mech., 4 (1968) p. 159.
11. M. Nageswararao, G. Kralik and V. Gerold, Z. Metallik, 66 (1975) p. 479.
12. M. Nageswararao and V. Gerold, Met. Trans., 7A (1976) p. 1847.
13. S. J. Hudak and R. P. Wei, Corrosion Fatigue, ed. O. Devereux, A.J. McEvily and R. W. Staehle; NACE, Houston (1981) p. 433.
14. C. Zapffe and C. Sims, Trans. Met. Soc. AIME, (1941), 145 p. 225.
15. R. M. Pelloux, Fracture 1969, op. cit., p. 731.
16. R. J. Selines and R. M. Pelloux, Met. Trans., 3 (1972) p. 2525.
17. R. E. Stoltz and R. M. Pelloux, Met. Trans., 3 (1972) p. 2433.
18. R.M.N. Pelloux, ASM Trans. Quart., 62 (1969) p. 281.
19. J. C. Grosskreutz, Surface Sci., 8 (1967) p. 173.
20. C. A. Stubbington, Metallurgica, 65 (1963) p. 109.

21. P.J.E. Forsyth, Acta Met., 11 (1963) p. 703.

22. R. P. Wei and J. D. Landes, Int. J. of Fract. Mech., 5 (1969) p. 69.

23. R. J. Jacko, Ph.D. Thesis, Rensselaer Polytechnic Institute, (1978).

24. F. P. Ford, Ph.D. Thesis, Cambridge University, 1973.

25. B. F. Brown, C. T. Fujii and E. P. Dahlberg, J. Electrochem. Soc., 116 (1969) p. 218.

26. A. J. Sedriks, J.A.S. Green and D. L. Novak, Localized Corrosion, op. cit., p. 569.

27. D. Whitwham and U. R. Evans, J. Iron and Steel Inst., 165 (1950) p. 72.

28. D. J. Duquette and H. H. Uhlig, Trans. ASM, 61 (1968) p. 449.

29. D. J. Duquette and H. H. Uhlig, Trans. ASM, 62 (1969) p. 829.
30. H. N. Hahn and D. J. Duquette, Acta Met., 26 (1978) p. 279.

31. K. Laute, Oberflachentech, 10 (1933) p. 281.

32. T. Pyle, V. Rollins and D. Howard, Corrosion Fatigue, Chemistry, Mechanics and Microstructure, op. cit., p. 312.

33. T. Pyle, V. Rollins and D. Howard, J. Electrochem. Soc., 122 (1975) p. 1445.

34. C. Patel, T. Pyle and V. Rollins, Met. Sci., 11 (1977) p. 185.

35. C. Patel, T. Pyle and V. Rollins, Nature, 266 (1977) p. 517.

36. F. P. Ford and T. P. Hoar, Proc. of 3rd Int. Conf. on Strengthening of Metals and Alloys, Cambridge, 1973, paper 95.

37. S. P. Lynch, in Mechanisms of Environment Sensitive Cracking of Materials, 1977, p. 201, the Metals Society, London.

38. G. M. Scamans and C.D.S. Tuck, Second Int. Cong. on Hydrogen in Metals, Paris, 1977, paper 4A11.

39. L. Montgrain and R. P. Swann, Hydrogen in Metals, op. cit., p. 575.

40. J. A. Donovan, Met. Trans., 7A (1976) p. 1677.

MODIFICATIONS IN MICROSTRUCTURE DEFORMATION AND FATIGUE BEHAVIOR BY ION IMPLANTATION

K. V. Jata and E. A. Starke, Jr.
Department of Materials Science
University of Virginia
Charlottesville, VA

A number of materials, copper, aluminum, titanium and steel, have been examined for microstructural evolution, deformation and fatigue behavior in the non-implanted, as-implanted and implanted + annealed conditions. A wide variety of implant species that produce residual compressive stresses, residual tensile stresses or cause precipitation have been chosen to examine the above effects. The main goal, however, has been to choose implant species that would enhance deformation and fatigue resistance through a modification in the surface microstructure and/or by providing residual compressive stresses. In instances where no major changes in the surface microstructure are observed, it appears that surface dislocation sources either become inoperative or become operative on a larger number of slip planes, limiting the size of the slip steps that would nucleate fracture. In materials where major changes in the microstructure are observed, slip is dispersed, also resulting in fine slip that enhances resistance.

Introduction

This paper will review work on surface modification of materials by ion plating and ion implantation that was sponsored by the Office of Naval Research under the program direction of Dr. Philip Clarkin. Ion implantation is being used to modify surface-related mechanical properties such as friction and wear, fatigue, corrosion and, recently, near surface deformation at high temperatures [1-5]. The major thrust has been in friction and wear, since small doses of implanted atoms produce large effects. Application to fatigue mainly stems from the fact that the fatigue cracks normally nucleate at the surface of a structure and propagate inward. The fatigue process may be divided into two stages, which are crack initiation and crack propagation. For a defect-free metal, the process of initiation and early microcrack linkage is usually associated with the cyclic deformation behavior of the surface layer. This process is found to occur in conjunction with slip band formation [6] in the surface region, or with incompatibility of deformation between two neighboring grains on the surface [7,8]. Any surface modification which reduces the magnitude or increases the homogeneity and reversibility of cyclical deformation is expected to improve the fatigue crack initiation resistance. Surface modification of materials can be achieved by a number of techniques such as shot peening, nitriding, ion plating, ion implantation and laser glazing. Of these, ion implantation has several unique advantages that the other techniques do not offer. It has the advantage of introducing almost any ion substitutionally and interstitially into the target substrate without affecting the desirable bulk properties. There are no dimensional changes and problems such as delamination of the layer do not exist. The dose of ions could be introduced in a well controlled manner and the property changes can therefore be easily reproduced. Although the implanted layer is usually a few hundred to a thousand nm thick, substantial changes in fatigue properties can be observed. This paper will give an overview of the various effects that ion implantation can have on microstructure, deformation behavior and fatigue crack initiation resistance. The materials include pure Cu, pure Al, two titanium alloys, 4140 steel and a 2124 Al alloy.

Discussion of Results

In this section, the results of ion implantation effects on various materials are discussed. We start with pure copper as this formed the basis of further work on complex alloys. Next, microstructural evolution in pure Al is discussed. This is followed by the discussion of ion implantation effects in commercial alloys.

Ion Plating and Implantation Effects in Cu

The initial work carried out by Chen and Starke [9] have shown that ion plating can have a major effect on the fatigue behavior of copper single and polycrystals. When they plated silver (low stacking fault energy, SFE) on copper, the cyclic deformation behavior of the surface changed toward that of silver. Crack initiation was retarded because of a reduction in the propensity for cross slip compared with the copper substrate and subsequent reduction of slip band formation. Nickel (high SFE) plating had an opposite effect.

Ion implantation studies were later performed on polycrystalline copper [4,10] to obtain a clear understanding of the mechanisms involved in the modification of fatigue properties. The purpose of the work was to study the change in monotonic and cyclic deformation behavior of copper with three different species -- aluminum, boron and chromium -- and to correlate measured mechanical properties with the deformation behavior of copper as modified by ion implantation. It was expected that all three elements will introduce a similar defect structure but of varying degrees of intensity. Also, boron atoms, because of their small size with respect to copper, were expected to introduce tensile residual surface stresses, and aluminum atoms, because of their larger size, were expected to introduce compressive stresses. X-ray diffraction results [11] of aluminum and boron implanted copper single crystals have shown this to be the case.

Specimens were implanted at 100 keV with either aluminum, boron or chromium ions to a dose of 5×10^{19} ions/m^2. To insure uniformity of implantation, the specimens were rotated in the beam which was scanned across an aperture spanning the gage length. Fatigue tests of ion implanted and non-implanted samples were conducted on a servohydraulic closed-loop testing machine in laboratory air at 298°K. Low cycle fatigue measurements were made using constant total strain control with a saw-tooth wave form at a strain rate of 4×10^{-3}/s. Stress control, high cycle fatigue tests were made using a frequency of 10 Hz.

The monotonic stress-strain curves of the various materials are given in Fig. 1(a). The figure shows that ion implantation reduces the flow stress at low strains. The reduction in stress is largest for the aluminum-implanted sample. The monotonic yield stress and degree of hardening appear to be reduced due to ion implantation, with aluminum implantation having a somewhat larger effect. The cyclic stress-strain response studies showed all materials to cyclic harden considerably which is typical of annealed copper. An initial rapid hardening is followed by a saturation stage. The saturation stress versus applied plastic strain amplitude for nonimplanted and implanted metals

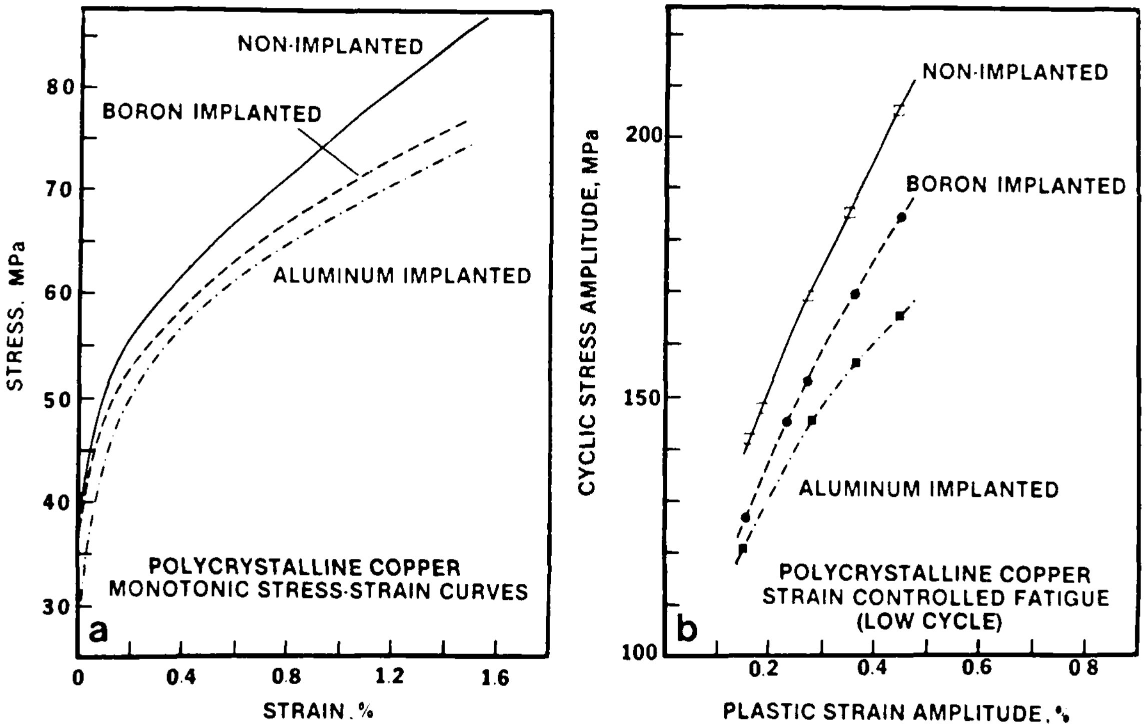

(a) (b)

Fig. 1 - The effect of ion implantation on (a) monotonic stress-strain curve, and (b) cyclic stress-strain relationship of polycrystalline copper.

are plotted in Fig. 1(b). The cyclic low stress appears to be lowered by ion implantation. Aluminum implantation again shows the most significant effect. The cyclic strain-life response (LCF) for the nonimplanted and implanted polycrystalline copper are presented in Fig. 2(a). The relationship between the number of cycles to failure and the plastic strain amplitude may be represented by a power function proposed by Coffin and Manson given by $\varepsilon_{pa} = \varepsilon_f(2N_f)^c$, where N_f is the number of cycles to failure, ε_f is the fatigue ductility coefficient and c is the fatigue ductility exponent. This relationship appears to hold for the materials tested in this research. The results indicate that ion implantation improves the fatigue ductility behavior. Aluminum implantation appears to have the most significant effect.

The effect of ion implantation on the high cycle fatigue life is shown in Fig. 2(b). Aluminum implantation gives rise to a significant improvement in fatigue life, with a greater improvement at lower stresses. Boron implanta-

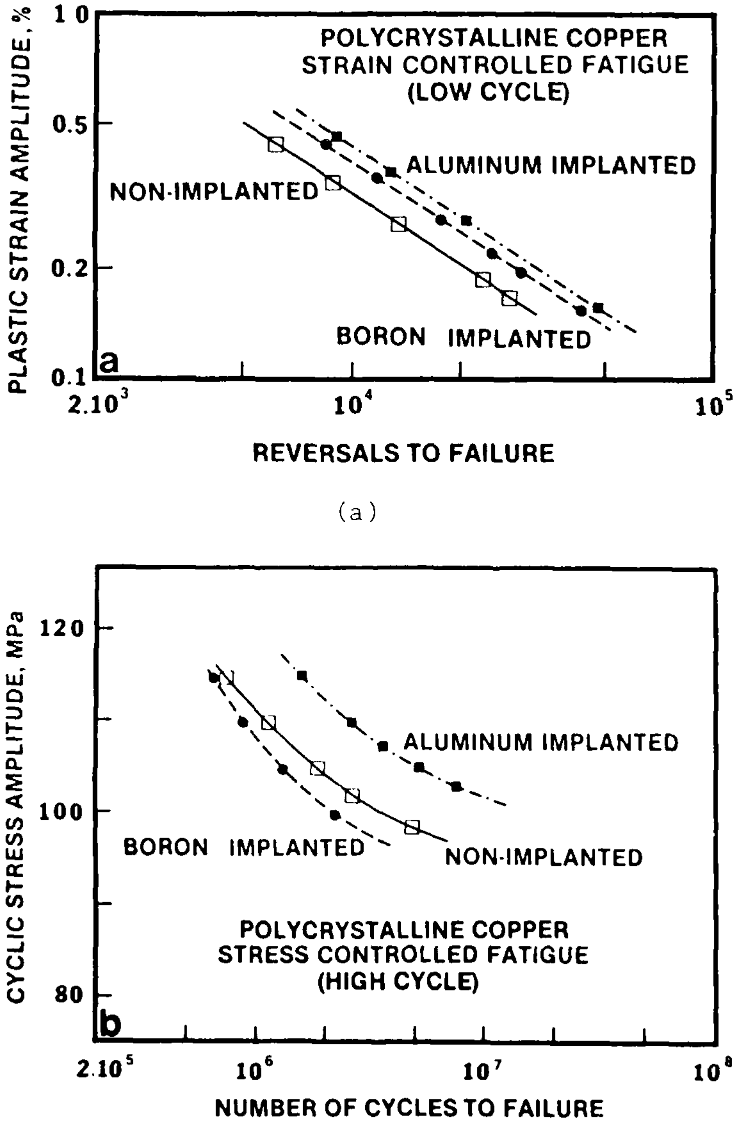

(a)

(b)

Fig. 2 - The effect of ion implantation on (a) cyclic strain-life relationship, and (b) cyclic stress-life relationship of polycrystalline copper.

tion, in contrast, shows a reduction in resistance to cyclic stress, with a greater reduction in life at lower stresses. The limited data on chromium implantation appeared to indicate that it improves the cyclic stress resistance almost as well as aluminum implantation.

The surface observations of the strain controlled fatigued samples showed the presence of persistent slip bands (PSB) and associated intrusions/extrusion. However, the propensity of PSB formation appeared to be reduced by ion implantation. Aluminum implantation had the most significant effect. Most of the microcracks were at the grain boundaries. Some cracks associated with PSB were also observed, being more frequent for the non-implanted samples and least for the aluminum implanted samples. Implanted samples showed a lower degree of surface rumpling and fewer surface microcracks compared with non-implanted samples deformed to the same degree. The stress controlled fatigue samples showed cracking to be more prominent with PSB than that of strain controlled fatigue samples.

The TEM results and the X-ray analysis by Spooner and co-workers [11] indicated that aluminum implantation gives rise to compressive residual surface stresses, a large number of small dislocation loops, and arrays of dislocations. Boron implantation, on the other hand, produces tensile residual stresses, a smaller number of larger loops, and dislocation arrays. Since the size of the chromium atom is not much different from that of copper, it may be assumed that chromium implantation does not produce any significant residual surface stresses. If the increase in the numbers of atoms by ion implantation forces implant or host atoms into the interstitial sites, creation of compressive residual stresses will be expected. However, with some diffusion (probably enhanced by radiation damage) these form an extra atom layer occupying substitutional sites (such a mechanism is reasonable since TEM studies showed that there is sufficient diffusion to create dislocation loops from the initial radiation damage). Therefore, significant compressive stress will not be created due to interstitials. This may explain why boron implanted copper has tensile residual stresses. Perhaps most of the boron atoms are in substitutional sites, and since they are considerably smaller than the copper atoms, tensile residual stresses are created. TEM contrast studies of some of the loops indicated that most are the result of a collapse of clusters of vacancies created by ion bombardment. It appears that since heavier (and larger) Cr and Al atoms have a more efficient transfer of energy than B atoms, the defect structure of Cr and Al implanted surfaces has greater density. Since the foils used for TEM observations are thicker than the damaged layer (which decreases with atomic number), the concentration of defects is actually even higher for Cr and Al implanted samples than it appears in their micrographs. In addition to the defect structure and residual surface stresses, the alloying of the surface material is expected to lower the stacking fault energy (SFE) of this region. It is likely that precipitation of chromium will occur in the chromium implanted samples during fatigue cycling. The effect of lowering SFE will be lost at that stage, and the presence of chromium precipitates has to be considered instead.

The implantation of Al, B, or Cr ions lowers the yield stress and the degree of monotonic and cyclic hardening. The reduction in yield stress and monotonic hardening at low strains is perhaps due to the availability of free dislocations on the surface which tends to promote slip at lower stresses. Aluminum implantation, which produces a larger degree of surface defects, consequently shows a larger reduction of monotonic flow stress.

The reduction of cyclic hardening was explained in terms of the lowering of the SFE and the presence of dislocation loops and arrays due to ion-implantation. Lowering the SFE leads to a reduction in the tendency for cross slip. This improves the reversibility of cyclic deformation and reduces cyclic hardening. Dislocation loops are barriers to slip and tend to homogenize deformation by reducing the slip distance. Improved homogeneity of slip due to implantation aids in reducing the resistance to cyclic deformation. Aluminum implanted samples have a higher degree of surface defects, the greatest reduction in hardening, and, therefore, the lower cyclic flow stresses. The chromium implanted samples have a similar defect structure. However, it appears that Cr precipitation during cycling increases cyclic hardening somewhat by tying up slip dislocations.

Under strain controlled fatigue, the microcrack formation and eventual failure of the materials follow what is expected from the foregoing discussion of the cyclic hardening behavior. The effect of ion implantation is to improve slip reversibility and homogeneity, and, in general, this leads to improvement in the low cycle fatigue life, regardless of the exact mechanism of cracking. The difference between the FCI resistance of boron and aluminum implanted samples is again due to the difference in defect structure. Aluminum implantation produces the most significant effect because it gives rise to a more intense defect structure. Even though chromium implantation results in a defect structure similar to aluminum, the expected intervention of chromium precipitation decreases the resistance to FCI under what is expected from its defect structure.

Under stress control, the ion implanted samples are expected to show improvement in fatigue life due to better slip homogeneity and reversibility. However, other parameters must be considered. Aluminum implanted samples have beneficial compressive surface stress. The compressive stress tends to reduce the more damaging (i.e., tensile) component of the cyclic stress and, hence, improves the fatigue life. The tensile residual surface stress produced by boron implantation decreases the resistance to stress cycling. The beneficial effects of surface defects due to implantation are overcompensated by the detrimental effects of the residual tensile surface stresses.

Microstructural Studies of Pure Aluminum

Ion implantation offers the possibility of obtaining alloys having: (i) a highly super-saturated solid solution with extended solid solubility over that predicted by the phase diagram; (ii) a solid solution with stable and metastable phases; and (iii) a disordered or amorphous structure in metal-metal or metal-metalloid systems. In many instances, alloy systems produced by rapid quenching have been duplicated by ion implantation [12,13] and parallels have been drawn between the two techniques. In ion implantation, the thermal spike concept [14] suggests that local heating of the target could take place on the impingement of an ion with energy values of the order of 50-500 keV. The temperatures in the hot zone produced by the thermal spike could exceed the melting point of the solid, however, the time scale of the thermal spike is only a few pico-seconds resulting in an ultra fast quench of the molten zone. Consequently, the diffusion required to form the metastable and stable phases cannot occur during the thermal spike. A second theory suggests that some precipitation could, however, occur due to radiation enhanced diffusion [15] which depends on the defect production rate and number of dislocations per unit area, since the radiation enhanced diffusion coefficient is many orders of magnitude larger than the thermal diffusion coefficient. The former phenomenon where a supersaturated solid solution exceeding the solubility limits of the solute can be obtained at room temperature is similar to the rapid solidification technique. The above concepts have been used in aluminum implanted with Fe [16]. Iron has a solubility limit of 0.05 wt. percent and a diffusivity of only 4.1×10^{-13} m^2/s and in normal wrought alloys is present as large inclusions which are detrimental to fatigue life. So, by adopting ion implantation technique it should be possible to obtain a fine dispersion of Al_6Fe or Al_3Fe precipitates which would homogenize slip and thereby improve fatigue life.

Discs of high purity Al of Marz grade quality with 3×10^{-3}m diameter and 2.54×10^{-4}m thickness were prepared. These discs were then thinned in a methanol-nitric acid electrolyte and subsequently implanted with iron on one face. Two energies were used, 50 and 100 + 50 keV and the doses were 5×10^{19} and 5×10^{20} ions/m^2. The double dosage 100 + 50 keV implantation was performed with a time interval of one hour between the 100 and 50 keV implantations. The temperature rise of the discs during implantation is estimated to be less than 373°K. Electrothinning was then completed by masking the implanted face with a lacquer. The thin foils were subsequently examined in TEM.

For both 50 and 100 + 50 keV dosages, extensively damaged substructure typical of ion implanted materials was observed. In Fig. 3(a) a bright field transmission electron micrograph for a 50 keV Al implanted foil is shown. The left part of the micrograph shows the implantation damage and the right part shows a typical modulated structure observed in these foils. The composition fluctuations in the modulation are found to be in <111> direction and 10 nm apart. The corresponding electron diffraction pattern, Fig. 3(b) of the modulated structure, shows satellite spots near the Bragg reflections. These satellite spots are not observed due to the presence of dislocation defects produced by implantation. It was difficult to observe the modulated structure under two beam conditions since this structure was masked by the implantation damage which comes under view for maximum contrast conditions. Moire fringes were also observed in the areas of the modulated structure. As expected, these fringes shifted their relative position with respect to the modulated structure as the specimen was tilted in the stage around the axis of the transmitted electron beam path. Thus, it was clearly possible to distinguish between the modulated structure and the Moire fringes. The micrograph, Fig. 4(a), was taken using the conditions when the fringes and the damaged structure were completely out of view. A further confirmation of the presence of the modulated structure was obtained from the 100 + 50 keV foil which was given an annealing treatment at 793°K for 15 minutes. This treatment removed

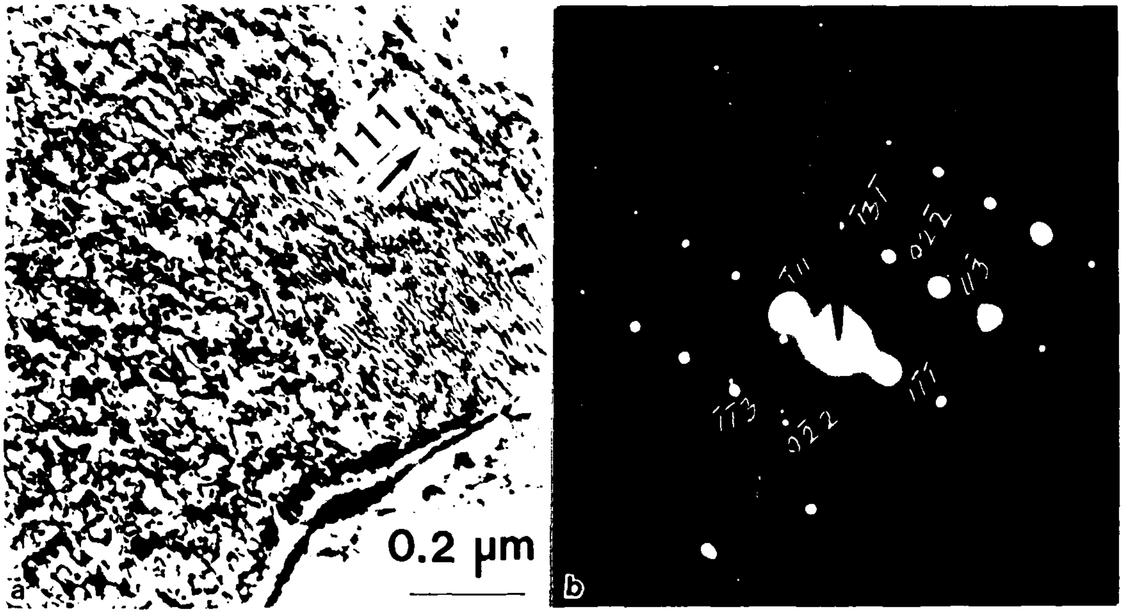

Fig. 3 - (a) TEM's of 50 keV as-implanted showing modulations in <111> direction and damage, (b) SAD of modulations showing satellites.

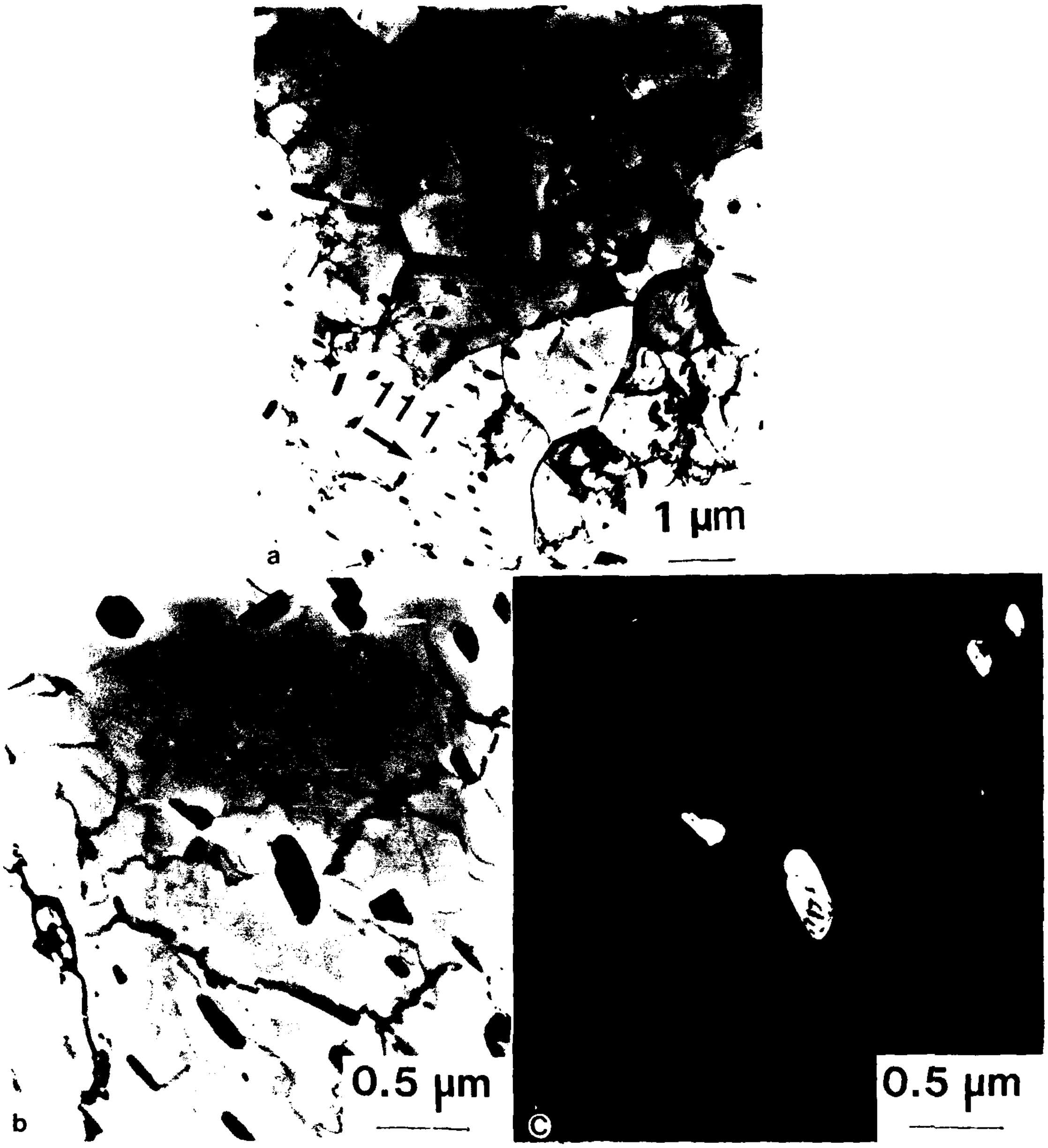

Fig. 4 - (a) TEM's of 50 keV + 30 min. annealing at 793°K showing Al_3Fe precipitates aligned along <111> direction; (b) bright field and (c) dark field images of Al_3Fe.

the extensive damage resulting from the double dosage ion implantation. The micrographs clearly revealed rod-like precipitates and many areas of retained modulated structure. The 50 keV foils were also examined after an annealing treatment of 30 minutes at 793°K. Al_3Fe precipitates were observed which were aligned in the <111> direction with respect to the matrix. These precipitates are shown in Fig. 4(a). A higher magnification pair of bright and dark field micrographs are shown in Fig. 4(b) and (c). The growth of these precipitates seems to bear an orientation relationship with the composition fluctuations found along <111> direction in Fig. 3(a). Figure 4(a) might also imply that the modulations in regions where the subgrain boundaries are tilted at small angles prefer the same orientation.

Fatigue Studies of Commercial Alloys

The concepts developed for pure copper were later applied to commercial alloys. A binary Ti-24V [17] alloy implanted with Al ions at 100 keV to a dose of 5 x 10^{19} /m^2 showed a minor improvement in the fatigue life at intermediate plastic strain amplitudes (Fig. 5). An examination of the fatigue hysteresis loops for these amplitudes showed that the number of cycles to reach saturation stress increased by about 40 percent with Al implantation. In order to understand the beneficial effect of ion implantation on the fatigue behavior additional experiments were run, where bioden replicas were extracted from the specimen surface at different intervals of cycles during the course of the fatigue experi[illegible]. The bioden replicas were carbon shadowed at an angle of 30 degrees to [illegible] ess axis and were observed under an optical microscope. A pair of m[illegible] is illustrating the difference in the slip activity on the surface a[illegible] ic strain amplitude of 8 x 10^{-3} and at 150 cycles is shown in Fig. 6. [illegible] clear that the non-implanted specimen exhibits a number of parallel slip lines, suggesting major activity in only one slip system. With continued cycling, slip is concentrated along these lines, eventually leading to slip band cracking. In Fig. 6(b), it can be clearly seen that Al implantation homogenizes slip. The slip is accommodated in more than one slip system and thus the slip lines remain fine with continued cycling. Cracks were initiated only at grain boundaries where the slip lines impinge. No cracks were observed at slip line intersections. It is, however, surprising that in spite of a major change in the mode of cyclic slip behavior the fatigue life changed so little.

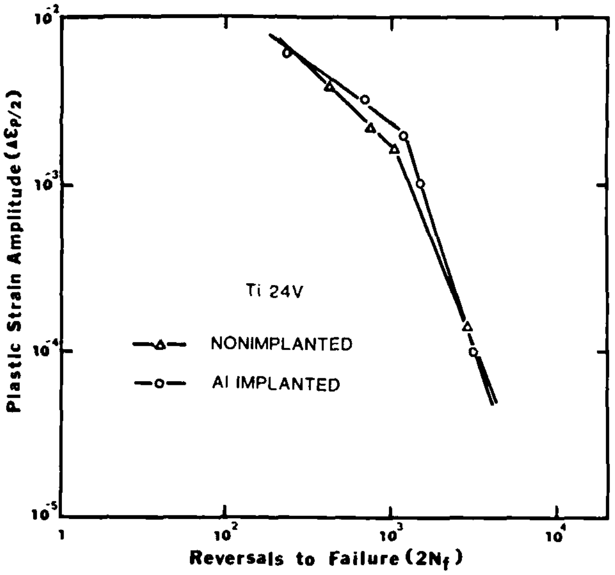

Fig. 5 - Coffin-Manson plot showing the plastic strain amplitude versus number of cycles to failure for the Ti-24V Al alloy.

In stress controlled experiments the beneficial effect of ion implantation is observed at all stress levels employed for testing, Fig. 7. In these tests, the tensile component of the stress amplitude ranged between 0.6 and 0.85 of the monotonic yield stress. At a stress amplitude of 400 MPa, the increase in life for the implanted samples is almost two orders of magnitude. Similar increases in fatigue life with ion implantation have been associated with compressive residual stresses as discussed before for the case of Cu. The residual stresses are significant since the range of stress amplitudes employed for the present study are well below the elastic limit of the material. The lattice parameter of Ti-24V is about 0.322 ± 0.001 nm and the

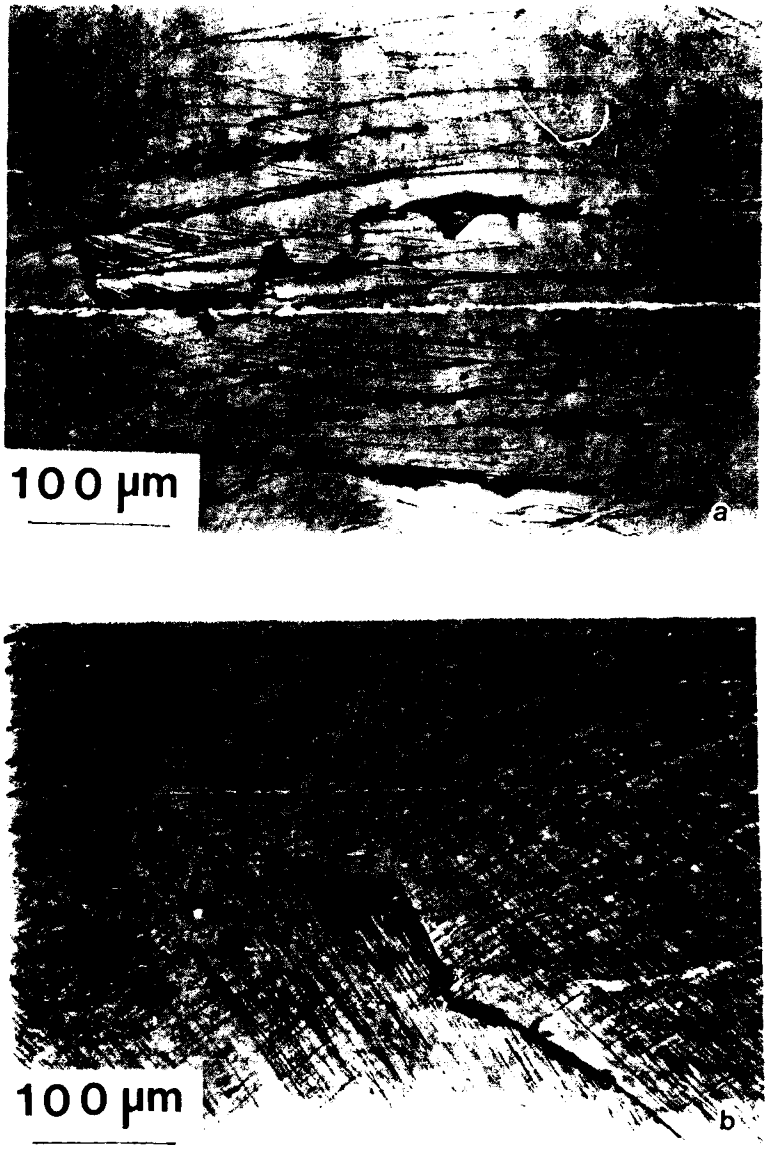

Fig. 6 - (a) Replica micrographs showing fatigue crack initiation in the non-implanted specimen, and (b) Al implanted specimen, at 150 cycles and $(\Delta\varepsilon_p/2) = 8 \times 10^{-3}$.

Goldschmidt's radii of Al, Ti and V are 0.143, 0.147 and 0.136 nm, respectively. Misfit strains due to the implantation of aluminum were calculated and found to be + 1.73%. This should result in a compressive residual stress which enhances the fatigue life in stress controlled conditions.

In contrast to the above materials, α/β Ti implanted with Al and 4140 steel with N [18] showed a decrease in life time in strain controlled tests. The mechanisms in α/β Ti were discerned by replica study and SEM examination of the surfaces of the samples fatigued to different number of cycles. These studies showed that the decrease in life time was due to an increased number of microcracks in the implanted case as observed in the replicas and a transition from wavy to planar slip as observed in the SEM. It was observed that the density of crack initiation sites in the implanted condition was almost

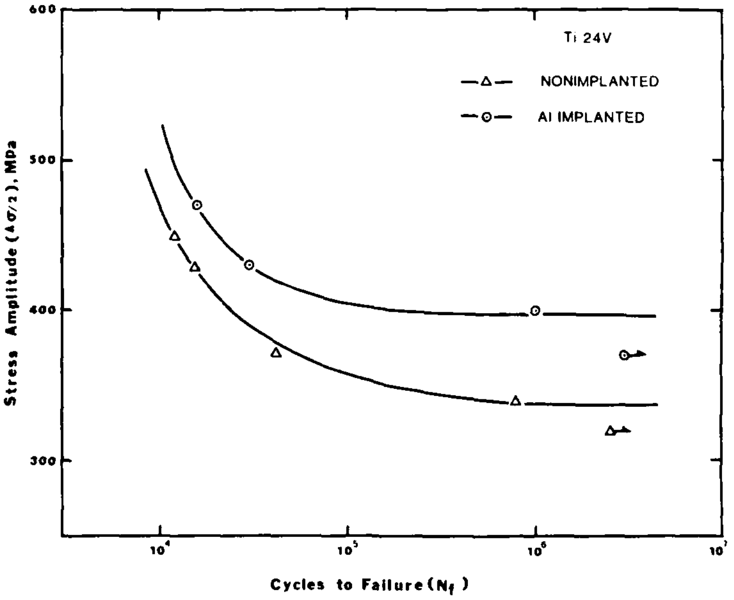

Fig. 7 - Stress amplitude vs. cycles to failure.

two times more than that in the non-implanted, thus easing the linkup of microcracks. Since these microcracks are formed in intense planar slip bands, the driving force for the linkup would be much more due to an additional hydrostatic stress component that results in a decreased fatigue life. In the case of 4140 steel, the mechanisms involved in the decrease of fatigue life were not studied. A more interesting finding was that the cyclic stress amplitude increased dramatically by 12-15 percent with nitrogen implantation. This is shown in Fig. 8 for two different strain amplitudes. The reason for this is the formation of Fe_4N (γ^1) precipitates, Fig. 9, which hardens the surface layer considerably. This hardening increases the high cycle fatigue life and endurance limit, as shown in Fig. 10.

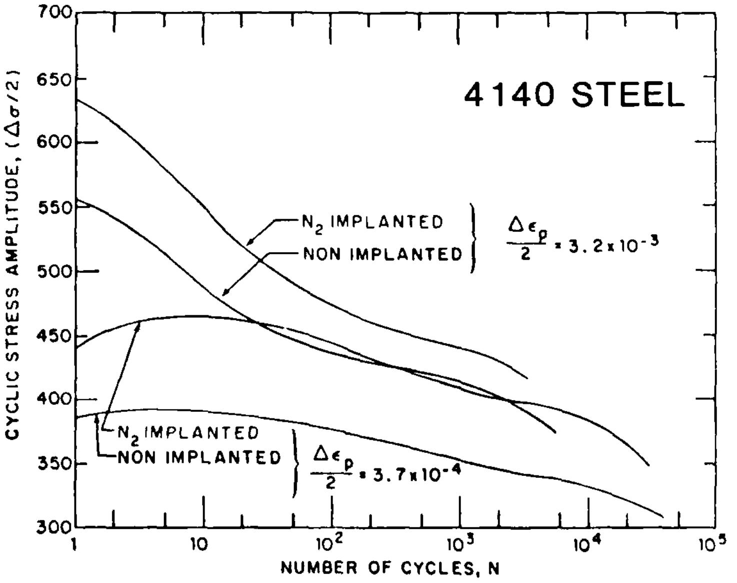

Fig. 8 - Cyclic stress amplitude curves for 4140 steel showing the increase in the stress amplitude with N implantation.

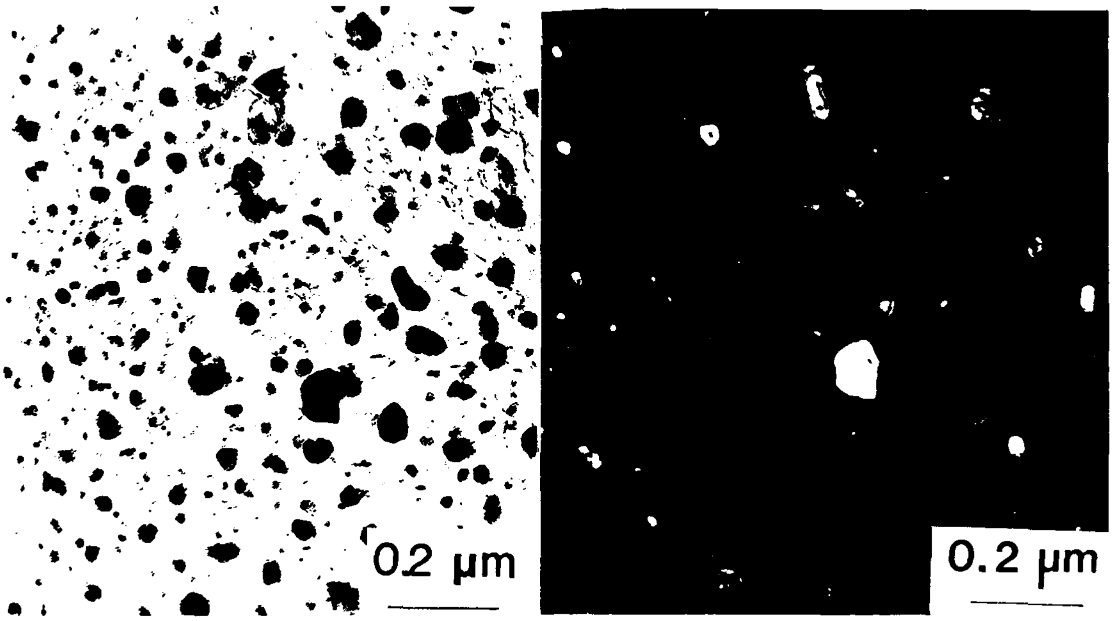

Fig. 9 - A pair of bright and dark field TEM's showing the Fe_4N precipitates.

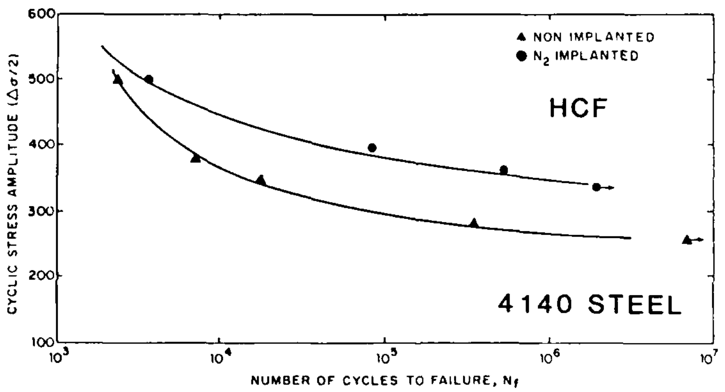

Fig. 10 - High-cycle fatigue curve for the 4140 steel showing increased fatigue resistance with implantation.

High Temperature Studies of Commercial Al Alloy 2124

In a recent investigation [19] we have examined the strain response at high temperatures, under a constant load in a 2124 Al alloy in the unimplanted, as-implanted with Fe and Ce and implanted plus annealed conditions. The 2124 alloy was chosen in the peakaged condition and as shown in Fig. 11(a), the microstructure consists of $S(Al_2CuMg)$ precipitates within the grains and some grain boundary equilibrium precipitates with the same composition and large Mn dispersoids. Fe and Ce were implanced at 150 keV to achieve a similar penetration depth which was 0.1 μm and the resulting atomic percent concentrations were 8Fe and 4Ce.

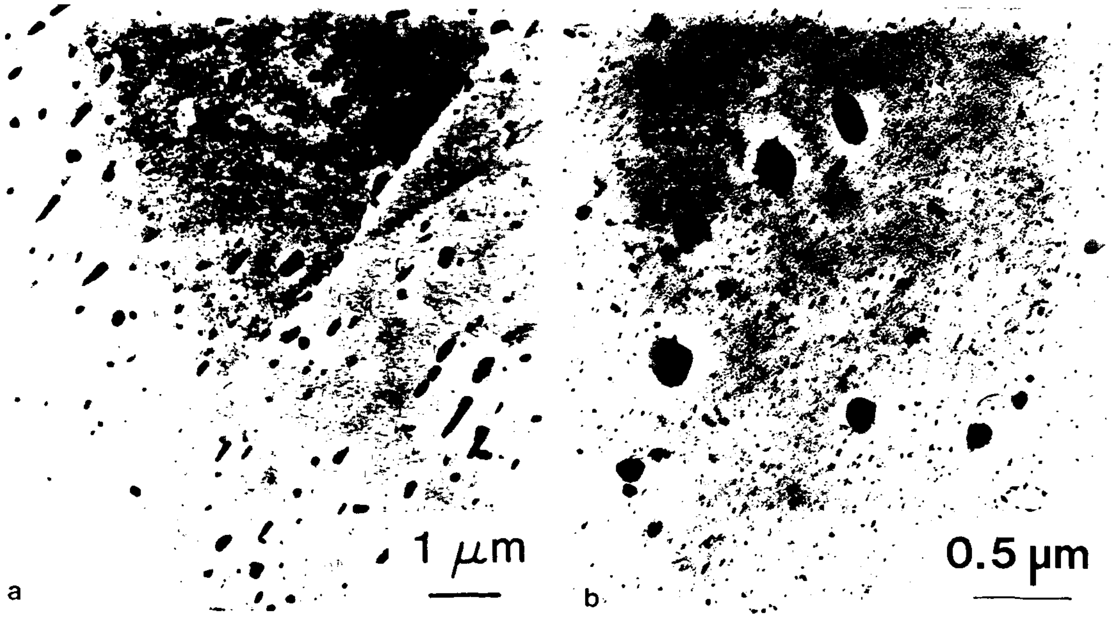

Fig. 11 - (a) Microstructure of the 2124 Al alloy, (b) Al_3Fe and $Al_{10}Fe_2Ce$ precipitation in the implanted plus annealed alloy.

Some implanted TEM foils were mounted in the hot stage of the electron microscope and were observed for microstructural evolution at 473°K. In the as-implanted condition, dislocation loops arising from the collapse of point defect clustering was observed. There was some evidence of microcrystallinity as inferred from the rings of the diffraction pattern. With annealing, much of the damage was removed and precipitation started to occur after 90 minutes of exposure at this temperature. Although the initial precipitates were round and 55 nm in diameter, subsequent annealing resulted in additional rod shaped precipitates which were 66 nm long. These precipitates did not coarsen and the fine dispersion was retained at least for four hours of constant examination. Both Al_3Fe and $Al_{10}Fe_2Ce$ precipitates were observed and these are shown in the micrograph of Fig. 11(b).

The retention of the strength at elevated temperatures in aluminum alloys essentially lies in its ability to maintain thermally stable microstructure. In this context, the implant species used in the present work provide excellent candidates due to their extremely small diffusion coefficients. In the preliminary experiments of creep, tests have been conducted in air to observe if any significant changes in creep strain would occur considering that the volume percent of the implanted material is only one hundredth of the total volume of the sample. In these tests, a single sample was first loaded to a stress level of 138 MPa and the temperature was rapidly increased to the desired starting temperature of 505°K by an induction heater. The sample was allowed to creep for a period of three and one-half hours and the strain was monitored with a high temperature extensometer. At the end of this period, the same sample was used for the next testing temperature of 533°K. This temperature was obtained within a period of two to three minutes and the strain was again monitored for one and one-half hours. In a similar fashion, the next test was performed at 573°K. The as-implanted sample failed at the beginning of the third segment of the test and the unimplanted sample failed rapidly at the end of the third segment of the test indicating that the sustenance to creep in the annealed condition was far superior than the other two tested conditions. It was also evident from these tests that the creep strain rates in the as-implanted condition were higher than the rates in the other conditions. The response of creep strain in the first period of testing is shown in Fig. 12. The analysis of the data of minimum creep strain rates at the end of each testing period shows that the rates diverge as the test temperature is increased. The present observations are similar to the results obtained by Hall on Mo implanted with heavy ions of Te, In and Ge.

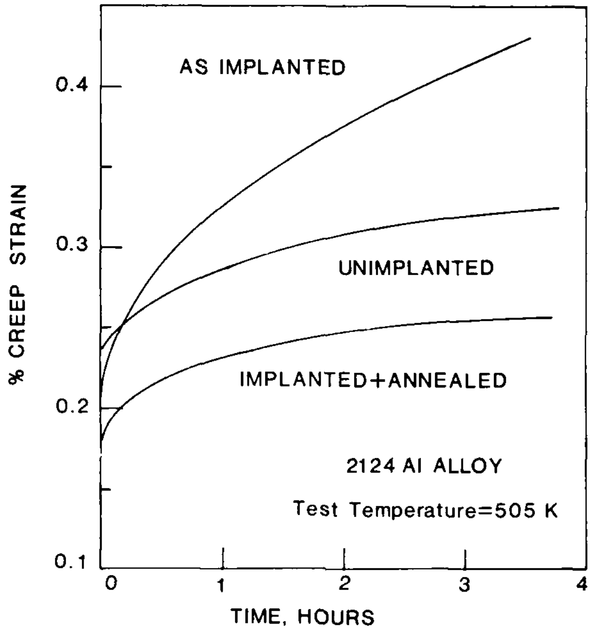

Fig. 12 - Creep strain versus time in the 2124 alloy at 138 MPa and T = 505°K.

The severe degradation in the creep resistance and early failure of the as-implanted specimen suggests that some drastic alteration in the microstructure has occurred upon ion implantation with Fe and Ce. Considering firstly, that the heavy Fe and Ce ions were used at 150 keV energy, which would produce a large flux of vacancies, and, secondly, that the grain size of the alloy in the long and long-transverse direction is greater than 100 μm, leads us to believe that the vacancies have migrated large distances beneath the surface and coalesced as voids at the grain boundaries. If this possibility exists, then further application of stress at high temperatures might have caused grain boundary failure either by boundary migration or void coalescence. This reasoning would also imply that void growth and coalescence or boundary migration which led to premature failure took place at a much faster rate than precipitate nucleation and growth during creep testing under the application of stress.

The specimens which were annealed at 463°K for 10 hours prior to creep testing exhibited stable Al_3Fe and $Al_{10}Fe_2Ce$ microstructure. These would impart both particle and subgrain boundary strengthening to the alloy by blocking dislocation movement and pinning the subgrains. Whether the annealing treatment eliminated the voids - which could have been formed as discussed above - is difficult to predict. The great improvement in the creep resistance and high failure strains, upon implantation plus annealing certainly suggests that the attained precipitate structure plays a major role. Further investigations are currently being conducted to confirm and understand the above proposed mechanisms.

Conclusions

Ion implantation can have a major effect on the cyclic deformation and fatigue life. When the deformation changes to a more homogeneous nature, reversibility of slip could increase which enhances low cycle fatigue life. It is also found that in such a situation the resulting cyclic flow stresses are lower in the implanted as compared to non-implanted. In complex alloys such as steel, nitrogen implantation hardens the surface considerably through dislocation-particle interactions which does not increase the low cycle fatigue life. In high cycle fatigue, compressive residual stresses are beneficial. Tensile residual stresses decrease fatigue life. In steel, high cycle fatigue life improves due to a hardened surface layer by dislocation-particle interactions. Generally, ion implantation produces a supersaturated solid solution unless precipitation took place by radiation enhanced diffusion. However, precipitation could be controlled by proper thermal annealing treatments after implantation has been performed. This could be exploited to obtain desirable fatigue and high temperature deformation properties, particularly in Al alloys.

Acknowledgements

We would like to thank our colleagues who contributed to this work: Dr. S. B. Chakrabortty, Dr. K. O. Legg, J. Han and D. Janoff. This research was sponsored by the Office of Naval Research under contract No. 00014-78-C-0270, Dr. Philip A. Clarkin, Program Manager.

References

1. J. K. Hirvonen, ed., Treatise in Materials Science and Technology - Ion Implantation, Academic Press, 13 (1980).

2. V. Ashworth, W. A. Grant and R. P. M. Procter, eds., Ion Implantation into Metals, Pergamon Press (1982).

3. G. K. Hubler. O. W. Holland. C. R. Clayton and C. W. White, eds., "Ion Implantation and Ion Beam Processing of Materials", Elsevrev Science Publishing Co., Inc. (1984).

4. A. Kujore, S. B. Chakrabortty, E. A. Starke and K. O. Legg, "The Effect of Ion Implantation on the Fatigue Properties of Polycrystalline Copper", Nuc. Inst. Meth, 182/183 (1981) pp. 949-958.

5. I. W. Hall, "The Effect of Ion Implantation on the High Temperature Deformation of Molybednum", Met. Trans 12A (1981) pp. 2093-2099.

6. M. L. Eben and W. A. Backofen, "Fatigue in Single Crystals of Copper", Trans. AIME, 215 (1959) pp. 510-520.

7. W. H. Kim and C. Laird, "Crack Nucleation and Stage 1 Propagation in High Strain Fatigue-I. Microscopic and Interferometric Observations", Acta Met., 26 (1978) pp. 777-787.

8. W. H. Kim and C. Laird, "Crack Nucleation and Stage 1 Propagation in High Strain Fatigue-II Mechanism", Acta Met., 26 (1978) pp. 789-799.

9. E. Y. Chen and E. A. Starke, Jr., "The Effect of Ion Planting on the Low Cycle Fatigue Behavior of Copper Single Crystals", Mat. Sci. Eng., 24 (1976) pp. 209-221.

10. S. B. Chakrabortty, A. Kujore and E. A. Starke, Jr., "The Effects of Ion Implantation on Cyclic Stress Strain Response of Polycrystalline Copper", Thin Solid Films, 73 (1980) pp. 209-219.

11. S. B. Chakrabortty, S. Spooner and E. A. Starke, Jr., "The Effect of Ion Planting and Ion Implantation on Cyclic Response and Fatigue Crack Initiation in Metals and Alloys", Technical Report 79-2, Office of Naval Research, April 1980.

12. J. M. Poate and A. G. Cullis, "Implantation Metallurgy - Metastable Alloy Formalism" in cf. 1, pp. 85-131.

13. S. P. Singhal, H. Herman and J. K. Hirvonen, "Spinodal Decomposition in Amorphous Au - Implanted t", Appl. Phys. Lett. 32, 1 (1978) pp. 25-26.

14. P. Sigmund, "Energy Density and Time Constant of Heavy Ion-Induced Elastic Collision Spikes in Solids", Appl. Phys. Lett. 25, 3 (1974) pp. 169-171.

15. S. M. Myers, "Implantation Metallurgy - Equilibrium Alloys", in cf. 1, pp. 51-82.

16. K. V. Jata, D. Janoff and E. A. Starke, Jr., "Modulated Structures in Ion Implanted Al-Fe System", in cf. 3, pp. 157-162.

17. K. V. Jata, J. Han, E. A. Starke, Jr., and K. O. Legg, "Ion Implantation Effect on Fatigue Crack Initiation in Ti-24V", Scr. Met, 17 (1983) pp. 479-483.

18. K. V. Jata and E. A. Starke, Jr., "Surface Modification by Ion Implantation - Effects on Fatigue", J. of Metals, 35, 8 (1983) pp. 23-27.

19. K. V. Jata and G. K. Hubler, "The Effect of Fe and Ce Ion Implantation on the High Temperature Deformation Behavior of a 2124 Al Alloy", Accepted for publication in J. of Vac. Sci. and Tech.

ENVIRONMENTAL ALTERATION OF FATIGUE CRACK PLASTICITY

David L. Davidson
Southwest Research Institute
P. O. Drawer 28510
San Antonio, Texas 78284 USA

The alteration of fatigue crack growth by a moist air environment was investigated for low carbon steel and several aluminum and titanium alloys. Two new techniques were used to determine material response to cyclic loading within the plastic zone of the crack. The results indicated that the effect of environment is concentrated at the crack tip rather than further ahead in the plastic zone, and that the specie responsible for the environmental effect was hydrogen.

Introduction

The growth of fatigue cracks is controlled by failure of the microstructure ahead of the crack tip and within the plastic zone, if not exactly at the crack tip itself. To understand how fatigue cracks lengthen, it is necessary, therefore, to examine material response within a small volume of material near the crack tip. Our research has concentrated (a) on measuring the response of microstructure near the tips of fatigue cracks growing in vacuum or a high humidity environment, and from this information (b) deducing the events accompanying crack growth. It has been necessary to develop new experimental techniques in the course of this work because of the very small volume of material affected by the crack, particularly for cracks grown in the near threshold region, where environmental effects are known to be the largest.

This paper reports on measurements of microstructural change and crack tip micromechanics which have been made for the alloys listed in Table I. The technique used to study each alloy is also given, as are the references reporting the full research results for that material.

Table I. Alloys Studied, Technique Used and Range of Stress Intensities Investigated

Vacuum (or Dry Nitrogen) and High Humidity Environments

Alloys	ΔK Range ($MPa-m^{1/2}$)	Technique	References
Fe-.05C	7.5-12.3	channeling contrast & stereoimaging	1-4
7075-T651	6-12	stereoimaging	14-16
7091 (MA-87)	5.5-11	stereoimaging	15-18
Ti-6Al-4V	7-11	stereoimaging	19

The investigation began by using electron channeling contrast to image subcell formation caused by fatigue crack growth in low carbon steel [1]. This technique allowed information to be obtained to within about 0.5 μm from the crack tip. The size and distribution of subcells was found to be sensitive to the environment in which the crack was grown [2]. With this information, it was then possible to determine stresses within the plastic zone, plastic zone size and shape, and the energy dissipated by the growing crack as functions of environment and stress intensity factor [3].

With discovery of the stereoimaging technique [5,6], it became possible to determine three elements of the in-plane strain tensor at the crack tip and within the plastic zone. The spatial resolution used was comparable to that attained using channeling contrast. Since it is not possible to use channeling contrast for aluminum and titanium alloys, development of the stereoimaging technique allowed those materials to be investigated.

Stress Distribution in Low Carbon Steel

The distribution of stresses near the crack tip, as deduced from subcell formation, is shown in Fig. 1. The effect of water vapor on material response is to increase the size of the subcells formed, which effectively decreases the plastic zone size and lowers the stress within it, including the stress at the crack tip [1]. Lowering the stress intensity factor towards threshold causes the plastic zone size and stress magnitude to decrease rapidly for cracks grown in water vapor, but to change much less for cracks grown in the dry environment.

Work Expended During Crack Growth in Low Carbon Steel

Application of the cyclic force which lengthens the crack causes work to be expended within the crack tip plastic zone. It has been proposed that the crack growth is accompanied by the expenditure of a critical amount of work within the plastic zone [7,8]. Thus, a method was derived to compute the work dissipated per unit area of new crack from the distribution of subcells [3,9]. Since subcell size depended upon environment, so did the work dissipated, as

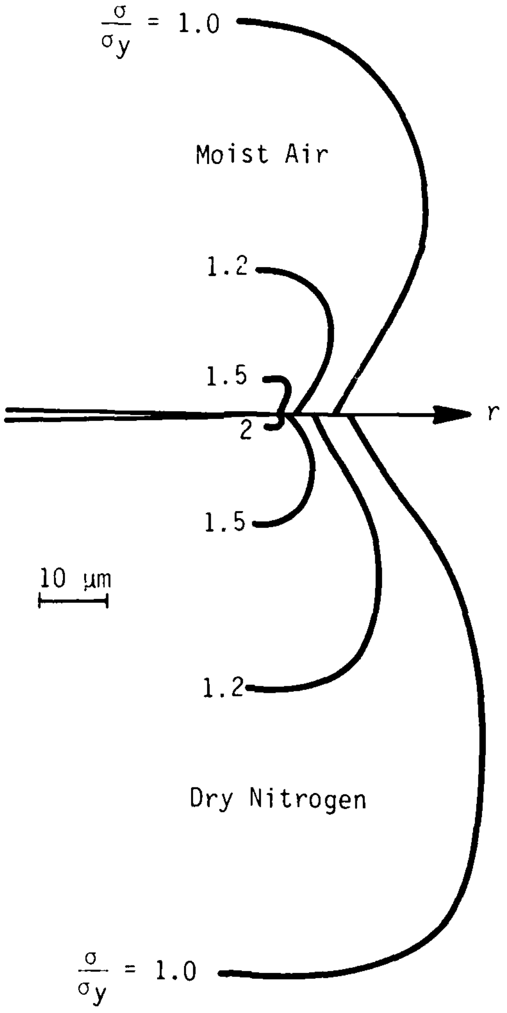

$\frac{\sigma}{\sigma_y} = 1.0$
Moist Air
1.2
1.5
2
r
1.5
10 μm
1.2
Dry Nitrogen
$\frac{\sigma}{\sigma_y} = 1.0$

Fig. 1 - The effect of environment on the crack tip stress range distribution in low carbon steel at $\Delta K = 8$ MPa-m$^{1/2}$.

shown in Fig. 2. Superimposed on the data are lines hypothesizing the trends which would be expected by making measurements over a broader range of stress intensity factor [4]. The data clearly indicate that the work dissipated within the plastic zone is not a constant value, as would be required if this quantity was to be used as a failure criterion. This same trend was also found for 7075-T651 aluminum alloy using strain measurements by stereoimaging [10], and we concluded that the dissipation of work could not be used as a criterion for fatigue crack growth.

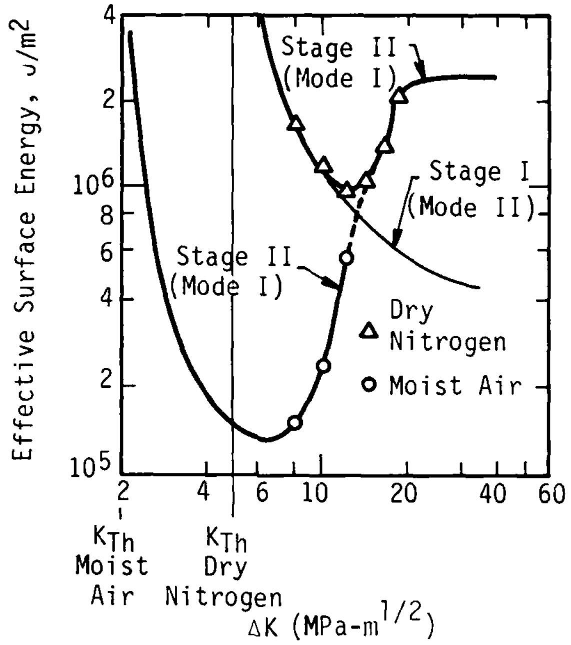

Fig. 2 - Variation in work dissipated during fracture due to changes in stress intensity factor and environment for low carbon steel. Extrapolations indicate expected trends and related conditions.

Strain Distribution Within the Crack Tip Plastic Zone

With development of the stereoimaging technique, it became possible to look in detail at the effect of water vapor on the magnitude and distribution of strains within the plastic zone, not only in low carbon steel, but also in other alloys of interest, Table I. The distribution of strain within the plastic zones of cracks in 7075 aluminum alloy had already been determined using selected area electron channeling patterns [11] to be described by the function

$$\varepsilon = A + M \log (B + R) \qquad (1)$$

where A, M and B are fitting parameters and R is the distance from the crack tip in μm. Strain ahead of the crack tip determined by using stereoimaging also may be described using this function. The total effective strain is used for these determinations because the individual coordinate strains have complex distributions not easily described by a simple function such as Eq. (1).

For low carbon steel, the effect of environment on the normalized (effective) strains (ε') ahead of fatigue cracks is shown in Fig. 3, and for two of the other materials studied in Figs. 4 and 5. For all of the alloys listed in

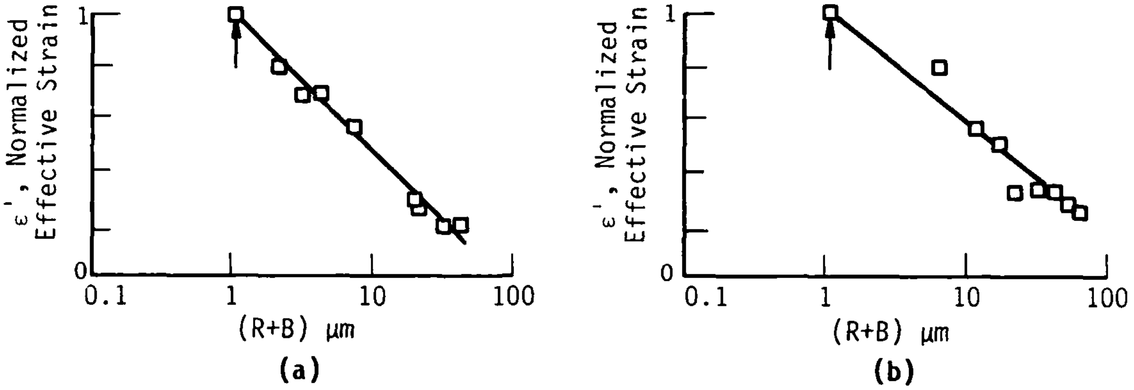

Fig. 3 - Distribution of normalized effective strain ahead of fatigue cracks in low carbon steel at ΔK = 11 MPa-m$^{1/2}$; (a) dry nitrogen and (b) moist air. Arrow indicates crack tip.

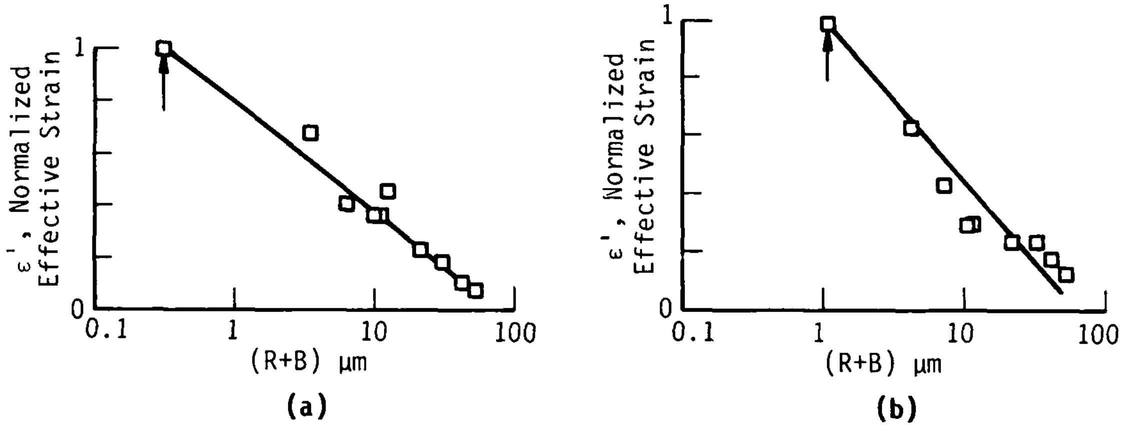

Fig. 4 - Distribution of normalized effective strain ahead of fatigue cracks in 7075-T651 aluminum alloy at ΔK = 8 MPa-m$^{1/2}$; (a) vacuum and (b) moist air. Arrow indicates crack tip.

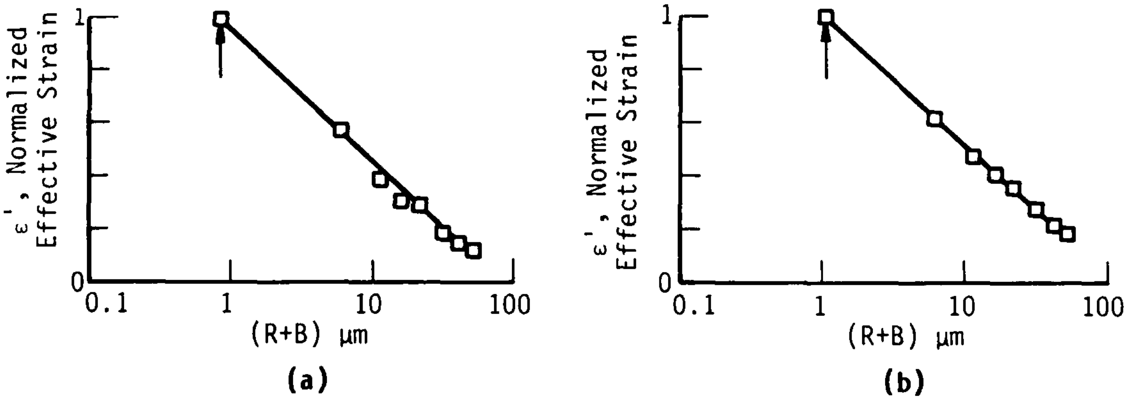

Fig. 5 - Distribution of normalized effective strain ahead of fatigue cracks in Ti-6Al-4V (RA) at ΔK = 8 MPa-m$^{1/2}$; (a) vacuum and (b) moist air. Arrow indicates crack tip.

Table I, and others as well, there is no indication that water vapor alters the form of the strain distribution function [12]; only the magnitude of strains is changed by environment. Therefore, the effect of having moist air in the environment is to decrease strain at the crack tip and within the plastic zone ahead of it, which also decreases the plastic zone size. Changing the applied cyclic stress intensity factor (ΔK) alters only the crack tip strain, but not the strain distribution [12].

It is possible to compute stresses from the strains determined by stereoimaging [13] and this was done for the low carbon steel in order to compare with those values determined from subgrain size. The comparison, Fig. 6, is remarkably good considering the differences in technique used.

Crack Tip Strain

After realizing that the distribution of strain ahead of the crack tip was not being altered by environment or stress intensity factor, values of the crack tip strain itself were considered in greater detail. When correlated with applied or effective stress intensity factor (ΔK_{eff}), there appears to be considerable scatter in crack tip strain, but when correlated against crack tip opening displacement (CTOD), the scatter is considerably reduced. Environment affects both the correlations between crack tip plastic strain ($\Delta\varepsilon_p$) and CTOD and between strain and ΔK [14,17]; the former is shown in Fig. 7, and the functions describing the latter correlation are given in Table II. In order to be consistent, CTOD has been defined as the crack opening 1 μm behind the tip for each alloy.

Crack tip strains for fatigue cracks grown in water vapor were found to be lower than for those grown in vacuum for all the alloys studied except Ti-6Al-4V [19] which showed essentially no change. The relations between crack tip strain and ΔK in Table II give average values; scatter in this correlation is due to the crack growth process, which causes crack tip strains to fluctuate during the time cyclic strain is accumulating prior to the growth step [17,19].

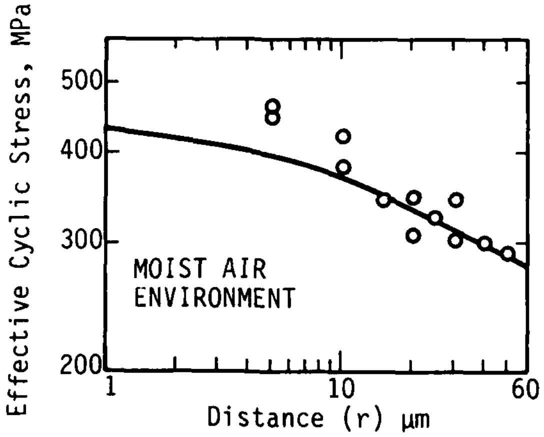

Fig. 6 - Stresses near a fatigue crack tip in low carbon steel in the direction parallel to loading as determined from subcells (line) and computed from strains (symbols) determined by stereoimaging.

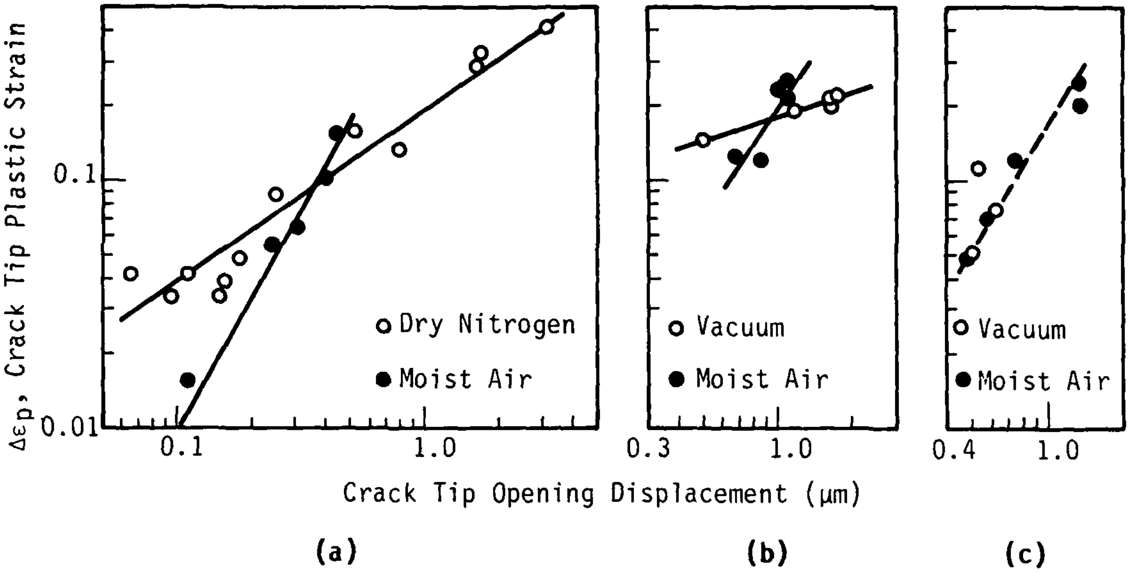

Fig. 7 - Correlation between crack tip strain $\Delta\varepsilon_p$ and crack tip opening displacement; (a) 7075-T651, (b) 7091 (MA-87), and (c) Ti-6Al-4V (RA).

Table II. Crack Tip Plastic Strain Values

$$\Delta\varepsilon_p = K_o \, \Delta K_{eff}{}^r$$

$$\Delta K_{eff} = \Delta K - \Delta K_{Th} \text{ (MPa-m}^{1/2}\text{)}$$

Alloy	Environment	ΔK_{Th}	K_o	r
7075-T651	dry$^+$	0*	$1.3\text{x}10^{-4}$	3.0
	air	0*	$5.8\text{x}10^{-5}$	3.2
7091 (MA-87)	vac	3.5	$1.2\text{x}10^{-1}$	0.32
	air	1.7	$3.9\text{x}10^{-2}$	0.79
Ti-6Al-4V	vac	7.7	$7.1\text{x}10^{-2}$	0.28
	air	1.6	$2.4\text{x}10^{-3}$	1.9

+Most work done in nitrogen having < 10 ppm water vapor.
*ΔK_{Th} was derived from shape of crack growth rate vs ΔK curves; 7075 only evidenced a straight line over the range in ΔK studied.

Crack Opening Displacements

High resolution measurements of crack opening displacement have shown that fatigue cracks open in both Mode I (direction of loading) and Mode II (direction of crack growth). All of the alloys studied exhibited mixed mode openings, but the powder metallurgy alloy 7091 showed the greatest amount of Mode II opening [16]. Although the effect of moisture was not large, the amount of Mode I was decreased by moisture, as is illustrated in Fig. 8. The ratio of Mode I to Mode II opening sharply decreases as ΔK is lowered towards threshold, for all alloys.

One of the effects of having a relatively large Mode II crack opening component is that rubbing occurs between the crack faces. Evidence for this is found during fractography as both a smoothing of the fracture surfaces and the creation of wear debris. When the crack is grown in water vapor, oxides on the fracture surfaces result and the creation of wear debris consisting mainly of these oxides has been found [18]. This abrasion of the fracture surfaces assists in the accumulation of thicker oxide layers than would ordinarily be expected, and this has a marked effect on the value of ΔK_{Th}, as shown by other investigators [20].

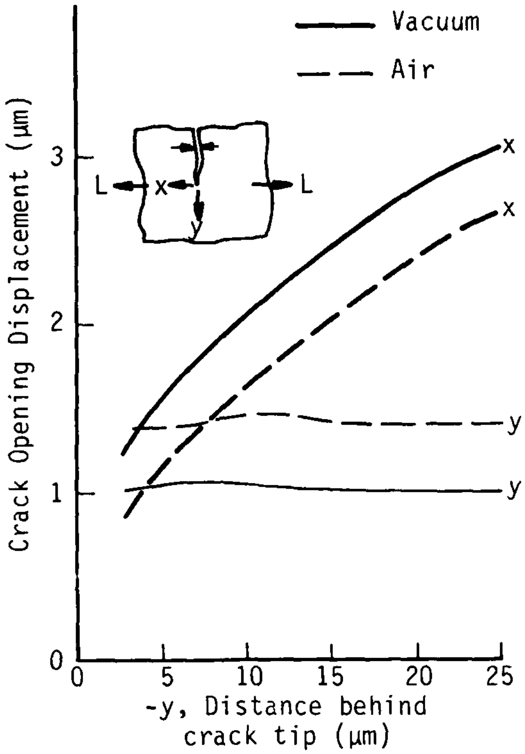

Fig. 8 - Effect of water vapor on crack opening displacement parallel and perpendicular to loading direction for 7091 (MA-87) powder metallurgy aluminum alloy, $\Delta K = 10$ MPa-m$^{1/2}$.

Hydrogen Distribution Near Crack Tips by Autoradiography

The distribution of hydrogen near the tips of fatigue cracks in low carbon steel was determined by growing the cracks in tritiated water vapor and locating the resulting tritium by autoradiographic techniques [21]. An example of the distribution of silver photographic emulsion grains exposed by tritium in the vicinity of a fatigue crack tip is shown in Fig. 9. Although there is also considerable background x-ray noise, the concentration of silver in the grain boundaries is clearly indicated. There is probably some tritium within the grains themselves, although no concentration appears near the crack tip. Fractography, Fig. 10, indicated that crack growth in water vapor was partially intergranular, in agreement with the location of hydrogen in grain boundaries.

This work is interpreted as showing that hydrogen can be liberated from water vapor at the tip of a fatigue crack tip and transported to points well within the plastic zone by dislocations emitted at the crack tip. The hydrogen is then deposited at locations of high disorder, such as grain boundaries, in agreement with previous autoradiographic work [21].

Discussion

The distribution of strain within the plastic zone of fatigue cracks, for a variety of materials, is not altered by water vapor in the environment, but the magnitude of those strains is lowered. Catalysis of water into hydrogen and hydroxyl ions occurs on the fresh metallic surfaces created by crack growth [22], and the presence of hydrogen causes the magnitude of strain sustained at the crack tip to be lowered, which, in turn, lowers strain throughout the plastic zone and shrinks its size. Crack growth in a moist environment thus dissipates less energy, requiring less input of work, than crack growth in an inert environment.

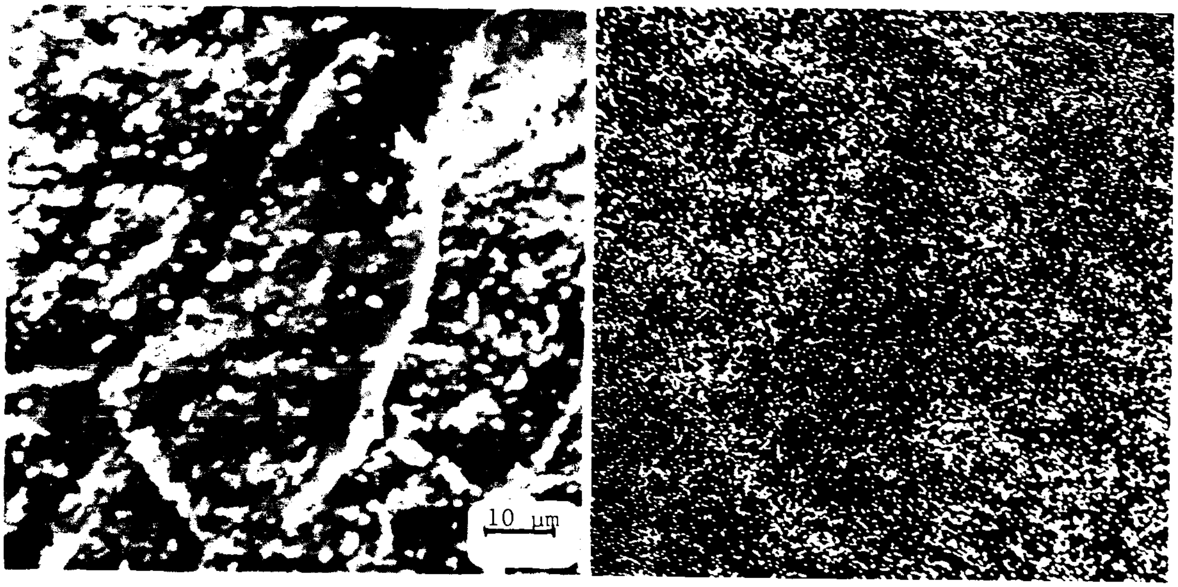

(a) (b)

Fig. 9 - (a) Secondary electron image and (b) map of silver x-ray line showing location of hydrogen near a crack tip (arrow) in low carbon steel which was grown in tritiated water vapor.

For low carbon steel, the tritium autoradiography result indicates that hydrogen may be transported into the material of the plastic zone by dislocations, but that fact is important only because it causes partial intergranular fracture in that particular material. A similar transport process may also be operative in the other alloys, but it is apparently not principally responsible for the observed environmental effect.

A model for crack growth which incorporates measured crack tip and microstructural parameters and other factors related to crack growth has been advanced [23]. The element of material just ahead of the crack tip which is being broken by cyclic loading is considered, as with several previous models, as a small, low cycle fatigue specimen, which is described by

$$\Delta\varepsilon_p(\Delta N)^\beta = \varepsilon_c \qquad (2)$$

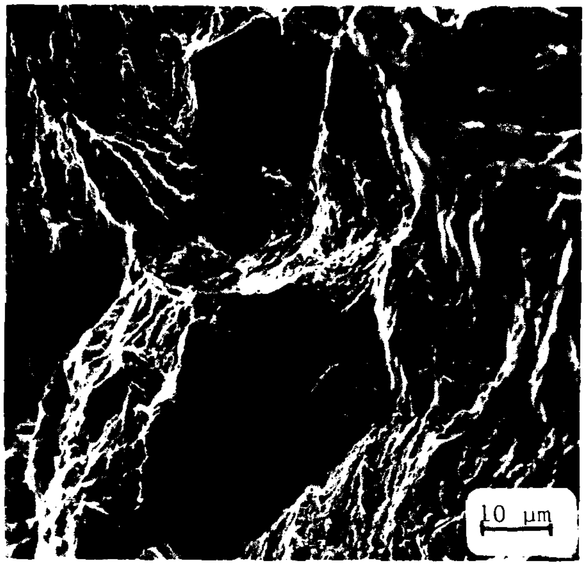

Fig. 10 – Fracture surface of low carbon steel specimen cycled in air at $\Delta K = 11\ \text{MPa-m}^{1/2}$ showing intergranular growth facets.

where ε_c and β are material constants and ΔN is the number of cycles required to break the specimen. The effect of water vapor is to alter the values of ε_c and β for the aluminum alloys [24], Table III. This model, of course, does not describe how hydrogen causes the material to break differently, but only indicates that an element cycled in hydrogen would be expected to break at a lower strain and with fewer cycles than if cycled in vacuum. In other words, the material at the crack tip is "hydrogen embrittled" by a mechanism as yet unknown in sufficient detail to be able to include it in fatigue crack growth models.

Table III. Derived Low Cycle Fatigue Parameters for Crack Tip Elements

$$\Delta\varepsilon_p \Delta N^{\beta} = \varepsilon_c$$

Alloy	Environment	ε_c	β
7075-T651	dry	0.37	0.49
	air	0.09	0.64
7091 (MA-87)	vac	0.34	0.17
	air	0.23	0.28

Modeling of the crack tip as a low-cycle fatigue specimen, Eq. (2), requires that crack advance occurs only after a number of cycles have been applied, with the number being dependent on the level of crack tip strain. Dynamic observation of growing cracks has shown just such a behavior, which is environmentally dependent [1,14,17]. Water vapor in the crack growth environment causes the number of cycles required for growth to be reduced, compared to the same ΔK in vacuum [14,17].

Future Directions for Research

If we are to be able to design materials having a greater tolerance to fatigue crack growth, both in benign and aggressive environments, then the relationship between the microstructure and mechanism of crack growth must be better understood. Exactly what events occur at a fatigue crack tip when the crack lengthens? How does the microstructure break down? What are the essential elements of the microstructure which control the crack growth process?

The effect of hydrogen is to cause the microstructure at the crack tip to break down with a lower expenditure of mechanical input work than would be required in an inert environment. Somehow the sequence of events leading to this result must be determined and related to the microstructure by basic physical understanding. Can this process be defeated by microstructural manipulation or intervention in some other way? Is it possible that hydrogen interaction provides a fundamental limitation to the use of metallic alloys, and that other materials, such as composites, are required to surmount this limitation? The alteration of crack closure by environment is poorly understood and has been examined only by macroscopic measurements. What is the origin of crack closure, excluding environment? How does environment alter non-oxide induced closure?

For statically loaded cracks, the complex interaction between environment and crack tip mechanics is virtually unexplored. The reader is referred to the Workshop Summaries in Ref. [25] for further insights into the state of knowledge and what research is needed on this failure mode. From the viewpoint of crack tip mechanics, stress corrosion cracking is far from being as well characterized as fatigue cracking.

Acknowledgment

The work described herein was funded under contract N00014-75-C-1038 which was in effect during the period June of 1975 to September 1982. We are grateful to everyone who contributed to this work, including D. R. Williams, J. Buckingham, J. B. Campbell, and S. R. Bodner. Dr. James Lankford, Jr. of Southwest Research Institute was Co-Principal Investigator for this work.

References

1. D. L. Davidson and J. Lankford, "The Effect of Water Vapor on Fatigue Crack Tip Stress and Strain Range Distributions and The Energy Required for Crack Propagation in Low-Carbon Steel", International Journal of Fracture, 17(3) (1981) pp. 257-275.

2. D. L. Davidson and J. Lankford, "The Influence of Water Vapor on Fatigue Crack Plasticity in Low Carbon Steel", paper presented at Fourth International Conference on Fracture, Vol. 2, Waterloo, Canada, 1977.

3. D. L. Davidson and J. Lankford, "Determination of the Energy of Fatigue Crack Propagation and Alteration by Wet Air", pp. 581-594 in Proceedings of the Symposium: Environment Sensitive Fracture of Engineering Materials, Z. A. Foroulis, ed.; AIME, 1979.

4. D. L. Davidson, "Incorporating Threshold and Environmental Effects into the Damage Accumulation Model for Fatigue Crack Growth", Fatigue of Engineering Materials and Structures, 3 (1981) pp. 229-236.

5. D. L. Davidson, "The Observation and Measurement of Displacements and Strain by Stereoimaging", pp. 79-86, in Scanning Electron Microscopy/1979/II, SEM, Inc., AMF O'Hare, IL, 1979.

6. D. R. Williams, D. L. Davidson, and J. Lankford, "Fatigue Crack Tip Plastic Strains by the Stereoimaging Technique", Experimental Mechanics, 20(4) (1980) pp. 134-139.

7. S. R. Bodner, D. L. Davidson, and J. Lankford, "A Description of Fatigue Crack Growth in Terms of Plastic Work", Engineering Fracture Mechanics, 17 (1982) pp. 189-191.

8. M. E. Fine and D. L. Davidson, "Quantitative Measurement of Energy Associated with a Moving Fatigue Crack", pp. 350-370, ASTM STP 811, 1983.

9. P. K. Liaw, M. E. Fine, and D. L. Davidson, "Comparison of Plastic Work of Fatigue Crack Propagation in Low-Carbon Steel Measured by Strain Gages and Electron Channeling", Fatigue of Engineering Materials and Structures, 3 (1980) pp. 59-74.

10. D. L. Davidson and J. Lankford, "Fatigue Crack Tip Strains in 7075-T6 by Stereoimaging and Their Use in Crack Growth Models", pp. 371-399, ASTM STP 811, 1983.

11. D. L. Davidson and J. Lankford, "Fatigue Crack Tip Plastic Strain in High Strength Aluminum Alloys", Fatigue of Engineering Materials and Structures, 3 (1981) pp. 289-303.

12. D. L. Davidson, "The Distribution of Strain Within Crack Tip Plastic Zones", Journal of the Mechanics and Physics of Solids (1985) in press.

13. D. L. Davidson, D. R. Williams, and J. Buckingham, "Crack Tip Stresses as Computed from Strains Determined by Stereoimaging", Experimental Mechanics, 23 (1983) pp. 242-248.

14. D. L. Davidson and J. Lankford, "The Effect of Water Vapor on Fatigue Crack Tip Mechanics in 7075-T651 Aluminum Alloy", Fatigue of Engineering Materials and Structures, 4(3) (1983) pp. 287-290.

15. J. Lankford and D. L. Davidson, "Fatigue Crack Micromechanics in Ingot and Powder Metallurgy 7XXX Aluminum Alloys in Air and Vacuum", Acta Metallurgica, 31 (1983) pp. 1273-1284.

16. D. L. Davidson and J. Lankford, "Mixed Mode Crack Opening in Fatigue", Materials Science and Engineering, 60 (1983) pp. 225-229.

17. D. L. Davidson and J. Lankford, "Fatigue Crack Tip Mechanics of a Powder Metallurgy Aluminum Alloy in Humid Air", Fatigue of Engineering Materials and Structures, 7 (1984) pp. 29-39.

18. J. Lankford and D. L. Davidson, "Wear Debris Due to Mode II Opening of Mode I Fatigue Cracks in an Aluminum Alloy", Metallurgical Transactions A, 14A (1983) pp. 1227-1230.

19. D. L. Davidson and J. Lankford, "Fatigue Crack Growth Mechanics for Ti-6Al-4V (RA) in Vacuum and Humid Air", Metallurgical Transactions A (1984) in press.

20. S. Suresh, A. K. Vasudevan and P. E. Bretz, Metallurgical Transactions A 15A (1984) pp. 369-379.

21. C. Paes de Olivera, M. Aucouturier and P. La Combe, Corrosion, 36 (1980), pp. 53-59.

22. G. W. Simmons, P. S. Pao and R. P. Wei, Metallurgical Transactions A, 9A (1978) pp. 1147-1158.

23. D. L. Davidson, "A Model for Fatigue Crack Advance Based on Crack Tip Metallurgical and Mechanics Parameters", Acta Metallurgica, 32 (1984) pp. 707-714.

24. D. L. Davidson and J. Lankford, "The Effects of Aluminum Alloy Microstructure on Fatigue Crack Growth", Materials Science and Engineering (1985) in press.

25. Surface Effects in Crystal Plasticity, NATO Advanced Study Institute Series E, edited by R. M. Latanision and J. T. Fourie, Noordhoff International Publishing, 1977.

FATIGUE CRACK PROPAGATION IN HY80 AND HY130 STEELS

Morris E. Fine
Department of Materials Science and Engineering
Northwestern University
Evanston, Illinois

An increase in the threshold stress intensity range for HY80 steel was achieved by a heat treatment to form a dual phase microstructure; ΔK_{th} was 5.4 MPa-m$^{1/2}$ for the dual phase structure compared to 4.2 MPa-m$^{1/2}$ for the conventional microstructure. While some of the effect was due to crack closure, the intrinsic threshold stress intensity range was also increased. The crack closure was due to crack surface roughness combined with shear displacements. These were quantitatively determined. The threshold stress intensity range for HY130 is lower, 3.8 MPa-m$^{1/2}$, and no heat treatment was found to increase it.

The fatigue crack propagation rate studies in the range where log da/dN is proportional to log ΔK emphasized the role of plastic work in determining the rate of fatigue crack propagation. The plastic work term is larger for HY80 than for HY130 resulting in slower crack propagation rates for the former. Some suggestions for obtaining more crack propagation resistant pressure vessel alloys are given. Dual ferrite-tempered martensite microstructures are suggested to hold promise.

Introduction

From the point of view of the physical metallurgist, the aim of research on fatigue of metals is to obtain more fatigue resistant metals by alloying or mechanical and thermal treatment and also to provide information to the design engineer so that he may design more efficiently and with more certainty.

A fatigue failure occurs by initiation of one or more microcracks on a pre-existing flaw or on a grain boundary or on a slipband followed by growth or coalescence of microcracks into a macrocrack and then growth to final failure. A popular and important current design strategy is to assume that a small crack is already present because inspection cannot guarantee the absence of a small crack and to design on the basis of crack propagation rates as functions of stress intensity amplitude taking cognizance of mean stress. Such a strategy gives no credit to the crack initiation stage nor the lifetime between microcracks and formation of a macrocrack. The traditional design strategy utilizing the endurance limit does include these stages. At some future date, more quantitative knowledge of the initiation and microcrack stages will no doubt allow these to be incorporated into a more sophisticated design procedure. Materials need to be evaluated for each stage separately and separately related to and understood in terms of the microstructure.

The present research was aimed at relating fatigue crack propagation rates to microstructure for microcracks in HY80 and HY130 pressure vessel steels. Besides being of great interest to the Navy, these steels may be prepared with an extremely wide variety of microstructures through thermal treatment alone. HY80 was of special interest because it may be heat treated to give a dual phase microstructure. McEvily and co-workers [1] had reported remarkably large values of the threshold stress intensity range for fatigue crack propagation in dual phase 1018 steel. Because of the secondary hardening in HY130 due to VC, quite different microstructures having the same yield stress may be prepared.

Environmental effects, of course, must be determined and considered but our understanding of fatigue crack propagation is most easily established in an inert environment and such understanding forms a basis for understanding and mitigating against environmental effects. The research reported herein was done in air or in an inert environment, purified argon. The results of this research have been for the most part published [2-5]. The final report [6] gives the complete results.

The propagation of macro-fatigue cracks is usually divided into three stages: (a) the near threshold region where the rate of fatigue crack propagation, da/dN, increases very rapidly with an increase in stress intensity range, ΔK, from a threshold value, ΔK_{th}, (b) the mid-region where the Paris relation $da/dN = C(\Delta K)^m$ is followed (C and m are considered to be constants for a given material), and (c) growth to final failure where K_{max} approaches K_c. Only the near threshold and Paris regions were studied in the present research.

Alloys Studied

For this research, HY80 and HY130 of the compositions shown in Table I in weight percent, were obtained from the U. S. Steel Research Lab., courtesy of Dr. L. F. Porter. The standard heat treatments for these are: HY80, austenitized at 900°C and tempered 1 h at 700°C; HY130, austenitized at 815°C and tempered 1 h at 610°C.

Table I. Compositions of HY80 and HY130 Studied (in weight percent)

Steel	C	Ni	Cr	Mo	Mn	V	Si
HY80	0.18	3.00	1.58	0.50	0.32	0.006	0.27
HY130	0.10	5.33	0.49	0.57	0.35	0.064	0.23

Near Threshold Fatigue Crack Propagation Rates in HY80 and HY130, Standard Heat Treatment

Initially, near threshold fatigue crack propagation rate measurements were made on HY80 and HY130 with the standard heat treatments. The tests were done on panel specimens, 100 mm by 3.5 mm by 25 mm containing a 3 mm by 0.2 mm center notch introduced by spark machining, in laboratory air of 47% humidity using the load shedding technique. The load was reduced in steps less than 8% of the previous load but the steps were less than 5% as ΔK_{th} was approached. ΔK_{th} was taken to be that value below which no crack growth was detected in 3×10^6 cycles. After ΔK_{th} was determined, the load was increased and da/dN was measured under constant nominal stress. The results are shown in Fig. 1.

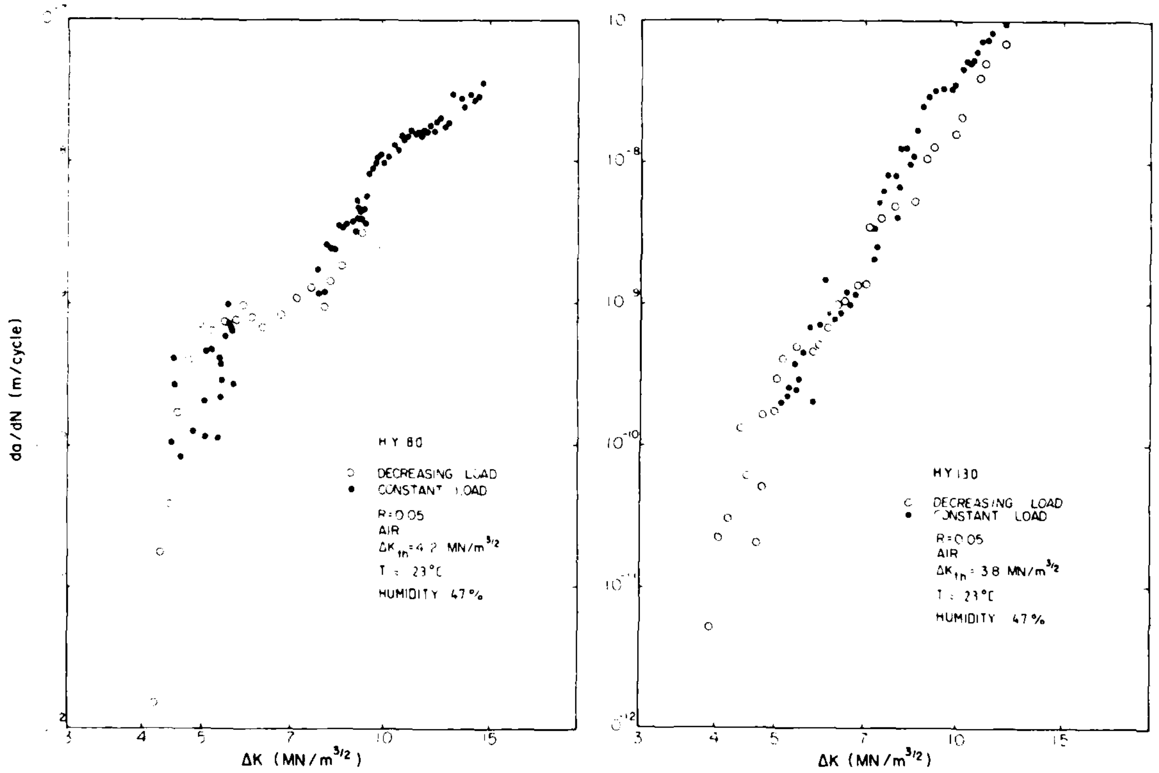

Fig. 1 - Fatigue crack propagation rate near threshold versus ΔK for (a) HY80 steel, and (b) HY130 steel.

The lowest data point plotted is the maximum crack advance which could not be detected divided by the number of cycles. HY80 has the higher threshold, 4.2 MPa-m$^{1/2}$, compared to 3.8 MPa-m$^{1/2}$ for HY130.

It is generally considered that the threshold stress intensity range, ΔK_{th}, for macrocrack propagation decreases as the yield stress increases [7]. This probably arises because the material's ductility reduces the local stress at the crack tip more for a low yield stress material than for a high yield stress material. The difference in ΔK_{th} between HY80 and HY130 was small (4.2 vs. 3.8 MPa-m$^{1/2}$) even though there are large differences in monotonic yield stress (626 vs. 1042 MPa) and cyclic yield stress (521 vs. 868 MPa).

Effect of Tempering Temperature on Threshold Stress Intensity for Fatigue Crack Propagation in HY130

In order to determine possible microstructural effects on ΔK_{th} at constant yield stress, four tempering heat treatments for HY130 were devised to give the same approximate hardness, 31-33 Rockwell C. These were (A) 10 h at 400°C, (B) 5 h at 550°C, (C) 1 h at 610°C, and (D) 1/2 h at 650°C. Heat treatment C is, of course, the standard one. While the carbides were not identified in this study, some hardening due to VC replacing Fe_3C must have occurred at all temperatures compensating for the softening due to tempering of the martensite. As shown in Table II, the standard treatment gave the highest value of ΔK_{th}. The difference between 3.8 MPa-m$^{1/2}$ in air and 3.6 MPa-m$^{1/2}$ in argon for HY80 treatment C may be due to build up of oxide at the crack tip.

Table II. ΔK_{th} and Fatigue Crack Propagation Rates for HY130 Steel with Different Tempering Treatments (Argon atmosphere)

Tempering	Hardness Rockwell C	ΔK_{th} MPa-m$^{1/2}$	da/dN (10^{-8} m/cycle) at ΔK = (MPa-m$^{1/2}$) of		
			15	20	30
A 10 h 400°C	33	2.8	1.6	4.3	21
B 5 h 550°C	33	3.0	1.8	4.3	15
C 1 h 610°C	33	3.6	2.1	4.7	14
D ¼ h 650°C	31	3.2	1.9	4.8	18

Near Threshold Fatigue Crack Propagation Rate of HY80 with Dual Phase Microstructure

Dual phase structured steels containing comparable amounts of martensite and ferrite have been shown to have a very good combination of strength and ductility when compared with traditionally heat-treated steels. McEvily and co-workers [1] observed that ΔK_{th} in 1018 steel for a dual phase microstructure with martensite as the continuous phase is much higher than that for the normalized condition even though the former is stronger.

Two different dual phase microstructures were developed in HY80. Table III shows the heat treatment procedures. The dual phase microstructures resulting from heat treatments IAA and IAB steels are shown in Fig. 2(a) and (b), respectively. As determined by SEM microprobe analyses, the bright phase which contains larger amounts of Ni, Mo and Cr is martensite and the dark phase is ferrite. From TEM thin foil observation (Fig. 2(c) and (d)), the martensite width is 0.2-1.0 μm in IAB and 0.5-2.0 μm in IAA.

Table III. Heat Treatment of HY80 to Produce Dual Phase Microstructures

Condition	Heat Treatment	Hardness (R_c)
Dual Phase IAA	1000°C, 3 h → furnace cool → 750°C, 2 days → water quench	38
Dual Phase IAB	1000°C, 3 h → furnace cool → 900°C, 1 h → water quench → 700°C, 1 h → water quench → 750°C, 2 days → water quench	35
Standard Heat Treatment	1000°C, 3 h → furnace cool → 900°C, 1 h → water quench → 700°C, 1 h → water quench	20

The threshold stress intensity fatigue testing was done in dry argon using the procedures given in the previous section. Because crack closure was known to play a role, the closure stress was measured by the foil strain gage method [8]. Foil strain gages (Micro-Measurements MA-06-008CL-120) were cemented on the specimen near the expected crack path at different distances from the notch tip. The closure stress was determined by the deviation from linearity in the stress-local strain curve.

The near-threshold fatigue crack propagation rates are plotted versus ΔK in Fig. 3 and ΔK_{th} values are given in Table IV. The dual phase heat treatment, IAA, much reduces the fatigue crack propagation rate in the low ΔK

Table IV. Near-threshold Closure and Stress Intensity Measurements in HY80 Steel (Argon atmosphere)

Condition	Hardness (R_c)	ΔK_{th} (MPa-m$^{1/2}$)	$K_{cl,th}$ (MPa-m$^{1/2}$)	$\Delta K_{eff,th}$ (MPa-m$^{1/2}$)	Prior Austenite Grain Size (μm)
Dual Phase IAA	38	5.4	2.5	3.2	35
Dual Phase IAB	35	4.3	-	-	12
Standard Heat Treatment	20	3.1	1.7	1.7	12
IAA + 650°C, 1 h	20	4.4	2.4	2.2	35

region. Compared with the standard heat treatment (1000°C austenizing), ΔK_{th} is raised 40% by the IAB treatment and 75% by the IAA treatment. At higher ΔK values, the differences among the propagation rates become small. Additionally, the dual phase IAA structure was tempered at 650°C for one h to achieve the same hardness as the standard heat treatment. The threshold value is 42% higher than that resulting from the standard heat treatment.

The closure stress intensity (K_{cl}) is plotted vs. ΔK and ΔK_{eff} ($=K_{max} - K_{cl}$) in Figs. 4(a) and 5(a), respectively. The closure stress intensity is constant for the higher ΔK region but the value increases when ΔK_{th} is approached. This effect is more apparent when K_{cl}/K_{max} is plotted, Figs. 4(b) and 5(b). The IAA structure has the highest threshold value and also the highest closure stress intensity. Tempering after the dual phase IAA treatment reduced ΔK_{th}, but ΔK_{th} and the closure stress intensity are still higher than for the standard heat treatment. Figure 3 also compares the fatigue crack propagation rates versus ΔK_{eff}. In each structure, the convergence of the ΔK and ΔK_{eff} curves show that the crack closure effect is not significant in the intermediate ΔK regime. At low ΔK, the difference among ΔK_{eff} of the

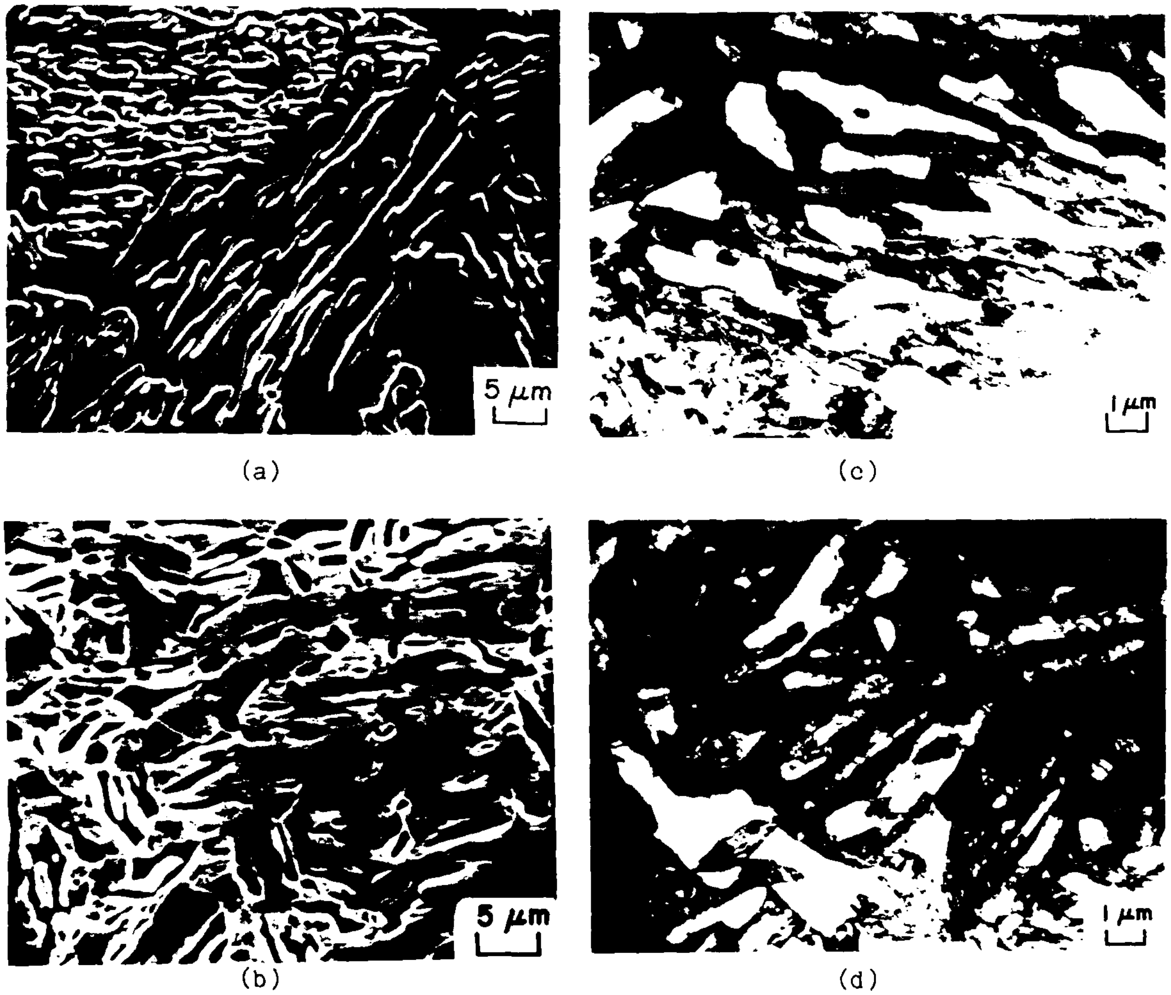

(a) (c)

(b) (d)

Fig. 2 - Electron micrographs of HY80 dual phase steel.

(a) SEM of the dual phase IAA
(b) SEM of the dual phase IAB
(c) TEM of martensite structure in a dual phase IAA sample
(d) TEM of martensite structure in a dual phase IAB sample

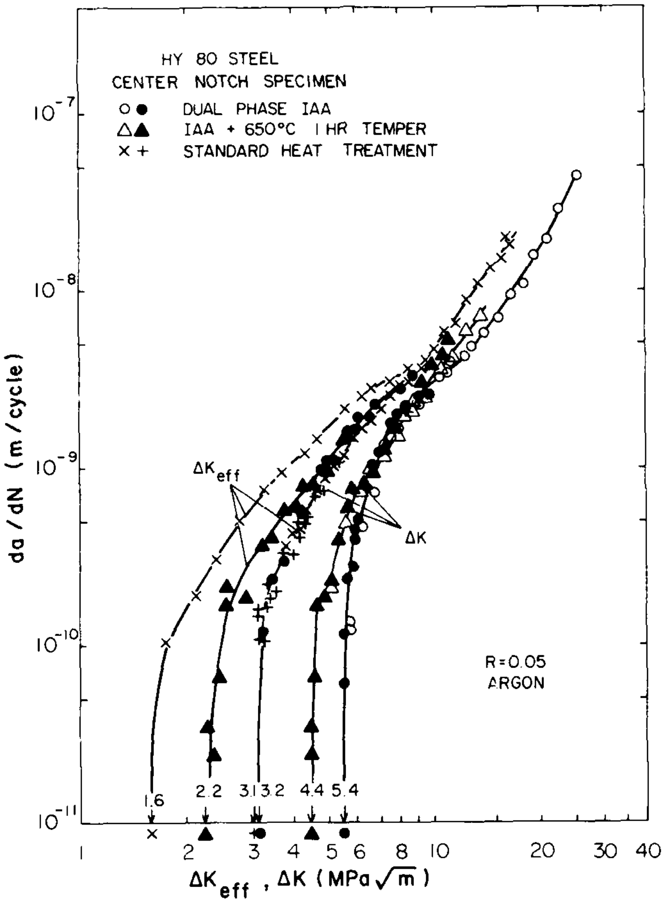

Fig. 3 - Fatigue crack propagation rate near threshold vs. ΔK and ΔK_{eff} in HY80 steel with various heat treatments.

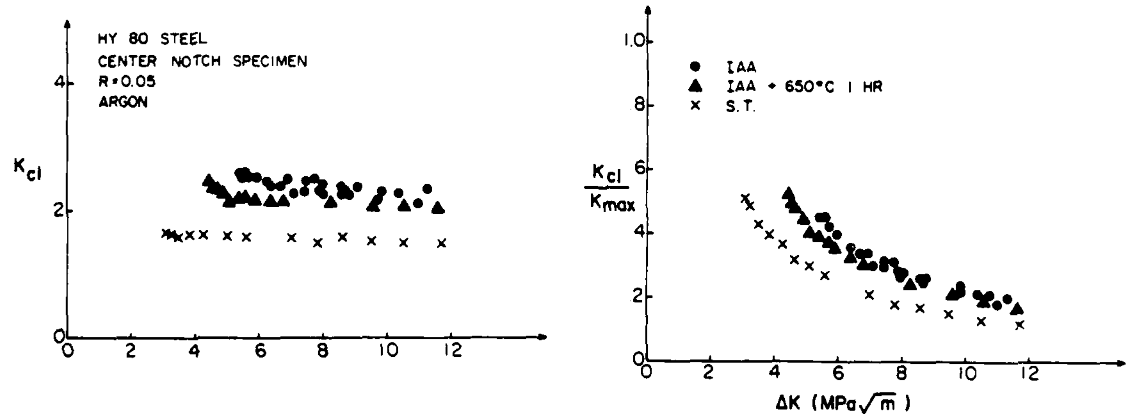

(a) (b)

Fig. 4 - The crack closure behavior of HY80 steel.

(a) Crack closure stress intensity K_{cl} versus ΔK
(b) K_{cl}/K_{max} versus ΔK

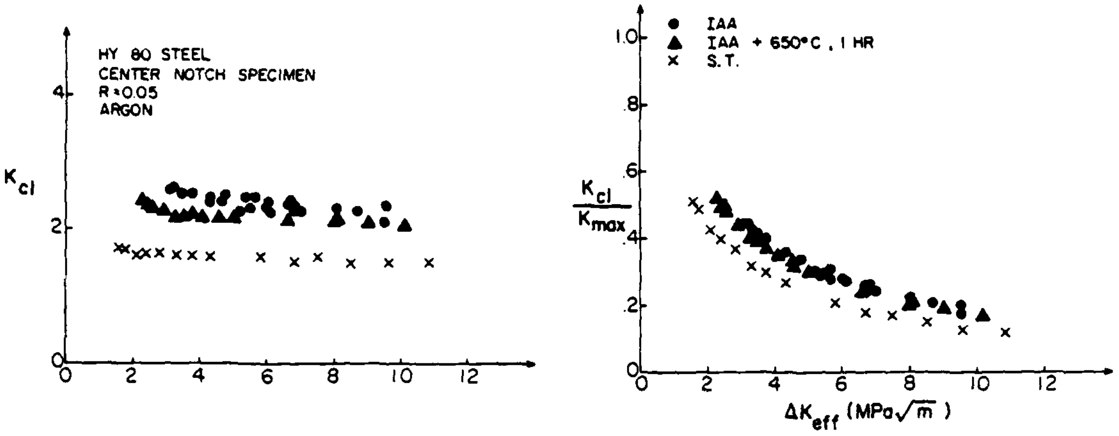

(a) (b)

Fig. 5 - The crack closure behavior of HY80 steel.

(a) Crack closure stress intensity K_{cl} versus ΔK_{eff}
(b) K_{cl}/K_{max} versus ΔK

three structures is smaller than the difference among the ΔK curves; however, a significant difference remains. Table IV summarizes the results.

The surface roughnesses of the dual phase IAA and SHT HY80 were measured in the thickness direction by a profilometer with 2000 times magnification. The surface roughness was taken to be the standard deviation of the recorded surface profile. As shown in Fig. 6(a), the surface roughness monotonically increases with ΔK. Near threshold, the roughness of the dual phase IAA HY80 is higher than for the SHT HY80. These results are consistent with the SEM observations (not shown). Since the roughness level of the fatigue surface is expected to increase with crack opening displacement, the measured surface roughness divided by CTOD is a better indicator and is shown in Fig. 6(b). The relative surface roughness indeed increases as ΔK is decreased toward the threshold. Near threshold, the higher closure level correlates with the higher level of the relative surface roughness. At the same ΔK, the relative roughness of IAA is always higher than that for the SHT HY80.

Discussion of Near Threshold Fatigue Propagation Results in Dual Phase Steels

As shown by the present experiments, crack closure in each structure becomes increasingly important as ΔK_{th} is approached. There are three models for crack closure in fatigue crack propagation: (a) plastic stretching at the crack tip [9], (b) oxide bridging [10], and (c) surface roughness coupled with shear displacements [11]. The first is not important near threshold. During fatigue crack propagation in air or moist environments, an oxide deposit on the fracture surface has been observed to increase in thickness with time due to stress-assisted fretting [10]. Since our experiments were conducted in dry argon, oxidation at the crack tip was minimized and does not appear to play an important role in the present investigation.

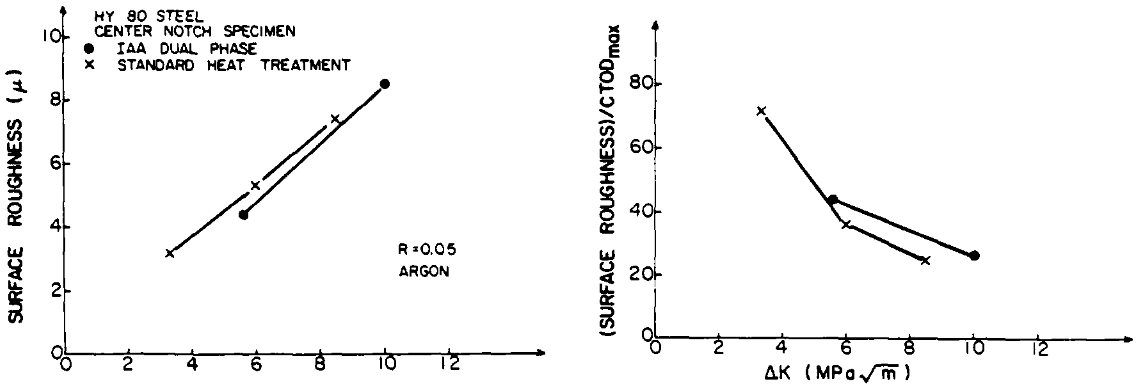

Fig. 6 - Comparison of the surface roughness behavior between the dual phase IAA and the standard heat treatment of HY80 steel.

(a) Surface roughness versus ΔK
(b) (Surface roughness)/CTOD_{max} versus ΔK. CTOD_{max} was calculated from $0.49(K_{max}^2/\sigma_y E)$ where E = 204 GPa

Thus, the present crack closure seems due to surface roughness coupled with shear displacements. The correlation of the closure stress intensity with surface roughness is further evidence for this conclusion. Recently, Suresh and Ritchie [11] proposed a geometrical model based on the assumption that near the threshold a significant amount of Mode II displacements occur during cyclic loading. Their equation to quantify the proportion of Mode II displacements (μ_{II}) to Mode I displacements (μ_I), x, is expressed by

$$x = \frac{(K_{cl}/K_{max})^2}{1 - (K_{cl}/K_{max})^2} \frac{w}{2h} \qquad (1)$$

where w and H are the average wavelength and average height of the asperities respectively. This equation is in agreement with the present results [3,4,5].

The effect of microstructure on ΔK_{th} can then be divided into two parts, extrinsic and intrinsic. The extrinsic part is due to the crack closure effect. The crack surface roughness and crack closure stress are expected to increase with the controlling microstructural size parameter, perhaps the grain size. The effect of grain size on ΔK_{th} in iron is almost all due to $K_{cl,th}$ [12]. In the present case, the values of $K_{cl,th}$ are almost the same for the IAA and IAAT structures presumably because the size of the ferrite patches are the same during tempering. The higher $K_{cl,th}$ for HY80-IAAT compared to HY80-SHT is attributed to the relatively large carbide free ferrite patches in the former. $K_{cl,th}$ is not a material property since it depends on specimen geometry being larger for edge notched specimens than for center notched specimens [5].

The present results clearly show that $\Delta K_{eff,th}$ varies with microstructure in the same alloy. $\Delta K_{eff,th}$ is 3.1 $\text{MPa-m}^{1/2}$ for the IAA and 1.6 $\text{MPa-m}^{1/2}$ for the SHT microstructures in HY80 steel. It has been suggested that $\Delta K_{eff,th}$ is determined by the stress (σ_s) necessary to operate a dislocation source located a distance s from the crack tip [12]. For low R values:

$$\Delta K_{eff,th} = \alpha\sigma_s\sqrt{2\pi s} \qquad (2)$$

where α is a factor which takes account of the fact that plastic yielding reduces the stress in the plastic zone from that calculated by fracture mechanics. Considering Eq.(2), σ_s, which is related to yield strength, and s, which is related to a characteristic microstructural size parameter, are both larger after the IAA treatment than the standard heat treatment. The ferrite patches in the dual phase structures are thought to alleviate the decrease in α which normally occurs with increase in σ_y. Tempering the IAA structure to give the IAAT structure reduces σ_s and thus $\Delta K_{eff,th}$. Comparing the IAAT and ST structures, the strength levels are the same, thus α and σ_s are the same to a first approximation; however, $\Delta K_{eff,th}$ is higher for the IAAT structure. The microstructural size parameter is larger in the IAAT structure compared to the SHT structure giving larger s. Also α is larger because of the ferrite patches. Thus, Eq. (2) may be a basis for qualitatively understanding the effect of microstructural parameters on $\Delta K_{eff,th}$.

Since crack closure was not measured, it is not possible to discuss as definitively the variation of ΔK_{th} in HY130 with tempering temperature. However, increasing the tempering temperature is expected to increase the microstructural size parameter which could increase both crack surface roughness as well as s in Eq. (2). The fracture surfaces were compared using SEM, and the 400°C tempered structure gave the smoothest fracture surface. It is thus likely that most of the increase in ΔK_{th} is due to crack closure.

Much of the effect of microstructure on the near threshold fatigue crack propagation rate is due to crack closure arising from crack surface roughness coupled with mixed mode crack propagation. The ratio of near threshold Mode I-Mode II fatigue crack propagation is a function of specimen geometry and thus near threshold fatigue crack propagation rate data must be used with extreme caution by the design engineer. This is especially true for specimen geometries where the loading is asymmetric such as the standard ASTM COD specimen geometry.

Fatigue Crack Propagation in Mid-ΔK Range

Many theoretical and empirical equations for fatigue crack propagation in the mid-range can be reduced to the approximate form [13,14]:

$$\frac{da}{dN} = \frac{(\Delta K)^4}{\mu\sigma^2 U} \qquad (3)$$

This equation is derivable on thermodynamic grounds and is not specific to any model. In Eq. (3) μ is the shear modulus, σ is the appropriate cyclic flow stress, U is the plastic work required for a unit area of fatigue crack propagation, and A is a dimensionless universal constant whose value will be discussed later. The 0.2% cyclic yield stress σ_y' is used for σ since the metal at the crack tip has been cyclically strained. Weertman [15] proposed that when $m = 4$, U is independent of ΔK but when m is less than 4, U is a function of ΔK according to the equation:

$$U = B(\Delta K)^n \qquad (4)$$

with n = 4-m. This was experimentally verified [14].

A procedure [16] was developed for measuring U by cementing small strain gages (Micro-Measurements MA-06-008CL-120) astride and above the expected crack path. The measurements were done at constant ΔK in dry argon at R = 0.05 and a frequency of 30 Hz. The stress intensity range, ΔK, was kept constant by decreasing the load every 100 μm increase in crack length. A set of stress-local strain hysteresis loops were determined as the crack moved toward or below the strain gages. For determination of U, local stress is needed rather than nominal stress. Local stress was determined from stress-strain hysteresis loops for unnotched specimens using the strain amplitudes determined with foil strain gages. The plastic work U is made up of two parts: hysteretic (U^h) and permanent (U^p). The latter was measured in several alloys and found to be much less than 1% of U [14].

From the local stress versus local strain hysteresis loops, (U_{XY}), the local hysteretic plastic work per unit area of crack advance for the coordinates in the plastic zone X and Y was determined:

$$U_{XY} = \frac{\int_{\varepsilon_1}^{\varepsilon_2} \sigma_u d\varepsilon - \int_{\varepsilon_1}^{\varepsilon_2} \sigma_t d\varepsilon}{\delta C} \qquad (5)$$

where X and Y are the distance from crack tip to the gage center in the horizontal and vertical directions, σ_u and σ_t refer to local stresses in the upper and lower curves of the hysteresis loop. Since the experiment is done at constant ΔK, according to linear elastic fracture mechanics, a plastic zone of constant size and shape advances with the crack. A contour map of U_{XY} in the plastic zone may thus be drawn; those shown in Fig. 7 are for HY80 and HY130 [2]. The plastic zones are butterfly-wing shaped, since the maximum shear stress is 45° from the loading direction. As expected, the plastic zone size increases with decrease in yield stress.

The plastic work per unit area of fatigue crack propagation was obtained by integrating over the plastic zone:

$$U = \iint U_{XY} \, dXdY \qquad (6)$$

Because the foil gage fails when the crack enters it, U_{XY} closer than 100 μm to the crack tip cannot be measured directly and was determined by an extrapolation method [13,16].

Introducing measured values for U (using SI units) at different ΔK's gave $A = [2.9 \pm 0.8 \text{ (S.D.)}] \times 10^{-3}$ for 13 Fe and Al base alloys, many with several different heat treatments. For HY80 and HY130 of standard heat treatment at ΔK of 20 $MPa\text{-}m^{1/2}$, U values were 7.7 and 2.2×10^5 J/m^2 respectively, as shown in Table V.

Table V. Values of Quantities in Equation (1) for HY80 and HY130 (Atmosphere: Dry argon)

Material	σ_y' MPa	ΔK MPa-$m^{1/2}$	da/dN at ΔK = 20 MPa-$m^{1/2}$ (m/cycle)	U (J/m^2)	A
HY80 (700°C temper)	521	20	3.5×10^{-8}	7.7×10^5	3.6×10^{-3}
HY130 (610°C temper)	868	20	5.0×10^{-8}	2.2×10^5	4.0×10^{-3}

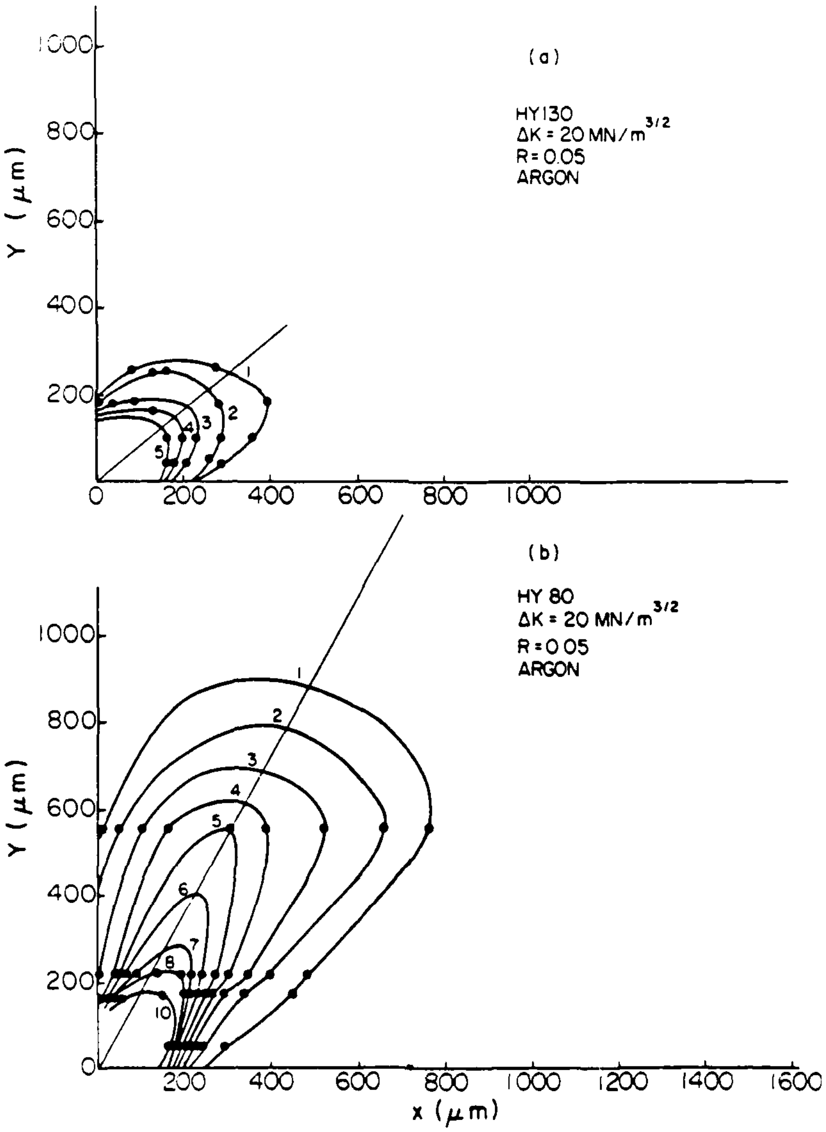

Fig. 7 - Local plastic work density contour lines versus distance from crack tip: (a) HY80, (b) HY130. Units are 10^{11} J/m^{-4}.

To obtain lower crack growth rates, Eq. (3) states that U and/or σ_y' must be increased. To a first approximation σ_y' and U are inversely related because as σ_y' increases the plastic zone size for a given ΔK decreases. Recall that the local plastic work is integrated over the plastic zone to obtain U. Liaw et al. [13] examined the relation between σ_y' and U. A general hyperbolic decrease of U with increase of σ_y' is observed but there are some interesting exceptions; for instance, the U-value for Al-6.3Cu-T4 lies above the curve. This alloy contains dispersed phases which homogenize the plastic deformation so that it is not so highly localized in the plastic zone. The local plastic work density for the coordinates X and Y in the plastic zone (U_{XY}) is approximately

$$U_{XY} = \frac{|\sigma^{\ell}\varepsilon^{\ell}|_{XY}}{|dC/dN|} \tag{7}$$

where σ^{ℓ} is the maximum local stress and ε^{ℓ} is the local plastic strain range. Even though σ_{XY}^{ℓ} increases with σ_y' because the plastic zone can sustain higher stresses, U_{XY} for constant value of X and Y is usually smaller for higher strength alloys because ε_{XY}^{ℓ} is smaller [13]. A comparison of HY130 and hot-rolled Nb-HSLA [13] steel shows that the former has higher strength and lower U. The values of dC/dN at ΔK of 20 MPa-$m^{1/2}$ are comparable. For X = 100 μm and Y = 30 μm, σ_{XY}^{ℓ} for HY130 is 540 MPa and ε_{XY}^{ℓ} is 0.012. On the other hand, for the hot-rolled Nb-HSLA steel, at the same X and Y, σ_{XY}^{ℓ} is 270 MPa but ε_{XY}^{ℓ} is 0.094. We need to have a better understanding of the factors which determine ε_{XY}^{ℓ}. The hysteresis loop width versus stress range $\Delta\sigma$ in uncracked-unnotched specimens (a much easier set of measurements to obtain than those to determine U) should quantitatively indicate how σ_{XY}^{ℓ} and ε_{XY}^{ℓ} vary in the plastic zone ahead of a fatigue crack. Such a study versus microstructure would appear to be very helpful towards developing alloys which have low fatigue crack propagation rates.

Thus Eq. (3) points the alloy designer towards the development of increasing hysteresis loop area, as measured on smooth specimens, while not allowing much change in σ_y'. Likewise, an increase in modulus, for example, through fiber reinforcement, should also decrease crack growth rates, if all other factors are kept equal.

In order to see whether changing microstructure might increase U keeping σ_y constant, the same constant hardness treatments given previously to HY130 steel A, B, C, and D, were investigated for their fatigue crack propagation rates in the mid-ΔK region. The results for ΔK of 15, 20, and 30 MPa-$m^{1/2}$ are shown in Table II. The differences are rather minor.

Suggestions for Future Research

Dual phase ferrite-tempered martensite microstructure steels appear to be excellent candidates for future research to develop steels which are more resistant to fatigue crack propagation in the near threshold and mid-ΔK regions. The mixture of soft ferrite to increase plastic strain and α in Eq. (1) and tempered martensite for strength may be the optimum type of microstructure for this purpose. These principles would appear to apply to other systems than ferritic steels.

In the region near ΔK of 10 $\mathrm{MPa\text{-}m}^{1/2}$ the da/dN versus ΔK curves for the dual phase and conventionally heat treated HY80 came together; however producing an optimum dual phase microstructure might be a way to increase ε^{ℓ} in Eq. (6) without reducing σ^{ℓ}. If the mean free path in the ferrite is too large, then crack propagation in the soft ferrite alone would prevail so there would seem to be an optimum morphology to give maximum integration of Eq. (6). Consequently, dual phase microstructures where the crack must go through both phases should be investigated for the mid-ΔK region.

Acknowledgement

Supported by ONR under ONR Contract No. N00014-78-C-0565, "Threshold and Plastic Work of Fatigue Crack Propagation in HY80 and HY130 Steels", September 1, 1978 to August 31, 1982, Final Report dated October 1, 1982.

References

1. H. Suzuki and A. J. McEvily, "Microstructural Effects on Fatigue Crack Growth in a Low Carbon Steel", Met. Trans. A, 10A (1979) pp. 475-481; K. Minakawa and A. J. McEvily, "On Crack Closure in the Near Threshold Region", Scripta Met., 15 (1981) pp. 633-636.

2. S. I. Kwun and M. E. Fine, "Fatigue Macrocrack Growth in Tempered HY80, HY130, and 4140 Steels: Threshold and Mid-ΔK Range", Fatigue of Engineering Materials and Structures, 3 (1980) pp. 367-382.

3. J. L. Horng and M. E. Fine, "Near Threshold Mixed Mode I-II Fatigue Crack Propagation Parallel Superposition Model", Scripta Met., 17 (1983) pp. 1427-1430.

4. J. L. Horng and M. E. Fine, "Near Threshold Fatigue Crack Propagation of HY80 and HY130 Steels", pp. 115-129 in Fatigue Crack Growth Threshold Concepts, D. L. Davidson and S. Suresh, eds.; TMS-AIME, Warrendale, PA, 1984.

5. J. L. Horng and M. E. Fine, "Near Threshold Fatigue Crack Propagation Rates of Dual-Phase Steels", Matls. Sci. & Engr., 67 (1984) pp. 85-195.

6. M. E. Fine, "Threshold and Plastic Work of Fatigue Crack Propagation in HY80 and HY130 Steels", Final Technical Report covering period 9/1/78-8/31/82, ONR Contract #N00014-78-C-0565, ONR, Arlington, VA, Oct. 1, 1982.

7. M. E. Fine and R. O. Ritchie, "Fatigue Crack Initiation and Near-Threshold Crack Growth", Proceedings of 1978 ASM Materials Science Seminar: Fatigue and Microstructure, p. 245, ASM, Metals Park, OH, 1979.

8. D. Gan and J. Weertman, "Crack Closure and Crack Propagation Rates in 7050 Aluminum", Engr. Frac. Mech., 15 (1981) pp. 87-106.

9. W. Elber, "The Significance of Fatigue Crack Closure", pp. 230-242 in Damage Tolerance in Aircraft Structure, ASTM STP 486, American Society for Testing Materials, Philadelphia, PA, 1971.

10. S. Suresh, D. M. Parks and R. O. Ritchie, "Crack Tip Oxide Formation and Its Influence on Fatigue Threshold", p. 391 in Fatigue Threshold, J. Backlund, A. Blom and C. J. Beevers, eds.; EMAS Publ. Ltd., Warley, U.K., Vol. 1, 1982.

11. S. Suresh and R. O. Ritchie, "A Geometric Model for Fatigue Crack Closure Induced by Fracture Surface Roughness", Met. Trans. A, 13A (1982) pp. 1627-1631.

12. G. M. Lin and M. E. Fine, "Effect of Grain Size and Cold Work on the NearThreshold Fatigue Crack Propagation and Crack Closure in Iron", Scripta Met., 16 (1982) pp. 1249-1254.

13. P. K. Liaw, S. I. Kwun and M. E. Fine, "Plastic Work of Fatigue Crack Propagation in Steels and Aluminum Alloys", Met. Trans., 12A (1981) pp. 49-55.

14. M. E. Fine and D. L. Davidson, "Quantitative Measurement of Energy Associated with a Moving Fatigue Crack", pp. 350-369 in Fatigue Mechanisms: Advances in Quantitative Measurement of Physical Damage, J. Lankford, D. L. Davidson, W. L. Morris, and R. P. Wei, eds., ASTM STP 811, American Society for Testing Materials, Philadelphia, PA, 1983.

15. J. Weertman, "Fatigue Crack Propagation Theories", Proceedings of 1978 ASM Materials Science Seminar: Fatigue and Microstructure, p. 279, ASM, Metals Park, OH, 1979.

16. S. Ikeda, Y. Izumi and M. E. Fine, "Plastic Work During Fatigue Crack Propagation in a High Strength Low Alloy Steel and in 7050 Al-Alloy", Engr. Frac. Mech., 9 (1977) pp. 123-136.

MODELING OF ENVIRONMENTALLY ASSISTED CRACK GROWTH

R. P. Wei and G. W. Simmons
Department of Mechanical Engineering and Mechanics
and Department of Chemistry
Lehigh University
Bethlehem, PA 18015

As a result of research performed under the ARPA Coupling Program on Stress Corrosion Cracking from 1966 to 1971, it became apparent that significant progress in the understanding of environmentally assisted crack growth required a fundamental and multi-disciplinary effort. Such a program, involving principally fracture mechanics and surface chemistry, was initiated at Lehigh University under the auspices of the Office of Naval Research in 1972, and has been complemented over the years by programs supported by other governmental agencies and by industry. In this paper, a perspective summary of this effort is presented, and important areas of further research are discussed.

The initial effort was narrowly focused and addressed the issue of rate controlling processes for crack growth in high strength steels exposed principally to gaseous environments. Identification of the rate controlling processes (namely, gas transport, surface reaction and hydrogen diffusion) then led to modeling of environmentally assisted crack growth for both static and fatigue loading, which broadened the approach and understanding to high-strength aluminum and titanium alloys. The modeling effort has been extended now to the consideration of crack growth in aqueous environment, and serves to guide research in this scientifically and technologically important area.

The important topics for future research include the kinetics and mechanisms of chemical reactions with clean metal surfaces, the mechanisms and methods for the inhibition of these reactions, and the kinetics and mechanisms of hydrogen-metal interactions (namely, embrittlement). The principal benefits of these efforts would include the formulation of methods for mitigating environmentally assisted cracking, and the development of procedures for making reliable predictions of long-term service and of rational accelerated tests.

Introduction

Environmentally assisted crack growth in high strength alloys is an important technological problem, because it bears directly upon the reliability and durability of engineering structures and systems in service. It is a multi-faceted problem, and involves complex interactions of loading (mechanical), environmental and metallurgical variables. Its importance and its multi-disciplinary nature have been well recognized, and the problem has received considerable attention particularly during the last twenty years. In this paper, a perspective summary of the efforts from a program at Lehigh University, supported by the Office of Naval Research and shepherded by Dr. Philip A. Clarkin since 1972, is presented. Important areas of further research are discussed.

To provide perspective, it is useful to consider the various efforts in relation to the following hierarchy of analytical (or conceptual) and experimental processes that are required to arrive at quantitative understandings of physical phenomena [1]:

- Formulation of Problem and Working Hypotheses
  - Exploratory Experiments
  - Development of Approaches
    - Screening Experiments
    - Model Development
      - Model Evaluation
      - Formalization of Quantitative Theory and Understanding
        - Applications of Theory and Understanding

Typically several iterations through these processes are needed before the understanding can be formalized into a quantitative theory. In practice, limited information is often obtained at various intermediate levels and used in making engineering decisions. This information, however, is usually of little value in terms of fundamental understanding and of quantitative design.

The ONR sponsored program at Lehigh University, involving principally fracture mechanics and surface chemistry, was initiated in 1972, and followed from the ARPA Coupling Program on Stress Corrosion Cracking (circa 1966-1972) [2]. The program was based on the realization that significant progress in the understanding of environmentally assisted crack growth required a fundamental approach and a multi-disciplinary effort, and has been complemented over the years by programs supported by other governmental agencies and by industry. It capitalized on the background and insight gained, and most importantly on the approaches developed from the ARPA Coupling Program and its counterparts during 1966-1972. Beginning with fundamental considerations of the rate controlling process for environmentally assisted crack growth in 1972, the efforts have advanced logically to the level of modeling of environmentally assisted crack growth, both for stress corrosion cracking and corrosion fatigue, and of model evaluation through the 1970's. The modeling effort now provides a formalized basis and the driving force for further advances in understanding. From an engineering perspective, it provides a rational basis for the development and utilization of data and for the formulation of life prediction methods for design.

A perspective summary of the significant contributions from this extended effort can be best gleaned through a consideration of the processes that control crack growth and through modeling.

Crack Growth Processes

The processes that are involved in environmental enhancement of crack growth in high-strength alloys by hydrogen and hydrogenous gases (such as H_2O and H_2S) and by aqueous environments are as follows, and are illustrated schematically in Fig. 1 for the case of gaseous environments [3] and more generally in the block diagram in Fig. 2:

1. Transport of the deleterious environment to the crack tip.
2. Reactions of the deleterious environment with newly produced crack surfaces to evolve hydrogen.
3. Hydrogen entry (or absorption).
4. Diffusion of hydrogen to the fracture (or embrittlement) site.
5. Partitioning or distribution of hydrogen among the various microstructural sites.
6. Hydrogen-metal interactions leading to embrittlement (that is, the embrittlement reaction) of the microstructural sites.

These processes operate consecutively or in sequence, and presuppose hydrogen embrittlement as the responsible mechanism. Crack growth is controlled by the slowest process in this sequence. The overall crack growth response is governed by one or more of these processes in conjunction with the mechanical driving force for crack growth, and reflects the rate controlling process. The mechanical driving force is characterized here by either the applied or local stress or the crack tip stress intensity factor K [4,5]. It should be noted that high temperature processes (such as, internal oxidation, sulfidation and hydrogen attack) are not included.

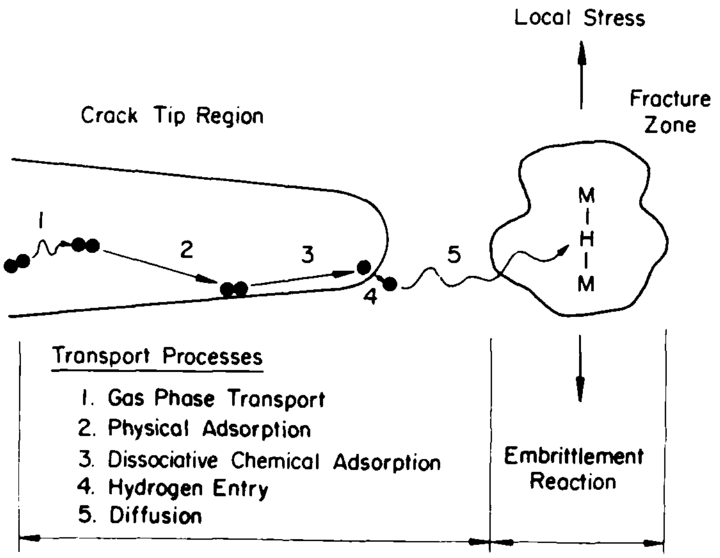
Local Stress
Fracture Zone
Crack Tip Region
1
2
3
4
5
M
I
H
I
M
Transport Processes
1. Gas Phase Transport
2. Physical Adsorption
3. Dissociative Chemical Adsorption
4. Hydrogen Entry
5. Diffusion
Embrittlement Reaction

Fig. 1 - Schematic illustration of sequential processes in environmental enhancement of crack growth by hydrogenous gases. Embrittlement by hydrogen is assumed and is schematically depicted by the metal-hydrogen-metal bond. (After Ref. 3.)

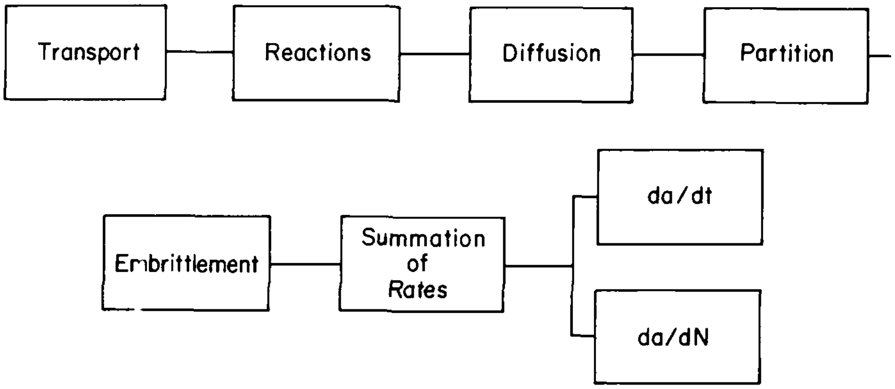

Fig. 2 - Block diagram of processes that can control environmentally assisted crack growth, leading to overall crack growth rate under sustained loading or in fatigue.

Embrittlement, or the final step in the aforementioned sequence, however, is expected to be a function of microstructure. The extent of embrittlement or the rate of cracking along each microstructural path is expected to be a function of the local hydrogen concentration, which in turn is expected to depend on the external environmental conditions of pressure, electrode potential, temperature, etc. Cracking along the various microstructural elements is expected to take place concurrently or in parallel. The overall crack growth rate is the weighted average of the individual rates along the different crack paths or of the various micromechanisms.

Clearly, understanding and modeling of crack growth required identification and quantification of the rate controlling process. The latter can be obtained only through well defined and coordinated chemical/electrochemical, mechanical and metallurgical experiments.

Rate Controlling Processes and Modeling in Perspective

It was recognized from the outset that the aforementioned processes govern both stress corrosion (or sustained-load) and corrosion fatigue crack growth. Although the ONR program at Lehigh was directed towards research on corrosion fatigue, it allowed sufficient flexibility to utilize both modes of crack growth in exploring the fundamental issues. Because of the identification of a K-independent stage (Stage II) of sustained-load crack growth with the underlying rate controlling process, the initial efforts were directed at detailed studies of the kinetics and mechanisms of reactions of water with iron and steel, and the correlation of this information with the temperature dependence for Stage II crack growth [6-10]. These efforts led to an unambiguous identification of iron-water reaction as the rate controlling process for crack growth in high-strength steels in 1977, and a realization of the very limited extent of these reactions [6-10] (see Fig. 3).

With the additional work on surface reactions and on crack growth, under programs sponsored by AISI, ERDA/FE (now DoE), NASA-Lewis and NSF, a broader based understanding of rate controlling processes began to emerge during the remainder of the 1970's, and considerations of modeling of sustained-load crack growth was begun. In 1977, the ALCOA Foundation awarded a grant to R. P. Wei to encourage research on aluminum alloys. A similar grant to G. W. Simmons was initiated in the following year, with both grants in effect from 1977 to 1979. With this seed funding and concurrence by Dr. Clarkin, a temporary expansion was made in the scope of the ONR program to examine the role of water vapor in enhancing fatigue crack growth in high-strength aluminum alloys. This excursion triggered the effort on modeling of corrosion fatigue crack growth [11-12], which led in turn to the recognition and modeling of transport-controlled crack growth under sustained loading [13].

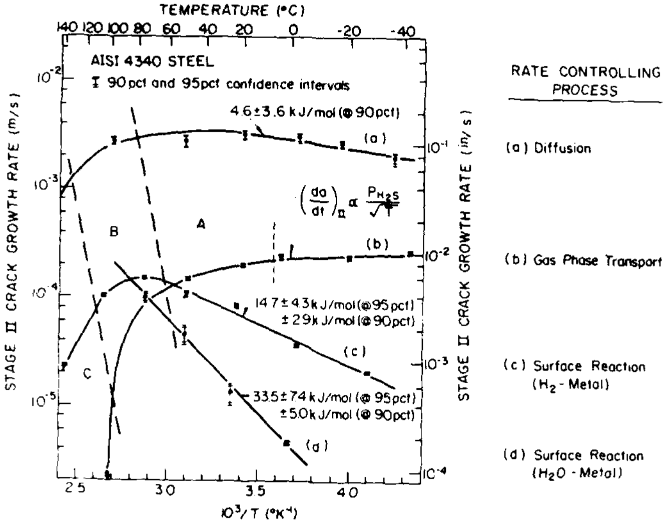

Fig. 3 - Temperature dependence for Stage II crack growth and the corresponding rate controlling processes at low temperatures for AISI 4340 steel in various hydrogenous environments: (a) H_2S at 2.66 kPa, (b) H_2S at 0.13 kPa, (c) H_2 at 133 kPa, and (d) H_2O (liquid) [10,13,14].

Modeling of Crack Growth

Modeling of crack growth may be sub-divided in terms of loading conditions. Additionally it may be divided in accordance with the various processes that affect crack growth (see Fig. 2). Assuming that hydrogen embrittlement is the responsible mechanism, modeling can then be grouped in terms of hydrogen supply (transport, reactions and diffusion), hydrogen distribution within the material (partition), and embrittlement reactions (which determine the rates of cracking along the various microstructural paths). Suitable models must also be developed to obtain an average or overall (macroscopic) crack growth rate. The effort at Lehigh has been concentrated in the first area, and reflects the primary thrust in understanding the chemical and mechanical aspects of environmentally assisted crack growth. This effort has been extended to include hydrogen distribution and thereby incorporating the influence of microstructure. The development of the various models is briefly described. The need for further development and for examining the role of embrittlement mechanism is discussed in a subsequent section.

Sustained-Load Crack Growth

Initial modeling of sustained-load crack growth was largely phenomenological and was limited to the case of hydrogen-supply controlled Stage II crack growth in the lower temperature region (i.e., Region A in Fig. 3). The principal thrust was directed at obtaining reliable chemical reaction and crack growth data to confirm the concept of rate controlled crack growth and to identify the controlling process. Obvious deviations of the crack growth response curves (Fig. 3) from those of single rate controlling processes and the observed changes in fracture paths (or micromechanisms) led to the consideration of transfers of control and of the role of microstructure.

Models Based On Hydrogen Supply. Based on extensive data on the kinetics of surface reactions and crack growth for high-strength steels in water/water vapor, hydrogen and hydrogen sulfide [6-15], models for Stage II crack growth were proposed. When the rates of reactions are slow (e.g., in hydrogen and in water), crack growth rate would be controlled by the rate of surface reactions. On the other hand, when the reactions are rapid (e.g., in hydrogen sulfide), then the rate may be controlled either by the rate of external transport of the gases to the crack tip, or by the rate of internal transport (diffusion) of hydrogen to the embrittlement site. The models, expressing the specific dependence on pressure (p_o) and temperature (T) are as follows [16-17]:

Transport Control: $$(da/dt)_{II} = C_t p_o / T^{1/2} \quad \text{(for Knudsen flow [18])} \tag{1}$$

Surface Reaction Control: $$(da/dt)_{II} = C_s p_o^m \exp(-E_s/RT) \tag{2}$$

Diffusion Control: $$(da/dt)_{II} = C_d p_o^{1/2} \exp(-E_d/2RT) \tag{3}$$

The constants C_i contain chemical and physical quantities that relate to gas transport, surface reaction, etc., and reflect the susceptibility of specific alloys to embrittlement by specific environments (viz., the embrittlement reaction term). E_s and E_d are the activation energies for surface reaction and hydrogen diffusion respectively. Good agreement with experimental observations in the low temperature region (Region A) is indicated in Fig. 3.

In these models, a single process is assumed to be in control, and the constants C_i are assumed to be sensibly constant. It is to be recognized that transfer of control from one process to another may occur as the environmental conditions are changed. The consequences of this transfer have been discussed in [16]. In formulating these phenomenological models, simple (single step) reactions were implicitly assumed. Because the reactions tend to be much more complex, these models should be viewed as guides and as starting points for developing further understanding of environmentally assisted crack growth.

Partitioning of Hydrogen. The observed decrease in crack growth rate with increasing temperature in the "high temperature" region (Region C in Fig. 3) for carbon martensitic steels (such as, AISI 4340 steel) has been analyzed from the point of view of surface chemistry [19-21]. These analyses, however, have largely ignored the important role of microstructure and micromechanism in hydrogen embrittlement, or have made unrealistic assumptions regarding surface coverage by hydrogen. The models proposed on the basis of these analyses, therefore, cannot explain the observed changes in fracture mode with temperature [22,23].

To quantitatively account for the role of hydrogen-microstructure interactions in hydrogen assisted crack growth, a "hydrogen partitioning" model has been developed [23,24]. The model suggests that the rate of hydrogen assisted crack growth is essentially determined by two basic factors: (i) the rate of hydrogen supply to the fracture process zone, which is controlled by one of the processes for hydrogen supply indicated previously, and (ii) the partitioning of hydrogen amongst different microstructural elements or traps (principally between the prior-austenite grain boundaries and the matrix), which is controlled by the hydrogen-trap interactions and determines the contribution by each element to the overall crack growth rate. This model is illustrated schematically in Fig. 4 for hydrogen assisted crack growth in a high strength steel [23,24].

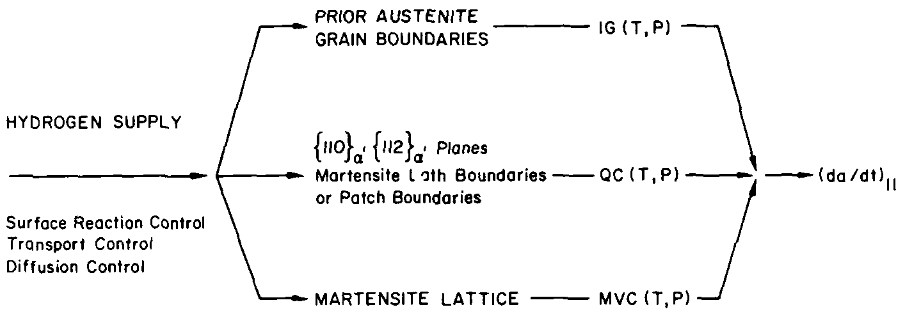

Fig. 4 - Schematic illustration of the partitioning of hydrogen, and its relationship to hydrogen supply and the resulting Stage II crack growth rate [23,24].

At low temperatures (in Region A of Fig. 3), hydrogen would reside primarily at grain boundaries and slip planes. Cracking, therefore, tended to be predominantly intergranular (IG) and included a small amount of quasi-cleavage (QC). Because of the relatively slow rate of supply of hydrogen from the external environment, crack growth would be controlled by one of the hydrogen supply processes. With increasing temperature (into Region C), hydrogen concentration at the grain boundaries and in the slip planes would be expected to drop quickly, and more hydrogen entered into the martensite lattice. Increasing amounts of microvoid coalescence (MVC) or dimpled failure now occurred and resulted in slower crack growth rates. The overall crack growth rate is the weighted average of rates of cracking along the different microstructural paths, or by these concurrent micromechanisms. Accordingly, the changes in crack growth rate and crack growth response with temperature are attributed now to the transfer of micromechanisms of fracture instead of the processes of hydrogen supply.

Detailed considerations and derivation of the model are given in [23,24]. In the limit, the model conforms to the phenomenological models given by Eqns. (1) to (3) at low temperatures. Based on reasonable estimates of various parameters (including the binding enthalpy of hydrogen, H_B), the temperature and pressure dependence for Stage II crack growth predicted by the model for high-strength steels was found to be consistent with expectations, and is in good agreement with the experimental results for AISI 4340 steel in both hydrogen and hydrogen sulfide (see Figs. 3 and 5) [23,24]. Clearly, partitioning of hydrogen among the different microstructural elements plays an important role in determining the kinetics of crack growth and the crack growth response. The partitioning model has provided needed insight, and a clear indication of the need for a broadly based understanding, including that of embrittlement mechanisms.

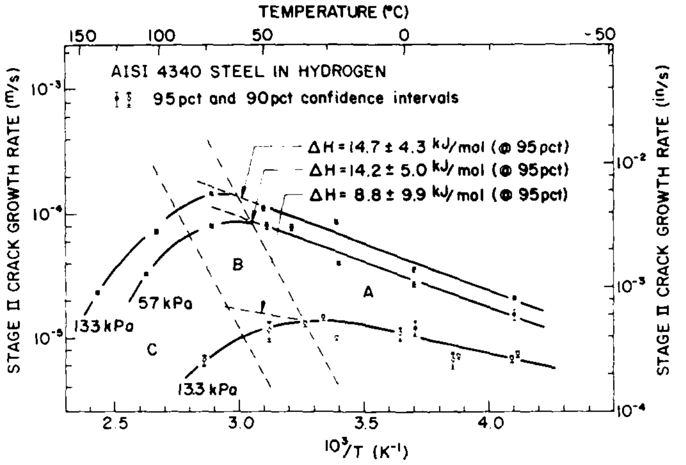

Fig. 5 - Comparison between model predictions and crack growth data on AISI 4340 steel tested in hydrogen at different pressures and temperatures [14,23,24].

Fatigue Crack Growth

Based on the understanding developed for sustained-load crack growth, models for surface reaction and transport controlled fatigue crack growth were developed under this program [11,12], and have been used successfully to explain the observed dependence of fatigue crack growth rates on cyclic load frequency and pressure in gaseous environments [11,12,25,26]. Insight obtained from this effort has been applied to the consideration of corrosion fatigue in aqueous environments, and to the investigation of compositional and microstructural variables.

Superposition Model. Modeling was based on the proposition that the rate of crack growth in a deleterious environment, $(da/dN)_e$, is composed of the sum of three components, Eqn. (4) [3].

$$(da/dN)_e = (da/dN)_r + (da/dN)_{cf} + (da/dN)_{scc} \tag{4}$$

Equation (4), is the modification of a simpler model first proposed by Wei and Landes [27]. In this equation, $(da/dN)_r$ is the rate of fatigue crack growth in an inert (reference) environment, $(da/dN)_{scc}$ is the contribution by sustained-load crack growth, $(da/dN)_{cf}$ represents a cycle-dependent contribution requiring synergistic interaction of fatigue and environmental attack. Important understanding of corrosion fatigue response in gaseous environments has been developed through chemical modeling and experimental verification of the role of gas transport and surface reactions on $(da/dN)_{cf}$ [25,26].

It is now recognized that mechanical (or "pure") fatigue and cycle-dependent corrosion fatigue proceed by different micromechanisms and occur concurrently or in parallel, with the rate of corrosion fatigue crack growth given by Eqn. (5) [28].

$$(da/dN)_e = (da/dN)_r\ (1 - \phi) + (da/dN)_c\phi \tag{5}$$

For simplicity, the sustained-load growth or stress corrosion cracking (SCC) term, which is considered as a sequential contribution, is not included. In Eqn. (5), $(da/dN)_r$ is interpreted as the mechanical fatigue rate, $(da/dN)_c$ as the "pure" corrosion fatigue rate, and ϕ as the fractional area of crack that is undergoing pure corrosion fatigue. In the limit, for $\phi = 0$ or for a test in an inert environment, $(da/dN)_e = (da/dN)_r$, which corresponds to pure fatigue. For $\phi = 1$, corresponding to saturation [1,6-8], $(da/dN)_e = (da/dN)_{e,s} = (da/dN)_c$, and the measured growth rates now correspond to the pure corrosion fatigue rates. It should be noted that these rates themselves may be composed of contributions from several concurrent micromechanisms. Through an appropriate regrouping of terms, it can be readily seen that the cycle-dependent environmental contribution is still correctly represented by the $(da/dN)_{cf}$ term and the previous modeling development remains unaltered [28].

$$(da/dN)_e = (da/dN)_r + [(da/dN)_c - (da/dN)_r]\,\phi = (da/dN)_r + (da/dN)_{cf} \qquad (6)$$

For convenience, the original notation shall be retained in discussing the chemical contributions to corrosion fatigue.

Corrosion Fatigue in Gaseous Environments. Modeling of corrosion fatigue crack growth in gaseous environments was reported by Weir et al. [11] and by Wei and Simmons [12]. Although the modeling effort involved simplifications, the results have nevertheless provided considerable insight and have served as basis for further advances in understanding. The following governing differential equations, based on perfect gas law and simple first-order reactions, were used [11,12]:

$$dp/dt = -(SN_o\mathbf{k}T/V)(d\theta/dt) + (F/V)(p_o - p) \qquad (7)$$

$$d\theta/dt = k_c p(1 - \theta) \qquad (8)$$

The terms in the equations are as follows: p = pressure of gas at the crack tip (i.e., local pressure); p_o = pressure of gas in the surrounding environment; $\mathbf{k}$ = Boltzmann's constant; S = effective area of crack tip surfaces that participate in the reactions per cycle; T = absolute temperature; V = volume associated with the surface S; N_o = density of surface sites; θ = fractional surface coverage, or extent of surface reactions as a fraction of the maximum coverage; F = flow parameter that depends on the nature of flow, the dimension and shape of the capillary (or crack), the molecular weight of the gas and the temperature; and k_c = reaction rate constant. Equation (7) is the mass balance equation for one-dimensional flow. Knudsen (or molecular) flow [18] was assumed in estimating the parameter F. For simplicity, only a single reaction step was considered and the reaction was assumed to follow Langmuir kinetics [29]. Langmuir kinetics in turn imply that the extent of reaction is limited; in other words $\theta \rightarrow 1$.

Assuming that environmental enhancement of fatigue crack growth results from embrittlement by hydrogen that is produced by the reactions of hydrogenous gases with the freshly produced crack surfaces, two limiting cases were obtained from the solution of Eqns. (7) and (8) [11,12]. For highly reactive systems (that is, when k_c is large), crack growth is controlled by the rate of transport of the gases to the crack tip. On the other hand, when k_c is low, it is controlled by the rate of surface reactions at the crack tip.

Transport Control:

$$(da/dN)_{cf} = (da/dN)_{cf,s}[(p_o/2f)/(p_o/2f)_s] \qquad (9)$$

$$\text{for } (p_o/2f) < (p_o/2f)_s$$

Surface-Reaction Control:

$$(da/dN)_{cf} = (da/dN)_{cf,s}[1 - \exp(-k_c p_o/2f)] \qquad (10)$$

The terms in square brackets in Eqns. (9) and (10) represent the fractional surface coverage (θ), and $(da/dN)_{cf,s}$ is identified with the rate $[(da/dN)_c - (da/dN)_r]$ from Eqn. (6) [28]; that is, with the maximum enhancement in the rate of cycle-dependent corrosion fatigue crack growth. Hence, the fractional surface coverage, or extent of surface reaction (θ), may be identified with the areal fraction (ϕ) of surfaces produced by pure corrosion fatigue during crack growth [28]. Good agreement between these models and experimental data has been obtained (see Fig. 6 for example) [25,30]. The transport controlled case is represented by aluminum alloys in water vapor [12,25,31] and steels in hydrogen sulfide [26], and the surface reaction controlled case by high strength steels in water and water vapor [30].

In deriving Eqns. (9) and (10), $(da/dN)_{cf}$ was assumed to be proportional to the amount of hydrogen produced by the surface reactions per cycle, which is proportional in turn to the effective crack area and the available time, in addition to the kinetic parameters. The time available for reactions was assumed to be one-half of the loading period, or the reciprocal of twice the loading frequency (1/2f). The effective crack area was assumed to be proportional to the "saturation" crack growth rate $(da/dN)_{e,s}$. This per cycle increment of crack growth allows the surface reaction to reach completion during one loading cycle. The processes that control corrosion fatigue crack growth response are localized to a region of about 10^{-5} to a few millimeters from the crack tip.

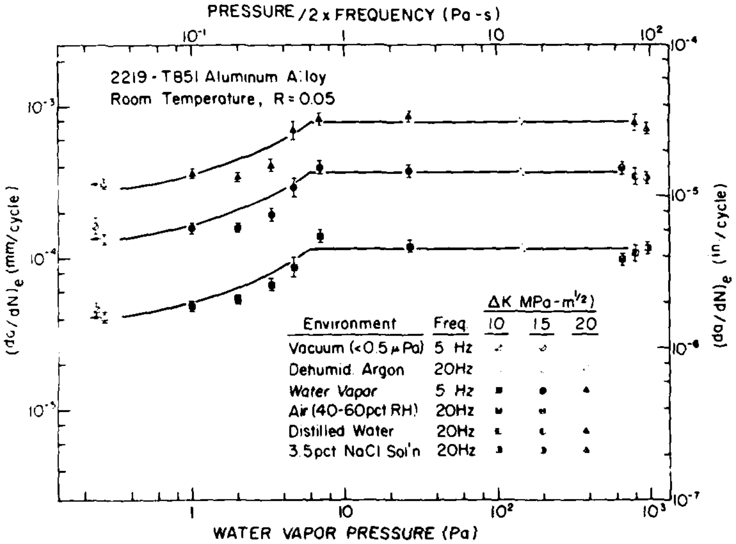

Fig. 6 - Influence of water vapor pressure (or pressure/2xfrequency) on corrosion fatigue crack growth rate in 2219-T851 aluminum alloy at room temperature. Solid lines represent predictions of model for transport-controlled growth [25].

It is recognized that the form of the response, for the case of surface-reaction controlled crack growth, would depend on the specific nature and mechanism(s) of the reactions. The reactions may not follow Langmuir kinetics, and may involve more than one step. For example, the reactions of H_2S with iron and high-strength steels involve two steps; one of which is very rapid and the other, much slower [13,26,32]. As a result, fatigue crack growth in H_2S exhibited two regimes (see [26]). At low pressures (or exposures), crack growth response reflected transport control. At the higher pressures or exposures, a further increase in crack growth rate was observed which reflected the contributions of the second reaction step, where crack growth is surface-reaction controlled. A similar situation exists for crack growth of high-strength steels in water vapor, which may be further complicated by capillary condensation at the crack tip [14]. An example of two region crack growth response for a high-strength steel is illustrated in Fig. 7, which shows a smooth transition between the gaseous and aqueous environments [30]. For a complete understanding and modeling of corrosion fatigue crack growth response, therefore, detailed information on the kinetics and mechanisms of the relevant surface reactions is required. In addition, information on the various other processes (including diffusion and distribution of hydrogen, and the physico-chemical processes of embrittlement) is needed to complete the understanding and to allow for the "prediction" of actual crack growth rates.

The results shown in Fig. 7 suggested strongly that a comparable approach be used in developing a better understanding of corrosion fatigue crack growth in aqueous environments.

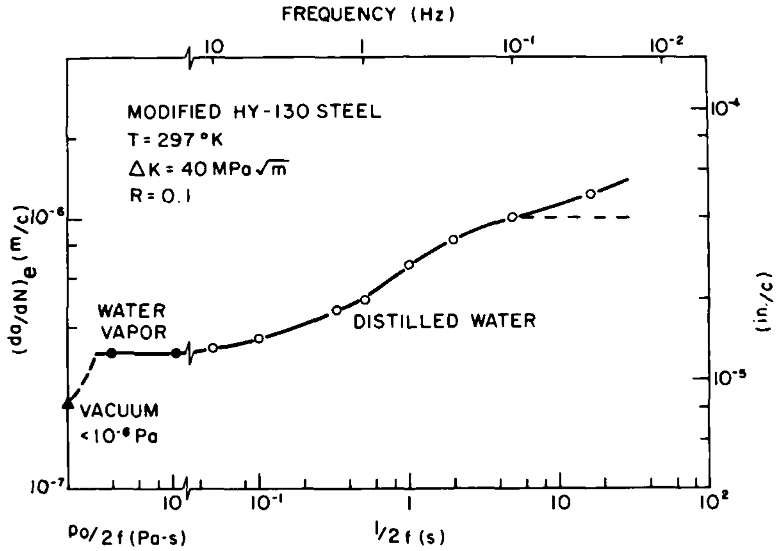

Fig. 7 - Influence of frequency and exposure on fatigue crack growth for a modified HY130 steel in water vapor and in distilled water at room temperature [30].

Corrosion Fatigue in Aqueous Environments. Corrosion fatigue crack growth is considered to occur in aqueous environments as a result of embrittlement by hydrogen that is produced by local reactions at the crack tip. The rate of reaction is governed by the electrochemical conditions (such as, solution chemistry, electrode potential and pH) and the surface conditions (bare versus oxidized) at the crack tip. The electrochemical conditions near the crack tip can be different from those of the external (bulk) environment, and are expected to depend on the kinetics of the transport processes and of the reactions with the crack surfaces. As in the case of gaseous environments, correct representation and modeling of corrosion fatigue crack growth response depend on the proper recognition of which one of the processes is in control, coupled with quantitative characterization and description of that process [7,8,14]. Suitable models, therefore, must address either separately or collectively the following problems: (i) the formation of the crack-tip electrochemical environment, and (ii) the kinetics of reactions with the crack-tip environment. In other words, there are two basic problems:

- Modeling of chemical/electrochemical environment at the crack tip.
- Modeling of corrosion fatigue crack growth rate in relation to the reactions with this environment.

It is essential to establish an unambiguous connection between the kinetics of electrochemical reactions and corrosion fatigue crack growth as a first step. The principal current effort of the ONR program at Lehigh is directed at establishing this correlation for steels.

For corrosion fatigue crack growth in high strength steels in aqueous environments, it is reasonable to assume that embrittlement is by hydrogen, while the crack growth rate, or the growth response, is governed by the rate of electrochemical reactions. This assumption is based on the study of reactions of water vapor with iron and steels [6-9], and on the observed crack growth responses [30,33] (see Fig. 7, for example). Two of the important variables in corrosion fatigue are temperature and frequency; temperature through its effect on the kinetics of reactions, while frequency establishes the time available for reactions during a given loading cycle. Data similar to those shown in Fig. 7 have been obtained on a modified HY-130 steel in distilled water and in acetate buffer solution as a function of frequency and temperature, and for other steels in different electrolytes.

The results clearly support the concept of electrochemical reaction control. The connection between corrosion fatigue and electrochemical reactions, however, has been difficult to establish. To make this connection, a method has been developed to simulate the electrochemical reactions at the crack tip. The experiment is based on the assumptions that a galvanic cell is formed at the crack tip between the new crack surfaces (as the anode) and its neighboring surfaces (acting as the cathode), and that this cell can be readily simulated in a corrosion cell using a "clean" steel surface to represent the anode and an "oxidized" surface of the same steel as the cathode. The "clean" surface is obtained by fracturing a notched specimen within the corrosion cell. The current transient between the suddenly produced fracture surface and oxidized surfaces would then reflect the reactions at the crack tip. Initial results suggest that this procedure is superior to an earlier one which utilized cathodic cleaning to produce the "clean" surface [33,34], and further advances in understanding can be expected.

Even though hydrogen production may be responsible for the enhancement of fatigue crack growth, the rate controlling step may be either the anodic or the cathodic portion of the reactions. The particular process that is in control is expected to be a function of temperature. Furthermore, akin to corrosion fatigue in gaseous environments, proper modeling of crack growth response requires detailed understanding and characterization of the mechanisms and kinetics of the underlying reactions. In this case, the complexities associated with electrode potential and solution pH must be taken into account.

Discussions and Research Needs

In the foregoing sections, a perspective summary of the effort to establish a quantitative connection between the chemical and physical processes and crack growth response and of the associated modeling was given. The work, spanning a period of nearly two decades, represents only a beginning, but does provide the framework for a more concerted effort that would be required for a more complete understanding of environmentally assisted crack growth. From an initial effort that was narrowly focused to address the issue of rate controlling processes for crack growth in steels exposed to gaseous environments, the ensuing studies have broadened the understanding to cracking in high-strength aluminum and titanium alloys and have extended the approach to the complex problem of crack growth in aqueous environments. The simplified models now serve as a framework for research and for design. They serve also as a basis for furthering the understanding of environmentally assisted crack growth. The understanding that has been achieved was made possible only through the support of a large number of governmental agencies and industry over the years; notably, the continuous and understanding support by the Office of Naval Research and Dr. Philip A. Clarkin over the past 13 years.

Some of the problems that still require attention are as follows:

(i) Detailed understanding of the kinetics and mechanisms of surface/electrochemical reactions with clean metal surfaces, and of their relations to crack growth kinetics and crack growth response is needed, over a broader range of environmental conditions: (a) to establish the form and quantity of hydrogen that is produced, and the fraction that can enter the material to effect embrittlement, (b) to explore and confirm the indicated transfer of rate controlling processes with changes in environmental conditions, and (c) to determine the relationship between the kinetics of surface reactions and crack growth response over a wide range of conditions to improve the predictive capability of crack growth models.

(ii) Greater effort is needed to understand the factors and processes that control or inhibit electrochemical reactions of bare (fresh) metal surfaces with electrolytes.

(iii) Quantitative understanding of the physical-chemical interactions between hydrogen and metal (i.e., the embrittlement mechanisms) is needed to establish the roles of microstructure and of other metallurgical variables in determining the rate of crack growth, or the degree of susceptibility.

(iv) Better understanding of the influences of alloying and impurity elements, and of microstructure is needed. It is essential to determine whether the influences result from alterations of the reaction kinetics by these elements and by changes in structure (chemical effects), or from their influence on mechanical properties of the alloys (physical effects), or both (physical-chemical effects).

(v) For engineering applications, better understanding of the processes that control crack initiation and its early growth (viz., threshold and Stage I crack growth) is needed.

Results from these studies would aid in the development of alloys and of methods to minimize sensitivity to environmentally assisted cracking, and of procedures for making reliable predictions of long-term service.

Summary

Experimental and analytical work in the past decade has contributed significantly to both the phenomenological and mechanistic understanding of environmentally assisted crack growth. Crack growth response reflects the complex interplay among chemical, mechanical and metallurgical factors, and is dependent on the rate controlling processes, and on the micromechanisms for crack growth and the mechanisms of the relevant chemical reactions. On the basis of this understanding, modeling of environmentally assisted crack growth, under sustained-load and in fatigue, has been made. This modeling effort has placed the study of this technologically important problem on a sound footing, and provides a framework for new understanding and for the development and utilization of data in design. To make significant further advances in understanding, continued emphasis on multi-disciplinary approaches and incorporation of chemistry, physics, materials science and fracture mechanics, and long-term support are essential.

Acknowledgment

Support of this work by the Office of Naval Research under Contract N00014-K- 83-0107, NR 036-097 is gratefully acknowledged.

References

1. R. P. Wei and J. T. Fong: unpublished discussions, 1983.

2. Stress Corrosion Cracking in High Strength Steels and in Titanium and Aluminum Alloys, B. F. Brown, ed.; Advanced Research Projects Agency, Department of Defence, Washington, D.C., 1972.

3. R. P. Wei: in Fatigue Mechanisms, J. T. Fong, ed., pp. 816-840; ASTM STP 675, Am. Soc. Testing & Mater., Philadelphia, PA, 1979.

4. H. H. Johnson and P. C. Paris: J. of Engr. Frac. Mech., 1 (1968) pp. 3-45.

5. R. P. Wei: Engr. Frac. Mech., 1 (1970) pp. 633-651.

6. G. W. Simmons and D. J. Dwyer: Surf. Sci., 48 (1975) p. 373.

7. D. J. Dwyer, G. W. Simmons and R. P. Wei: Surf. Sci., 64 (1977) p. 617.

8. D. J. Dwyer: Ph. D. Dissertation, Lehigh University, 1977.

9. R. P. Wei and G. W. Simmons: in Stress Corrosion Cracking and Hydrogen Embrittlement of Iron Base Alloys, R. W. Staehle, J. Hochmann, R. D. McCright and J. E. Slater, eds., pp. 751-765; NACE-5, Nat. Assoc. Corro. Engrs., Houston, TX, 1979.

10. G. W. Simmons, P. S. Pao, and R. P. Wei: Met. Trans A, 9A (1978) p. 1147.

11. T. W. Weir, G. W. Simmons, R. G. Hart, and R. P. Wei: Scripta Met., 14 (1980) pp. 357-364.

12. R. P. Wei and G. W. Simmons: in FATIGUE: Environment and Temperature Effects, John J. Burke and Volker Weiss, eds.; Sagamore Army Materials Research Conference Proceedings, 27 (1983) pp. 59-70.

13. M. Lu, P. S. Pao, T. W. Weir, G. W. Simmons, and R. P. Wei: Met. Trans. A, 12A (1981) pp. 805-811.

14. M. Lu, P. S. Pao, N. H. Chan, K. Klier and R. P. Wei: in Hydrogen in Metals, Suppl. to Trans. Japan Inst. Metals, 21 (1980) p. 449.

15. N. H. Chan, K. Klier, and R. P. Wei: in Hydrogen in Metals, Suppl. to Trans. Japan Inst. Metals, 21 (1980) p. 305.

16. R. P. Wei: in Hydrogen Effects in Metals, I. M. Bernstein and A. W. Thompson, eds., p. 677; The Metall. Soc.-AIME, Warrendale, PA, 1981.

17. R. P. Wei and Ming Gao: in Hydrogen Degradation of Ferrous Alloys, R. A. Oriani, J. P. Hirth and M. Smialowski, eds., pp. 579-607; Noyes Publications, Park Ridge, N. J., 1985.

18. S. Dushman: in Scientific Foundations of Vacuum Technique, 2nd ed., pp. 87-104; J. M. Lafferty, ed., Wiley, 1962.

19. H. G. Nelson, D. P. Williams and A. S. Tetelman: Met. Trans., 2 (1971) p. 953.

20. R. W. Pasco and P. J. Ficolora: Scripta Met., 15 (1980) p. 1019.

21. R. W. Pasco, K. Sieradzki and P. J. Ficalora: Scripta Met., 16 (1982) p. 881.

22. M. Gao, M. Lu and R. P. Wei: Met. Trans. A, 15A (1984) pp. 735-746.

23. Ming Gao: Ph.D. Dissertation, Lehigh University, Bethlehem, PA, 1983.

24. M. Gao and R. P. Wei: "A Hydrogen Partitioning Model for Hydrogen Assisted Crack Growth", Met. Trans. A, 16A (1985) pp. 2039-2050.

25. R. P. Wei, P. S. Pao, R. G. Hart, T. W. Weir, and G. W. Simmons: Met. Trans A, 11A (1980) pp. 151-158.

26. Brazill, G. W. Simmons, and R. P. Wei: J. Engr. Matls. & Tech., Trans. ASME, 101 (July 1979) pp. 199-204.

27. R. P. Wei and J. D. Landes: Mater. Res. Stand., 9 (7) (1969) pp. 25-28.

28. R. P. Wei and Ming Gao, Scripta Met., 17 (1983) pp. 959-962.

29. I. Langmuir, J. Chem. Soc., (1940) pp. 511-543.

30. R. P. Wei and Gunchoo Shim: in Corrosion Fatigue, ASTM STP 801, pp. 5-25 T. W. Crooker and B. N. Leis, eds., Am. Soc. Testing & Mater., Philadelphia, Pa, 1983.

31. True-Hwa Shih and R. P. Wei: Engr. Frac. Mech., 18 (4) (1983) pp. 827-837.

32. T. W. Weir: Ph.D. Dissertation, Lehigh University, Bethlehem, PA, 1983.

33. Gunchoo Shim: Ph.D. Dissertation, Lehigh University, Bethlehem, PA, 1983.

34. A. Alavi and R. P. Wei: Unpublished results, Lehigh University.

STRESS CORROSION CRACKING AND HYDROGEN EMBRITTLEMENT

HYDROGEN EMBRITTLEMENT OF STEEL

J. P. Hirth
Metallurgical Engineering Department
The Ohio State University
Columbus, Ohio 43210

A brief outline is presented of experimental observations and theoretical interpretations of hydrogen embrittlement of steels. Detailed results on the effect of precharged hydrogen on reduction in ductility of low-strength steels under plane strain loading are discussed. Under such conditions hydrogen is shown to degrade the steels by promoting plastic instability in the form of shear bands, lowering the critical strain for various events without changing the locally ductile mode of fracture.

Introduction

Years ago, Toh and Baldwin [1] showed that precharging of low strength steels with hydrogen at moderate fugacities degraded properties by lowering the elongation and reduction in area without much effect on flow stress. A "rule of thumb" in those days was that steels with yield strengths below 700 MPa were immune to catastrophic hydrogen embrittlement in the form of delayed brittle failure. Yet there were abundant controversies (see reviews in refs. [2-5]) with a number of competitive mechanisms for embrittlement (pressurization of voids, lowering of surface energy, lowering flow stress, increasing flow stress, and decohesion or bond-breaking at the crack tip), widely scattered diffusion data for H in steel, puzzlement about kinetics, and questions about the importance of dislocation transport of H.

The situation today is much improved, although some issues remain unresolved. Work on very pure iron [6,7] clearly showed that precharged or dynamically charged H lowers the flow stress of pure iron at low strain (≤ 0.20) and above 200 K. Later TEM work [8] indicated that gaseous charging of iron foils by H increases dislocation velocity. The scatter in H diffusivity is now attributed to trapping on defects [9], with good agreement for low dislocation density, high purity iron, the value at room temperature being about 10^5 cm^2/s [5,10,11]. Work has defined different rate controlling processes under different conditions, for example any among diffusion in the environment, interface reaction of hydrogen containing gases, or diffusion in the steel can control mode I crack propagation kinetics in the presence of hydrogen for alloy steels, depending on gas pressure and hydrogen fugacity [12].

The critical strength, 700 MPa, rule has been shown to be inapplicable. Brittle, stable mode I crack propagation can occur in iron exposed to dry hydrogen gas at a pressure much less than one atmosphere [13] and in low *strength steels exposed to high fugacity hydrogen,* such as H_2S gas [14]. Also microstructure [15] and minor alloy additions [16] have an influence on the embrittlement tendency. In our own work, we have found that at moderate hydrogen fugacity (corresponding to a gas pressure of 240 MPa or less [17]), precharging of a low yield strength, 400 MPa, spheroidized steel causes a reduction in ductility but still leads to a mixed mode I-II ductile fracture [18]. Yet dynamic charging, that is, charging while straining, leads to a brittle mode I fracture at a strain little removed from the yield strain [18].

Hence, the issue of what causes the ductile, mixed mode, moderate strain failure to brittle, mode I, low strain failure transition depends on many variables and is still incompletely resolved. Under very ideal conditions of oriented cracks and low fugacity dry hydrogen, the transition in Fe-3% Si single crystals [19] seems to be a genuine transition between crack tip bond breaking and dislocation emission: the crack tip opening angle increases with decreased hydrogen fugacity from near zero to ≈ 70 degrees. A complicating factor in many cases is the screening of the crack tip by emitted or matrix dislocations [20]. The local crack tip process may be brittle, operating at the Griffith condition, yet the macroscopic stress intensity may be orders of magnitude larger because of dislocation activity away from the near tip region.

Our own work has focussed on the influence of hydrogen on ductile fracture by enhancing the onset of plastic instability in the form of shear bands. This has occurred at a time when there has been great activity from the viewpoint both of observations [21] and of theoretical mechanics calculations [22,23] for such instabilities. The remainder of our presentation concerns this type of degradation. While many materials were studied, we discuss for brevity only the work on spheroidized AISI 1090 steel.

The steel had a composition in weight percent of 0.88 C, 0.75 Mn, 0.017 P, 0.036 S, 0.19 Si, 0.17 Cu, 0.09 Cr, 0.06 Ni, 0.01 Mo, 0.003 Ti, balance Fe. The carbide volume fraction was 11 percent, the mean particle size was 0.8 μm and the mean particle spacing was 1.2 μm.

Indirect Evidence for Hydrogen Enhancement of Plastic Instability

In all cases, hydrogen was charged electrolytically in a 1N sulfuric acid solution containing 1 g/ℓ of the hydrogen recombination poison thiourea. Charging was done at a current density of 80 to 100 A/m^2. Permeation measurements [17] show that this corresponds to moderate hydrogen pressures of 200 to 240 MPa. The permeation measurements and measurements of reversible softening [24] of the steel after hydrogen charging show that these current densities are below the critical value of 135 A/m^2 (equivalent hydrogen pressure 270 MPa) that produces irreversible damage and softening. Precharging was performed for 2 h. Other experimental details such as precautions to avoid oxygenation of the solution, are presented elsewhere [18].

The first manifestation of the enhancement of plastic instability was the observation [25] of hydrogen induced Lüders band formation on polished, blunt-notched plane-strain tensile bars. Later work [18] was performed on U-notched, plane-strain, 3-point bend bars with varying notch root radii, producing varying internal stress concentrations, maximum at the elastic-plastic boundary. The results showed that tests in air or with precharged $\underline{H}$ were of the mixed mode I-II type, following the traces of the characteristic slip lines of plasticity theory, Fig. 1. As noted in Table I, $\underline{H}$ caused a reduction, by about a factor of two, in the critical strain to failure, independent of notch curvature and hence of stress concentration. Those observations showed that the failure was probably associated with plastic shear instability bands propagating in from the surface where the strain is a maximum.

Table I. Critical Maximum Principal Surface Strains, 3-Point Bend Specimens

	Radius of Curvature of Notch		
	0.59 mm	1.19 mm	1.59 mm
Void Initiation			
Uncharged	0.13	0.15	0.13
Precharged	0.06	0.07	-
Void Profusion			
Uncharged	-	0.36	0.35
Crack Initiation			
Uncharged	0.36	0.42	0.38
Precharged	0.21	0.23	0.22

Microstructural study of specimens strained to varying amounts showed that voids formed, also along the traces of characteristic slip lines, and eventually there was a profusion of voids formed at a strain slightly below the fracture strain. Table I indicates that hydrogen also reduces the critical strain for these events by about a factor of two.

Micrographs, for example, Fig. 2, showed that most of the voids formed between two carbide particles closely spaced along the direction of maximum principal tensile force. The void configuration can be understood in terms of incompatibility stresses, arising at particles in the path of a shear band, which add to the maximum applied principal stress. The overlap of the added tensile fields for two closely spaced particles favors void nucleation at such a pair. Moreover, as proved by analog experiments [18], void growth is also favored at such sites.

Thus, the indirect interpretation of the data was that hydrogen enhanced plastic instability in the form of shear bands emanating from the surface and following the shear paths of plasticity theory. The localized shear produced voids in the same path because of the incompatibility effect. The voids further enhanced shear localization and finally profuse void formation and crack opening because of occurrence of the mode I loading component.

Other work had indicated that the major effect of $\underline{H}$ was on void nucleation [26], on growth and coalescence [27], or failed to find a reduction in instability strain [28]. However, the former tests [26,27] were on notched round bars where instability is much less prominent while the latter [28] were on the plane stress region at the lateral surface of plane stress specimens. As indicated both by this set of experiments and by theory [22,23], only under plane strain conditions do the marked reductions in strain and pronounced shear instabilities occur.

On the other hand, theory [29] also indicated that voids can provide an added enhancement of shear localization. Thus the possibility existed that $\underline{H}$ actually promoted void nucleation near the surface and the voids caused the localization. However, theory [23] also predicted that an earlier form of instability would be rumpling of the surface. Thus, we proceeded to study surface rumpling of polished plane-strain specimens as a more direct test of the effect of $\underline{H}$.

Direct Evidence for Hydrogen Enhancement of Plastic Instability

Polished surfaces of 3-point loaded bend bars were studied as a function of strain: rumpling was observed [30]. As summarized in Table II, $\underline{H}$ again lowered the critical strain, in this case for rumpling, by about a factor of two [31]. Further studies [32] on plane strain tensile specimens and round bar tensile specimens verified the effect, and demonstrated the more severe influence of plane-strain loading, Table III. The results in air are in fair agreement with the theoretical prediction [23,30]

Table II. Critical Strain for the Onset of Surface Rumpling, 3-Point Bend Specimens

Theory	Experiment	
	Uncharged	Precharged
0.25	0.28	0.12

$$\frac{d\sigma/d\epsilon}{\sigma/\epsilon^*} = \epsilon^*(1 - e^{-2\epsilon^*}) \qquad (1)$$

Table III. Critical Strains, Tensile Specimens

	Round Bar Uncharged	Round Bar Precharged	Plane Strain Uncharged	Plane Strain Precharged
Uniform elongation	0.21	0.20	0.24	0.17
Surface rumpling	-	-	0.18	0.07
Surface cracks	-	-	0.28	0.10
Failure	1.04	0.63	0.71	0.34

relating the critical strain for rumpling to the properties of the stress σ - strain ε curve.

Most recently [33], similar tests have been performed on plane-strain, U-notched, four-point bend specimens where the notch can be loaded in tension or compression. The critical strain for rumpling in compression, Table IV, was less than that in tension, in agreement with theory, Eq. (1). The effect of H was present in compression, but it was less marked than in tension. However, with H present, mixed mode microcracks formed in compression.

Table IV. Critical Strain for the Onset of Surface Rumpling and Crack Initiation, 4-Point Bend Specimens

	Tension Uncharged	Tension Precharged	Compression Uncharged	Compression Precharged
Rumpling	0.26	0.14	0.15	0.12
Cracking	0.67	0.41	0.31	0.37

Thus, the direct tests confirmed the indirect tests and supported the hypothesis that the effect of H on the onset of plastic instability is a direct one. The mechanism of the enhancement is not clear. We can say that since H lowers ε^* while leaving $d\sigma/d\varepsilon$ and σ at ε unchanged, it is not an effect on the continuum plasticity level manifested in Eq. (1). The H must promote instability on a local, microstructural scale. In this connection, it is noteworthy that TEM studies have shown dislocation structures indicating that hydrogen promotes local deformation, between carbide particles, akin to shear localization and prior to microvoid formation [34].

Three possibilities are suggested. First, the lowering of surface energy of a slip step in the presence of hydrogen may promote a larger local slip event. The slip band in turn is effectively a mode II crack nucleus. Second, hydrogen both lowers the flow stress for dislocations (in iron and in spheroidized steel) and promotes planar slip on {110} planes. The absence of grain boundary compatibility effects near free surfaces would also tend to promote single slip. These effects again would tend to produce planar local slip events, near the surface, that could act as mode II crack nuclei. Third, a set of such crack nuclei could indirectly lead to a marked reduction of ε in Eq. (1) in a manner analogous to that of imposing an initial sinusoidal roughening in finite element calculations used to test the continuum theory [23]. Further work is needed to resolve the detailed mechanism.

Conclusions

A. Low strength steels, exemplified by spheroidized plain carbon alloys, fail as a consequence of shear instability in the form of localized shear bands. The critical strain is least under plane-strain conditions where initiation is favored at a free surface.

B. Metallographic observations indicate that the sequence of events leading to failure in plane strain is surface roughening, shear localization, void formation as a consequence of strain incompatibility in the shear path, crack initiation at a surface valley, and crack propagation in a mixed mode I-II manner along the shear path.

C. Precharged hydrogen reduces the critical strain for all of the above events by a factor of two but leaves the essential ductile nature of the fracture unchanged and has little effect on the flow stress at strains less than the critical value. Dynamically charged hydrogen changes the fracture to a mode I type with a drastic reduction in ductility. The detailed mechanism by which hydrogen enhances plastic instability is undetermined although possible models are suggested.

D. The critical strain for initiation of surface roughening is in fair agreement with continuum mechanical, theoretical predictions. The critical value in the presence of hydrogen is not in agreement, implying that hydrogen exerts its effect on a local microstructural scale.

Acknowledgment

I am pleased to be able to participate in this volume honoring Dr. P. A. Clarkin and am grateful to him, as project monitor, and to the Office of Naval Research for research support. At the request of the symposium organizers I have included in my contribution results from work supported both by the Office of Naval Research and by the National Science Foundation, for which I am also grateful.

References

1. T. Toh and W. M. Baldwin, Jr.: Stress Corrosion Cracking and Embrittlement, W. D. Robertson, ed., pp. 176-86, Wiley, New York, 1956.

2. I. M. Bernstein and A. W. Thompson: Int. Met. Rev., 21 (1976) pp. 269-287.

3. J. P. Hirth and H. H. Johnson: Corrosion, 32 (1976) pp. 3-25.

4. R. A. Oriani: Ann. Rev. Mater. Sci., 8 (1978) pp. 327-357.

5. J. P. Hirth: Metall. Trans. A, 11A (1980) pp. 861-890.

6. H. Matsui, H. Kimura and S. Moriya: Mater. Sci. Eng., 40 (1979) pp. 207-216.

7. S. Moriya, H. Matsui and H. Kimura: Mater. Sci. Eng., 40 (1979) pp. 217-225.

8. T. Tabata and H. K. Birnbaum: Scripta Met., 17 (1983) pp. 947-950; 18 (1984) pp. 231-236.

9. J. Völkl and G. Alefeld: Topics in Appl. Phys., 28 (1978) pp. 321-348.

10. N. R. Quick and H. H. Johnson: Acta Met., 26 (1978) pp. 903-907.

11. H. G. Nelson and J. E. Stein: NASA Rept. TND-7265, NASA, Ames Research Center, Moffett Field, CA, 1973.

12. R. P. Wei, K. Klier, G. W. Simmons and Y. T. Chou: in Hydrogen Embrittlement and Stress Corrosion Cracking, R. Gibala and R. F. Hehemann, eds., Am. Soc. Met., Metals Park, OH, (1984) pp. 103-133.

13. G. G. Hancock and H. H. Johnson: Trans. TMS-AIME, 236 (1965) pp. 513-516.

14. R. S. Treseder: Corrosion, 32 (1973) pp. 20-21.

15. A. W. Thompson and I. M. Bernstein: Adv. Corros. Sci. Technol., 7 (1979) pp. 53-175.

16. G. Sandoz: Metall. Trans., 3 (1972) pp. 1169-1176.

17. S. X. Xie and J. P. Hirth: Corrosion, 38 (1982) pp. 486-93.

18. T. D. Lee, T. Goldenberg and J. P. Hirth: Metall. Trans. A, 10A (1979) pp. 199-208.

19. H. Vehoff and W. Rothe: Acta Met., 31 (1983) pp. 1781-1794.

20. R. Thomson: J. Mater. Sci., 13 (1978) pp. 128-142.

21. D. Peirce, R. J. Asaro and A. Needleman: Acta Met., 31 (1983) pp. 1951-1976.

22. J. W. Rudnicki and J. R. Rice: J. Mech. Phys. Solids, 23 (1975) pp. 371-394.

23. J. W. Hutchinson and V. Tvergaard: Int. J. Mech. Sci., 22 (1980) pp. 339-354.

24. S. X. Xie and J. P. Hirth: Mater. Sci. Eng., 60 (1983) pp. 207-212.

25. T. D. Lee, T. Goldenberg and J. P. Hirth: Fracture, 2, Univ. of Waterloo Press, Waterloo, Canada (1977) pp. 243-248.

26. H. Cialone and R. J. Asaro: Metall. Trans. A, 12A (1981) pp. 1373-1387.

27. R. I. Garber, I. M. Bernstein and A. W. Thompson: Metall. Trans. A, 12A (1981) pp. 225-234.

28. J. K. Lin and R. A. Oriani: Acta Met., 31 (1983) pp. 1071-1078.

29. V. Tvergaard, A. Needleman and K. K. Lo: J. Mech. Phys. Solids, 29 (1981) pp. 115-142.

30. O. A. Onyewuenyi and J. P. Hirth: Metall. Trans. A, 13A (1982) pp. 2209-2218.

31. O. A. Onyewuenyi and J. P. Hirth: Metall. Trans. A, 14A (1983) pp. 259-269.

32. S. C. Chang and J. P. Hirth: Metall. Trans. A, (in press).

33. V. Rajan, Ph.D. Thesis, Ohio State University, Columbus, OH, 1984.

34. T. D. Lee and I. M. Bernstein: Metall. Trans. A, (in press).

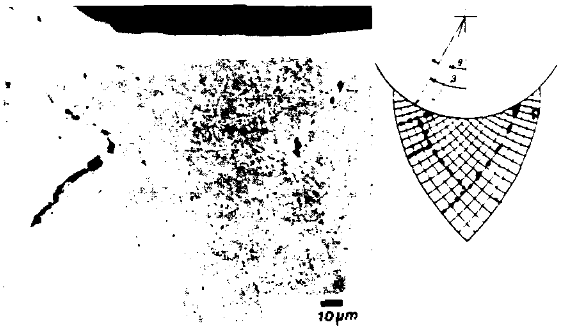

Fig. 1 - Cross-section showing microcrack starting at surface and following characteristic slip traces. Inset shows voids aligned along the characteristics.

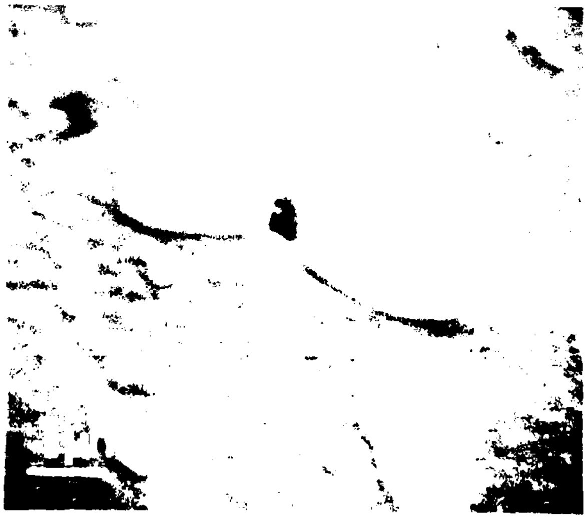

Fig. 2 - Void between two closely spaced carbides aligned along maximum principal force direction (horizontal on page).

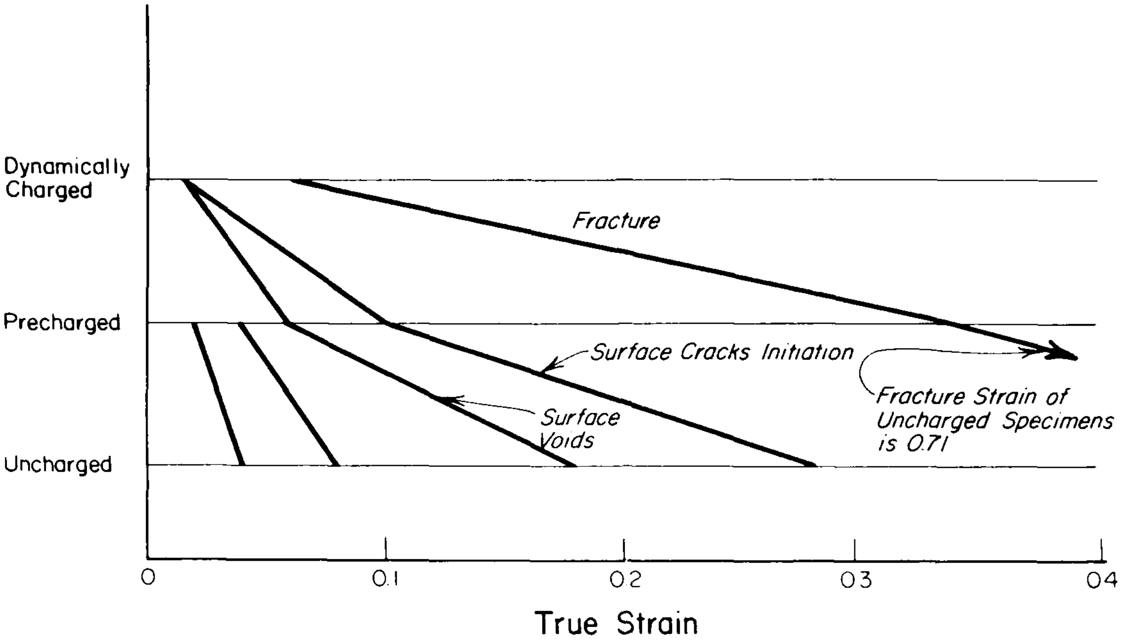

Fig. 3 - Equi-slip band diagram for plane-strain specimens tested under different charging conditions.

THE ROLE OF TRAPPING ON HYDROGEN EFFECTS IN FERROUS ALLOYS

I. M. Bernstein
Carnegie-Mellon University
Metallurgical Engineering and Materials Science
Pittsburgh, PA 15213

The evidence for trapping by mobile and stationary defects in ferrous alloys is reviewed and new results presented to demonstrate that the trap theory of hydrogen embrittlement can rationalize the many different ways by which hydrogen modifies subsequent mechanical properties.

Introduction

The preferential interaction of hydrogen with such features as free surfaces, grain boundaries, local and global stresses and strain fields, and chemical heterogeneities such as precipitates is describable by the general term "trapping". This concept has important ramifications both in terms of the thermodynamics and kinetics of entry, solubility and diffusion (permeability) of hydrogen and the variable concentrations concomitant with the presence of a trap population of differing strengths. It has now been established in many investigations and for a broad number of model and alloy systems that the presence of such features can impact significantly on the entire range of mechanical properties associated with deformation and fracture [1-10]. Furthermore, paradigms are now being developed [2,9,10] in response to earlier suggestions [7,8] that hydrogen embrittlement, as manifested by a degradation of tensile ductility, fracture toughness or fatigue crack initiation or growth, is controllable either by decreasing the population of trapped hydrogen at potential crack sites (C_H), or by increasing the critical concentration necessary to initiate failure at a given trap, C_K.

In this paper, the concept, validity and limitations of the "trap theory of hydrogen embrittlement" will be discussed using ferrous systems as the primary exemplar, although a number of non ferrous cases would have served equally as well. The bulk of the results will come from work either directly supported or stimulated by the long term, quality support of the Office of Naval Research at Carnegie-Mellon University and a number of other universities and research laboratories.

Fundamental of Hydrogen Trapping

Pressouyre has extensively developed the concepts of trapping [11,12] and the allied concepts of repellers and obstacles [2,9,13]; others have also provided reviews of hydrogen trapping primarily in iron and steels [14,15].

The general viewpoint here, as elsewhere [8], is that trapping can be schematically described as in Fig. 1. Five different types of trapping centers can be present either as independent entities or capable of interacting amongst each other:

1. The surface is a trap of multiple origins, including surface oxides and work functions. Except for its role as a kinetic barrier to hydrogen entry, it is believed less important than sub-surface traps in influencing a change in embrittlement susceptibility. However, it may be more important in its effect on strain localization or other dislocation related characteristics, where surface sources could dominate.

2. The lattice is, of course, a generalized trap in that there is a finite (but in iron a small) activation energy for interstitial diffusion. This intrinsic effect could become important at high, non-equilibrium hydrogen fugacities due to a concentration dependence of the lattice diffusivity.

3. There are mobile traps which for a large number of experimental conditions are reversible in nature, in that the dislocation type of trap can gain or lose hydrogen within a time scale less than or of the order of the length of a mechanical test. Differences are possible when the dislocations are present as sessile arrays.

4. There are static, reversible (r) traps which can rapidly lose or gain hydrogen from dislocations, assuming the absence of significant kinetic barriers to such an interchange. Type I is weaker than dislocations and traps less hydrogen than dislocations, and Type II is stronger and traps more. Examples of the former could be substitutional impurities, while for the latter examples include high angle grain boundaries and dislocations of other types.

5. Irreversible (r) traps have a much higher trapping energy than either the thermal energy, kT, or any other heterogeneity and can irreversibly keep their hydrogen for the length of a test, thereby acting as a strong hydrogen sink. Note that all of these trap centers have an influence diameter which we consider as the maximum range over which a hydrogen atom is said to be trapped and over which different traps can interact with one another.

More recently Pressouyre [13] has suggested that features with different properties than those illustrated in Fig. 1 can also interact with hydrogen. These are illustrated in Fig. 2.

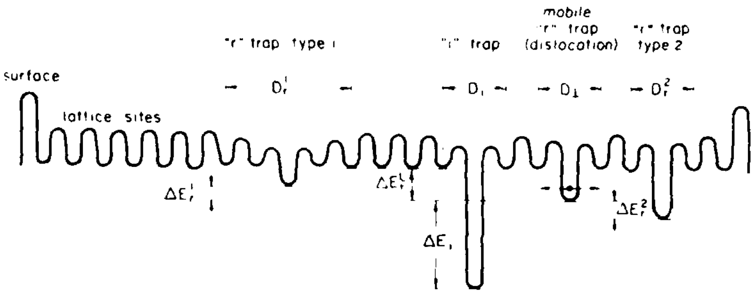

Fig. 1 - Schematic of general trap types illustrating comparative trapping energies and influence diameters.

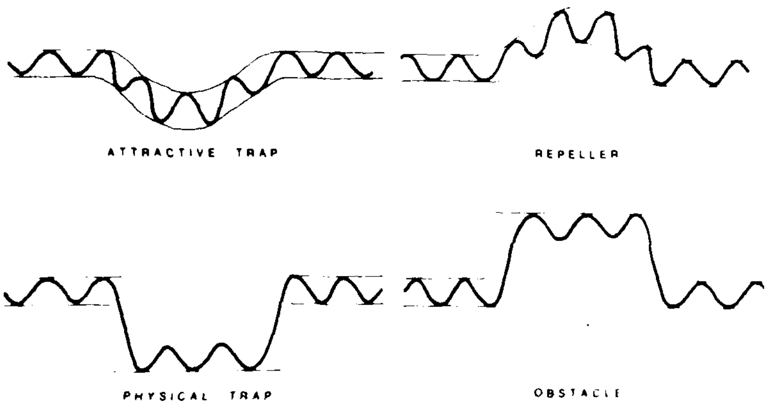

Fig. 2 - Schematic of the broader class of heterogeneities capable of interacting with hydrogen: traps, repellers and obstacles.

The depicted attractive and physical traps are like those described by Fig. 1; however, counterparts to these also exist. For example, repellers are the opposite of attractive traps in that a repulsive force exists relative to hydrogen. Examples include atoms with a positive interaction coefficient with hydrogen [11], or local compressive stress fields. A hydrogen obstacle is the opposite of a physical trap and is most likely a discontinuity through which hydrogen has no significant mobility, such as a coherent particle with no hydrogen solubility.

While it is likely that, in general, most heterogeneities will combine mixed characteristics, the advantage of the above characterizations is that they allow the properties of each trapping feature to be identified in terms of measurable (if as yet unknown) thermodynamic or kinetic parameters. Further, as discussed in detail elsewhere [9], the critical trapping parameters which impact on mechanical properties can often be more easily identified and analytically described. Such parameters include the ability of traps to saturate and the rate at which this can be achieved; the change in trap strength with time and the possible transformation of traps to antitraps as a function of hydrogen concentration or deformation. The major points to be appreciated in the context of this development is that trap characteristics are not fixed properties and that the evolutionary or changing nature of traps must be a part of any attempt to model the role of microstructure on hydrogen embrittlement.

Evidence for Microstructural Trapping

There are a number of techniques available for identifying and monitoring the extent and location of hydrogen trapping. The electrochemical or gaseous permeation test can provide considerable data on trapping types and capacity. While such studies should ideally be carried out on simple model systems so that the specific trap species can be known [8,16], useful results can also be obtained in quite complex alloy systems [17,18]. For example, Fig. 3(a) shows consecutive transients for purified iron and an Fe-0.15Ti alloy, while Fig. 3(b) depicts the behavior for a higher strength Fe-Ti HSLA steel [18]. In Fig. 3(a), it is seen that the first permeation transient can be considerably slower than subsequent ones both at breakthrough and during the rise to saturation. This shift has clearly been shown to be a direct result of the presence of strong, irreversible traps that fill during the first cycle and retain their hydrogen during subsequent permeation cycles. As discussed in detail elsewhere [16], the extent of such differences can be quite variable, depending on alloy content, microstructure and temperature, but such strong traps when present can impact significantly on the degree of embrittlement, both positively and negatively.

The second characteristic, seen in Fig. 3(a), and much more strongly in Fig. 3(b), is the presence of an inflection point and a considerable plateau region in the flux-time behavior. The presence of both features has been shown to likely result from irreversible or reversible trapping [10]. The plateau itself is taken as evidence for strong reversible trapping, for conditions of a low hydrogen release rate and trap coverage. The value of both Pressouyre's [11] and Iino's [10] analyses is that they permit estimates to be made of capture and release rates and trapping energies, and permit a direct monitoring of how the trapping characteristics change with heat treatment. As will be described shortly, this approach has been successfully used to rationalize the role of a changing microstructure on the relative susceptibility of alloys to hydrogen induced embrittlement [17,18].

A newer monitoring technique for evaluating trapping and transport by mobile dislocations has been developed [19,20], making use of concurrent straining during hydrogen permeation through a membrane of material of interest. A very extensive study has recently been carried out by Hwang [20,21], who monitored hydrogen flux behavior in single crystal purified iron of special orientations, chosen so that the trapping and transport behavior of screw, edge and mixed dislocation could be separately analyzed. Some of these

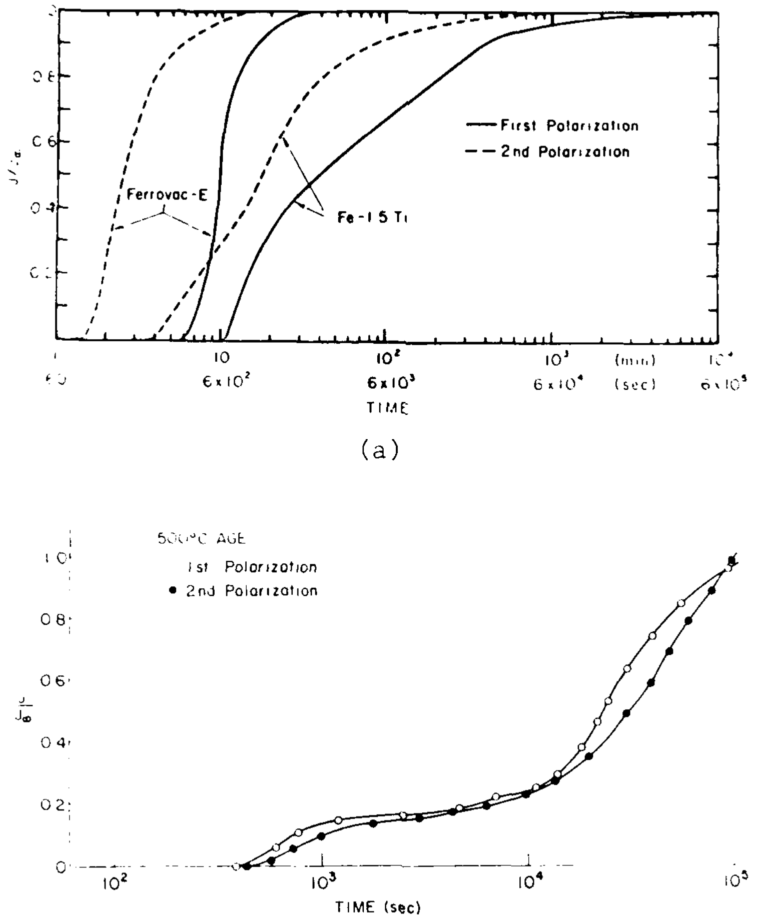

(a)

(b)

Fig. 3 - (a) Normalized first and second permeation transients for purified iron with and without the addition of titanium illustrating the existence of irreversible trapping and the role of substitutional alloy additions on permeability. (b) Normalized first and second permeation transients through a quenched and 500°C aged Fe-0.05C-0.22Ti alloy.

results are shown in Fig. 4 for both screw and edge dislocations. For the former, the discrete discontinuous permeation pulses were attributable to the rapid release of a core population of hydrogen when the entire dislocation line intersected the monitored crystal surface. For the latter (as well as for the mixed case), the intersecting dislocation segments are now kinks travelling along the screw dislocation, since the screw continues to be the predominant source of strain at room temperature for crystals of this purity. The hydrogen flux in this case is more continuous, reflecting the high emission frequency of kinks on the monitored surface. The strain rate dependence was also studied; at slower rates edge kinks have the greatest capacity to transport hydrogen consistent with their higher binding energy, while at higher strain rates the edge kinks can achieve a great enough velocity to break away from the hydrogen [20] and screws now dominate the transport process. These are compelling results in that they clearly demonstrate the significant contribution of dislocation transport, even in ferrous materials of high lattice diffusivity. Further, the different response of edges and screws may be of importance when considering hydrogen-dislocation interactions in regions like the plastic zone in the vicinity of a crack.

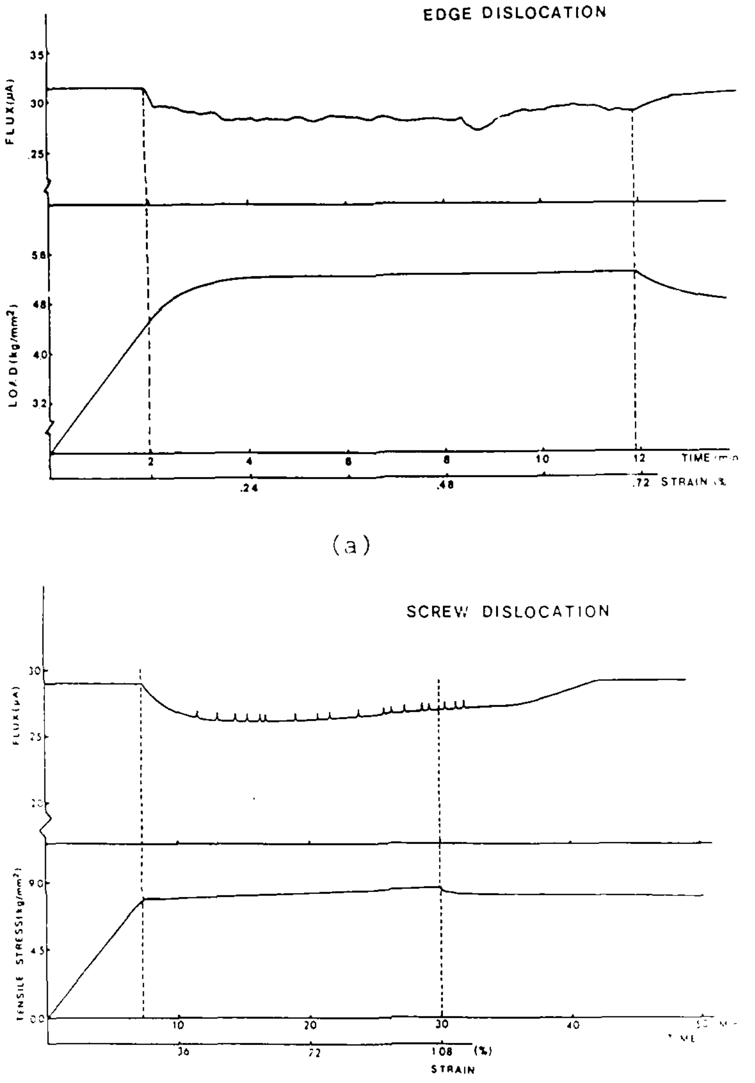

(a)

(b)

Fig. 4 - Typical changes of the steady state hydrogen flux due to concurrent deformation for:

(a) edge dislocations
(b) screw dislocations

A final technique to mention is one that is most direct and persuasive, viz, tritium microradiography, which has clearly revealed the spectrum of hydrogen traps in bcc ferrous alloys [22,23], as well as in austenitics and other fcc alloys [24]. Some typical behavior is illustrated in Fig. 5, showing trapping on decorated dislocation walls in an Fe-1.5Ti alloy (5(a)); on $Cr_{23}C_6$ in an Fe-9Cr alloy (5(b)), and on dislocations in a 304L stainless steel (5(c)). Figure 6 reveals the role of strain on the extent of hydrogen trapping in a cathodically-charged spheroidized 1320 steel. Significant trapping only occurs beyond the necking strain and this has important ramifications on the way hydrogen accelerates the ductile fracture process in such an alloy [25], as will be discussed. Further, this serves as clear proof that trap character can change, in this case, due to strain.

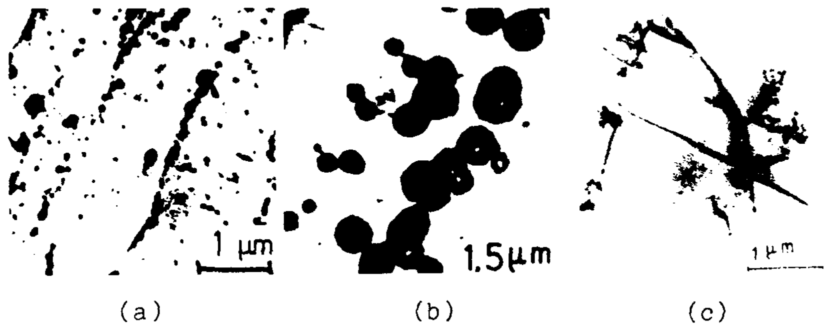

Fig. 5 - Trapping sites as revealed by high resolution tritium microradiography in ferritic and austenitic steels. Hydrogen revealing silver grains appears as dark dots.

(a) replica of Fe-1.5Ti
(b) replica $Cr_{23}C_6$ in Fe-9Cr
(c) TEM of 304L stainless steel

Effect of Trapping on Mechanical Properties

The first effect to be discussed will be how hydrogen, when trapped or while being transported by mobile dislocations modifies the deformation response of ferrous alloys. This is most often considered for high purity iron, which generally is softened in the presence of hydrogen near room temperature, while being hardened at lower temperatures [26]. The former effect is believed due to the enhanced mobility of screw dislocations, while the latter may be caused by hydrogen clusters, which hinder the sidewise motion of non-screw kinks. The softening also leads to an enhanced Stage I regime for properly oriented single crystals. The modifying effects of hydrogen on work hardening have also been reported [27].

Support for a strong effect of hydrogen on the character and response of screw dislocations is evident from the dislocation transport studies of Hwang [20], described earlier, as illustrated in Fig. 7. This micrograph supports previous suggestions that hydrogen reduces cross slip of screw dislocations, leading to more planar arrays. Of perhaps more interest are the TEM results illustrated in Fig. 8, which show the dislocation behavior in the vicinity of inert dispersoids, in screw oriented iron single crystals [20,28]. It is quite apparent that straining such crystals in the continuous presence of a cathodically-generated hydrogen environment produces a dense localized tangle of dislocations absent in hydrogen-free material, or in the rest of the hydrogen-containing sample, and is akin to reported effects of hydrogen enhancing macroscopic strain localization [3]. An analysis of these results revealed that localization was associated with the presence of a third slip system, absent in the matrix, and it was suggested that the presence of an anti-twinning primary slip system catalyzed the formation and growth of strain localization [20,28]. Importantly, in the same study, it was shown that the orientation of the band was identical to subsequently produced hydrogen-induced cracks.

These results have now been extended to, and demonstrated in, a polycrystalline spheroidized 1320 steel. Figure 9 shows the early stage, at about 4% strain, and the further development of a strain localization band, at about 8% strain; in this case the bands emanate from iron carbide particles [29]. Note the discontinuous nature of the band, suggestive of the appearance of hy-

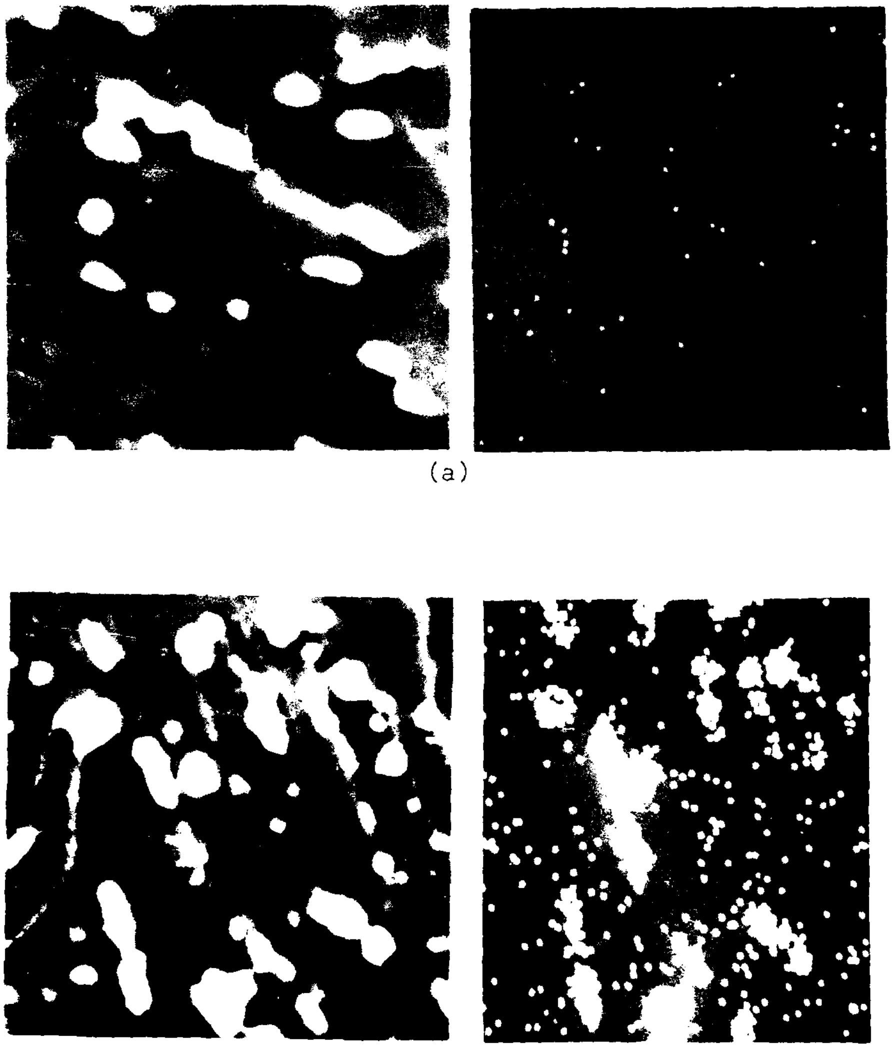
(a)

(b)

Fig. 6 - Trapping in the vicinity of iron carbide particles in a 1320 (Mn containing) steel as revealed by tritium microradiography. The extent of hydrogen trapping is revealed by white dots on a SEM mapping image.

(a) unstrained
(b) strained beyond necking

drogen induced cracking and void growth frequently seen in steels. The importance of such observations, beyond their fundamental scientific interest, is that they serve to unify behaviors that have previously appeared poorly established or conflictual. Thus, hydrogen can be trapped at mobile and stationary defects, which themselves can mutually interact; it can be redistributed to different sites; it not only can enhance slip, but it can localize it; and each of these can combine for different sets of conditions to enhance or degrade toughness or ductility. While we are not yet in a position to generalize these events, we can use them to rationalize the hydrogen behavior of a number of different ferrous alloys.

For example, a study has recently been completed in a titanium containing low carbon HSLA steel, where the response to hydrogen and microstructure in both tensile and fracture mechanics tests was assessed [18,30]. Following

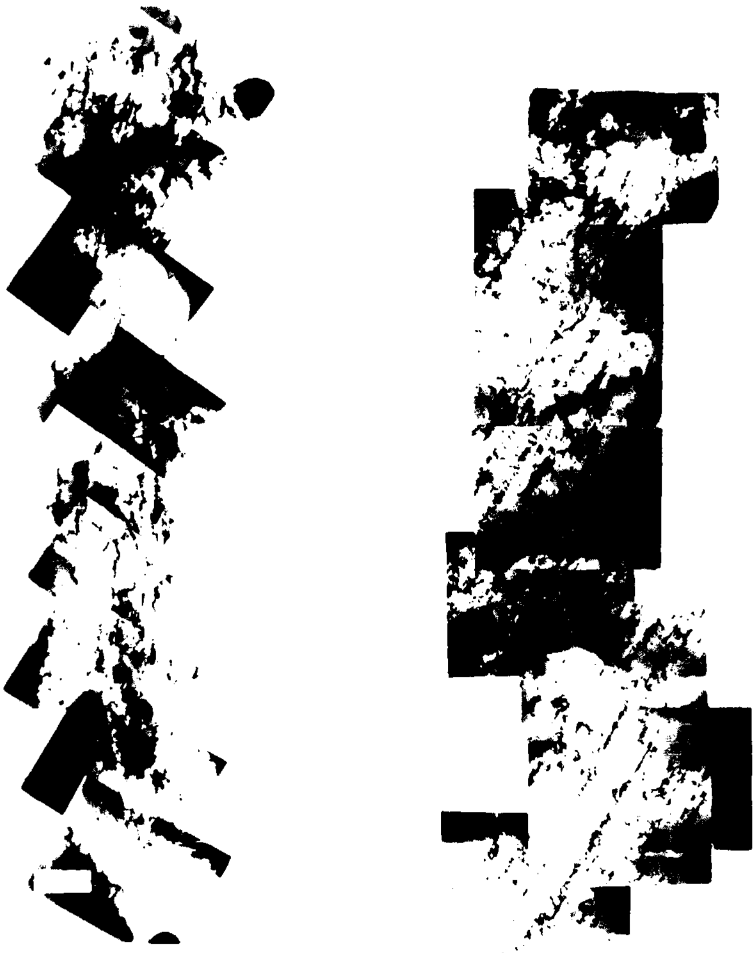

(a) (b)

Fig. 7 - Dislocation structure in a screw-oriented iron single crystal after about 5% easy glide strain.

(a) hydrogen free region
(b) hydrogen containing region of the same crystal as (a)

quenching, the alloy was aged at successively higher temperatures, producing the following microstructural sequences: cementite nucleation at lath boundaries at about 400°C; clustering of Ti(C,N) plus grain boundary cementite below 500°C; pre-emption of cementite by Ti(C,N) formation at higher temperatures, followed at still higher temperatures by precipitate coarsening and coherency loss. The effects of these different microstructures with similar strength levels, in both cathodically charged tensiles and double cantilever beam fracture mechanics specimens are summarized in Figs. 10 and 11, respectively.

The tensile results were interpreted as being strongly dependent on the transition from primary cementite to primary TiC or Ti(C,N) formation below 500°C, and to the rejection of metalloids to prior austenite grain boundaries at higher temperatures. In the context of the present focus on trap types, the behavior is separable on the basis of the strength and competition between traps. When cementite is the primary microstructural constituent, the trapping is strong, but reversible in nature (see Fig. 3(b)). Presumably the

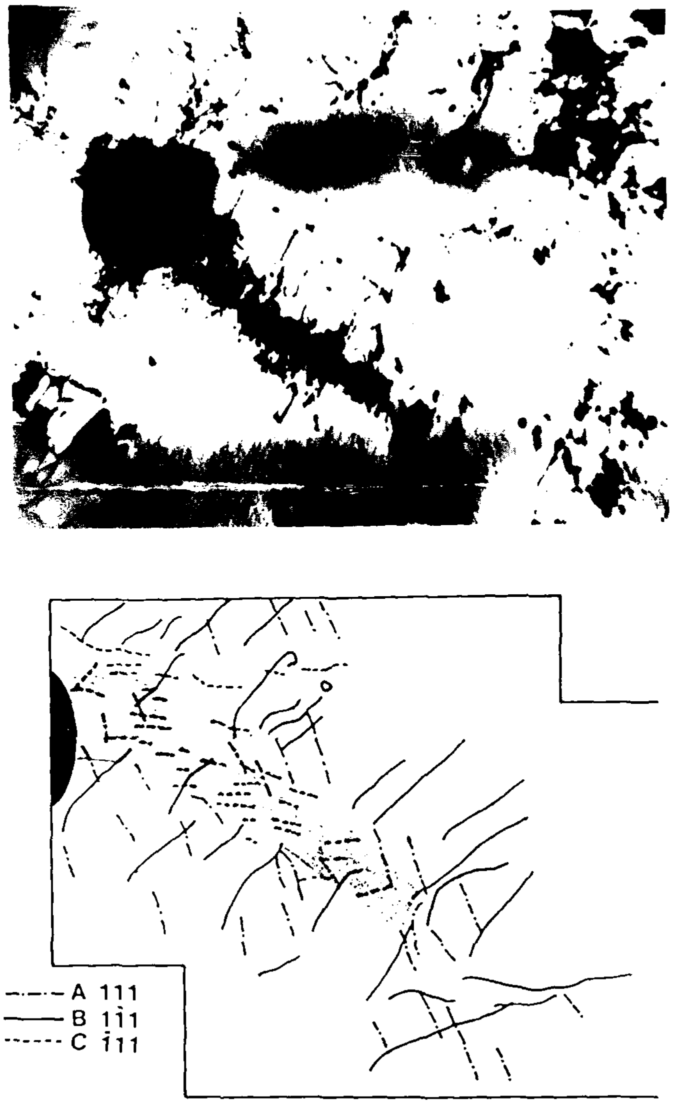

(b)

Fig. 8 - Hydrogen induced strain localization in the same single crystal shown in Fig. 7(b).

(a) TEM of localization band emanating from a silicon rich spherical particle.
(b) A sketch of dislocations on different slip systems participating in the strain localization structure

kinetics of detrapping is such that such sites are not efficient enough to significantly improve hydrogen response compared to the as-quenched structure. The very fine coherent TiC particles, on the other hand, provided strong irreversible traps, whose presence significantly improved ductility. However, at still higher temperatures, P rejection from the growing carbides to grain boundaries created regions with an even stronger interaction for hydrogen than the carbides. The resultant total loss of ductility concomitant with a 100% intergranular fracture, suggests that such catastrophic embrittlement requires both hydrogen and metalloids to coexist at sufficient concentrations at grain boundaries. Surprisingly, this embrittlement occurs even though a high densi-

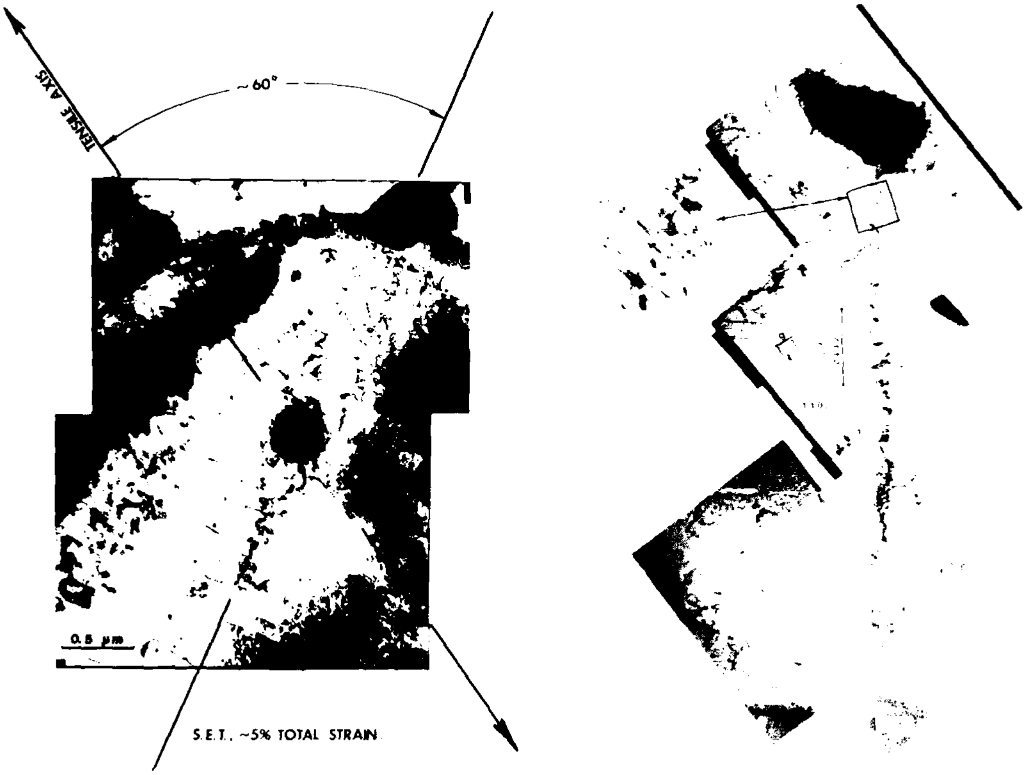

Fig. 9 - Strain localization in a polycrystalline spheroidized 1320 steel. The diffracting conditions were such that only 2 of the 3 operating slip systems within the band were imaged. Note the discontinuous nature of the band, particularly at lower strains.

(a) 5% total strain
(b) 8% total strain

ty of irreversible, fine (and, therefore, presumably innocuous) traps are present in the microstructure [29]. The apparent deleterious effect of P is in conflict with the prediction of Pressouyre [2,9,13] that this element should act as a hydrogen repeller, improving susceptibility by reducing the extent of other solute segregation. These current results and others [9] suggest that P can act very differently than the behavior predicted solely from thermodynamic considerations, when present as a segregant to grain boundaries and interfaces.

A quite different microstructural response is observed when the hydrogen effect is monitored by changes in the stress intensity for initiating crack growth and/or the subsequent rate of growth (Fig. 11). (The associated very discontinuous nature of the crack response is beyond the scope of this paper, but has been treated elsewhere [18].) Hydrogen embrittlement was found to be most severe for the microstructural conditions of negligible deep trapping and a high concentration of short circuit diffusion paths, while resistance was greatest in the presence of deep trapping, which produced both a lower quantity of diffusible hydrogen and slower kinetics of internal redistribution. This type of microstructural response is much more in the spirit of the trap theory of hydrogen embrittlement [8], since in the more susceptible condition, C_K, is reached more quickly, while in the more resistant condition, C_H, is significantly reduced, as discussed in the Introduction.

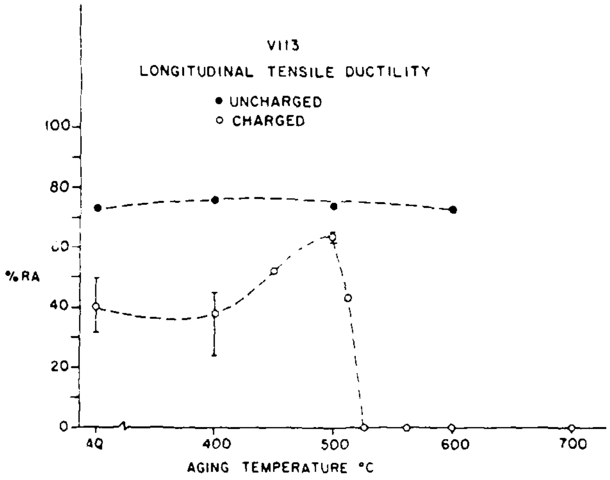

Fig. 10 - Comparison of internally charged and uncharged ductility response in tensile specimens of a Fe-0.05C-0.22Ti alloy as a function of aging temperature.

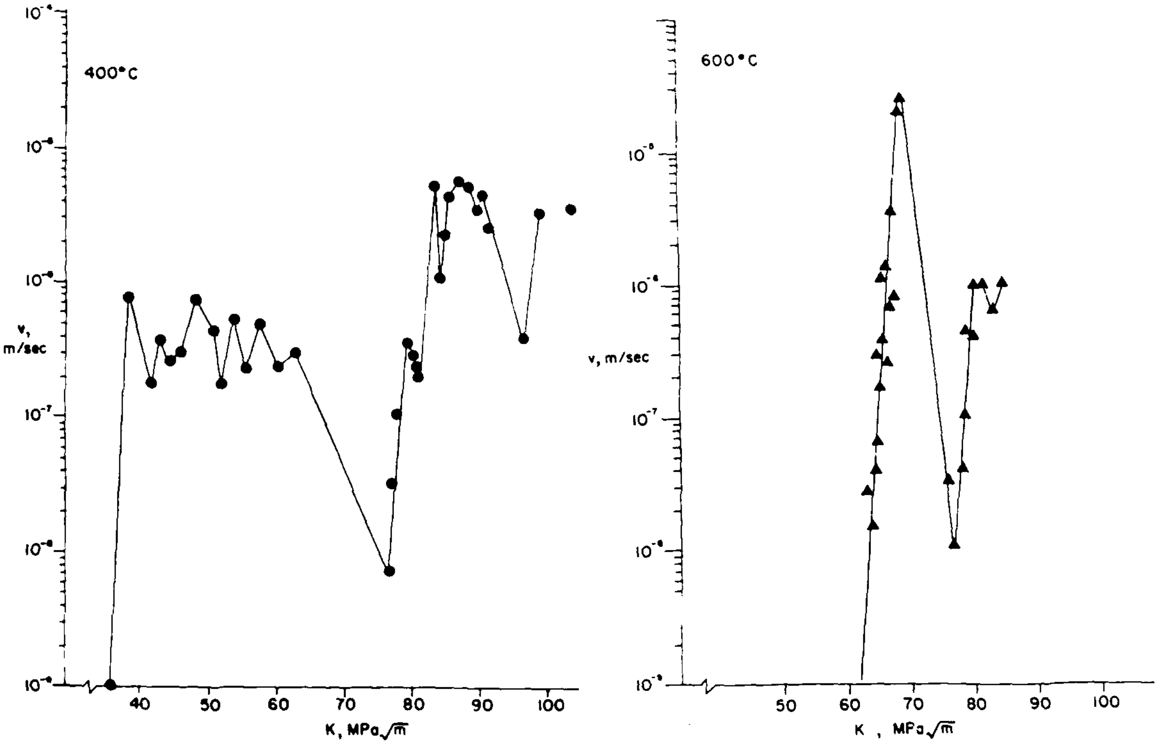

(a) (b)

Fig. 11 - Stress intensity dependence of hydrogen induced cracking in the same alloy as Fig. 10.

(a) Quenched and aged 1 h at 400°C
(b) Quenched and aged 1 h at 600°C

The difference between these results and for tensile specimens indicates the importance of kinetics in determining the usefulness of trapping to ameliorate embrittlement. In fracture mechanics type specimens, continuous deformation is not involved, reducing possible redistribution by dislocation transport. The fact that time is now a less critical variable implies that long range lattice diffusion through the matrix and the concomitant ease of redistribution in response to local stress changes should control the embrittlement process. Because such variable behavior exists, the comparison of short term tensile testing to long term hydrogen induced cracking can be quite useful as a probe to assess the influence of trapping. The fact that trapping is not effective in reducing embrittlement, if the aging process itself degrades other previously innocuous traps (e.g., grain boundaries) such that they become preferred sites for crack initiation and propagation seems reasonable, but it is not clear why this should not be manifested also under fracture mechanics conditions.

The final example to be presented is the hydrogen response of HY130 steel, a low carbon "clean" steel containing about 5% nickel. We have previously shown, as illustrated in Fig. 12, that heat treatment can have a dramatic effect on the threshold and crack growth rate under conditions where hydrogen is continuously being introduced from aqueous solution [17]. A very

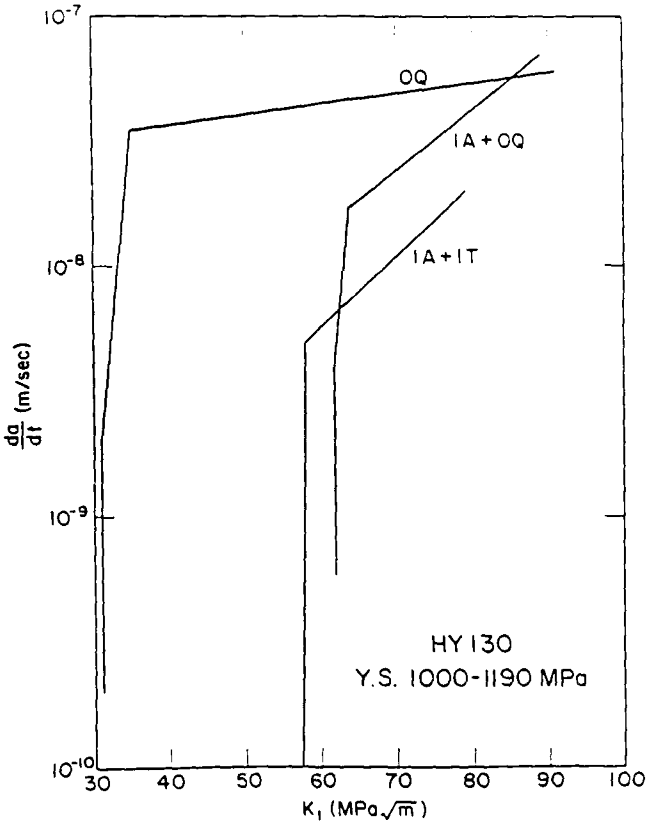

Fig. 12 - The effect of heat treatment on stress corrosion crack initiation and growth in a .09C5Ni HY130 steel tested in 3% NaCl, with zinc coupling to increase the hydrogen activity. The symbols designate the following heat treatments

OQ: Austenitized 1 h at 900°C, oil quench
IA + OQ: OQ treatment + 1 h at 675°C, oil quench
IA + IT: OQ treatment + 1 h at 675°C, isothermally transformed 3 h at 375°C.

detailed characterization of the microstructure was directed primarily at identifying the possible contribution of a varying amount of retained austenite. For this steel, the retained austenite was varied from about 3% to 10%, and was mechanically unstable, converting to untempered martensite at strains of the order of those found in the plastic zone in the vicinity of the crack tip [17,30]. The increasing presence of such austenite was found to be beneficial and could be correlated with the energy consumed in the transformation, which reduced the mechanical driving force for crack advance [30]. The threshold stress in turn scaled with the apparent solubility of hydrogen, derived from an analysis of permeation transients [12]. The solubility itself increased with the initial level of retained austenite, suggesting that the presence of the fcc phase is beneficial, particularly at larger concentrations, where there is a greater probability of it being present near the crack and in the plastic zone. In terms of trap theory, the retained austenite acts as a solubility trap and a diffusion obstacle, with the net result being a reduced C_H. However, retained austenite need not be always beneficial. In fact, in cases where the austenite is mechanically stable and is present as an interlath film, it was shown to degrade hydrogen performance in 300 M, a silicon modified 4340 steel [17].

Summary

The evidence continues to mount persuasively that the hydrogen performance of ferrous (and likely many non-ferrous alloys) is controlled by the distribution and redistribution of hydrogen to heterogeneities. These can be innocuous traps which, if fine enough and plentiful enough, can reduce C_H. Alternatively these sites can be localized precursors to crack or void formation and can lead to a reduced C_K if hydrogen's presence accelerates the onset of localized plasticity. As is always necessary when analyzing such a complex subject, some cautionary notes are required. Stress state and testing technique variations can modify expected performance, as can unexpected synergistic interactions between trap features which independently can be beneficial. Nevertheless, the picture which has developed of hydrogen-related trapping and changes in dislocation response, lends credence to an earlier claim that alloy design, through microstructure and compositional control, to improve hydrogen embrittlement resistance, is both feasible and attainable [7].

Acknowledgements

I want to express my sincere thanks to Dr. Philip Clarkin for his support and encouragement. He made a pleasant and productive relationship with the Office of Naval Research even better. Professor A. W. Thompson has provided stimulating and insightful discussions over a number of years which have greatly influenced the research direction for myself and my other coworkers.

References

1. I. M. Bernstein and A. W. Thompson, Int'l. Metall. Reviews, 21 (1976) p. 269. (ONR Tech. Report 4-NR036-099 (CMU))

2. G. M. Pressouyre, in Current Sol'ns to Hydrogen Problems in Steels, C. G. Interrante and G. M. Pressouyre, eds.; ASM, Metals Park, Ohio, (1982) p. 18.

3. J. P. Hirth, in Hydrogen Embrittlement and Stress Corrosion Cracking, R. Gibala and R. F. Hehemann eds.; ASM, Metals Park, Ohio, (1984) p. 29.

4. R. P. Wei, K. Klier, G. W. Simmons and Y. T. Chou, *ibid.*, p. 103.

5. A. W. Thompson and I. M. Bernstein, in *Advances in Corrosion Science and Technology*, R. W. Staehle and M. Fontana, eds.; Plenum, New York, (1980) p. 53.

6. H. K. Birnbaum, in *Atomistics of Fracture*, R.M. Latanision and J. R. Pickens, eds.; Plenum, New York, (1983) p. 733.

7. I. M. Bernstein and A. W. Thompson, in *Alloy and Microstructural Design*, J. K. Tien and G. Ansell, eds.; Academic Press, New York, (1976) p. 269. (ONR Tech. Report 3-NR036-099)

8. G. M. Pressouyre and I. M. Bernstein, *Met. Trans.*, *12A* (1981) p. 835. (ONR Tech. Report 14-NR036-099)

9. I. M. Bernstein and G. M. Pressouyre, in *Hydrogen Degradation of Ferrous Alloys*, R. A. Oriani, J. P. Hirth and M. Smialowski, eds.; Noyes Publ., N.J., (1985) p. 641. (ONR Tech Report 17-NR 036-099)

10. M. Iino, Acta Met., *30* (1982) p. 367 and p. 377.

11. G. M. Pressouyre, Ph.D. Thesis, Carnegie-Mellon Univ. (1977).

12. G. M. Pressouyre and I. M. Bernstein, *Met. Trans.*, *9A* (1978) p. 157. (ONR Tech. Report 10-NR 036-099)

13. G. M. Pressouyre, *Met. Trans.*, *14A* (1983) p. 2189.

14. R. Gibala and A. J. Kumnik, in *Hydrogen Embrittlement and Stress Corrosion Cracking*, R. Gibala and R. F. Hehemann, eds.; ASM Metals Park, Ohio, (1984) p. 61.

15. J. P. Hirth, *Met. Trans.*, *11A* (1980) p. 861.

16. I. M. Bernstein and A. W. Thompson, in *Advanced Techniques for Characterizing Hydrogen in Metals*, N. F. Fiore and B. J. Berkowitz, eds.; TMS, Warrendale, PA (1982) p. 89.

17. R. Kerr, F. Gutierrez-Solana, I. M. Bernstein and A. W. Thompson, *Met. Trans.*, (in press).

18. M. F. Stevens, Ph.D. Thesis, Carnegie-Mellon Univ. (1984). (ONR Tech. Report 19-NR 036-099)

19. M. Kurkela and R. M. Latanision, *Scripta Met.*, *13* (1979) p. 927.

20. C. Hwang, Ph.D. Thesis, Carnegie-Mellon Univ. (1984). (ONR Tech. Report 18-NR 036-099)

21. C. Hwang and I. M. Bernstein, *Scripta Met.*, *17* (1983) p. 1299.

22. M. Aucouturier, in *Current Sol'ns to Hydrogen Problems in Steels*, C. Interrante and G. M. Pressouyre, eds.; ASM, Metals Park, Ohio, (1983) p. 407.

23. Tuyen D. Le and B. E. Wilde, *ibid.*, p. 413.

24. J. Chene, *ibid.*, p. 265.

25. R. Garber, I. M. Bernstein and A. W. Thompson, Met Trans., 12A (1981) p. 225. (ONR Tech. Report 13-NR036-099)

26. H. Kimura, H. Matsui, S. Takaki, A. Kimura and K. Oguri, in Mechanical Properties of BCC Metals, M. Meshi, ed.; TMS, Warrendale, PA. (1982) p. 125.

27. T. Kosco and A. W. Thompson, Scripta Met., 16 (1982) p. 1367.

28. C. Hwang and I. M. Bernstein, Acta Met., 34 (1986) p. 1011.

29. Tuyen Le and I. M. Bernstein, work in progress.

30. M. F. Stevens and I. M. Bernstein, Met Trans., 16A (1985) p. 1379.

31. C. Takamadate, F. Gutierrez-Solana, I. M. Bernstein and A. W. Thompson, Met. Trans., (in press).

ON THE MECHANISMS OF HYDROGEN RELATED FRACTURE IN METALS

H. K. Birnbaum
Department of Metallurgy and Mining Engineering
University of Illinois at Urbana-Champaign
1304 W. Green Street
Urbana, Illinois 61801

Premature failure of materials due to the introduction of hydrogen has been recognized as a serious materials problem since the late 1800's. Progress in the understanding of hydrogen related failures has been made and has resulted from the efforts of many researchers. One significant advance in understanding has resulted from the recognition that there are several different mechanisms of "hydrogen embrittlement" rather than a single global mechanism which applies to all materials or to a single material under all conditions. A second important advance resulted from the realization that the mechanistic considerations are quite separate from the kinetic aspects of these failures. This paper will discuss evidence for a multiplicity of hydrogen related fracture mechanisms and will focus on the work carried out at the University of Illinois during the last 15 years. The issue of kinetics versus mechanisms will be considered also, although somewhat more briefly.

Premature failure of materials due to the introduction of hydrogen has been recognized as a serious materials problem since the late 1800's [1]. Despite a huge literature characterizing this phenomenon, it has only been in the past twenty-five years that significant progress has been made towards understanding the various mechanisms which contribute to this type of environmentally related failure. The support of the ONR in general and of Phil Clarkin in particular has been essential in the recent progress towards understanding hydrogen related fracture. In the best of government service tradition, Phil has used the resources available to him for the good of science and of our society.

Progress in the field of hydrogen related failures has resulted from the efforts of many researchers and these efforts have been recently reviewed from my particular perspective [2,3]. One significant advance in our understanding has resulted from the recognition that there are several different mechanisms of "hydrogen embrittlement" rather than a single global mechanism which applies to all materials or to a single material under all conditions. The present paper will discuss evidence for a multiplicity of hydrogen related fracture mechanisms and will focus on the work carried out at the University of Illinois. A second important advance resulted from the realization that the mechanistic considerations are quite separate from the kinetic aspects of these failures. We will also touch on this important point although somewhat more briefly.

More than anything else, this review is a tribute to the numerous students, research associates, and colleagues with whom I have interacted over the years and to the O.N.R. and Phil Clarkin who helped make these interactions possible.

Hydrogen related fracture is almost ubiquitous. A short number of years ago many systems were considered to be "immune" from hydrogen embrittlement. e.g., Al, W, Mo, and Cu although it was known that these systems did form defects related to the precipitation of supersaturated hydrogen gas. At present, the number of "immune" systems is few indeed and it may he suspected that even these will show hydrogen related fracture if they are stressed in a sufficiently high fugacity of hydrogen or if a sufficient quantity of solute hydrogen is introduced prior to stressing.

The source of hydrogen which causes failure may be solute hydrogen, gaseous hydrogen, or hydrogen introduced by a chemical reaction such as the interaction between metals and aqueous solutions (stress corrosion cracking). These differ principally in two main aspects: the hydrogen fugacity and the location of the hydrogen source. The fugacity of hydrogen can vary by many orders of magnitude depending on the source; gaseous hydrogen which causes failure can have a fugacity as low as a fraction of an atmosphere while hydrogen derived from a chemical reaction, such as is the case in stress corrosion cracking, may have a fugacity of 10^6 atmospheres. The fugacity can determine which failure mechanism dominates or indeed whether or not hydrogen related fracture occurs. For example, in many systems a threshold for hydrogen embrittlement is observed which depends on the hydrogen fugacity and the stress intensity at the crack tip [4-8]. At stress intensities and/or hydrogen fugacities above the threshold values hydrogen related failure occurs at rates which are complex functions of parameters such as hydrogen fugacity, stress intensity, temperature, the structure of the material, etc., while below the threshold the behavior is completely ductile.

The existence of this threshold has been interpreted as support for the decohesion mechanism of fracture. The phenomena occurs in systems which do not form hydrides under the conditions of the fracture [4-6] as well as in systems which do [7,8]. In the latter, the threshold stress intensity for fracture is clearly associated with the formation of hydrides at the crack tip while in the former case the detailed mechanism of fracture is not yet established. Threshold phenomena which involve varying the hydrogen fugacity [4] in the ferrous systems are analogous to those observed in hydride forming systems wher the chemical potentials of the solid solution and the hydride are varied relative to each other by controlling the temperature [9-10]. Careful consideration of these experiments leads to the conclusion that the existence of the threshold in stress intensity or in hydrogen fugacity does not support any particular mechanism, as a variety of fracture mechanisms can be expected to have a threshold behavior. In the decohesion mechanism [4] the threshold corresponds to achieving a local stress sufficient to break the atomic bonds at the crack tip under the local enhancement of the H concentration which is a function of the local stress intensity [12]. In those systems which form hydrides the threshold corresponds to a stress induced shift of the relative chemical potentials of hydrogen in the solid solutions and in the hydrides to the point where the hydrides can form at the crack tip [13,14]. At that point, the hydrides undergo cleavage due to their very limited dislocation mobility [15] and the crack propagates by repeated hydride formation and cleavage [7].

The magnitude of the hydrogen fugacity may also, in some systems, determine which of several operative mechanisms cause failure. Nickel undergoes hydrogen related fracture at relatively low fugacities by a mechanism which, while not yet completely understood, is the result of increased dislocation mobility and enhanced plastic deformation when H is present in the material [16-20]. The fracture propagates by a local reduction of the resistance to dislocation motion and enhanced plastic deformation at the crack tip as first suggested by C. Beachem [22]. At higher H fugacities, such as those which pertain to cathodic charging conditions (straining electrode tests), a hydride is formed on the surface of the Ni [22]. At low stress intensities the fracture proceeds by cleavage of this hydride followed by the formation of additional hydride at the crack tip [23]. At higher stress intensities, the hydride forms and fractures but the crack can then precede the hydride into the region of high H concentration in front of the hydride by the localized plasticity mechanism [23]. Thus, in the Ni system, the H fugacity determines which of several mechanisms is responsible for the hydrogen related failure.

Another example of this fugacity dependence is provided by the behavior of α titanium alloys in gaseous hydrogen. In situ TEM studies of the effects of H on the deformation and fracture of Ti alloys has shown that fracture can occur as a result of the hydrogen enhanced local plasticity mechanism [24] as well as by the stress induced formation and fracture of hydrides [24]. It was also shown that these two mechanisms are competitive in the sense that the failure occurs by whichever of the two leads to fracture most rapidly. At high stress intensities, the localized plasticity mechanism appears to dominate while, at low stress intensities and slow crack growth, the hydride formation and cleavage mechanism is dominant. It would be expected, but not yet proven, that this same order of dominance would occur at low and high H fugacity respectively.

Implicit in the discussion above is the useful distinction between hydride forming and non-hydride forming systems. However, even this distinction depends to some extent on the hydrogen fugacity under which the fracture is proceeding. Systems such as the Group Vb metals, Nb, Ta, and V, alloys of Mg, Ti, Zr, and a number of other metals, have been clearly shown to form hydrides under the conditions which lead to environmentally related fracture. However, even in these systems it may be possible to obtain "hydrogen embrittlement" under conditions which do not form stable hydrides. In evaluating this possibility, the effects of stress on hydride formation must be considered [12-14]. Hydrides may be formed at the crack tip under stress at temperatures and hydrogen fugacities which would not normally form hydrides. Since these hydrides may disappear when the external stress is removed or when the crack tip advances [25], examination for these metastable hydrides must be carefully carried out before the stress induced formation and cleavage of hydrides is discarded as a fracture mechanism. Candidates for possible metastable hydride formations are the Ni, Al and stainless steel systems. The Ni observations [23] have been summarized above. We have looked for metastable hydrides in Al and have not yet found any evidence for them. The situation in stainless steels is discussed below.

We have studied the non-hydride forming systems, Fe (of various purities), Ni (at fugacities below those which form hydrides), pure Al, Al alloys in various tempers (7075 and 7050), IN 703, α-Ti (under stress concentrations such that the hydride cannot form at a rate great enough to keep up with the crack propagation), and β-Ti. The results of our studies using in situ environmental cell TEM, slow strain rate tensile tests, fracture mechanics studies of subcritical crack growth, SEM fractography and other methods is that the dominant hydrogen related fracture mechanism is failure by a localized ductility which results from hydrogen induced softening of the material at the crack tip. This conclusion applies to both transgranular and intergranular fracture in a variety of materials where both have been studied [20,26-28]. We see no evidence for the "decohesion" mechanism although it may play a role which has not yet been recognized. This matter is discussed further below.

As indicated above, our studies have resulted in the classification of stainless steels as possible "metastable hydride formers" with respect to their behavior under high H fugacity conditions as in stress corrosion. In the metastable austenitic stainless steels the role of the hydrides in fracture may be taken by other phases, such as the martensitic α and ε phases. These have been shown by us and others, to form under conditions of high H fugacity and high stresses [29,30]. The presence of these phases has been shown on fracture surfaces of 304 stainless steel which failed in a slow strain rate test in one atmosphere of hydrogen gas or in a stress corrosion test. In situ TEM studies have shown the α martensite phase present in front of the crack tip and that the crack propagates through the martensite phase [31]. The formation of these martensitic phases requires the presence of both stress and hydrogen (i.e., formation in excess of the normal ρ strain induced α martensite). They appear to play the role of stress induced "hydrides" in providing a relatively brittle phase through which the crack can propagate and/or providing a high diffusivity path through which hydrogen can be transported into the interior of the material. If these martensitic phases play a dominant role in the hydrogen related cracking and stress corrosion cracking of stainless steels, primary consideration must be given to the stability of the austenitic phase in controlling the behavior of these steels in aggressive environments.

In addition to the role of martensitic phases in the metastable stainless steels, the formation of an expanded fcc structure under high H fugacity conditions has been reported [30] in both the unstable and stable austenitic stainless steels (type 304 and 310, respectively). It has been proposed that this γ' phase is essentially a "hydride" in the sense that Ni forms a "hydride", i.e., it is a solid solution phase on the high composition side of a miscibility gap [30]. The properties of this "hydride" in stainless steels are poorly known but by analogy to the Ni hydride it may be expected to be rather brittle and to provide a path for the propagation of a relatively low ductility fracture.

The second major factor, other than the H fugacity, which is determined by the source of hydrogen, is the location of the hydrogen source. While this factor primarily affects the kinetics of the fracture process, it has often entered into discussions of the operative fracture mechanisms. External hydrogen sources such as gaseous H_2, SCC environments, etc., deliver the hydrogen in molecular or atomic form at the surface of the crack. In these cases the hydrogen must be transported across the surface into the material in order that many of the operative fracture mechanisms be viable. This process can be controlled by any of a number of steps [32] and the rate controlling mechanism may vary with temperature, H_2 pressure, the presence of hydrogen recombination poisons and catalysts on the surface, and many other factors. As a result, the kinetics of fracture often exhibit great complexity [33]. While these kinetic problems are of great importance in understanding and controlling environmentally related fracture, their effects should not lead to confusion in understanding the mechanism of fracture.

In many situations, hydrogen is present as a solute or in the material as a hydride. In these cases, the kinetics of hydrogen related fracture are controlled by hydrogen diffusion to the crack tip or possibly by the dissolution kinetics of hydrides under the influence of a non-uniform stress field.

A review of the available data suggests that in all cases the hydrogen related fracture requires that a critical concentration of hydrogen be present at the crack tip, be it for the formation of a hydride, the breaking of atomic bonds or for the reduction of the local flow stress to allow plastic deformation processes. As discussed above, the value of this critical concentration depends on many factors such as the local stress intensity, temperature, the fugacity of the reference phase such as the hydride, etc. In the absence of such a critical concentration, the material behaves in a normal ductile manner particularly as solute. Hydrogen does not have a large effect on the plastic response of the material [34]. Consequently, the response of the metal-hydrogen systems to stress is to show an "inverse strain rate effect," i.e., an increase of ductility with strain rate, and a return of ductility at low temperatures. Both of these result from the intervention of the normal ductile failure processes prior to the achievement of the critical hydrogen concentration at the crack tip. At high strain rates and at low temperatures, the material fails in the normal manner before the hydrogen can diffuse to the crack tip or be transported across the surface barriers in sufficient quantities to cause hydrogen related failure.

These processes have been recently investigated in the Ni-H system using tensile tests at 77 K; a temperature at which no hydrogen diffusion or transport could take place during the test [35]. Hydrogen was introduced at controlled concentrations by quenching from various temperatures and from controlled hydrogen partial pressures. The distribution of H in the specimens was varied by aging at low temperatures during which hydrogen segregated to the grain boundaries [36]. Solid solutions of Ni-H containing up to about 800 appm of H exhibited completely ductile behavior indicating that the embrittlement in Ni was not due to H in solid solution. On aging, the extent of intergranular embrittlement increased, reaching a maximum value on aging for greater than a critical aging time which depended on the aging temperature. The extent of intergranular embrittlement depended on the amount of H in solid solution and could be 100%. These r sults indicate that embrittlement of Ni by solute H results from segregation of the H at grain boundaries and the kinetics and thermodynamics which characterize these results are consistent with this model. These studies yield a H-grain boundary binding enthalpy of about 12 kJ/mole and are consistent with SIMS studies of H segregation to grain boundaries and surfaces in Ni [36]. The synergistic effects of S segregation on the hydrogen embrittlement process at grain boundaries was also demonstrated [35]. Sulfur concentrations at the grain boundaries at a level of S/Ni = 0.11 did not give rise to intergranular embrittlement in the absence of H in solid solution. However, small concentrations of H segregated at the grain boundaries in addition to the S caused severe intergranular embrittlement. The amount of solute hydrogen required to attain maximum intergranular embrittlement was greatly reduced by the co-segregation of S. These results are in agreement with the SIMS studies which showed enhanced H segregation in the presence of S [36].

These studies of the specificity of the fracture process to the location of the H solutes also examined the possibility of H transport during the deformation process [37]. Although this is a complicated phenomena, our results showed that significant diffusion of H to grain boundaries could occur during aging at room temperature prior to the mechanical property tests as well as during the tests for temperatures near 300 K when relatively low strain rates are used. Thus most of the previously reported measurements on Ni are characterized by a somewhat variable degree of H segregation to the grain boundaries and a possible history dependent behavior. The evidence of the controlled aging experiments is that the important phenomenon is diffusion during the aging or during the tensile test itself rather than hydrogen transport by moving dislocations.

While we have not seen any phenomena which give rise to support for the concept of fracture by decohesion, the concept is still widely supported and has recently received some theoretical underpinning [38,39]. The theoretical validity of these calculations is still a matter of some debate and will not be addressed here. However, we wish to make a number of comments concerning the experimental evidence bearing on the question of whether H causes a significant weakening of the atomic bonds. Unfortunately, many of the experimental techniques which bear on this question cannot be applied to systems of interest such as the Fe-H system due to the low H solid solubility.

The elastic moduli of the Group Vb-H systems hav been measured at various temperatures and over a wide range of H concentrations [40,41]. Over composition ranges up to H/Nb = 0.8 both increases (C_{44}, B) and decreases (C_{11}, C') of the moduli are observed; in particular the bulk modulus exhibits only an increase as the H/Nb is increased [41]. In view of the very large volume increase which accompanies the solution of H in Nb, these changes do not indicate any weakening of the atomic bonding. Furthermore, measurements of the phonon dispersion curves and analysis of the data in terms of interatomic force constants in the Group Vb-H systems show an increase in the phonon frequencies and a corresponding increase in the force constants as H is added to the system [42]. Decreases in the phonon frequencies are observed in the fcc systems on alloying with H but these are relatively smaller in magnitude than those observed in the bcc systems [43].

Measurements of the equilibrium surface free energies in Ni have been carried out with and without H in solid solution [44]. No significant differences were measured. The fracture surface energies of NbH (containing H/Nb = 0.8) was measured and shown to be about equal to that of Nb; again indicating no significant decrease in the effective surface energy with H even at very high concentrations [15]. The brittleness of the hydride was associated with limited dislocation mobility caused by disordering of the hydride structure when dislocation motion occurred.

In contrast to these experimental data which do not support the concept of decohesion, there are very few results which do suggest that the presence of H weakens the atomic bonds. One which may be cited is the decrease of the field evaporation field in a field ion microscope experiment by the presence of a small partial pressure of H_2. One difficulty with this experiment is that the field ion tips are at a very high stress state compared to any crack tip material.

Thus, while the definitive experiments on this subject have not been devised or carried out, we conclude that the preponderance of evidence is that H does not significantly reduce the strength of the atomic bonds. The decohesion mechanism of hydrogen related fracture will necessarily remain a "Maxwell's Demon" until significant experimental evidence or convincing theoretical support is obtained. Until that time, the weight of the evidence supports hydrogen related fracture due to stress induced hydride (or other suitable second phase) formation and cleavage or hydrogen induced local plasticity; depending on the system and the experimental constraints imposed.

Acknowledgement

Much of the work which is described was made possible by generous support by the Office of Naval Research, USN-N00014-83-K00468, by the Department of Energy, DE-AC02-76ER01198, and by the National Science Foundation, DMR-84-05520. The author would like to express his personal appreciation to Dr. Phil Clarkin for continued support and encouragement over the years.

References

1. W. H. Johnson, Proc. Roy. Soc., No. 158 (1875) p. 168.
2. H. K. Birnbaum, Environment-Sensitive Fracture of Engineering Materials, (AIME, Warrendale, PA), ed. by Z. A. Foroulis (1979) p. 326.
3. H. K. Birnbaum, Hydrogen Embrittlement and Stress Corrosion Cracking, (ASM, Metals Park OH) ed. by R. Gibala and R. F. Hehemann (1984) p. 153.
4. R. A. Oriani and P. H. Josephic, Acta Met., 22 (1974) p. 1065.
5. R. P. Gangloff and R. P. Wei, Met. Trans. A, 8A (1977) p. 1043.
6. W. Wei, Ph.D. Thesis, University of Illinois (1983).
7. B. Hindin, Ph.D. Thesis, University of Illinois (1981).
8. R. Dutton, K. Nuttall, M. P. Puls, and L. A. Simpson, Met. Trans. A, 8A (1977) p. 1553.
9. S. Gahr, M. L. Grossbeck and H. K. Birnbaum, Acta Met., 25 (1977) p. 125.
10. M. L. Grossbeck and H. K. Birnbaum, Acta Met., 25 (1977) p. 135.
11. S. Gahr and H. K. Birnbaum, Acta Met., 26 (1978) p. 1781.
12. J.C.M. Li, R. A. Oriani, and L. S. Darken, Z. Physik Chem. Neue Folge., 49 (1966) p. 271.
13. H. K. Birnbaum, M. L. Grossbeck and M. Amano, J. Less Common Metals, 49 (1976) p. 357.
14. T. B. Flannagan, N. B. Mason, and H. K. Birnbaum, Scripta Met., 15 (1981) p. 109.
15. S. Gahr and H. K. Birnhaum, Acta Met., 26 (1978) p. 1781.
16. T. Tabata and H. K. Birnbaum, Scripta Met., 17 (1983) p. 947.

17. H. Matsui, S. Moriya, and H. Kimura, Mat. Sci. Eng., 40 (1979) p. 807.

18. T. Tabata and H. K. Birnbaum, Scripta Met., 18 (1984) p. 231.

19. J. Eastman, F. Heubaum, T. Matsumoto and H. K. Birnbaum, Acta Met., 30 (1982) p. 1579.

20. I. M. Robertson and H. K. Birnbaum, Acta Met., (in press).

21. C. D. Beachem, Met. Trans., 3 (1972) p. 437.

22. A. Janko and A. Szummer, Bull. Acad. Polon. Sci., Ser. Sci. Chim., 14 (1966) p. 885.

23. A. Kimura and H. K. Birnbaum, (in preparation).

24. S. Shih, I. M. Robertson, and H. K. Birnbaum (in preparation).

25. S. Takano and T. Suzuki, Acta Met., 22 (1974) p. 265.

26. I. M. Robertson, T. Tabata, W. Wei, F. Heubaum, and H. K. Birnbaum, Scripta Met., 18 (1984) p. 841.

27. F. Heubaum, M.S. Thesis, University of Illinois (1981).

28. J. Eastman, T. Matsumoto, N. Narita, and H. K. Birnbaum, Proc. of Int. Conf. on Hydrogen in Metals, (AIME, Warrendale. PA). ed. by I. M. Bernstein and A. W. Thompson (1981) p. 397.

29. R. Lui, N. Narita, C. J. Altstetter, H. K. Birnbaum, and E. N. Pugh, Met. Trans., 11A (1980) p. 1563.

30. N. Narita, C. J. Altstetter, and H. K. Birnbaum, Met. Trans., 13A (1982) p. 1355.

31. N. Narita and H. K. Birnbaum, Scripta Met., 14 (1980) p. 1355.

32. R. Latanision, Hydrogen Effects in Metals, (AIME, Warrendale. PA), ed. by I. M. Bernstein and A. W. Thompson (1981) p. 379.

33. D. P. Williams, P. S. Pao, and R. P. Wei, Environment Sensitive Fracture of Engineering Materials, (AIME, Warrendale, PA). ed. by Z. A. Foroulis (1979) p. 3.

34. H. K. Birnbaum, M. Grossbeck, and S. Gahr, Hydrogen in Metals, (ASM, Metals Park, OH), ed. by I. M. Bernstein and A. W. Thompson (1974) p. 303.

35. D. Lassila and H. K. Birnbaum, Acta Met. (in press).

36. H. Fukashima and H. K. Birnbaum, Acta Met., 32 (1984) p. 851.

37. J. K. Tien, S. V. Nair, and R. R. Jensen, Hydrogen Effects in Metals (AIME, Warrendale, PA) ed. by I. M. Bernstein and A. W. Thompson (1981) p. 37.

38. R. P. Messmer and C. L. Briant, Acta Met., 30 (1982) p. 457.

39. M. S. Daw and M. I. Baskes, Phys. Rev. B, 29 (1984) p. 6443.

40. A. Magerl, B. Berre, and G. Alefeld, *Phys. Status Solidii*, a, *36* (1976) p. 161.

41. F. M. Mazzolai and H. K. Birnbaum, *J. Phys. F: Met. Phys.*, *15* (1985) p. 507, p. 525.

42. T. Springer, *Hydrogen in Metals I*, (Springer-Verlag, Berlin), ed. by G. Alefeld and J. Volkl (1978) p. 75.

43. J. M. Rowe, J. J. Rush, H. G. Smith, M. Mostoller, and H. E. Flotow, *Phys. Rev. Lett.*, *33* (1974) p. 1297.

44. E. A. Clark, R. Yeske, and H. K. Birnbaum, *Met. Trans. A*, *11A* (1980) p. 1903.

MECHANISMS OF STRESS-CORROSION CRACKING

IN Al-Zn-Mg AND Al-Mg ALLOYS

J.R. Pickens, T.J. Langan, J.A.S. Green
MARTIN MARIETTA CORPORATION
Martin Marietta Laboratories
1450 South Rolling Road
Baltimore, Maryland 21227

The major developments in understanding the mechanisms of stress-corrosion cracking (SCC) in Al-Zn-Mg and Al-Mg alloys will be briefly reviewed. In particular, evidence for the involvement of hydrogen embrittlement in the SCC mechanisms will be addressed.

The research at Martin Marietta Laboratories that contributed to the understanding will be emphasized. Specifically, the effect of the loading mode on SCC, the role of grain boundary segregation in cracking, and our overall view of the mechanisms of SCC will be discussed.

Introduction

Stress-corrosion cracking (SCC) is an embrittlement phenomenon occurring in alloys under the combined influence of tensile stress and environment. The stress may either be applied or residual stress, and, for aluminum alloys, the environment is most often aqueous, i.e., containing liquid or gaseous water.

Many service failures of high-strength, structural aluminum alloys have been attributed to SCC [1]. In fact, the highest strength aluminum alloys are generally the most susceptible to SCC, and Speidel [1] estimated that there were over 450 SCC failures in high-strength aluminum alloys in aerospace products during 1968. The highest strength aluminum alloy system, the Al-Zn-Mg (7XXX) alloys, is often extremely susceptible in the peak-strength tempers [2-4]. Furthermore, SCC most often occurs in thick sections, which are often subjected to short transverse (ST) stresses. Susceptibility is generally highest in the ST orientation because of the pancake-shaped grain morphology there. SCC failures have the potential to be catastrophic, in the event that routine inspections fail to detect stress-corrosion (SC) cracks.

The usefulness of both Al-Zn-Mg alloys and a medium-to-high strength system, the Al-Mg (5XXX) alloys, is often limited by SCC susceptibility. High-strength 7XXX alloys are often used in the overaged (OA) condition to reduce susceptibility, but at the expense of about a 15% loss in strength. In addition, weldable 7XXX [5] and 5XXX [6] alloys are often extremely susceptible in the heat-affected-zone (HAZ) of weldments, which thereby limits their usefulness.

Many alloy development efforts have been undertaken to reduce the SCC susceptibility of Al-Zn-Mg alloys in the peak-aged temper and thus avoid the strength penalty accompanying overaging. A greater understanding of the SCC mechanism(s) would be extremely helpful in attaining this goal and, consequently, this area has been extensively studied [2-4]. In addition, SCC of Al-Zn-Mg alloys is an intriguing phenomenon because it is usually intergranular, is affected by grain boundary (GB) segregation, and involves both anodic dissolution and hydrogen embrittlement (HE). Thus, mechanistic SCC studies of Al-Zn-Mg alloys have been performed for their overall implications to embrittlement phenomena in general.

In the present work, key developments in understanding the SCC mechanisms in Al-Zn-Mg and Al-Mg alloys are briefly reviewed. Contributions made by Martin Marietta Laboratories' investigators are emphasized, and significant findings by others are also discussed.

Mechanisms of SCC

A widely accepted theory of SCC, proposed by Dix [7] and Mears, Brown, and Dix [8] in the 1940's, attributed it to a synergism between tensile stress and corrosion; most often anodic dissolution. That is, corrosion occurred along localized paths, producing fissures that served as stress-concentrators for an applied tensile stress. SCC was generally found to be intergranular, and the anodic $MgZn_2$ GB precipitates were assumed to preferentially dissolve. Dissolution of the $MgZn_2$ was subsequently observed by Jacobs [9].

Numerous studies were performed to elucidate the dissolution mechanism of SCC. For example, Sedriks et. al. [10] explained the decrease in SCC susceptibility in the OA temper as compared with the peak-aged (PA) temper by there being a greater mean-free-path between the anodic GB $MgZn_2$ precipitates in the OA temper. Subsequent SCC simulation studies were performed to establish the corrosion behavior of the individual microstructural components of the GB region of a Al-Zn-Mg ternary alloy [11]. In this work, comparisons were made of the relative corrosion rates of (1) a relatively massive $MgZn_2$ crystal, (2) pure aluminum, which simulates the solute-depleted region adjacent to the GB, and (3) the as-quenched ternary alloy, which simulates the vacancy-depleted zone somewhat removed from the boundary. The results indicated that the dissolution rate of $MgZn_2$ under comparable electrochemical conditions was far greater than that of the other GB components. Furthermore, the results indicated that the crack-tip environment was governed by solubility product considerations [11-12].

In 1963, Gruhl [13] observed that Al-Zn-Mg specimens that were pre-exposed to a saline solution had shorter time-to-failure (TTF) during subsequent SCC testing than non-exposed specimens. Furthermore, he found that this "pre-exposure embrittlement" (PEE) could be eliminated by repeating the entire heat-treatment on the specimens. This reversible PEE led Gruhl to propose that hydrogen, resulting from the corrosion reaction, permeates into the alloy and promotes embrittlement under the influence of the subsequently applied tensile stress. Thus, Gruhl proposed that HE is involved in the SCC mechanism.

Gruhl's observations and proposed mechanism were initially viewed with skepticism. However, PEE was also noted in subsequent work by Swann and coworkers. For example, Montgrain and Swann [14] observed fracture of pre-exposed specimens at lower stress levels than those not pre-exposed. Furthermore, fracture occurred without apparent dissolution of the GB precipitates. Moreover, pre-exposed specimens that were subsequently fractured in a vacuum chamber released hydrogen, as measured in a mass spectrometer. In addition, Scamans, Alani, and Swann [15] observed reversible PEE in specimens exposed to moist air.

Additional evidence for the role of HE in the SCC of Al-Zn-Mg alloys was provided by Speidel [3] who observed SC crack growth in moist air at a humidity level believed to be too low to effect significant dissolution. Speidel also compiled the existing evidence for the role of HE in the SCC mechanisms in a stimulating review [16].

Gest and Troiano [17] cathodically charged hydrogen into 7075 T651 specimens, and tested both them and uncharged specimens in tension at various strain rates. The two groups of specimens displayed similar ductilities at high strain rates, but the ductility was lower for the charged specimens at lower strain rates. In addition, the embrittlement was reversible by degassing the charged specimens at elevated temperatures. Furthermore, charged specimens demonstrated increased SCC susceptibility compared with uncharged specimens. Each of these results indicates a role for hydrogen in the fracture process.

The aforementioned studies, as well as others not discussed, indicate that Al-Zn-Mg alloys can be susceptible to HE, and that HE plays a role in the SCC mechanism of these alloys. Research at Martin Marietta Laboratories over the past decade has provided additional evidence for the involvement of HE in SCC and has also elucidated the overall mechanism by which SCC occurs. Some of these major contributions are discussed in the following sections.

Mechanistic Studies of SCC at Martin Marietta Laboratories

Loading Mode Experiment

Investigators at Martin Marietta Laboratories [18-19] and elsewhere [20-22] developed the loading mode test to determine whether HE is involved in the SCC mechanism of a particular alloy system in a specific environment. In Mode I (tension), a triaxial tensile stress field exists ahead of the crack-tip. This stress field provides a driving force for hydrogen concentration, which can lead to embrittlement. In Mode III (antiplane shear, i.e., torsion), little or no triaxiality exists, thereby reducing or eliminating this driving force for hydrogen concentration and subsequent embrittlement, even in alloys susceptible to HE. Thus, the response of an alloy to this difference in triaxiality may be used as a diagnostic tool to determine if cracking under load in a corrosive environment involves HE, or is primarily attributable to dissolution.

Green and Hayden [18] and Green, et al. [19] used the loading mode technique on a Ti-8wt%Al-1wt%Mo-1wt%V alloy in a saline environment, where HE has been clearly established to play a role in SCC, and on alpha-brass in an aqueous ammonia environment, where HE is believed to play no role in the cracking process. The TTF in Modes I and III was measured for each alloy-environment-experiment, and differences in TTF at a given normalized stress intensity -- K_I/K_{IC} and K_{III}/K_{IIIC} -- were taken as evidence that HE was operating. For the titanium-base alloy in the saline environment, the plot of normalized stress intensity versus TTF for Mode I revealed much greater susceptibility (shorter TTF) than that for Mode III (Fig. 1(a)). This is strong evidence of HE involvement in the SCC mechanism. For the alpha-brass in the aqueous ammonia environment, the normalized stress intensities versus TTF curves in Modes I and III were virtually coincident, indicating that HE was not operating (Fig. 1(b)).

With the validity of the test method demonstrated, Green et al. [19] then applied it to 7075 T6 aluminum alloy and found results similar to those for the titanium alloy, i.e., shorter TTF in Mode I than in Mode III (Fig. 1(c)). Furthermore, the addition of 10 ppm of As, a well-known hydrogen recombination inhibitor [23], increased embrittlement in Mode I and reduced embrittlement in Mode III. They rationalized that under Mode I loading, where hydrostatic stresses force the concentration of hydrogen to the region of triaxial stress ahead of the crack-tip, the addition of arsenic retards the kinetics of hydrogen evolution, thereby increasing hydrogen concentration within the metal, which enhances the hydrogen embrittlement. Under Mode III loading, however, where there is insufficient hydrostatic stress to cause the localized concentration of hydrogen, the slower dissolution mechanism takes precedence. In this experiment, the arsenic merely served to retard the cathodic reaction ($2H^+ + 2e^- \longrightarrow H_2$), which controls the rate of the overall dissolution process. Thus, the SCC mechanism in 7075 was shown to involve HE by a test that does not precharge hydrogen into the specimens.

SCC is most often intergranular in aluminum-base alloys [2], so the role of grain boundary (GB) segregation has been studied extensively to elucidate the cracking mechanism [24-31]. Furthermore, with HE clearly contributing to SCC, the issue of how hydrogen interacts with the grain boundary and the local segregation there clearly becomes important.

Early Segregation Studies

Most of the early work on GB segregation in Al-Zn-Mg alloys was performed using electron energy loss measurements and X-ray microanalysis on GB profiles in thin foils in a transmission electron microscope [24,26]. However, these techniques were limited in spatial resolution and, consequently, offered only limited information on the composition of the actual GB surface. Green and coworkers [27-31] endeavored to use the excellent surface sensitivity of Auger electron spectroscopy (AES) to obtain segregation information from the actual grain boundary. Specimens of several Al-Zn-Mg-Cu alloys were fractured under

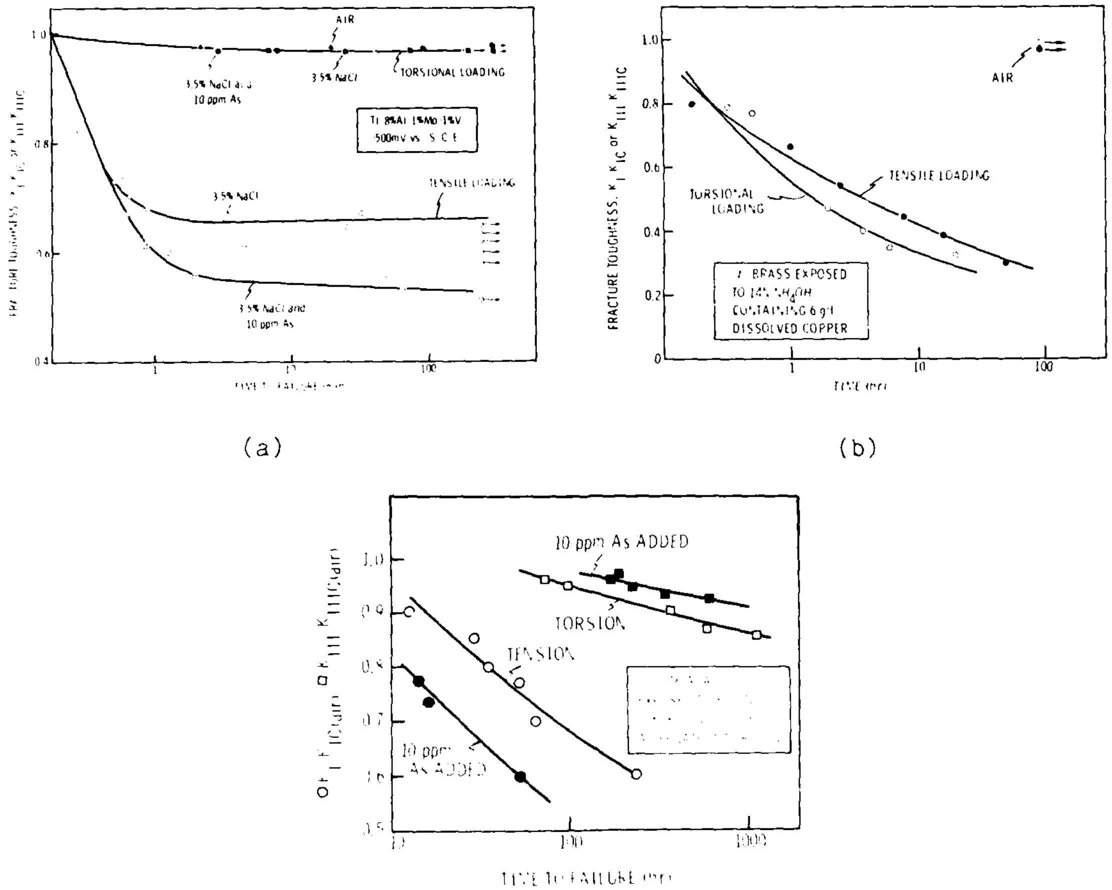

(a)

(b)

(c)

Fig. 1 - Influence of loading mode on the susceptibility of (a) Ti-8Al-1Mo-1V to SCC in various salt solutions, (b) α-brass exposed to tarnishing ammoniacal environments, and (c) 7075-T6 Al alloy to SCC in various saline solutions.

ultra-high vacuum (UHV) at approximately -194°C to produce intergranular fracture, and segregation was then measured by AES from the fracture surface. Information from each fracture was obtained to a depth of 3-6 atomic layers from about 6-8 grains under the electron beam, from which these investigators concluded that both Mg and Zn atoms segregate to the boundaries. The equilibrium GB precipitates in these alloys are $MgZn_2$, i.e., two Zn atoms for one Mg atom; however, the atomic concentration measurements revealed more Mg than Zn atoms, suggesting that some of the Mg atoms on the boundaries were not bound in the precipitates. The existence of this "free Mg" was further supported by measurements of the plasmon-loss energies of the Auger spectra, which indicated that in the solutionized, quenched, and aged temper, nearly all the Zn atoms, but only 40% of the Mg atoms, are in the GB $MgZn_2$ precipitates, leaving about 60% of the Mg atoms unbound in the interparticle space [30].

Viswanadham et al. [32] then extended these segregation studies to the surface oxide films on several Al-Zn-Mg alloys. They found that the film that forms during solutionizing -- i.e., the "thermal film" -- is enriched in Mg and contains mostly MgO, as opposed to Al_2O_3 as initially had been expected. Thus, Viswanadham et al. observed Mg segregation at the two critical regions of Al-Zn-Mg alloys pertinent to SCC: the GB and the surface oxide film.

Coupling this information with the great mutual affinity between Mg and H reported in the literature, they proposed in general terms the following Mg-H interaction mechanism of SCC. Mg and H atoms interact by forming a Mg-H complex which probably facilitates both hydrogen entry through the film and hydrogen accumulation on the boundaries, which then leads to embrittlement. Scamans independently proposed a similar Mg-H interaction mechanism of SCC in Al-Zn-Mg alloys [33].

Surface Oxide Film Studies

Pickens et al. [34-35] endeavored to determine whether the Mg-rich thermal film provides less protection than an alumina film. Such a comparison could not easily be made because the natural alumina film is typically 2.5 nm thick, whereas the thermal film is typically 200 nm thick. They compensated for this disparity by anodizing 200 nm thick alumina films on several specimen surfaces in tartaric acid. Specimens with comparable film thickness were tested and TTF was measured at various stress levels in the acetic acid-brine solution developed by Pistulka and Lange [36].

At the same thickness, TTF for the Mg-rich thermal film was about 50% shorter than that for the tartaric acid-anodized (TAA) Mg-free film -- Fig. 2 [35]. In fact, TTF for the 200 nm thermal film was similar to that for the 2.5 nm film that forms naturally after polishing. However, the Mg-rich film was subsequently found to be considerably more porous than the TAA film, so that the differences in TTF may not have been caused directly by the magnesium in the film, but possibly by the porosity of the thermal film resulting from Mg sublimation during solutionizing.

In subsequent work using surface science techniques, Pickens et al. [37] did not observe elemental Mg atoms in the thermal film; thus, it is unlikely that Mg would be available to form a Mg-H complex. Consequently, the reduced SCC resistance of the thermal film is probably caused primarily by its porosity.

In a follow-up investigation, Pickens et al. [38] studied the effect of surface oxide film thickness on SCC resistance, as measured by TTF in acetic acid-brine. Film thickness was varied from 2.5 to 200 nm by anodizing in tartaric acid at various voltages. SCC resistance (as measured by TTF) in-

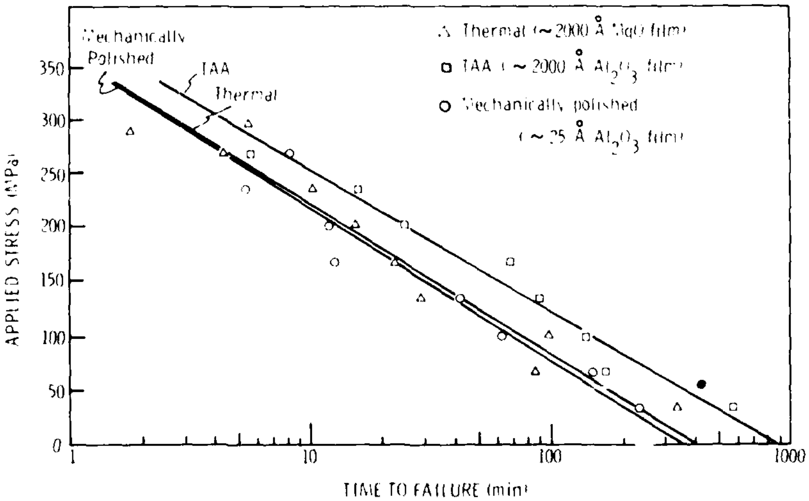

Fig. 2 - Comparison of susceptibility of Al6-4.4Zn-3.7Mg specimens with various oxide films.

creased with film thickness in the range of 2.5 to 200 nm. This information coupled with earlier work by Skoulikidis and Karageorgos [39-40] shows that SCC resistance increases with film thickness for smaller thicknesses (up to 0.2 μm, and from 1.7 to 3.4 μm) [39], but, in general, not for larger thicknesses.

Grain Boundary Fracture and Recent Segregation Studies

Pickens et al. [41-42] and Langan and Pickens [43] performed detailed investigations of GB segregation to further elucidate the SCC mechanisms in Al-Zn-Mg alloys. They examined the following three embrittlement techniques for exposing the grain boundaries for examination: (1) fracture at near-liquid nitrogen temperatures, (2) fracture after pre-exposure to liquid gallium (Ga_L) at ≈35°C for approximately 1 h, (3) fracture after pre-exposure to water-vapor saturated air (WVSA) at 100°C at 1 atmosphere (gauge). After each embrittlement procedure, specimens were fractured under ultra-high vacuum (UHV) and Auger measurements were then performed.

Fracture at near-liquid nitrogen temperature was intergranular, but at high magnifications, fine dimples were observed on the grain facets. Thus, the fracture was not entirely on the actual GB surface, but was most likely in the precipitate-free zone. Consequently, information obtained using this technique is, at least partly, not representative of the actual GB surface.

Gallium-induced liquid metal embrittlement (LME) of aluminum alloys is perhaps the most devastating embrittlement phenomenon for such alloys [44-46]. In fact, a Ga_L pre-exposed specimen can crumble intergranularly under its own weight. High-resolution scanning electron microscopy of Ga_L-embrittled Al-4.4wt%Zn-3.7wt%Mg specimens revealed intergranular fracture surfaces with no evidence of microdimpling up to a resolution limit of 3.0 nm [41-43]. Thus, Ga_L-embrittled fracture is believed to occur on the actual GB surface.

Unfortunately, Langan and Pickens [43] found that Ga interacts with the GB region such that measured Mg segregation increases with time after fracture. Furthermore, this effect is exacerbated at relatively poor vacuum levels (e.g., 1.33 μPa). In addition, the energies of several major Ga peaks in the Auger spectrum are similar to those for Zn, thereby making accurate Zn measurement difficult. Thus, pre-exposure to Ga_L does induce fracture on the actual GB surface, but also introduces difficulties in interpreting segregation measurements.

Numerous investigators [3,14-16] have found that pre-exposing Al-Zn-Mg alloys to liquid or aqueous environments reduces alloy ductility. Pickens, et al. [41-42] and Langan and Pickens [43] exposed various Al-Zn-Mg alloys to WVSA at 1 atmosphere (gauge) at 100°C. The specimens were severely embrittled, particularly in peak-strength tempers, and fracture was intergranular (Fig. 3(a)) with most regions appearing featureless (Fig. 3(b)) on a scanning electron microscope (SEM) with a resolution limit of 3.0 nm.

Hence, Langan and Pickens [43] concluded that hydrogen pre-exposure induces fracture on the actual GB surface and therefore is the most advantageous of the three techniques for exposing Al-Zn-Mg alloy boundaries for examination by AES.

Tuck [47] provided indirect evidence for the existence of the suspected Mg-H complex. He pre-exposed Al-Zn-Mg and Al-Mg alloy specimens to aqueous environments, and performed differential scanning calorimeter (DSC) scans on both the hydrogen-charged and uncharged specimens. In addition, he performed DSC scans on MgH_2. The charged specimens showed several exothermic peaks that were very similar to those observed for the MgH_2. However, not all the peaks observed for the MgH_2 were detected for the pre-exposed Al-Zn-Mg and Al-Zn specimens. Tuck interpreted these results as indirect evidence for the existence of the Mg-H complex in Al-Zn-Mg and Al-Mg specimens that were hydrogen charged. Furthermore, based on the great similarities between PEE and SCC [14,15], Tuck proposed that the Mg-H complex plays a role in the SCC mechanism.

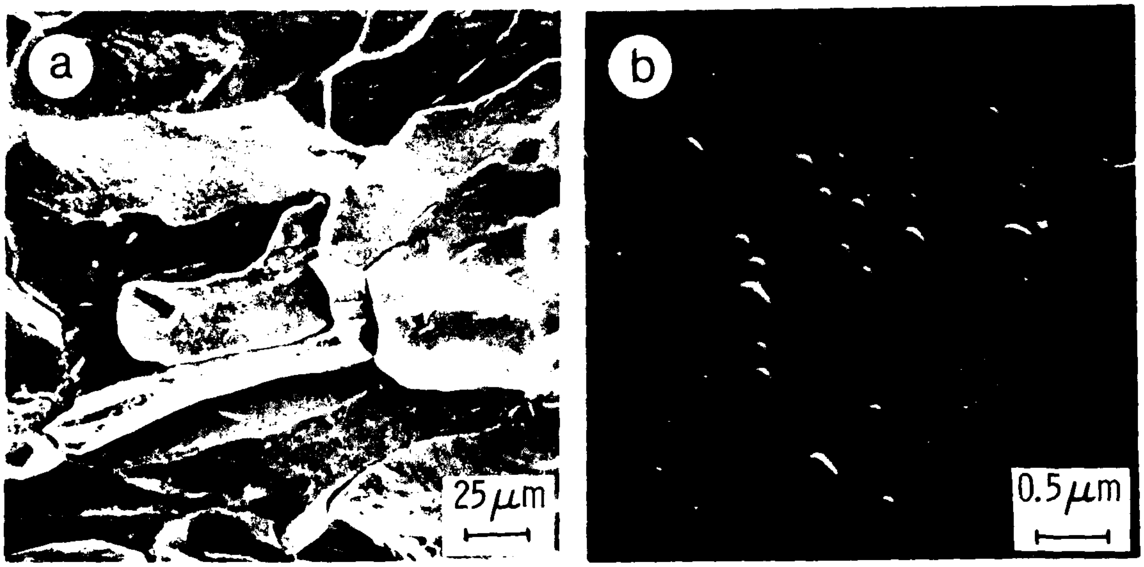

Fig. 3 - Al-Zn-Mg alloys pre-exposed to WVSA at 103 kPa gauge showing (a) induced intergranular fracture, and (b) its facets are often featureless at high magnifications.

To provide more conclusive evidence for the suspected Mg-H complex, Pickens et al. [37] cathodically charged Al-4.4wt%Zn-3.7wt%Mg specimens with hydrogen, fractured them under UHV, and performed high-resolution Auger scans to characterize the Mg spectrum. They had hoped to observe satellite peaks from which they could measure the plasmon loss energy (PLE). High-resolution survey scans were also performed on both MgH_2 and high-purity Mg as a basis for identifying PLE values in the charged specimens. Unfortunately, no MgH_2 satellite peaks could be discerned. In an attempt to identify a magnesium or an aluminum hydride, they also performed micro-diffraction on thin foil specimens of Al-4.4wt%Zn-3.7wt%Mg that were pre-exposed to distilled water. Unfortunately, no evidence for a hydride phase was found.

Following the failure of the sophisticated surface science techniques to elucidate the role of hydrogen and magnesium in cracking, Pickens and Langan [42,48] endeavored to seek unequivocal evidence for free Mg on the GBs of Al-Zn-Mg alloys, and to correlate its concentration with SCC susceptibility. The experiment they chose was to vary solution heat-treatment temperature (SHT) of an Al-Zn-Mg alloy, measure changes in GB segregation from in-situ fractures induced under UHV, measure SCC susceptibility as a function of SHT, and seek correlations between susceptibility and segregation.

For their experiment, they devised an extremely SCC-susceptible alloy composition -- Al-6.9wt%Zn-2.9wt%Mg-0.1wt%Zr (Al-3.0at%Zn-3.3at%Mg-0.03at%Zr) -- and carefully controlled thermo-mechanical processing and aging treatment to isolate SHT, and its effect on GB segregation, as a variable [42,48]. SCC susceptibility was assessed using precracked bolt-loaded double cantilever beam specimens in a chromate-inhibited brine solution [49]. SCC plateau velocity decreased with increasing SHT (Fig. 4(a)). The 100 nm probe of the scanning Auger microprobe (SAM) was placed on dimple-free intergranular facets, and Mg and Zn scans were obtained. The peak-to-peak heights were measured for Mg, Al, and Zn from the differentiated spectra, corrected using published sensitivity factors [50], and the following ratios were computed: Mg/(Mg+Zn+Al), Zn/(Mg+Zn+Al), and Al/(Mg+Zn+Al), where each symbol in these ratios signifies the corrected peak-to-peak height for the element.

Both Mg and Zn segregations were observed on the boundaries, and the segregation was similar for each SHT (Figs. 4(b) and 4(c)), with Mg/(Mg+Zn+Al) significantly greater on the boundaries than in the bulk. If it is assumed that all the Zn atoms on the boundaries are bound in the $MgZn_2$ precipitates, then the parameter (Mg - 1/2 Zn)/(Mg+Zn+Al) would be a measure of free Mg on the boundaries. Auger survey scans were made on a stoichiometric $MgZn_2$ crystal and verified that the Zn:Mg peak-to-peak ratio, corrected using published sensitivity factors, is 2:1. From the plot of the free Mg parameter versus SHT in Fig. 4(d), it is clear that there indeed is free Mg on the boundaries, and its concentration is essentially independent of SHT. We emphasize that we are assuming that free Zn does not exist, as claimed in earlier work [30]. Nevertheless, if some Zn atoms were not bound in the $MgZn_2$ precipitates, then there would be even more free Mg than is shown in Fig. 4(d).

The decrease in SCC susceptibility with increasing SHT is consistent with the work Taylor and Edgar [51] and Scamans [33], but opposite that of Vlasova et al. [53]. In addition, Joshi et al. [53] and Shastry et al. [54] found that SCC susceptibility passes through a minimum at a SHT of 438°C for an Al-Zn-Mg-Cu alloy -- results that differ from all of the above. There are many factors besides changes in segregation that can affect SCC susceptibility that could be altered by variations in SHT. For example, grain size can change by grain growth or static recrystallization. In addition, static recovery can change the substructure of the alloy. Along with these subtle changes, it must also be noted that none of these SHT studies was carried out on alloys with exactly the same composition. For example, the alloys had various Zn/Mg ratios, different total solute contents (wt%Zn + wt%Mg), and some alloys contained copper. Consequently, it would be easy to speculate on why different investigators have observed different trends in susceptibility with SHT. We can only emphasize that in the present work, we were as careful as possible in isolating SHT and its effect on segregation as an independent variable.

A correlation between SCC susceptibility and free Mg was not found [48], as would be expected from the proposed Mg-H interaction mechanism. Perhaps the boundaries were so saturated with free Mg that enough was present to contribute to the SCC mechanism, and the excess had no effect. Nevertheless, although the existence of free Mg on the GB of Al-Zn-Mg alloys has been unequivocally shown, the Mg-H interaction mechanism of SCC remains unproven.

As the evidence for the role of HE in the SCC mechanism of Al-Zn-Mg alloys became more extensive, Pickens et al. [55] endeavored to determine whether HE plays a role in the SCC of Al-Mg (i.e., 5XXX) alloys. In this alloy system, SCC was almost universally believed [2,56-59] to proceed by dissolution of the anodic Mg_2Al_3 (β) phase on the grain boundaries. The loading mode experiment advanced by Green et al. [19] was used with the following two improvements: specimens were precracked and crack velocity was measured in each mode.

Results of the experiments showed [55] that TTF was significantly greater in Mode III than Mode I, and that the addition of As, a hydrogen recombination inhibitor, decreased TTF in Mode I (Fig. 5). These findings show that HE is indeed involved in the SCC mechanism of 5XXX alloys, as shown earlier for 7XXX

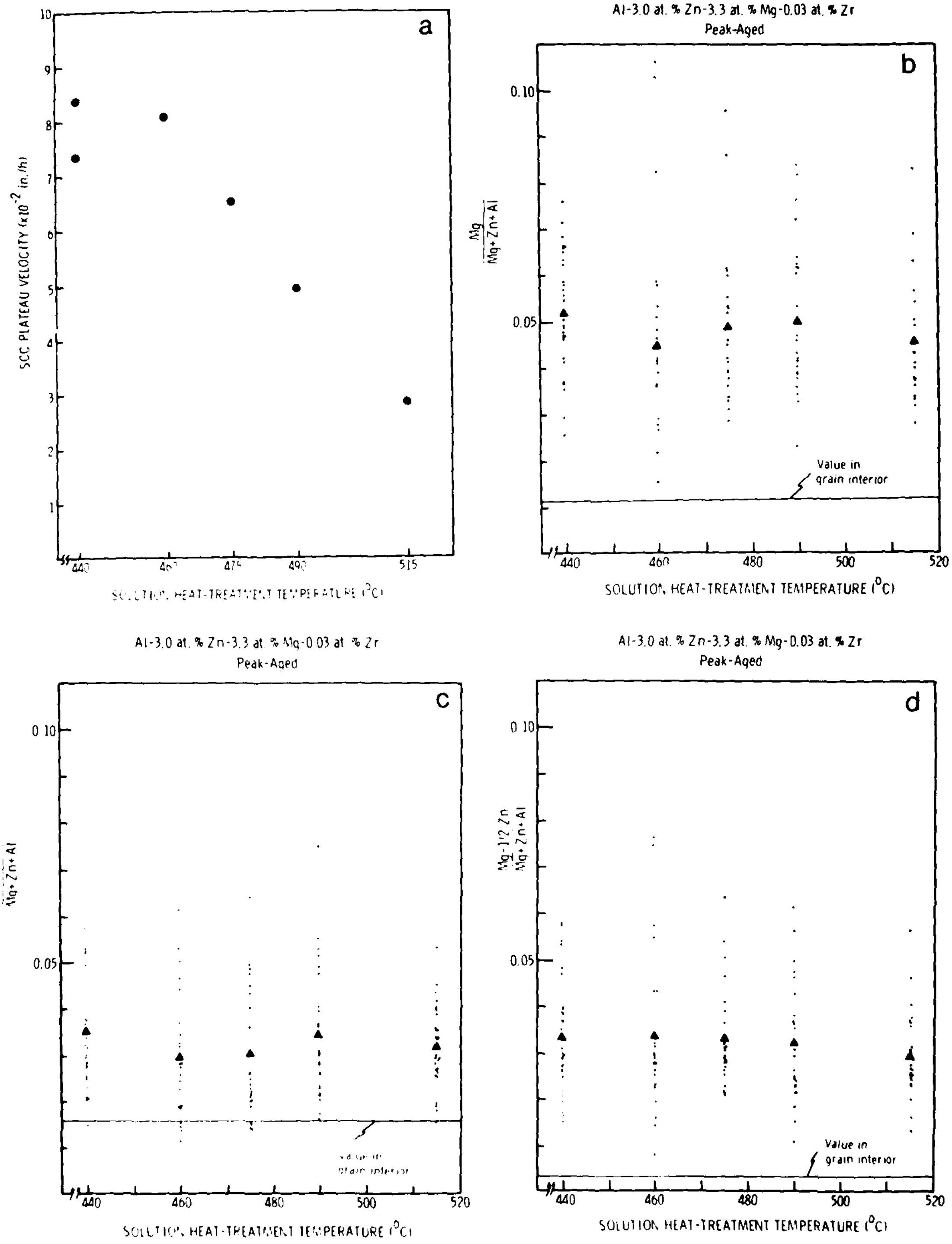

Fig. 4 - The influence of solution heat-treatment temperature on (a) SCC plateau velocity, (b) magnesium GB concentration, (c) zinc GB concentration, and (d) free magnesium parameter for Al-6.9Zn-2.9Mg-0.12Zr (wt%) alloy.

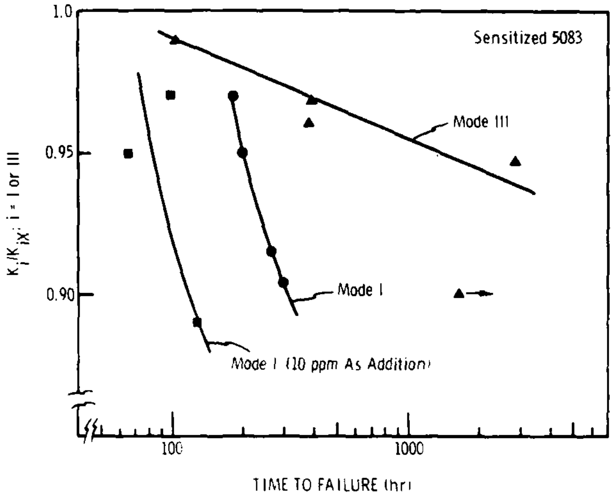

Fig. 5 - Normalized stress intensity versus TTF in Modes I and III for alloy 5083.

alloys. Furthermore, SC crack velocity in Mode III was an order of magnitude slower than that in Mode I -- in which there is no triaxial stress to concentrate hydrogen. Pickens et al. concluded that most of the crack advance during SCC is by HE, not dissolution. Thus, this research demonstrated that the conventional view of the SCC mechanism in 5XXX alloys is incorrect; SCC is not due solely to dissolution, but to a very different process -- cracking dominated by HE.

More recently, Pickens et al. [60] and Pickens [61] used the loading mode technique on Al-Zn-Mg powder metallurgy (P/M) alloy 7091 and found that SCC in this alloy is also dominated by HE.

Present View of the SCC Mechanism

After many years of studying SCC of Al-Zn-Mg and Al-Mg alloys at Martin Marietta Laboratories, we have developed the view of the SCC mechanism that is summarized in Fig. 6. This mechanism applies primarily to Al-Zn-Mg alloys, but is likely similar for Al-Mg alloys.

For SCC to occur, the surface oxide film must first be penetrated which most easily occurs at the coarse constituent particles and is facilitated by the presence of the Cl^- ion. Water -- either liquid or gaseous -- then has access to the exposed aluminum alloy. If liquid water contacts a GB-surface intersection, dissolution occurs in the GB region where anodic precipitates ($MgZn_2$ in 7XXX, Mg_2Al_3 in 5XXX) preferentially dissolve. We must emphasize that dissolution in the usual sense may not be a necessary condition for SCC. Montgrain and Swann [14] and Scamans [62] observed SCC in Al-Zn-Mg alloys exposed to moist air with no apparent evidence of dissolution on the SC fracture surface. Scamans performed the matching fractography to show that the $MgZn_2$ precipitates were still present on the fracture surface after cracking. In addition, Speidel [3] observed cracking at humidity levels too low to effect dissolution. Presumably, gaseous water can react with the exposed metal atoms as an adsorbed species, and produce hydrogen. We believe that it is the hydrogen produced as a result of adsorption and/or in dissolution reactions that is primarily responsible for cracking. This hydrogen enters

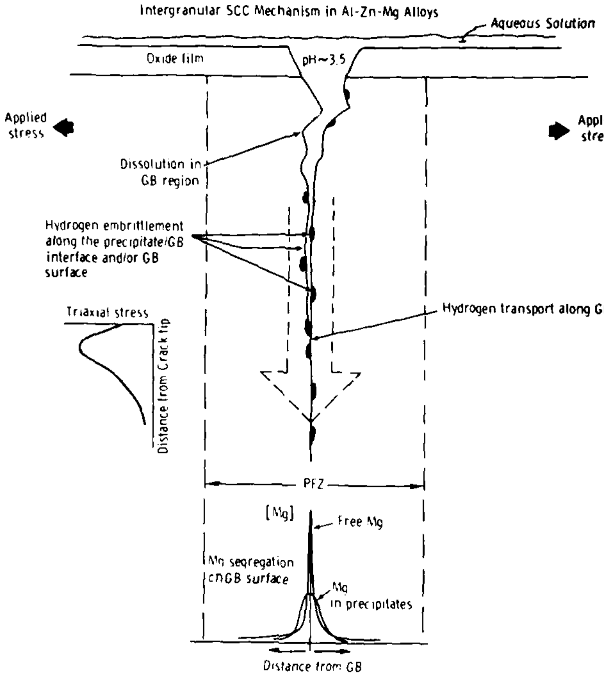
Intergranular SCC Mechanism in Al-Zn-Mg Alloys
Aqueous Solution
Oxide film
pH~3.5
Applied stress
Applied stress
Dissolution in GB region
Hydrogen embrittlement along the precipitate/GB interface and/or GB surface
Hydrogen transport along GB
Triaxial stress
Distance from Crack tip
PFZ
[Mg]
Free Mg
Mg segregation on GB surface
Mg in precipitates
Distance from GB

Fig. 6 - Schematic of SCC mechanism in Al-Zn-Mg alloys.

the alloy at GB-surface intersections and proceeds along the GB by interacting with the free Mg there. Although free Mg has not been shown to exist in Al-Mg alloys, we suspect its presence there based on the following observations of Scamans and Holroyd [63]. They provided indirect evidence for both the presence of free Mg on the boundaries of Al-Mg alloys and the role of Mg in SCC by showing far greater hydrogen permeation in as-quenched (i.e., minimal precipitation on GBs) Al-Zn-Mg and Al-Mg alloys than in as-quenched Al-Zn alloys and pure aluminum. Thus, only the Mg-containing alloys display rapid hydrogen permeation. The hydrogen collects at regions of triaxial tensile stress ahead of local fissures in the alloy and when the hydrogen concentration reaches a critical concentration, cracking occurs. This hypothesis is substantiated by the discontinuous crack growth during SCC of Al-Zn-Mg alloys reported by Scamans [64]. The mechanism* by which the hydrogen embrittles the GB is not known, but the following are plausible possibilities:

1. The hydrogen collects at the second-phase particle/GB interface, thereby embrittling the interface and serving to nucleate cracks.

2. A brittle hydride (i.e., Mg-H complex) forms on the GB surface.

---

*By mechanism, we refer to the microstructural features on the GBs that crack under the influence of H. It is also not known how H disturbs the atomic bonding of Al-Zn-Mg alloys -- e.g., by decohesion or facilitating dislocation nucleation.

3. The hydrogen collects along the entire boundary surface, thereby embrittling it.

4. Some combination of the above.

Number 1 is particularly intriguing because no one has unequivocally observed SCC in an alloy devoid of second-phase particles. Until recently, SCC has never been observed in Al-Zn-Mg or Al-Mg alloys without GB precipitates. Pickens et al. [65,66] recently demonstrated SCC in an Al-Mg-O-C P/M alloy that had no GB precipitates, but did have oxide (MgO, Al_2O_3) and carbide (Al_4C_3) particles on the boundaries. Thus, the presence of a second-phase particle/GB interface appears to be a necessary condition for SCC. Could a local triaxial stress state exist around such GB particles to cause high local concentrations of hydrogen and resulting embrittlement?

In summary, the SCC mechanism in these alloys is not completely understood. However, we do know that crack advance is largely a result of HE, that free Mg exists on the GBs -- the region where cracking occurs -- and that the presence of second-phase particles on the boundaries is likely a necessary condition for SCC.

Acknowledgements

The authors acknowledge with thanks the contributions to this work made over the past 18 years by Drs. E. N. Pugh, J. Sedriks, R. M. Latanision, W. Hayden, P. W. Slattery, R. Viswanadham, T. S. Sun, J. M. Chen, and L. Christodoulou, and Messrs. W. Montague, D. Venables, and J. R. Gordon. We are especially grateful to the insightful comments provided by Dr. G. M. Scamans. Most of all, we appreciate the unwavering support of contract monitor, Dr. P. Clarkin.

This work was supported by the Office of Naval Research under Contract No. N00014-84-C-0378.

References

1. M. O. Speidel: "Stress-Corrosion Cracking of Aluminum Alloy", Metall. Trans. A, 6A (1975) pp. 631-651.

2. D. O. Sprowls and R. H. Brown: "Stress Corrosion Mechanism for Aluminum Alloys", in Proceedings of the Conference on Fundamental Aspects of Stress Corrosion Cracking, R. W. Staehle, A. J. Forty, D. Van Rooyer, eds., pp. 466-506, discussion pp. 506-512, Ohio State University Press, Columbus OH, (1969).

3. M. O. Speidel, in The Theory of Stress-Corrosion Cracking in Alloys, J. C. Scully, ed., NATO, Brussels, (1971) pp. 289-344.

4. M. O. Speidel, and M. V. Hyatt: in Advances in Corrosion Science and Technology, 2, M. G. Fontana and R. W. Staehle, eds., Plenum Press, NY, (1972) pp. 115-335.

5. K. G. Kent: "Weldable Al:Zn:Mg Alloys", Review 147, Metallurgical Review, (1970).

6. R. V. Blewett: "Aluminum Alloys for Structural Use", FWP Journal, Jan. (1981), pp. 73-82.

7. E. H. Dix, Jr., "Acceleration of the Rate of Corrosion by High Constant Stresses", Trans. AIME, 137 (1940) p. 11.

8. R. B. Mears, R. H. Brown, and E. H. Dix: "A Generalized Theory of Stress Corrosion of Alloys", Symposium on Stress Corrosion of Metals, ASTM and AIME, (1944) p. 329.

9. A. J. Jacobs: "The Role of Dislocations in the Stress-Corrosion Cracking of 7075 Aluminum Alloy", Trans. ASM, 58, (1965) pp. 579-600.

10. A. J. Sedriks, J. A. S. Green, and D. L. Novak: "Comparison of the Corrosion and Stress-Corrosion Behavior of a Ternary Al-Zn-Mg Alloy", Metall. Trans., 1, (1970) pp. 1815-1819.

11. A. J. Sedriks, J. A. S. Green, and D. A. Novak: "Corrosion Processes and Solution Chemistry within Stress-Corrosion Cracks in Aluminum Alloys", in Localized Corrosion, NACE-3, (1974) pp. 569.

12. A. J. Sedriks, J. A. S. Green, and D. A. Novak: "On the Chemistry of the Solution at Tips of Stress-Corrosion Cracks in Al Alloy", 27(5) (1971) pp. 198-202.

13. W. Gruhl: Z. Metallkd., 54 (1963) p. 86.

14. L. Montgrain and P. R. Swann: "Electron Microscopy of Hydrogen Embrittlement in a High Purity Al-Zn-Mg Alloy", in Hydrogen in Metals, Proceedings of an International Conference on the Effects of Hydrogen on Materials Properties and Selection and Structural Design, ASM, Champion, PA (1973) pp. 575-584 .

15. G. M. Scamans, R. Alani, and P. R. Swann: "Pre-exposure Embrittlement and Stress Corrosion Failure in Al-Zn-Mg Alloys", Corros. Sci., 16(7) (1976) p. 443.

16. M. O. Speidel: "Hydrogen Embrittlement of Aluminum Alloys?" in Hydrogen in Metals, Proceedings of an International Conference on the Effects of Hydrogen on Materials Properties and Selection and Structural Design, I. M. Bernstein and A. W. Thompson, eds., ASM, Champion, PA, (1973) pp. 23-27.

17. R. J. Gest and A. R. Troiano: "Stress Corrosion and Hydrogen Embrittlement in an Aluminum Alloy", Corrosion - NACE, 30(8) (1974) p. 274.

18. J.A.S. Green and H. W. Hayden: in Hydrogen in Metals, I. M. Bernstein and A. W. Thompson, eds., ASM, Metals Park, OH (1974) pp. 235-244.

19. J.A.S. Green, H. W. Hayden, and W. G. Montague: "The Influence of Loading Mode on the Stress Corrosion Susceptibility of Various Alloy/Environment Systems", in Effect of Hydrogen on Behavior of Materials, A. W. Thompson and I. M. Bernstein, eds., AIME, Philadelphia, PA (1975) p. 200.

20. H. W. Hayden and S. Floreen: "Effect of Various Modes of Loading on Stress Corrosion Cracking of Maraging Steel", Corrosion-NACE, 27(10) (1971) p. 429.

21. C. St. John and W. W. Gerberich: Metall. Trans. A, 4 (1973) pp. 589-594.

22. R. E. Swanson, A. W. Thompson, I. M. Bernstein, and J. L. Maloney, III: in Hydrogen Effects in Metals, TMS-AIME, Warrendale, PA, (1980) pp. 459-466.

23. R. E. Swanson, I. M. Bernstein, and A. W. Thompson: Scripta Met., 16 (1982) pp. 321-324.

24. P. Doig and J. W. Edington: "Influence of Precipitate-Free Zones on the Stress-Corrosion Susceptibility of a Ternary Al-5.9wt%Zn-3.2wt%Mg Alloy", Corrosion-NACE, 31(10) (1975) pp. 347-352.

25. P. Doig and J. W. Edington: "Stress-Corrosion Susceptibility of As-Quenched Al-5.9wt%Zn-3.2wt%Mg Alloys", Br. Corros. J., (Quarterly) 9(4) (1974) pp. 220-222.

26. P. Doig, J. W. Edington, and G. Hibbert: "Measurement of Mg Supersaturations within Precipitate-Free Zones in Al-Zn-Mg Alloys", Philos. Mag., 20 (1973) pp. 971-981.

27. J.A.S. Green and W. G. Montague: "Observations on the Stress Corrosion Cracking of an Al-5%Zn-2.5%Mg Ternary and Various Quarternary Alloys", Corros., 31(6) (1975) p. 209.

28. J. M. Chen, T. S. Sun, R. K. Viswanadham, and J.A.S. Green: "Grain Boundary Segregation of an Al-Zn-Mg Ternary Alloy", Metall. Trans. A., 8A (1977) pp. 1935-1940.

29. J.A.S. Green, R. K. Viswanadham, T. S. Sun, and W. G. Montague: "Grain Boundary Segregation and Stress Corrosion Cracking of Aluminum Alloys", in Corros./77, Int. Corros. Forum, Paper 17, Nat'l. Assoc. Corros. Eng., San Francisco, CA, (1977) p. 17/1.

30. T. S. Sun, J. M. Chen, R. K. Viswanadham, and J.A.S. Green: "Plasmon-Loss Satellites in Auger Spectra of Alloy Surfaces", Appl. Phys. Lett., 31(9) (1977) p. 580.

31. R. K. Viswanadham, T. S. Sun, and J.A.S Green: "Grain Boundary Segregation in Al-Zn-Mg Alloys -- Implications to Stress Corrosion Cracking", Metall. Trans. A, 11A (1980) p. 85.

32. R. K. Viswanadham, T. S. Sun, and J.A.S. Green: Corrosion NACE, 36(6) (1980) pp. 275-278.

33. G. M. Scamans: "Intergranular Stress-Corrosion Cracking of Aluminum Alloys by Hydrogen or by Liquid Metal Embrittlement", in Environmental Degradation of Engineering Materials in Aggressive Environments, M. R. Louthan, Jr., R. P. McNitt, and R. D. Sisson, Jr., eds., Proceedings of Conf., Virginia Polytechnic Institute Press, Blacksburg, VA (1981) pp. 153-162.

34. J. R. Pickens, D. Venables, and J.A.S. Green: "The Delayed Fracture of Aluminum Alloys", End-of-Year Report for ONR Contract No. N00014-74-C0277, P0007, Martin Marietta Laboratories, January 1981.

35. J. R. Pickens, D. Venables, and J.A.S. Green: "Improved SCC Resistance of Al-Zn-Mg Alloys by Control of Mg Content in the Bulk Metal and in the Oxide Film", in Hydrogen Effects in Metals, I. M. Bernstein and A. W. Thompson, eds., AIME, (1981) pp. 513-523.

36. W. Pistulka and G. Lang, Aluminium (Dusseldorf), 53 (1979) p. 366.

37. J. R. Pickens, D. Venables, J. R. Gordon, L. Christodoulou, and G. D. Davis: "The Delayed Fracture of Aluminum Alloys", Progress Report for ONR, Contract No. N00014-820C-0342, Martin Marietta Laboratories, April 1982.

38. J. R. Pickens, D. Venables, and J.A.S. Green: "Effect of Tartaric Acid-Anodized Film Thickness on Susceptibility to Stress-Corrosion Cracking of Al-4.4wt%Zn-3.7wt%Mg", Br. Corros. J., 16(4) (1981) pp. 196-197.

39. Th. Skoulikdis and Karageorgos, Ath., Br. Corros. J., 10 (1975) p. 17.

40. Th. Skoulikdis and Karageorgos, Ath., Br. Corros J., 15 (1980) p. 41.

41. J. R. Pickens, T. J. Langan, G. D. Davis, L. Christodoulou, and L. Struble: "The Delayed Fracture of Aluminum Alloys", End-of-Year Report, No. MML-TR-83-11c, Contract No. N00014-82-C-0378, Martin Marietta Laboratories, March 1983.

42. J. R. Pickens and T. J. Langan: "The Delayed Fracture of Aluminum Alloys", Progress Report, Contract N00014-83-C-0380, Martin Marietta Laboratories, June 1985.

43. T. J. Langan and J. R. Pickens: "Intergranular Fracture of Al-Zn-Mg Alloys in Embrittling Environments", to be submitted to Mater. Sci. and Engin.

44. C. Roques-Carmes, M. Aucouturier, and P. Lacombe: Metall. Sci. J., 7 (1973) p. 128.

45. C. M. Preece and A.R.C. Westwood: Trans. Amer. Soc. Met., 62 (1969) p. 48.

46. J. R. Pickens, W. Precht, and A.R.C. Westwood: "Embrittlement of P/M X7091 and I/M 7175 Aluminum Alloys by Mercury Solutions", J. Mater. Sci., 18 (1983) pp. 1872-1880.

47. C. D. S. Tuck: "Evidence for the Formation of Magnesium Hydride on the Grain Boundaries of Al-Mg and Al-Zn-Mg Alloys During Their Exposure to Water Vapour", in Hydrogen Effects in Metals, A. W. Thompson and I. M. Bernstein, eds., AIME, Philadelphia, PA, (1979) pp. 503-511.

48. J. R. Pickens and T. J. Langan: "The Effect of Solution Heat Treatment Temperature on Grain Boundary Segregation and Stress Corrosion Cracking in Al-Zn-Mg Alloys", to be submitted to Metall. Trans. A.

49. D. O. Sprowls, M. B. Shumaker, J. W. Coursen, and J. D. Walsh: "Evaluations of Stress Corrosion Cracking Susceptibility Using Fracture Mechanics Techniques", Alcoa Technical Center, Pittsburgh, PA, Final Report, Part I (period July 1, 1968-August 31, 1972), Contract No. NAS 8-21487, George C. Marshall Space Flight Center, May 31, 1973.

50. Handbook of Auger Electron Spectroscopy, Second Edition, Physical Electronics Division, Perkin-Elmer Corp., Eden Prairie, Minnesota, 1978.

51. I. T. Taylor and R. L. Edgar: "A Study of the Stress-Corrosion Cracking in Al-Zn-Mg Alloys", Metall. Trans., 2 (1971) pp. 833-839.

52. T. A. Vlasova, E. K. Zenkova, L. N. Polyakova, and V. E. Silis: "Effect of Temperature and Rate of Quenching on the Properties of Al-Zn-Mg Alloys", Fiz. Metal. Metalloved., 23(2) (1967) pp. 357-359.

53. A. Joshi, C. R. Shastry, and M. Levy: "Effect of Heat Treatment on Solute Concentration at Grain Boundaries in 7075 Aluminum Alloy", Metall. Trans. A, 12A (1981) pp. 1081-1088.

54. C. R. Shastry, M. Levy, and A. Joshi: "The Effect of Solution Treatment Temperature on Stress-Corrosion Susceptibility of 7075 Aluminum Alloy", Corrosion Sci., 21(9) (1981) pp. 673-688.

55. J. R. Pickens, J. R. Gordon, and J.A.S. Green: "The Effect of Loading Mode on the Stress-Corrosion Cracking of Aluminum Alloy 5083", Metall. Trans. A, 14A (1983) pp. 925-930.

56. U. R. Evans: The Corrosion and Oxidation of Metals: Scientific Principles and Practical Applications, Edward Arnold Pub. Ltd., London, (1956) pp. 665-681.

57. E. C. W. Perryman: "Metallurgical Aspects of Stress Corrosion Cracking in Aluminum Alloys", in Stress Corrosion Cracking and Embrittlement, W.D. Robertson, ed., Symposium of Electrochem. Soc., Boston, October 1954, John Wiley and Sons, NY (1956) pp. 61-80.

58. U. R. Evans: "On the Mechanism of Chemical Cracking", in Stress Corrosion Cracking and Embrittlement, W. D. Robertson, ed., John Wiley and Sons, NY, 1956.

59. R. W. Revie: "Stress-Corrosion of Aluminum Alloys - A Review", Australian Corrosion Association 15th Annual Conference, Tasmania, Nov. 11-15, 1974.

60. J. R. Pickens, J. R. Gordon, and L. Christodoulou: "Stress-Corrosion Cracking and Hydrogen Embrittlement in P/M X7091 and I/M 7075", in High Performance Aluminum Powder Metallurgy, M. J. Koczak and G. J. Hildeman, eds., TMS-AIME, (Nov. 1983) pp. 177-192.

61. J. R. Pickens: "Techniques for Assessing the Corrosion Properties of Aluminum Powder Metallurgy Alloys", accepted for publication in Proceedings of the Conference, Rapidly Solidified Powder Aluminum Alloys, ASTM Committee B-9, Philadelphia Centre Hotel, Philadelphia, PA, 4-5 April 1984.

62. G. M. Scamans: "Discontinuous Propagation of Stress-Corrosion Cracks in Al-Zn-Mg Alloys", Scripta Metall., 13 (1979) pp. 245-250.

63. G. M. Scamans and N.J.H. Holroyd: Alcan Banbury Research Lab, Private Communication with J. R. Pickens, Sept. 1984.

64. G. M. Scamans: "Evidence for Crack-Arrest Markings on Intergranular Stress-Corrosion Cracks in Al-Zn-Mg Alloys", Metall. Trans. A, 11A pp. 846-850.

65. J. R. Pickens, L. Christodoulou, and T. J. Langan: "Stress-Corrosion Cracking of Aluminum Alloys from RS and Mechanically Alloyed Powders", Final Report on Army Research Office Contract No. DAAG-29-81-C-0031, Martin Marietta Laboratories, November 1983.

66. J. R. Pickens and L. Christodoulou: "The Stress-Corrosion Cracking Behavior of High-Strength Aluminum Powder Metallurgy Alloys", accepted for publication in Metall. Trans. A.

MODELING

CHEMICAL FACTORS IMPORTANT TO ENVIRONMENTALLY SENSITIVE FRACTURE

Jerome Kruger
Materials Science and Engineering
The Johns Hopkins University
Baltimore, Maryland 21218
USA

Over the past 15-20 years have come a refinement and sharpening of our ideas of the role of chemistry, in general, and electrochemistry, in particular, in environmentally sensitive fracture (ESF). These ideas have flowed out of some of the earlier concepts put forward by Logan [1] and Champion [2]. A number of workers have contributed to our present understanding of the role of chemical factors in ESF and a good review of these developments is given by Ford [3]. All of the models of chemical or electrochemical influences on ESF involve two competing processes, the breakdown of surface films (considering the role of alloy and environment chemistry on the film properties that affect breakdown) and the repair or repassivation of surface films (considering the role of alloy and environmental chemistry on the rate of depassivation). This paper describes ONR supported work, initiated by Dr. Philip Clarkin, that has been aimed at providing insights into the chemical and electrochemical influences on these competing processes for ductile alloys.

Film Breakdown Processes

Two kinds of chemical factors affecting the breakdown of surface films will be discussed, the influence of chemistry on film properties important to breakdown and the effect of environmental and alloy chemistry on film breakdown processes.

Film Properties

Pugh [4] in a recent review pointed out that "a brittle crack can be initiated in a thin surface film and attain a velocity sufficient to propagate, as a cleavage crack, for significant distances into the unaffected substrate". This idea was based on concepts developed at Brookhaven National Laboratory [5]. While Pugh was concerned mainly with trying to explain the transgranular ESF of pure copper, a very ductile FCC metal, this concept may also apply to some early ONR supported work [6] on the intergranular cracking of pure copper. That work was started to evaluate the role played by oxide film formation on the SCC of copper and its alloys.

It was pointed out that a study by Green, Mengelberg, and Yolken [7] had shown that the rate for formation of a tarnish film on copper and copper-zinc alloys in tarnishing ammoniacal solutions increases with the percentage of zinc. It is also known that the rate of cracking of α-brass in these ammoniacal environments increases significantly with increasing zinc content [8]. One theory of stress corrosion cracking (SCC), the "brittle-film" model of Forty and Humble [9], suggests that the rate of tarnish film formation determines the rate of cracking. The study by Green et al. showed that pure copper, which is nonsusceptible, does have a low rate of film formation in the tarnishing solution they used. If the predictions of the brittle-film model are valid, pure copper should crack in an environment that produces a similar film to that in the ammonia tarnishing solutions provided the rate is comparable to that observed for the susceptible α-brasses. Such environments are the cupric ion solutions (mostly cupric acetate and cupric sulfate) studied by Miller and co-workers [10]. These solutions produce epitaxial Cu_2O films on copper that are similar to those that form in ammonia solutions on α-brass. They also grow on pure copper at a rate that is comparable to a susceptible brass (90 Cu-10 Zn). Thus, the brittle-film model would predict that pure copper should crack in Miller's solution. The Escalante and Kruger study sought to determine if such cracking could be observed [6].

Escalante and Kruger found that both 99.9 and 99.999% purity copper will crack in an environment where the rate of tarnish film formation is comparable or greater than the rate of tarnish for susceptible brasses. Their results also indicated that cracking occurs in the oxide that forms by growth into the grain boundaries (Fig. 1). To discuss the meaning of the phenomena observed in connection with the formation of the oxide film, it is necessary to look at the electrochemical theory of copper corrosion as worked out by Ives and Rawson [11]. They proposed that the copper-cuprous oxide-solution system can be divided into three zones: zone 1 is made up of a compact, adherent film of Cu_2O and the copper substrate; zone 2 is a porous film of Cu_2O and zone 3 is the aqueous solution containing oxygen. Each of these zones has associated with it half-cell reactions. The half-cell reaction for zone 1 is the film growth process

$$Cu^\circ + 1/2\ H_2O \rightarrow 1/2\ Cu_2O + H^+ + e^- \qquad (1)$$

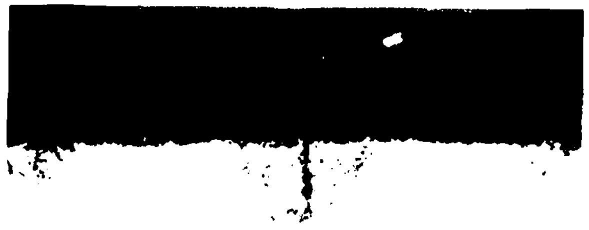

Fig. 1 - 99.9% copper specimen with cracks in oxide. Stressed in 0.05N cupric acetate. Magnification, 865X. From [6].

Both film growth and film dissolution occur in zone 2 and are regarded by Ives and Rawson as constituting a hypothetical redox electrode. These reactions are

$$Cu^{2+} + 1/2\ H_2O + e^- \rightarrow 1/2\ Cu_2O + H^+ \qquad \text{(film growth)} \qquad (2a)$$

$$1/2\ Cu_2O + H^+ \rightarrow Cu^{2+} + 1/2\ H_2O\ e^- \qquad \text{(film dissolution)} \qquad (2b)$$

Finally, the half-cell reaction at zone 3 is

$$1/4\ O_2 + H^+ + e^- \rightarrow 1/2\ H_2O \qquad (3)$$

The whole system of electrode reactions can be regarded as two cells coupled to each other, reactions (1) and (2a) are anodic and cathodic reactions, respectively, involving film dissolution.

This set of half-cell reactions was applied to four situations pertinent to the results obtained:

Film formation in the absence of light and stress. The results showed film growth over the entire surface. The film growth observed was simply a combination of reactions (1) and (2a),

$$Cu^\circ + Cu^{2+} + H_2O \rightarrow Cu_2O + 2H^+ \qquad (4)$$

or if all four reactions of Ives and Rawson are used

$$Cu^\circ + 1/4\ O_2 = 1/2\ Cu_2O \qquad (5)$$

Both Porterfield and Miller [10] and Green et al. [7] require a porous film to provide access of Cu^{++} or O_2 to the copper substrate. If there is a compact film at the substrate (zone 1) and it is sufficiently thin, rapid solid-state diffusion through it may be a possibility.

Film formation with stress applied in the absence of light. The results showed enhanced film growth at the grain boundaries normal to the direction of stress and diminished film growth elsewhere. To arrive at an explanation of these results it was necessary to determine which of the combinations of reactions (1), (2a), (2b), and (3) predominated in their contribution to the overall corrosion current. When there was no stress and when growth of Cu_2O was observed over the entire specimen, apparently the combination of reactions (1) and (2a) and/or (1) and (3) resulted in growth both in the grain interiors and in the boundaries. When stress was applied, very small areas of metallic copper were exposed by rupture of the Cu_2O film at the grain boundary, and reaction (1), because it involves metallic copper, predominated in the boundaries and was polarized to higher potentials than with no stress. This occurs because the current density at the bare sites must be high as a result of the small areas involved as compared to the large uncracked cathodic areas. Because stress probably makes reaction (1) the predominant growth reaction in the grain boundaries and causes oxide dissolution to occur in the interiors of the grains, it is reasonable to speculate that the current density for the growth reaction in the grain interiors decrease and the dissolution reaction ((2a) plus (3)) takes over.

Role of Illumination. Ives and Rawson [12] showed that illumination results in enhanced corrosion of copper with greater concentrations of Cu^{2+} ions found in the corroding media. Kruger and Calvert [13] showed that the effect of the light was to cause a dissolution of a Cu_2O film present on the surface. This means that reaction (2b) predominates. Thus, it appears that light retards or stops the growth of the Cu_2O that forms in the grain boundaries and, by doing so, retards or stops the cracking process.

From chemical and electrochemical considerations, Escalante and Kruger concluded that failure results under those circumstances which promote oxide formation at grain boundaries. This oxide formation in a sense results in a dissolution of copper from the grain boundary but it is not the same as simple dissolution without formation of oxide. Such dissolution (probably enhanced) can occur when copper is illuminated. This occurs because of an important property of the Cu_2O film. It is a p-type photo-conducting semi-conductor which, when illuminated, will cause a flow of electrons in a direction to favor the film dissolution reaction (2b) [14]. However, because oxide formation is retarded or stopped in the grain boundaries, no cracking results. These experiments showed that film formation is necessary for ESF and it appears that the brittle film theory of Forty and Humble [3] fits the results. It also seems reasonable that the complex relationships between the mechanical properties of the film, as affected by the metal and the environment, and the rate of film formation in the grain boundaries play a role. Kruger and Escalante in ONR sponsored work [15] showed that this was indeed so. They showed that metals more susceptible to ESF (for example, Al, in Fig. 2(a)) had films that were considerably less ductile than those less susceptible (for example Ta, Fig. 2(b)). This agreed with earlier work by Bubar and Vermilyea [16] who used an electrochemical technique.

Environment and Alloy Chemistry

Brown [17] pointed out the important role played by the chemistry of the environment in an "occluded cell" (such as that in a crack, pit, or crevice) on ESF. Kruger and Ambrose [18] developed an ellipsometric technique for examining the film breakdown processes occurring in an "occluded cell" that can lead to ESF.

They described how ellipsometry can be applied to the study of processes occurring inside an occluded cell by creating a crevice with a glass plate on top of the metal surface to be studied (Fig. 3). Use of such transparent windows for visual observation of a crevice is not new, but the results from

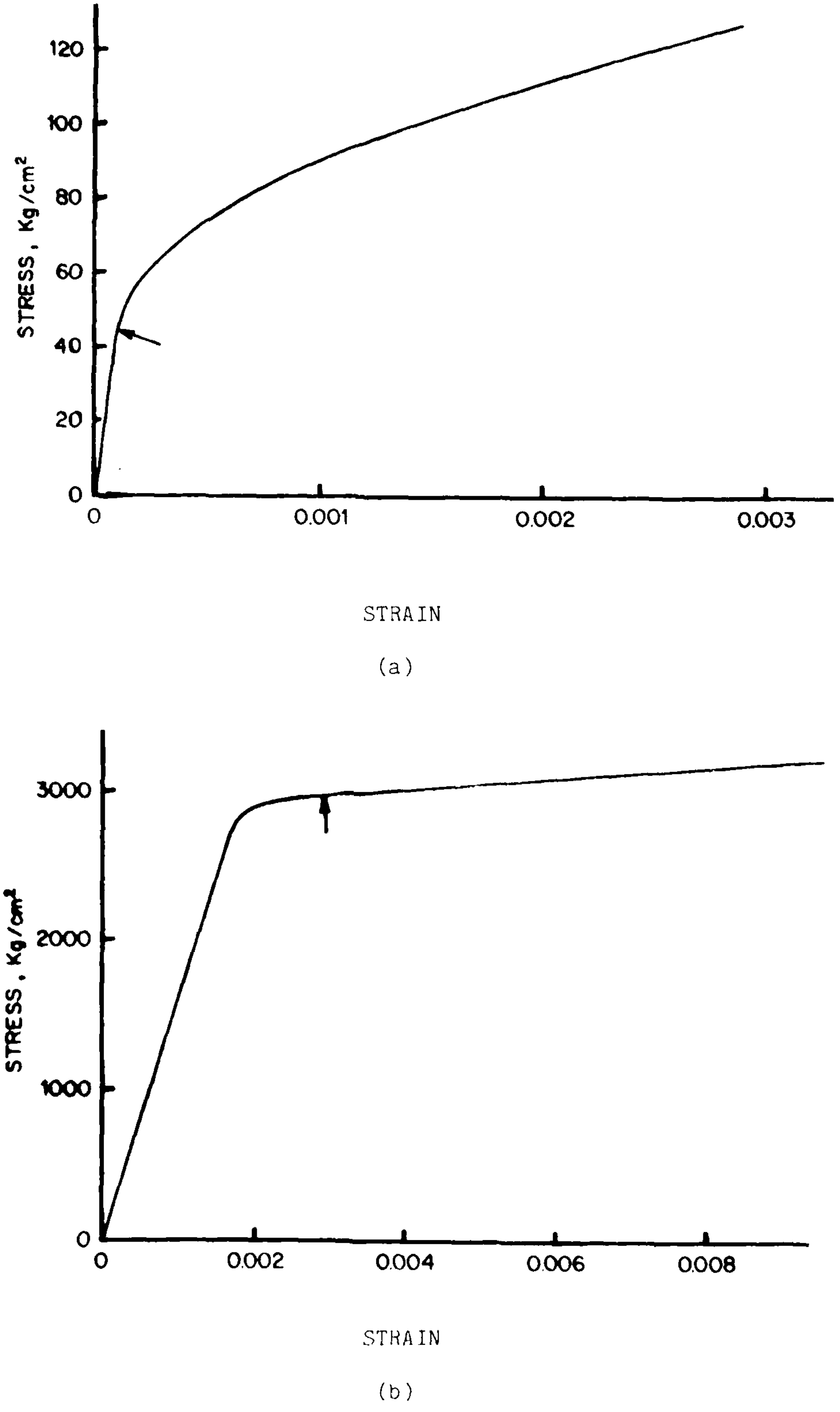

Fig. 2 - Stress strain curves for (a) Al and (b) Ta. Arrows indicate the strain at which the oxide films on these metals fractured. From [15].

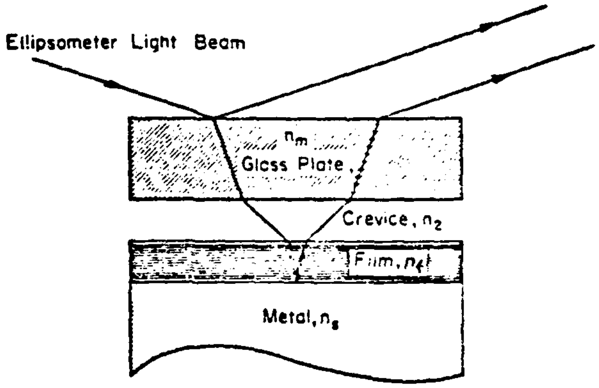

Fig. 3 - Model of the crevice system showing refraction of polarized light in various media. From [18].

such studies have been limited to detection of crevice corrosion in its advanced stages. The optical technique of ellipsometry, however, permits measurement of small changes in thickness and optical properties of surface films on metal substrates in the occluded cell environment.

Typical results from such an approach are shown in Fig. 4. It can be seen from this figure that three stages lead to film breakdown (low film repair rates) for 304 stainless steel:

(i) The initial decrease in Δ (the relative phase retardation, the ellipsometric parameter that is sensitive to film thickness and surface roughness changes) may correspond to the *concentration of metal and chloride* ions leading to an increase in the refractive index of the solution in the crevice

(ii) The subsequent increase in Δ may correspond to film thinning

(iii) The final decrease in Δ may correspond to both metal roughening and corrosion product deposition.

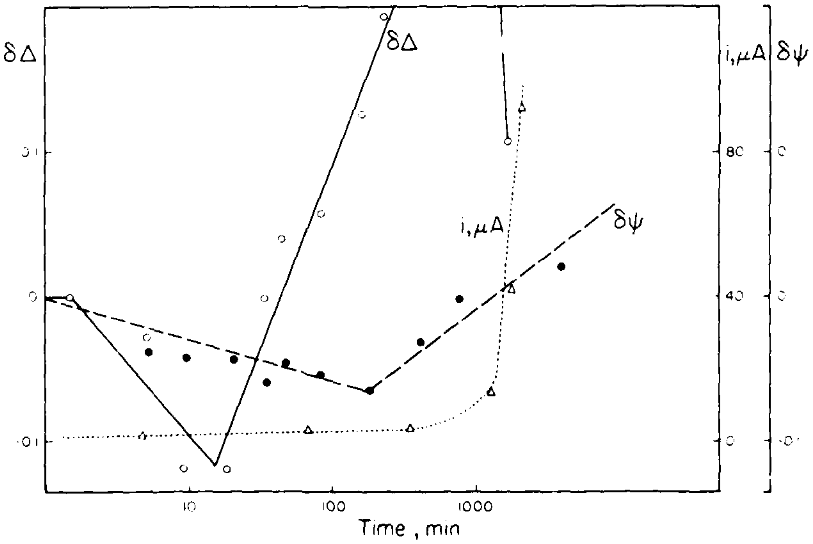

Fig. 4 - Effect of a crevice on ellipsometer parameters Δ and ψ, and the corrosion current as a function of $\log_{10}$ time for 304 stainless steel in 1.0N NaCl; specimen is potentiostated at +42 mV SHE. From [18].

In contrast, for a Ti alloy that does not suffer crevice corrosion, a constancy of ellipsometric and current measurements over the entire exposure period indicates that none of the crevice solution concentration effects which were detected for the susceptible 304 stainless steel had occurred. Figure 5 shows how alloying constituents affect the first stage (i) for a stainless steel and thereby their effect on the film breakdown processes that lead to the initiation of ESF.

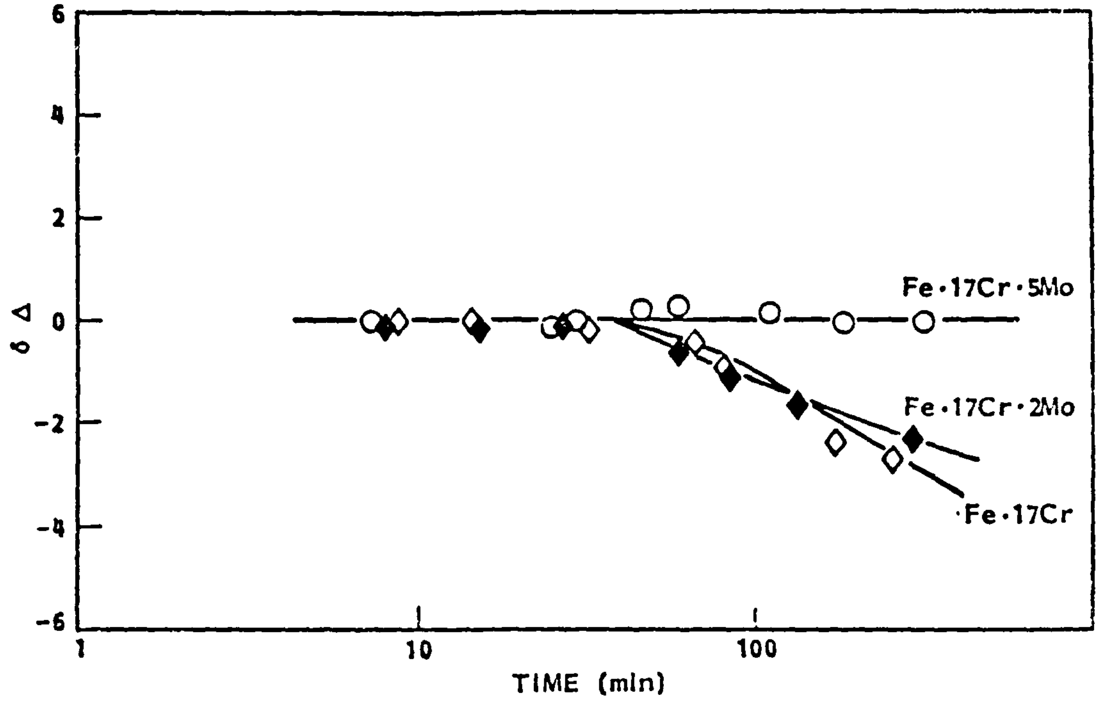

Fig. 5 - Change in Δ vs. $\log_{10}$ time for Fe-17Cr (-49 mV SHE), Fe-17Cr-2Mo (-62 mV SHE), and Fe-17Cr-5Mo (+20 mV SHE). From [19].

Film Repair Processes

The protective layer that exists on all technologically useful metal surfaces serves as a barrier to environmental attack. Film breakdown processes, mechanical and/or chemical in nature, result in the breaching of this barrier. Film repair or repassivation processes determine whether the "gate" opened by breakdown can be closed rapidly enough to limit the entry of hydrogen into the metal or the exit of metal ions into an aqueous solution.

This section will discuss three aspects of the factors involved in film repair that affect ESF susceptibility:

(a) the delicate balance between metal dissolution and film repair rate;
(b) the relation of film repair rate to the ESF mechanism; and
(c) the role of pH.

Delicate Balances

Work by Ambrose and Kruger [20] on the relationship between repassivation kinetics and the stress corrosion cracking (SCC) of low carbon steel illustrates the delicate balance between metal dissolution and film repassivation rate. Engell [21] pointed out that the relation of the rates of these two processes to each other has an important bearing on SCC susceptibility. The basis for this assumption is that, upon stressing, the protective film on the metal surface fractures, and unless its repair is sufficiently fast, metal dissolution occurs at the film fracture site leading to crack initiation. In other words, it is the delicate balance between film repair and metal dissolution that determines stress corrosion susceptibility.

Ambrose and Kruger [20] under ONR sponsorship developed a technique, triboellipsometry [22], to provide a measure of the relationship of repassivation to metal dissolution. They defined a parameter that contains this information and explored how this parameter was related to SCC susceptibility. This parameter R_p was defined in a manner that is convenient for triboellipsometric measurements as the ratio

$$R_p = \frac{\int_0^t i_t dt}{x_t} \tag{6}$$

where i_t is the total anodic current which flows for a given time interval, t, to a surface made bare by film removal (through rupture or by other means) and x_t is the thickness of the film at time t. R_p can also be expressed as

$$R_p = \frac{Q_T}{Q_f} = K\frac{Q_d + Q_f}{Q_f} \tag{7}$$

where Q_T is the total charge involved in the anodic process, Q_d is the charge involved in metal dissolution, Q_f is the charge involved in the film formation, and K is a constant.

The magnitude of R_p is a measure of the effectiveness of the repassivation process after film disruption. If repassivation is slow at first, Q_T increases rapidly, resulting in a large value of R_p. On the other hand, rapid repassivation, where Q_f does not differ greatly from Q_T, yields a small value R_p. Since R_p is measured as a function of time, it will be useful to examine what happens to dR_p/dt under different hypothetical situations which may exist at a crack tip. This is done in Table I.

Three of the environments examined by Ambrose and Kruger for a low carbon steel (AISI 1017-1018) illustrate how environment affects the delicate balance between film repair and metal dissolution. These were (1) an environment where mild steel is susceptible to SCC (Condition A in Table I), hot concentrated nitrate solution, (2) an environment where the steel does not corrode (Condition C), nitrite solution, and (3) an environment where the steel corrodes extensively (Condition D), chloride solution. Figures 6(a), (b), and (c) show the changes in R_p and film thickness with time for the three different environments just described.

These three different behaviors found for nitrate (Condition A), nitrite (Condition C) and chloride (Condition D) clearly fit the features U.R. Evans [23] referred to as: "chemical factors in the liquid mainly decide whether attack at any point will (a) heal [nitrite], (b) remain localized, developing into a crack [nitrate], or (c) spread out [chloride], leading to general attack."

Table I. Comparison of Repassivation Parameters of a Given Metal in an Environment (N) to Those for the Same Metal in An Environment (M) where SCC is Unlikely. From [19].

Condition	$R_p^{(1)}$	$dR_p/dt^{(1)}$	t_p	$dx/dt^{(2)}$	**Significance**
A	$R_pN \gg R_pM$	$\frac{dRN}{dt} \gg 0$	$t_pN \gg t_pM$	$(\frac{dx}{dt})_N \gg 0$	Non-protective film forms in N at high rate. Extensive dissolution at crack tip resulting in SCC in N or in corrosion at pre-existing active paths or sites.
B	$R_pN \gg R_pM$	$\frac{dR_pN}{dt} \leqslant 0$	$t_pN \gg t_pM$	$(\frac{dx}{dt})_N \ll (\frac{dx}{dt})_M$	Low dR_pN/dt values indicate a protective film in N but dx/dt slow. SCC more likely for N than M.
C	$R_pN \leqslant R_pM$	$\frac{dR_pN}{dt} \leqslant 0$	$t_pN \leqslant t_pM$	$(\frac{dx}{dt})_N \geqslant (\frac{dx}{dt})_M$	Protective film formed in N. Rate of film formation high enough so that no SCC likely for N.
D	$R_pN \gg R_pM$	$\frac{dR_pN}{dt} \gg 0$	$t_pN \gg t_pM$	$(\frac{dx}{dt})_N \ll (\frac{dx}{dt})_M$	Very little protective film formed in N, high dissolution rate resulting in crack tip blunting. Pitting or intergranular corrosion but SCC unlikely for N.

(1) At t_p.

(2) At beginning of film growth transient.

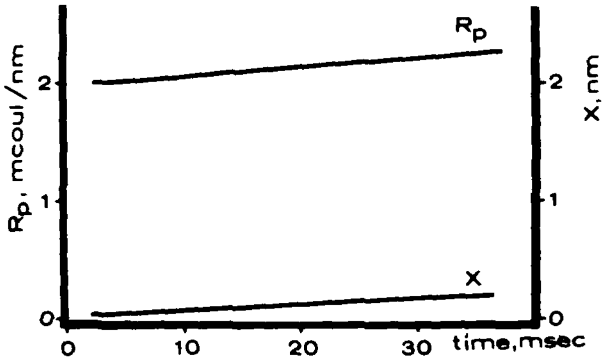

Fig. 6a - Change in thickness, x, and repassivation ratio, R_p, after removal of abrasion wheel of the triboellipsometric apparatus for low carbon steel in 4N $NaNO_3$ at 90°C. Steel is at open circuit potential -288 mV. From [20].

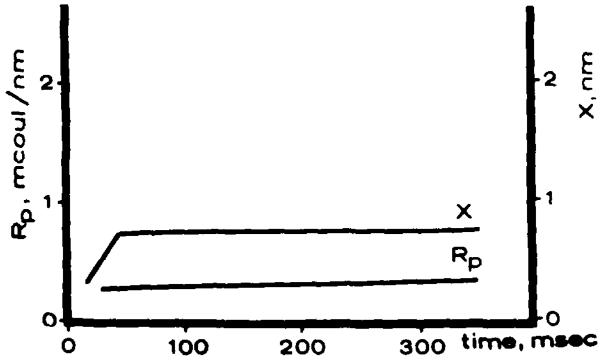

Fig. 6b - Change in thickness, x, and repassivation ratio, R_p, after removal of abrasion wheel of triboellipsometric apparatus for low carbon steel in 1N $NaNO_2$ at 25°C. Steel is at open circuit potential -180 mV. From [20].

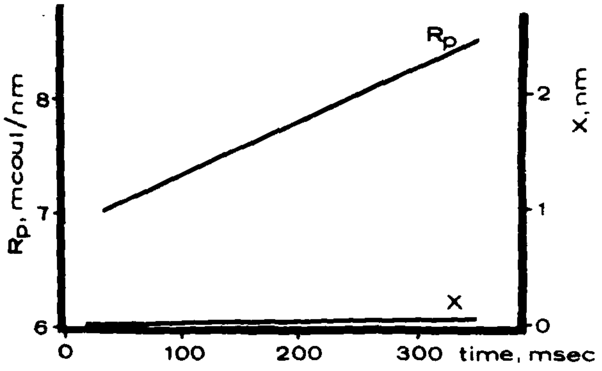

Fig. 6c - Change in thickness, x, and repassivation ratio, R_p, after removal of abrasion wheel of triboellipsometric apparatus for low carbon steel in 1N NaCl at 25°C. Steel is at open circuit potential -298 mV. From [20].

Film Repair Rate and ESF Mechanism

A second triboellipsometric study by Ambrose and Kruger [24] on the relationship between ESF susceptibility and repassivation kinetics for a Ti-8Al-1Mo-1V alloy shows how film repair processes can reveal the mechanism of cracking. Results from their triboellipsometric repassivation kinetics experiments conducted in 1N $NaNO_3$ (pH=6.08) and 1N NaCl (pH≈6.11) solutions at -222 mV SHE are shown in Figs. 7(a) and (b). At comparable film thickness, the value of the repassivation ratio, R_p, is *significantly higher* in the NaCl solution than in the $NaNO_3$ solution, approaching a limiting value of about 2 mcoulombs/nm when at a monolayer coverage of 0.3 nm (R_{plim} ≅ 0.3 mcoulomb/nm). The values of the ellipsometrically determined film thickness are also shown. In $NaNO_3$, an oxide thickness of 0.30 nm was present on the metal surface by the time the abrasion wheel had been retracted to allow ellipsometric measurements (≈5 msec), indicating extremely rapid early stage film growth. In NaCl, on the other hand, film growth was so slow that a film thickness of 0.30 nm was not reached until 38 msec after cessation of abrasion.

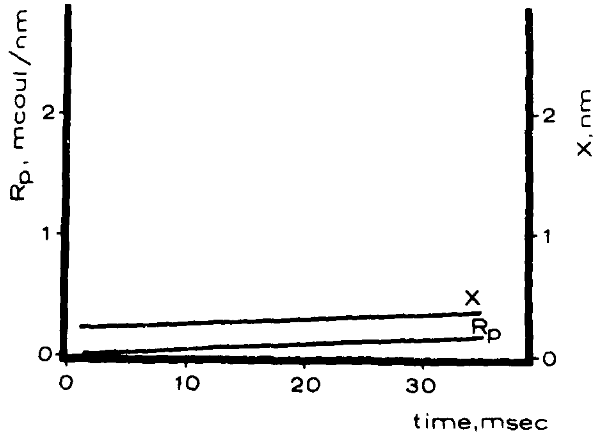

Fig. 7a - Change in thickness, x, and repassivation ratio, R_p, after removal of the abrasion wheel of the triboellipsometric apparatus for Ti 8-1-1 in 1N $NaNO_3$ at 25°C. The alloy is at the open circuit (corrosion) potential -222 mV SHE. From [24].

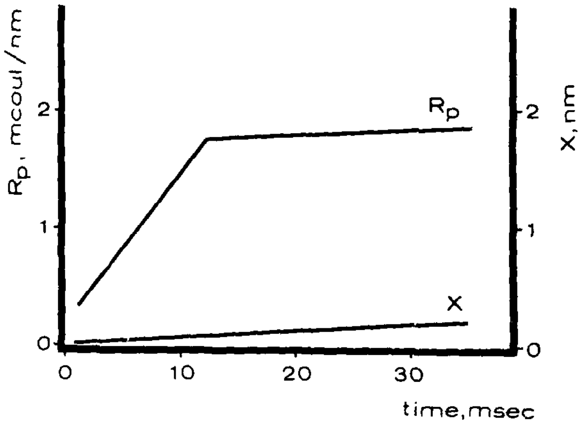

Fig. 7b - Change in thickness, x, and repassivation ratio, R_p, after removal of the abrasion wheel of the triboellipsometric apparatus for Ti 8-1-1 in 1N NaCl at 25°C. The alloy is at the open circuit (corrosion) potential -222 mV SHE. From [24].

From Fig. 7(a) it can be seen that, for Ti 8-1-1 in 1N $NaNO_3$ at the corrosion potential of -222 mV SHE, a low value of R_p was observed throughout the repassivation transient. Here $dR_p/dt=0$. Based on the size of the oxide ion, a monolayer of TiO_2 would be approximately 0.30 nm in thickness; it formed in 5<msec in this environment. These results are characteristic for repassivation transient in which most of the current transient is utilized in rapid film growth without significant metal dissolution. When this is compared to the results obtained in 1N NaCl at the same potential, where crack propagation velocities on the order of 10^{-2} cm/sec have been measured [25], it is seen that R_p is significantly higher as is dR_p/dt, indicating substantial metal dissolution which can be accounted for by low rates of film growth in 1N NaCl. Although monolayer coverage is not obtained until 38 msec following cessation of abrasion, R_p changes slope at about 12 msec. This indicates some inhibition of metal dissolution, perhaps by formation of a precipitated salt layer on the surface which results from saturation of the diffusion layer with $TiCl_3$ (Fig. 7(b)). At any rate, repassivation is eventually achieved.

Simultaneous determination of both film thickness and total current by triboellipsometry allows an estimate of the amount of metal dissolution occurring during the repassivation transient. Such an estimate would allow prediction of the crack propagation velocities to be expected if propagation proceeds via an electrochemical dissolution mechanism as suggested by Beck [25].

Assuming that metal dissolution occurs by Tafel kinetics on the bare metal between patches, it was concluded that total dissolution current over the entire surface is proportional to the area of bare metal exposed. It can be assumed, however, that the local dissolution current density on bare metal surfaces remains constant over the span of the repassivation transient until the patches coalesce. This would allow an estimate of the maximum penetration of metal by electrochemical dissolution.

Using data from Fig. 7(b) for Ti 8-1-1 in 1N NaCl at the open-circuit potential of -222 mV SHE, they obtained a maximum propagation velocity of 6.0 x 10^{-6}cm/sec assuming metal dissolution as Ti^{+3}. Even if the $i_{max} \approx i_d$ approximation was in error due to localized cathodic reactions, as well as overestimating bare metal surface area, propagation velocities based on electrochemical metal dissolution do not come close to the observed stress corrosion crack propagation velocities of 8 x 10^{-3} cm/sec by Beck at this potential [25]. Therefore, these triboellipsometric repassivation kinetics studies of

Ambrose and Kruger require that the ESF mechanism cannot be crack growth due to metal dissolution where the maximum crack growth velocity would be 6 x 10^{-6} cm/sec but must involve the higher velocity of 8 x 10^{-3} cm/sec that was observed by Beck. Such a high velocity indicates a brittle fracture mechanism, probably that produced by hydrogen embrittlement of the Ti alloy through the formation of a hydride. Thus, a study of film repair processes can indicate the ESF mechanism.

Environment pH

A major chemical factor that affects film repair and thereby ESF is pH. Ambrose [26] carried out triboellipsometric studies of the repassivation of AISI 304 stainless steel in acidic (pH=3), neutral (pH=7) and alkaline (pH=11) NaCl solutions to examine the effects of pH on R_p. The results of that study are shown in Fig. 8. He found that the repassivation ratio, R_p, in the acidic solution at +90 mV SHE (corrosion potential measured for 304 stainless steel in this environment) was higher than in neutral or basic solutions. This system was therefore selected as a starting point for the determination of the relationships between repassivation kinetics, rate of bare metal production, and ESF susceptibility. He then connected the repassivation kinetics results to ESF susceptibility by carrying out slow strain rate susceptibility tests in the acidified NaCl solution at several different strain rates using specimens polarized to +90 mV SHE; the repassivation kinetics in this environment appear to be favorable for ESF susceptibility. It can be seen from Fig. 8 that the repassivation ratio (R_p) determined by triboellipsometry was of sufficient magnitude (pH 3, +90 mV SHE) to indicate these conditions as the more likely of those studied for observing susceptibility to ESF.

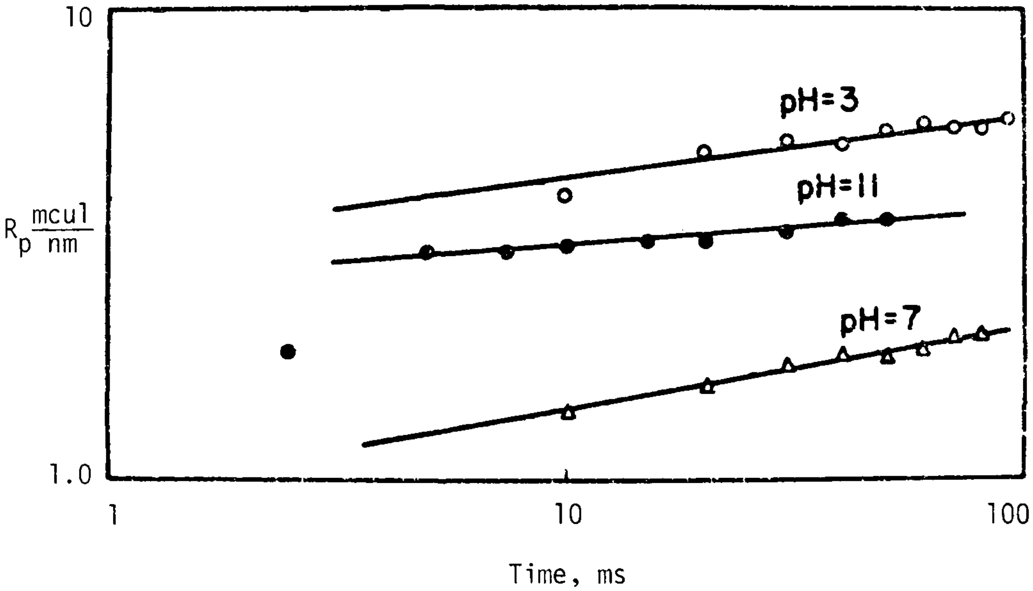

Fig. 8 - Changes in repassivation ratio, R_p ($\log_{10} R_p$ vs. $\log_{10}$ time) for 304 stainless steel in air saturated 1.0N NaCl solution (pH 3, 7 and 11) at +90 mV SHE following removal of surface film by abrasion at -1000 mV SHE. From [26]

Maximum load and time to failure data, normalized with respect to air, are given in Fig. 9. A scanning electron microscope was used to examine the fracture surfaces of both air fracture and in-situ fractures at the maximum strain rate. The data suggested the possibility of stress corrosion attack.

Some evidence of the cleavage characteristic of stress corrosion cracking in austenitic stainless steels was also observed. The slow strain experiments were performed at the same potential and strain rate on 304 stainless steel specimens exposed to neutral 1.0N $NaNO_3$, an environment in which the repassivation ratio was significantly lower. No change in maximum applied load or time to failure with respect to air was detected.

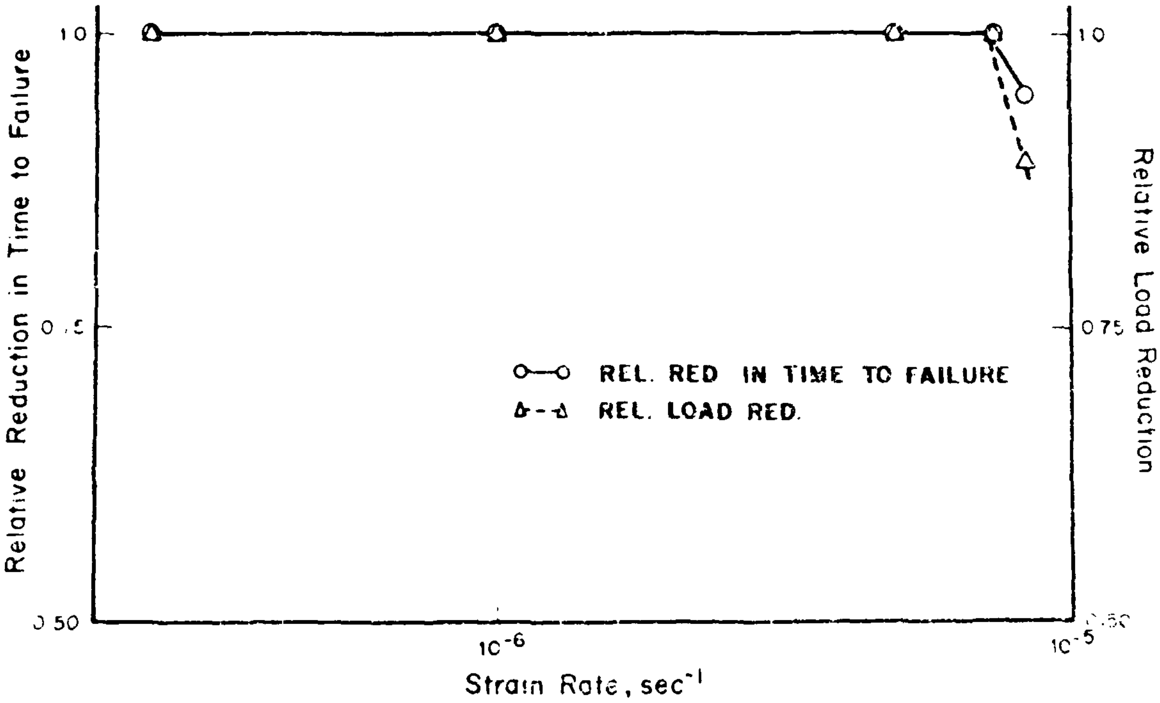

Fig. 9 -- Changes in time to failure and maximum sustained load (both normalized with respect to air) vs. strain rate for 304 stainless steel in acidified 1.0N NaCl solution (pH = 3.0). From [26].

These results indicated that the effect of potentiostatic exposure of 304 stainless steel in acidified sodium chloride solution on time to failure and maximum sustained load during slow straining must arise from a metal removal component occurring in conjunction with ductile tensile failure during the time span of the experiment. Anodic current density measurements made during the duration of exposure lead to a calculation of an average depth of metal penetration of 5×10^{-6}cm which cannot account for the measured decrease in maximum sustained load. One possibility is that localized attack in the form of pitting can reduce the effective cross sectional specimen area to such an extent as to reduce the sustained load. While examples of pitting were observed in SEM micrographs, the crystallographic pit density was low. The evidence of some cleavage in the same SEM micrographs lends better support to the conclusion that an ESF process was operative under these conditions.

Ambrose suggested that on the basis of relative repassivation kinetics of 304 stainless steel in neutral and acidified sodium chloride solution, a greater susceptibility to SCC seemed likely in the acid solution because this environment produced lower film growth kinetics. Although the still limited evidence he reported did not confirm a marked tendency for cracking in acidified chloride environments at any finite propagation velocity under service, it did suggest replacement of conventional susceptible/nonsusceptible criteria which, while valid for predicting failures that occur in short time spans, are not suitable for measuring susceptibility when crack propagation is very slow. For practical situations where failures take years to occur such slow crack growth rates are still important. Here, especially for ductile alloys where fracture mechanics techniques present problems, the combination of repassivation kinetics measurements and constant strain-rate tests may be a valuable failure predictive aid.

Acknowledgment

All of the work described in this paper by Kruger, Ambrose, and Escalante was supported by Dr. Philip Clarkin under the Office of Naval Research contract NAONR 18-69 NR 036-082. We are most grateful to him.

References

(1) H.L. Logan, J. Res. Nat. Bur. Stds., 48 (1952) p. 99.

(2) F.A. Champion, Symp. on Internal Stresses in Metals and Alloys, Inst. of Metals, London, 1948, p. 468.

(3) F.P. Ford, in "Embrittlement by the Local Crack Environment," R. P. Gangloff, Ed., T.M.S.-A.I.M.E., Warrendale, PA, (1984) p. 117.

(4) E.N. Pugh, Whitney Award Lecture, (1984) N.A.C.E..

(5) K. Sieradzki, R. Sabatini, R.C. Newman, Met. Trans., 15A (1984) p. 1941.

(6) E. Escalante and J. Kruger, J. Electrochem. Soc. 118 (1971) p. 1062.

(7) J.A.S. Green, H.D. Mengelberg, and H.T. Yolken, J. Electrochem. Soc. 117 (1970) p. 433.

(8) E.N. Pugh, J.V. Craig, and W.G. Montague, Trans, ASM, 61 (1968) p. 468

(9) A.J. Forty and P. Humble, Phil. Mag., 8 (1963) p. 247.

(10) W.W. Porterfield and G.T. Miller, Jr., J. Electrochem. Soc., 113 (1966) p. 528.

(11) D.J.G. Ives and A.E. Rawson, ibid., 109 (1962) p.458.

(12) D.J.G. Ives and A.E. Raswon, ibid., 109 (1962) p.447.

(13) J. Kruger and J.P. Calvert, ibid., 111 (1964) p. 1038.

(14) J. Kruger, ibid., 106 (1959) p. 847.

(15) E. Escalante and J. Kruger, NBS Report 10594, Nat. Bur. Stds., Washington, DC, May 13, 1971, p. 26.

(16) S.F. Bubar and D.A. Vermilyea, J. Electrochem. Soc., 114 (1967) p. 882.

(17) B.F. Brown, in "The Theory of Stress Corrosion Cracking in Alloys," J.C. Scully, Ed., NATO Sci. Affairs Div., Brussels, 1971, p. 197.

(18) J. Kruger and J.R. Ambrose, Surf. Sci., 56 (1976) p. 394.

(19) J.R. Ambrose and J. Kruger, NBS Report NBSIR 74-583. Nat. Bur. Stds., Washington, Sept. 1974, pp. 2-31.

(20) J.R. Ambrose and J. Kruger, Proc. 5th Int. Cong. on Met. Corr., N.A.C.E., Houston, 1974, pp. 406-409.

(21) H.J. Engell, in "The Theory of Stress Corrosion Cracking in Alloys," J.C. Scully, Ed., NATO Sci. Affairs Div., Brussels, 1971, p. 167.

(22) J.R. Ambrose and J. Kruger, Corrosion, 28 (1972) p.30.

(23) U.R. Evans, quoted by R.N. Parkins and R. User, Proc. 1st Int. Cong. on Met. Corr., Butterworths, London, 1962, p. 289.

(24) J.R. Ambrose and J. Kruger, J. Electrochem. Soc., 121 (1974) p. 600.

(25) T.R. Beck, in Ref. (20), p. 64.

(26) J.R. Ambrose, NBS Report, NBSIR73-244, Nat. Bur. Stds., Washington, 1973.

(27) J.R. Ambrose, in Ref. (19) pp. 33-40.

EFFECT OF GRAIN BOUNDARY STRUCTURE ON SENSITIZATION AND CORROSION OF STAINLESS STEEL

Bradley W. Bennett and Howard W. Pickering
Department of Materials Science and Engineering
Metallurgy Program
The Pennsylvania State University
University Park, PA 16802
USA

This paper reports on a study of intergranular corrosion, particularly the influence of the crystallography of a grain boundary (g.b.) on the sensitization and grain boundary corrosion of stainless steels. Since sensitization of stainless steels depends on g.b. energy, this study included a determination of the misorientation angle of grain boundaries in a sample. A scanning electron microscope was modified for application of the electron backscattering (EBS) technique in conjunction with normal SEM imaging of the sample surface. Using the EBS technique, the orientations of neighboring grains were readily obtained with an accuracy of ± 0.5°.

In austenitic stainless steel (Fe-18Cr-10Ni) samples annealed at 1200°C for 1 h, water quenched and aged for various times at 650°C, the degree of sensitization increased with increasing aging time. This was indicated by an increasing width of the g.b. groove. A plot of groove width vs. g.b. misorientation angle obtained by the EBS technique showed a range of groove widths for the same angle. Modeling the g.b. structure based on ideal crystallography and the coincident site lattice concept provided a rationalization of this observation. Similar results were found for ferritic stainless steel (Fe-19Cr) samples.

The Cr concentration profiles as a function of time were calculated, using a finite difference method, both along the g.b. and normal to the g.b. These profiles agree well with Cr profiles experimentally measured by other investigators. The calculation includes overlap of the chromium profiles in the boundary, and considers the dependence of sensitization on aging time, g.b. diffusivity, carbide spacing and g.b. width.

A major difficulty in understanding g.b. corrosion is the difference in the groove and Cr-profile widths. The observed groove widths are 10 to 100 times larger than the Cr-profile widths.

Introduction

This paper summarizes our progress to date on one of two thrusts of our current Office of Naval Research grant on grain boundary corrosion: The effect of grain boundary structure on the sensitization of stainless steels [1]. The other thrust concerns the characterization and mechanism of the electrochemical process which occurs in the grain boundary groove, and, more generally, in all localized cell corrosion.

Many examples of uneven attack at grain boundaries of a sample are available in the literature. The energy associated with grain boundaries makes them favorable sites for solute segregation, precipitation and electrochemical reactions, one or all of which can lead to corrosion at the grain boundary. Grain boundary energy is a function of g.b. structure and, therefore, varies among the boundaries of a sample. This can cause variations in the extent of any or all of these processes at the grain boundaries.

Many theoretical models and calculations in the literature consider the relationship of the grain boundary structure and grain boundary energy. Notable among them are the dislocation models proposed by Burger [2], Bragg [3] and Read and Shockley [4]. Cusps of lower grain boundary energy were predicted in the energy vs. misorientation angle at intermediate values of grain boundary misorientation [4]. These cusps have been rationalized on the basis of the coincident site lattice (CSL) model advanced by Bollman [5]. Coincident sites are those where atoms of the adjacent grains forming the grain boundary exactly register or coincide. Low energy cusps occur when coincidence occurs on the same atom at regular intervals of small (atomic) spacing. An increase in grain boundary energy is associated with both a deviation from a CSL orientation and a closer spacing of associated secondary grain boundary dislocations. Atomistic calculations can lead to the cusped nature of the grain boundary energy with misorientation, such as those performed by Sutton and Vitek [6].

Calculations have also been made on the solute redistribution associated with segregation or precipitation at a grain boundary. For example, a more quantitative understanding of grain boundary corrosion of stainless steel is obtained from the chromium depletion models proposed by Stawstrom and Hillert [7], Tedmon et al. [8] and Hall and Briant [9]. These models, however, do contain somewhat arbitrary assumptions, e.g., 20 nm for the minimum width of the Cr-depleted region [7]. Because of these and other assumptions, existing models are deficient, e.g., they do not adequately model the sensitization process when chromium profiles in the boundary overlap.

This paper describes a study of the relationship of grain boundary structure to the extent of the sensitization process in stainless steels. For determination of grain boundary structure, it was necessary to determine the orientations of the adjacent grains. This paper also describes a more complete kinetic model of the sensitization process.

Ideally, atom probe field ion microscopy would serve to determine orientation, grain boundary structure, precipitation of carbides and chromium depletion. Specimen preparation is difficult since it requires a grain boundary in the field of APFIM, although some encouraging progress has been made in the in-situ formation of grain boundaries in the APFIM using a laser [10]. Electron channelling patterns are widely used for such purposes but not all scanning electron microscopes (SEM) can be used in this way. On the other hand, the electron back scattering (EBS) technique can be used with virtually all scanning electron microscopes for the determination of crystal orientation [11-14].

Experimental

The EBS technique, originally developed by German researchers [11,12], can be operated with an SEM using a stationary electron beam at currents of 10 to 10^{-8} to 10^{-7} A [13,14]. The incident electrons are inelastically scattered by the sample and then elastically backscattered (Bragg reflected). In order to sense these Bragg reflected electrons, the sample is tilted between 60° and 85°, enabling the backscattered electrons to impinge on a phosphor screen. An SEM micrograph is taken in this position for grain identification. The patterns obtained on the phosphor screen are viewed and photographed through a glass window that is inserted in an unused port of the SEM sample chamber.

The patterns produced on the screen conform to stereographic projections of the planes of the crystal, thereby enabling both the orientation (to ± 0.5°) and structure of the crystal to be determined. In addition, the good spacial resolution enables grains as small as a few µm in a polycrystalline sample to be analyzed. The quality of EBS patterns depends strongly on the surface condition, degrading as reaction-product layers accumulate on the surface.

The patterns obtained from the two phases in a dual phase CD-4MCu alloy are shown in Fig. 1. The analyses of these patterns, representing a grain of each phase, austenitic above and ferritic below the micrograph, provides the orientations of the two grains and the structures of the two phases. As a result of the wide angle of coverage, most EBS patterns can be readily indexed by simply noting the major symmetry elements in the patterns. In the upper left pattern of Fig. 1, the two-fold symmetry elements about the <110> pole are apparent. The completely indexed pattern appears on the right, where major poles are labelled within the circle and the planes responsible for producing the respective bands are labelled outside of the circle. Other aids, in the indexing and structure determination, are the obvious presence or absence of major poles and the relative widths of bands in the pattern: both are consequences of Bragg reflection. Only for planes satisfying the appropriate structure factor conditions. for the particular crystal system, will EBS bands be formed*. As with Kikuchi or electron channelling bands, widths of EBS bands are proportional to 2 sin θ where θ is the Bragg angle. It follows that the planes having low indices produce narrow and well defined EBS bands. Further details on the EBS technique and its application in this study can be found elsewhere [14].

To establish grain boundary structure, orientation information obtained with the EBS technique was combined with the observation that grain boundaries are often near normal to the sample surface. Therefore, in analyses of the ideal (unrelaxed) grain boundary structure the boundaries were assumed to be perpendicular to the sample surface. The resulting boundary structure was plotted with a Houston Instruments DMP-29 plotter interfaced to a Commodore 64 microcomputer. Plots consist of overlays of the ideal atomic arrangements in the boundary plane of both crystals. Angle axis pairs were also calculated [15] and by manipulating the rotation matrix used in the calculation so as to maximize the diagonal terms, the minimum rotation (misorientation) angle was determined.

The effect of crystallography on grain boundary corrosion was studied in an austenitic Fe-18Cr-10Ni and a ferritic Fe-19Cr stainless steel. Their compositions are given in Table I. Following rolling to 500 µm, 0.5 x 1 cm^2 samples of Fe-18Cr-10Ni were cut, mechanically polished, cleaned ultrasonically, individually vacuum encapsulated in Vycor after purging with high purity argon and annealed at 1200°C for 1 h and water quenched. Subsequently, the Fe-18Cr-10Ni samples were isothermally aged at 650°C for 1, 10, 100 or 1000 h. The ferritic Fe-19Cr samples were prepared similarly after rolling to 1000 µm and prepared as above except that the samples were either water quenched or air cooled from the 1200°C anneal and not aged. Final grain sizes of both stainless steel samples varied from 10 to 250 µm. The austenitic samples were heavily twinned. The austenitic and ferritic samples were then mechanically polished through 0.05 µm alumina. Some of these samples were electropolished

---

*Note the prominence of the 211 pole in the EBS pattern of the austenitic phase, formed by the intersection of the $\bar{1}11$ and $0\bar{2}2$ bands. The pattern from the ferritic phase, however, prominently displays a 311 pole formed by the intersection of the $\bar{1}12$, $\bar{1}21$ and $01\bar{1}$ bands.

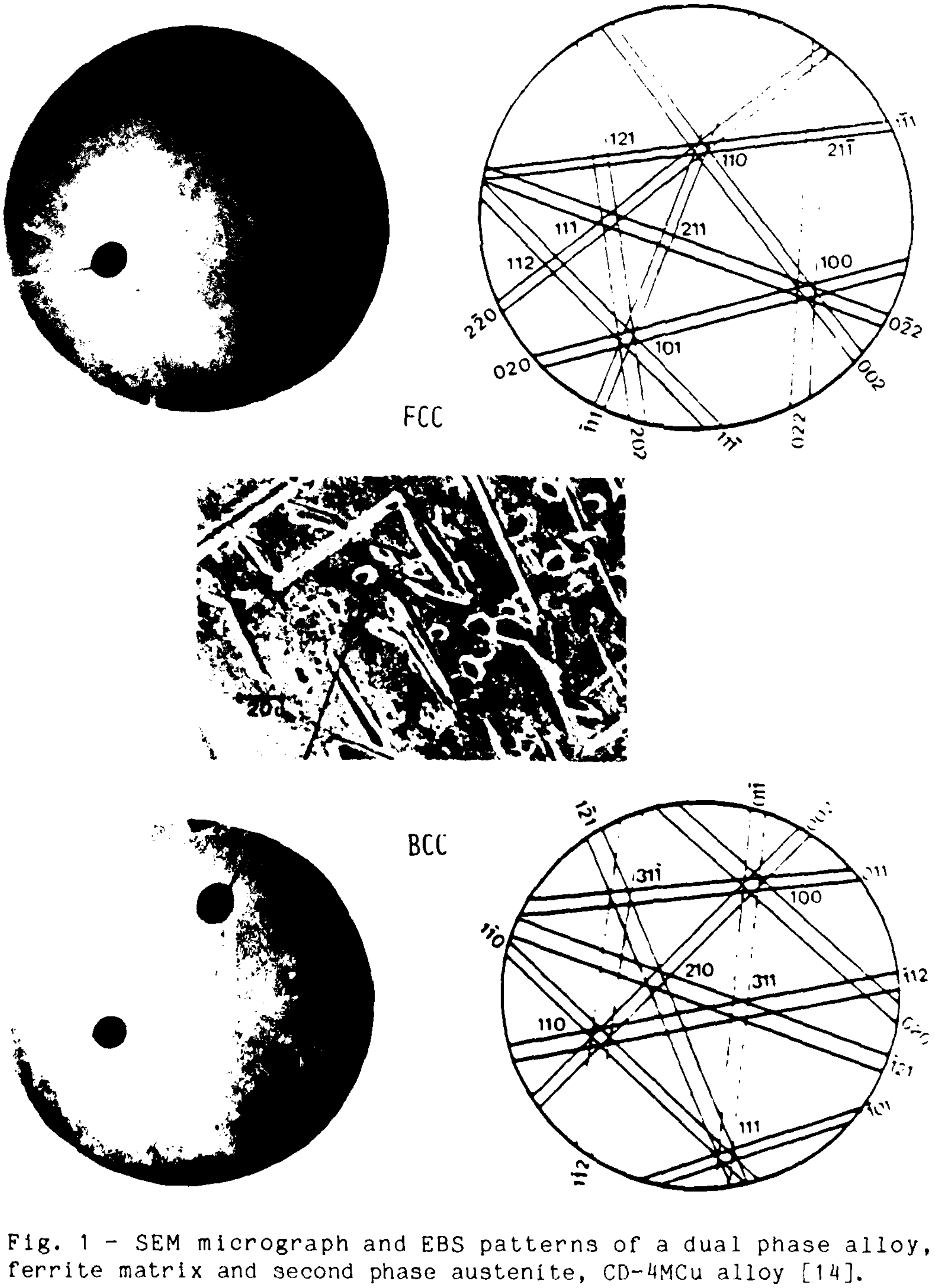

Fig. 1 - SEM micrograph and EBS patterns of a dual phase alloy, ferrite matrix and second phase austenite, CD-4MCu alloy [14].

in a 7% perchloric acid, 90% (glacial) acetic acid, 3% H_2O solution at 21 V for 30 to 60 s to remove the deformation layer in preparation for the EBS analysis.

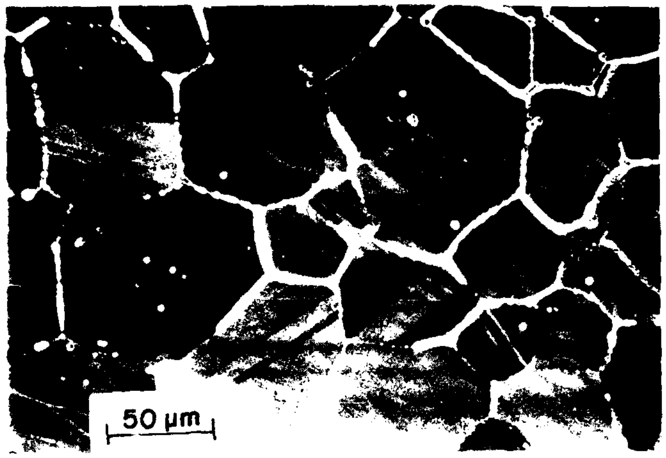

Fig. 2 - SEM micrograph of austenitic stainless steel aged 1 h at 650°C, and exposed to 1N H_2SO_4 at 0.34 V (SHE).

Table I. Compositions of Stainless Steels

Alloy	Cr	Ni	C	S	P	BAL
Fe-18Cr-10Ni	17.82	9.88	0.11	0.02	0.02	Fe
Fe-19Cr	19.47	-	0.09	0.02	0.02	Fe

The widths of the grooves that formed along the grain boundaries during anodic polarization were measured. The average values were used to represent the extent of corrosion at the different grain boundaries of the sample.

A three electrode closed cell was used to anodically polarize the samples. Saturated calomel and Pt cyclindrical mesh electrodes were used as the reference and counter electrodes, respectively. The electrolyte was 1N H_2SO_4 prepared from reagent grade sulfuric acid and doubly distilled water and deaerated with oxygen-free argon. The temperature of the solution was 21 ± 2°C. Electrode potentials are reported on the standard hydrogen scale.

After introducing the sample, the cell was allowed to stabilize until the corrosion potential approached a nearly constant value, typically after 10 minutes. Constant potentials of 340 and 140 mV (SHE) for the austenitic and ferritic samples, respectively, were used based on numerous trials which showed these potentials provided the greatest degree of intergranular attack in sensitized samples. Both alloys are passivated at these potentials in the nonsensitized condition. The time of these constant potential exposures ranged from 300 to 1800 s. The samples were then analyzed by light and scanning electron microscopy and the EBS technique.

The finite difference calculations of the diffusion profiles in, and normal to, the grain boundary required a large number of operations to perform an adequate simulation, and were accomplished using a high speed IBM 4381 computer. Typically, for an adequate simulation of a one hour sensitization process, computer execution times would range from approximately 10 to 15 minutes.

Results

Austenitic Stainless Steel

The anodic polarization curves for the Fe-18Cr-10Ni samples, annealed and isothermally aged at 650°C for various times, show that with increasing aging time, the active-passive transition occurs at more oxidizing potentials and the passive current density increases. Similarly, aged Fe-18Cr-10Ni samples were polarized at 340 mV (SHE) for 5 min and examined by SEM. Strong grain boundary corrosion occurred in contrast to unsensitized samples which showed no grain boundary attack. With increasing aging times, the degree of grain boundary corrosion increased, as indicated from the measured groove widths, approximately 0.5 to 1 μm and 2 to 3 μm for 1 and 1000 h at 650°C, respectively. After 1 h aging at 650°C, several grain boundaries were strongly attacked during polarization, whereas others remained intact, Fig. 2. Coherent twin boundaries also showed no sign of dissolution for the samples that were polarized after aging for 1 h at 650°C. With increasing aging time, the extent and density of corroded grain boundaries increased. After 100 h of aging, grain interiors also exhibited substantial localized attack, and the severely grooved grain boundaries revealed a continuous grain boundary phase, presumably $M_{23}C_6$. The continuity of this phase was even more visible after 1000 h of aging, since it stood in relief along all of the grain boundaries. The plate-like precipitate was oriented, for the most part, normal to the sample surface. After 1000 h of aging, the coherent twin boundaries were also heavily attacked and, in addition, contained a narrower groove centered along the major groove bottom. This narrower groove was visible because carbides were not present in the twin boundaries in contrast to their strong prominence along all of the grain boundaries.

Because one hour at 650°C produced the greatest variation in sensitization of the boundaries, EBS patterns were obtained for the grains in Fig. 2, and analysed for misorientation angle and ideal (unrelaxed) atomic structure of the boundaries. The misorientation angles varied over a wide range with a larger than random number of low angle boundaries. The groove width was not simply related to misorientation angle, e.g., a wide range of groove widths occurred for the same 14° angle, and there was no apparent relationship between groove width and misorientation angle.

Boundaries with similar misorientation angle, that exhibited different corrosion behavior after 1 h aging at 650°C, were examined in more detail. In the several boundaries examined, it was apparent that the underlying factor determining the degree of sensitization and grooving was the coincidence of the atomic positions of the two lattices at the boundary. Coincidence was found to be relatively low for heavily grooved boundaries and relatively high for lightly grooved boundaries of the same misorientation. A particularly striking example of a nearly perfect coincidence and a quite low coincidence is shown in Fig. 3 for the ferritic stainless steel.

Ferritic Stainless Steel

A variable amount of grain boundary attack was also observed in the Fe-19Cr alloy, anodically polarized following a quench from the 1200°C annealing temperature. EBS patterns from the individual grains were obtained, and the grain boundary atomic structures were determined. A relationship between misorientation angle and grain boundary groove width was observed as shown in Fig. 4, in contrast to the absence of a relationship in the austenitic samples. Atomic structures of a single boundary, which was heavily grooved over one segment and lightly grooved over another segment, are shown in Fig. 3. The misorientation angle, between the adjacent grains in Fig. 3, is 9°.

Finite Difference Model of Sensitization

By employing finite difference calculations, a kinetic model of sensitization was developed for stainless steel. It overcomes many of the limitations associated with earlier models. The phenomenological approach, assumptions, results and conclusions will be presented here.

The physical model consists of the growth of two parallel lath-like grain boundary precipitates, in which both the grain boundary and the volume diffusion play a role. Grain boundary diffusion produces a composition profile in the boundary. Volume diffusion produces profiles normal to the boundary. One way to envision the model is to consider a fast, but narrow diffusing grain boundary region bordered by a slowly leaking bulk phase. This is essentially the basis of the "collector plate" model, proposed by Aaron and Aaronson [16]. For the particular case of sensitization, the model also considers that a boundary is sensitized when the chromium concentration throughout the boundary falls below 13 at. % (atomic percent).

In developing the finite difference equation for the grain boundary concentration profiles, it is assumed that

1. Volume diffusion only occurs normal to the boundary.
2. The boundary composition is constant in the thickness direction, i.e., no y-direction profile in the boundary.
3. Carbide growth is slow enough so that the carbide matrix interface remains essentially stationary.

Some additional assumptions are the same as needed for the simpler one-dimensional diffusion problem.

The finite difference calculation of diffusion profiles in, and normal to, the grain boundary is a two-step process for each iteration. First, the chromium concentration profile in the boundary after an increment of time Δt is calculated. For the first iteration, all values are equal to the bulk Cr concentration, except for the boundary concentration at the carbide surface. The latter is the chromium concentration in the matrix in equilibrium with the $Cr_{23}C_6$ carbide at the matrix-carbide interface. After completion of the calculation of the Cr concentration profile in the boundary, Cr profiles are calculated normal to the boundary. This completes one iteration of the calculation. The process is repeated $t_s/\Delta t$ times, where t_s equals the total simulation time of diffusion.

Since the model includes sensitization time and temperature, precipitate spacing, grain boundary and volume diffusivity, and grain boundary width as parameters, it provides a powerful means to theoretically investigate the sensitization process with a strong emphasis on the effect of grain boundary structure.

Sensitization time as a variable is illustrated for an austenitic stainless steel containing 18Cr is shown in Fig. 5. The profiles in the boundary

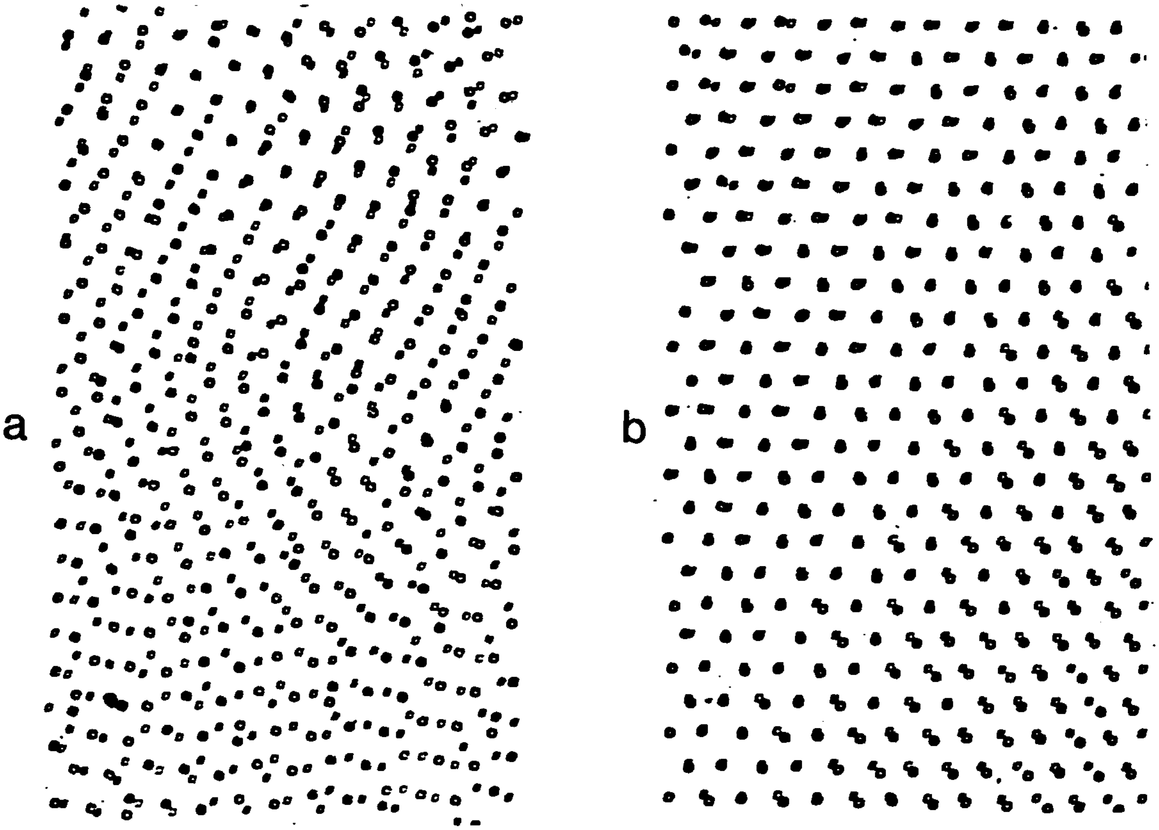

Fig. 3 - Ideal atomic arrangements for two segments of a grain boundary of 9° misorientation angle. (a) Heavily grooved segment, and (b) Lightly grooved segment.

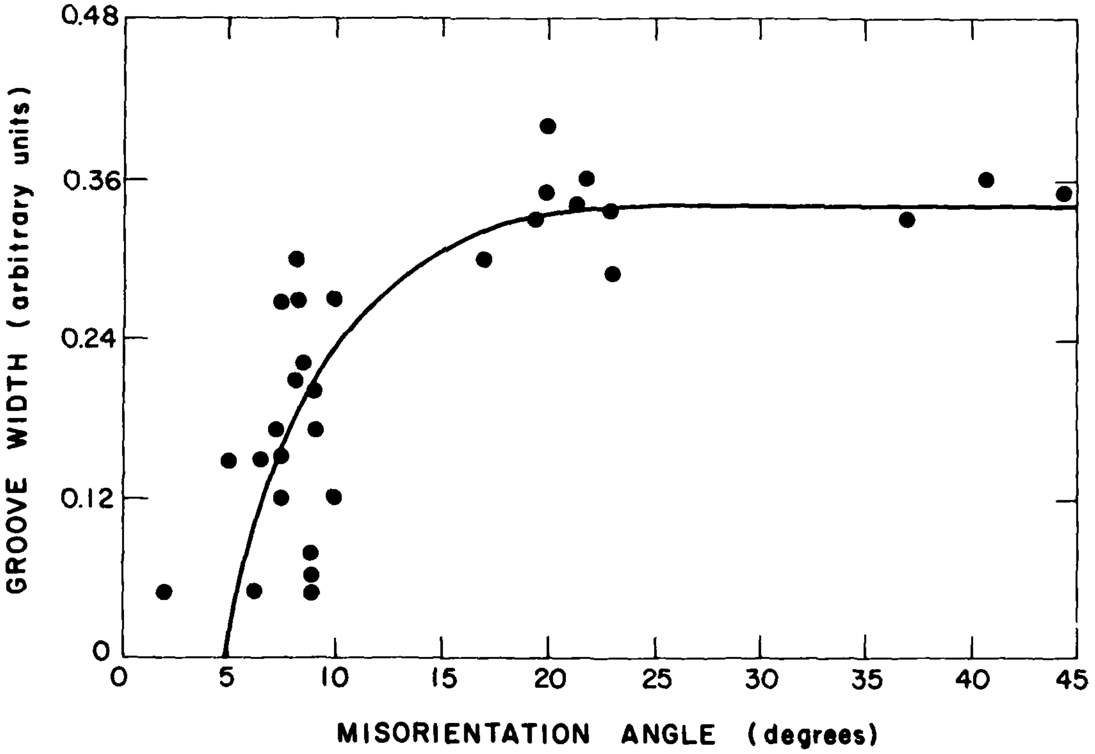

Fig. 4 - Grain boundary groove width as a function of misorientation angle for a sample of the ferritic stainless steel.

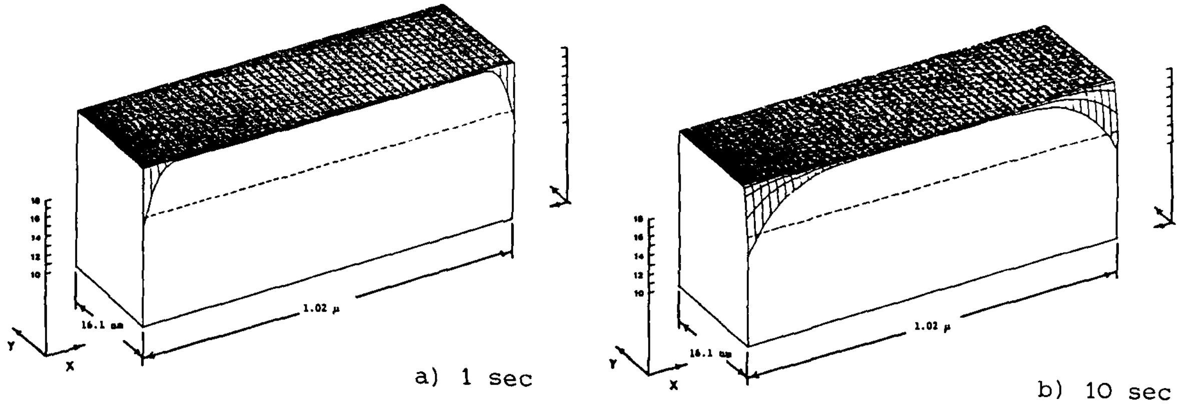

a) 1 sec

b) 10 sec

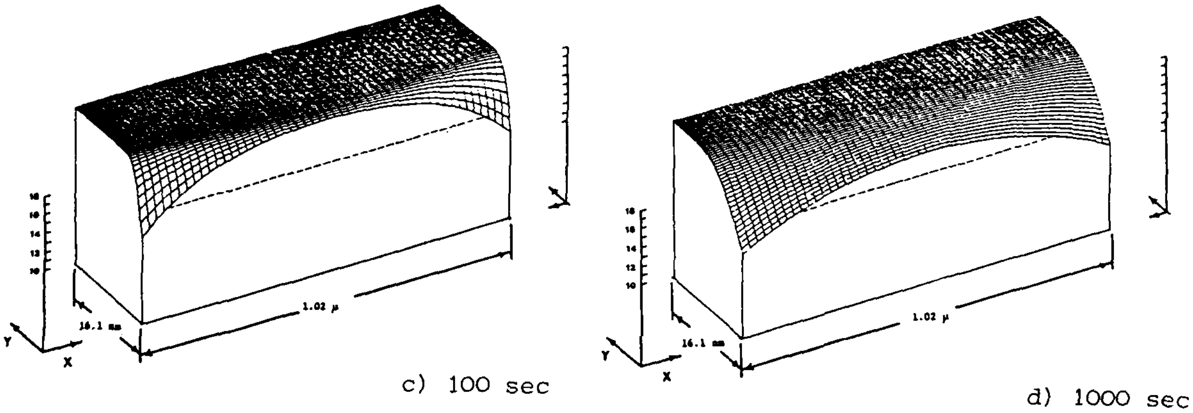

c) 100 sec

d) 1000 sec

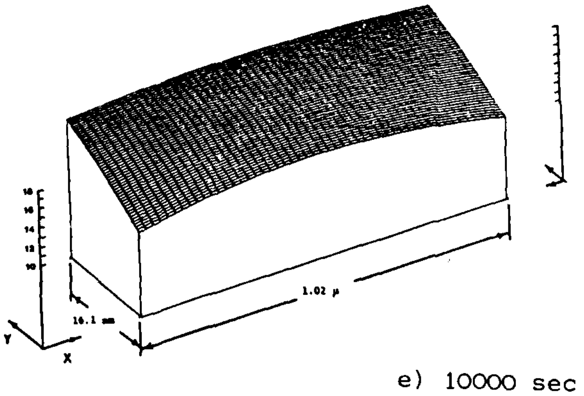

e) 10000 sec

Fig. 5 - Calculated Cr concentration profiles in the boundary (x direction) and normal to the boundary into one of the adjacent grains (y) for a carbide spacing of 1.02 µm in austenitic stainless steel aged at 650°C for various times. Cr concentration is plotted along the vertical axis (z direction).

(x direction) and normal to the boundary into one of the adjacent grains (y direction) are shown. The dashed line in the grain boundary plane represents the 13 at. % Cr level. For the calculation, a temperature of 650°C was chosen because it is near the "knee" of the time-temperature-sensitization curve [17]. The corresponding grain boundary and volume diffusivities for the austenitic stainless steel are $D_{gb} = 10^{-11}$ cm^2/s and $D_{vol} = 10^{-16}$ cm^2/s [18]. The matrix composition in equilibrium with the carbide precipitate was taken as 10 at. %. Grain boundary width was set at $\delta = 10^{-7}$cm, and carbide spacing was set at 1.02 μm based on a measured average carbide spacing of ≈1 μm for austenitic stainless steels sensitized near this temperature [19]. The calculation was done for sensitization times of 1, 10, 100, 1000 and 10,000 s.

After 1 s, a profile in the grain boundary is already forming while the concentration normal to the boundary remains essentially constant (Fig. 5(a)). After 10 s, the boundary profiles are more developed but still not overlapping and the profiles normal to the boundary are just becoming noticeable. Overlapping of the profile in the boundary plane appears after approximately 100 s. After 1000 s, overlapping is extensive and over one-quarter of the boundary (near the carbides) has less than 13 at. % Cr and the profiles normal to the boundary are also well developed. The profile normal to the boundary, however, is still quite shallow (≈10^{-6} cm). At 2290 s (≈50 min), the Cr concentration is below 13 at. % Cr at all points in the grain boundary, in agreement with most experimental results that indicate sensitization at 650°C occurs in approximately 1 h.

Several parameters can be varied in the model. Carbide spacing as a variable was illustrated, by comparing results for a spacing of 0.5 x 10^{-4} cm with the above results for 1.0 x 10^{-4} cm, keeping all other values the same. A marked difference was apparent once overlap of the profiles occurred in the boundary. Overlap occurs after only 10 s for the 0.5 μm spacing, whereas it does not occur in that time for the 1 μm spacing (Fig. 5(b)), i.e., with the narrower precipitate spacing, the chromium concentration is lower in the boundary plane. In contrast, overlap does not occur for either spacing after 1 s and, accordingly, the calculated profiles are identical. As time at 650°C increases to 100 s, the difference in Cr level in the boundary for the two carbide spacings increases and is still large at 1000 s. Furthermore, by 1000 s the chromium concentration falls below 13 at. % along the entire boundary for the narrower spacing, in contrast to the situation for the larger spacing (Fig. 5(d)). With further increase in time, the difference in Cr level in the boundary for the two spacings begins to decrease and eventually vanishes as the Cr concentration falls to the equilibrium value (≈10 at. %) everywhere in the boundary. At this time, the Cr concentration for the two spacings normal to the boundary also approach the same profile, expectantly an "erf" type profile in accord with a uniform boundary composition.

For ferritic stainless steels, sensitization occurs relatively quickly, typically within the period of a quench from a high temperature anneal. This is consistent with a volume diffusivity of chromium that is almost two orders of magnitude greater in ferritic than in austenitic stainless steel [20], as well as a higher interstitial diffusion. A higher diffusivity in the ferritic phase, coupled with little difference in the grain boundary diffusivities [18], provides for a smaller carbide spacing for the ferritic than the austenitic stainless steel. As a first approximation for application of the finite difference model to ferritic stainless steel, carbide spacing and sensitization temperature were assumed to be 5 x 10^{-6} cm and 550°C, respectively. At 550°C D_{gb} and D_{vol} were calculated to be approximately 1 x 10^{-12} and 3 x 10^{-15} cm^2/s, respectively. The bulk concentration was set at 18 at. % Cr, and the equilibrium carbide-matrix composition was assumed to be 10 at. % Cr. The grain boundary width was assumed to be 10^{-7} cm. The chromium profiles for 1, 10, 100 and 1000 s were calculated and appear reasonable based on continuous cooling results [21] but, unfortunately, no direct isothermal aging experimental results are available.

Calculations of the Cr profiles using the finite difference method were also done for the conditions of available experimental data in the literature. The finite difference calculations produced excellent agreement with the experimentally determined Cr profiles, in and normal to the grain boundary, by Hall and Briant [9].

Discussion

Effect of Grain Boundary Structure

In both the austenitic and the ferritic stainless steels, chromium carbide precipitation during heat treatment occurred to different extents among boundaries of the same sample. This was shown by different amounts of grooving among the boundaries. In the ferritic alloy the precipitation process is much faster, in accord with the higher bulk chromium and interstitial diffusivities in the matrix. As a result, precipitation in the ferritic alloy proceeds to the advanced stage of a continuous phase along grain boundaries during very brief excursions in the sensitization temperature range, e.g., during cooling from the 1200°C anneal. On the other hand, for the austenitic alloy, follow up isothermal aging for relatively long times is required to sensitize the grain boundaries. In this case, a qualitative relation between the required aging time for sensitization and boundary energy is evident: the lower the boundary energy, the longer the aging time. Even the very low energy coherent twin boundaries are sensitized after 1000 h at 650°C, although, apparently, they do not contain carbides in contrast to all of the grain boundaries which do. One explanation is that the energy of the coherent twin boundaries is so low that carbides do not nucleate. In this event sensitization of these boundaries would have had to occur by chromium diffusion along the twin boundaries to carbides in the adjacent grain boundaries.

The differences in the amount of corrosion among various grain boundaries in a sample were significant in both the ferritic and austenitic alloys. The total amount of carbide per unit length of grain boundary, nuclei density and growth rate are all expected to be strong functions of grain boundary structure which in turn depends on such parameters as the misorientation angle and the boundary plane orientation.

Misorientation angle was clearly found not to be sufficient by itself to determine the relative amounts of grain boundary grooving among the boundaries, particularly in the austenitic alloy where the carbide distribution along grain boundaries in the same sample ranged from small, widely spaced precipitates to a continuous phase. Misorientation angle, however, provided more insight in the case of the ferritic alloy where, in contrast to the austenitic alloy, a relation between groove width and misorientation angle was observed (Fig. 4). Boundaries, misoriented by less than 10 degrees, exhibited low degrees of corrosion. The number of grain boundaries with low misorientation angle was higher than that for a random distribution, in both the ferritic and austenitic alloys.

The sharp change in groove width with misorientation angle at approximately 8-10° in Fig. 4 suggests that below this angular range little or no carbide formation occurs: whereas above this value carbides nucleate and grow with the total amount of carbide formed being nearly constant with misorientation angle above 10°. In the 8-10° angle range, a wide spectrum of groove widths was observed, indicating that other parameters are required to describe the precipitation process in these boundaries. Analysis of the coincidence of atomic sites, at the grain boundary, of adjacent grains was helpful in this regard. In particular, a boundary with a misorientation angle of 9° provided a rare opportunity since one segment was heavily grooved while another segment was lightly grooved. The ideal atomic arrangements of these segments shown in Figs. 3(a) and 3(b) indicate that the heavily grooved segment has a low coincidence and, therefore, is of a high energy: whereas the lightly grooved segment has a high coincidence and is of low energy. These results are in accord with the expected behavior between the extent of the sensitization process and the boundary energy.

In the case of the austenitic stainless steel where no relation was apparent between groove width and misorientation angle over the entire angular range, it was again apparent from consideration of the atomic arrangements that the more heavily grooved boundaries were of lower coincidence and higher energy than the lightly grooved boundaries.

Corrosion Mechanism

Although the use of groove width as a relative measure of the extent of grain boundary carbide formation is largely borne out by the results, groove width is not simply related to the chromium concentration profile. The latter conclusion is also apparent from micrographs in papers by Briant [22] and Streicher [23]. The fact that groove width is one or even two orders of magnitude larger than the Cr profile normal to the boundary, indicates that the grain boundary dissolution process is more complicated than the simple dissolution of the Cr-depleted alloy. One possibility is that after dissolution of the Cr-depleted alloy, a localized corrosion condition develops. Stainless steel is susceptible to pitting and crevice corrosion at potentials in the passive region. The initial groove has the appropriate geometry and dimensions to function as a crevice. This, or some other two-step grain boundary corrosion process, is also indicated by the presence of a narrower groove at the bottom of the main groove of the coherent twin boundaries. The narrower groove could have formed by the dissolution of the Cr-depleted alloy.

Finite Difference Model

Of the several assumptions in the finite difference calculation, seemingly only in the case of the ferritic stainless steel is there some question. This concerns the assumption that the matrix/carbide interface is stationary. Because the carbides are so close together in the boundaries of the ferritic alloy, the actual motion of the boundaries becomes a significant fraction of the carbide spacing during the longer simulated aging times. Thus, for the ferritic stainless steels, a moving boundary calculation would give more realistic profiles. On the other hand, in the case of the austenitic stainless steels all of the assumptions seem well justified and this is borne out by the good agreement with the available experimental data [9].

Like the finite difference model in this work, models of sensitization applied by Tedmon et al. [8] and Hall and Briant [9] are based on the "collector plate" concept. The major improvement of these two models over the Stawstrom-Hillert model was the prediction of Cr concentration profiles in the boundary between carbide particles. The shortcoming of both these models, however, is that the concentration profiles between neighboring grain boundary carbides were not permitted to overlap. Thus, midway between the carbide precipitates, the grain boundary Cr concentration was fixed to the initial bulk level. While these models are representative of the very initial stage of sensitization, they cannot describe the condition where an entire boundary will be depleted to less than 13 at. % Cr. Nevertheless, during the initial stage of sensitization, the behavior of the finite difference model parallels that of these two limited analytical approaches.

Conclusions

1. The electron backscattering (EBS) technique is both a powerful and easily implemented method for accurately determining the crystallographic orientation and crystal structure of small samples.
2. Grain boundary structures of higher energy sensitize more readily and extensively, and are more corroded in both austenitic and ferritic stainless steels.
3. For ferritic stainless steel, grain boundary corrosion is low for misorientation angles below 10°.
4. A phenomenologically based finite difference model of the "collector plate" mechanism of grain boundary precipitate growth has been successfully developed and used to predict chromium concentration profiles that agree well with experimentally determined profiles. The model avoids certain limitations of existing models and has the capability of being applied in all situations (short, intermediate and long term). It also indicates in what situations existing analytical models can correctly be applied.
5. The model has been successful in treating for the first time the transient period when grain boundary chromium profiles overlap in the boundary.
6. The model relates aging time, temperature and grain boundary structure to sensitization times. Conversely, having Cr profiles in and normal to the grain boundary, carbide spacing or diffusion coefficients can be calculated.
7. Measured Cr depletion zones are much narrower than grain boundary groove widths. This suggests a corrosion mechanism that involves more than the simple dissolution of the Cr depleted regions.

Acknowledgement

The authors thank W. R. Bitler for helpful discussions, H. Shih and M. High for assistance in programming the finite difference model, and R. Iyer and R. Miller for help in preparing the manuscript. Financial support of the Office of Naval Research under Contract No. N00014-84-k-0201 is gratefully acknowledged.

References

1. Bennett, B. W., An Investigation of Intergranular Corrosion of Stainless Steels, Ph.D. Thesis, The Pennsylvania State University (1984).
2. Burgers, J. M., "Geometrical Considerations Concerning the Structural Irregularities to be Assumed in a Crystal", Proc. Phys. Soc., 52 (1940) pp. 23-33.
3. Bragg, W. L., Discussion to Ref. 2, Proc. Phys. Soc., 52 (1940) pp. 54-55.

4. Shockley, W. and Read, W. T., "Dislocation Models of Crystal Grain Boundaries", *Phys. Rev.*, *78* (1950) pp. 275-289.

5. Bollman, W., Crystal Defects and Crystalline Interfaces, Springer-Verlag, New York, NY, 1970.

6. Vitek, V., Sutton, A. P., Smith, D. A. and Pond, R. C., "Atomistic Studies of Grain Boundaries and Grain Boundary Dislocations", pp. 115-148 in Grain Boundary Structure and Kinetics, American Society for Metals, Metals Park, Ohio, 1979.

7. Stawstrom, C. and Hillert, M., "An Improved Depleted-Zone Theory of Intergranular Corrosion of 18-8 Stainless Steel", *J. Iron Steel Inst.*, *207* (1969) pp. 77-85.

8. Tedmon, C. S., Vermilyea, D. A., and Rosolowski, J. H., "Intergranular Corrosion of Austenitic Stainless Steels", *J. Electrochem. Soc.*, *118* (1971) pp. 192-202.

9. Hall, E. L. and Briant, C. L., "Chromium Depletion in the Vicinity of Carbides in Sensitized Austenitic Stainless Steels", *Metallurgical Trans.*, *15A* (1984) pp. 793-811.

10. Sakurai, T., Jimbo, A. and Pickering, H. W., "In-Situ Formation of a Grain Boundary in Field Ion Microscopy Using a Laser", pp. 107-109 in *30th Intern. Field Emission Symposium*, Univ. Pennsylvania, Philadelphia, PA, 1983; ibid, Applied Physics Letters, submitted for publication.

11. Meibom, R. von and Rupp, E., *Z. Phys.*, *82* (1933) p. 690.

12. Boersch, H., *Z. Tech. Phys.*, *18* (1937) p. 574.

13. Venables, J. A. and Harland, C. J., "Electron Back-scattering Patterns - A New Technique for Obtaining Crystallographic Information in the Scanning Electron Microscope", *Phil. Mag., Ser. A.* *27* (1973) pp. 1193-1200.

14. Bennett, B. W. and Pickering, H. W., "A Scanning Electron Microscope Stage for Crystal Orientation and Structure Determination", *Scripta Metallurgica*, *18* (1984) pp. 743-748.

15. Grimmer, H., "Disorientations and Coincidence Rotations for Cubic Lattices", *Acta Cryst.*, *A30* (1974) pp. 685-688.

16. Aaron, H. B. and Aaronson, H. I., "Growth of Grain Boundary Precipitates in Al-4% Cu by Interfacial Diffusion", *Acta Metall.*, *16* (1968) pp. 789-798.

17. Ebling, H. F. and Scheil, M. A., "Time-Temperature-Sensitization (TTS) Diagrams for Types 347, 304L and 316L Stainless Steels", pp. 275-282 in ASTM STP 369, Amer. Soc. Testing and Materials, Philadelphia, PA 1965.

18. Huntz, A. M., Aucoutier, M., and Lacombe, P., "Measure des coefficients de diffusion en volume et intergranulaire du chrome radioactif dans le fer α", *Compt. Rend. (Paris)*, *C265* (1957) pp. 554-557.

19. Singhal, L. K. and Martin, J. W., "The Growth of $M_{23}C_6$ Carbide on Grain Boundaries in an Austenitic Stainless Steel", *Trans. AIME*, *242* (1968) pp. 814-819.

20. Smithells Metals Reference Book, 6th Edition, E. A. Brandes, ed., E. A. Butterworths, London, 1983.

21. Hodges, R., "Intergranular Corrosion in High Purity Ferritic Stainless Steel: Effect of Cooling Rate and Alloy Composition", Corrosion, 27 (1971) pp. 119-127.

22. Briant, C. L., "The Effects of Sulfur and Phosphorus on the Intergranular Corrosion of 304 Stainless Steel", Corrosion, 36 (1980) pp. 497-509.

23. Streicher, M. A., "General and Intergranular Corrosion of Austenitic Stainless Steels in Acids", J. Electrochem. Soc., 106 (1959) pp. 161-180.

POSITRON STUDIES OF HYDROGEN EFFECTS IN ALLOYS

J. G. BYRNE
Departments of Metallurgy and
Materials Science and Engineering
University of Utah
Salt Lake City, Utah 84112
USA

The effects of cathodic and thermal charging of hydrogen into Cu and two Cu-Al alloys were studied primarily with positron annihilation and microhardness measurements. These measurements were performed as a function of distance through a gradient of plastic deformation imposed after thermal charging and imposed both before and (separately) after cathodic charging. Some TEM and SEM observations also are reported.

Introduction

Cathodic charging of hydrogen into Ni was earlier [1] found to produce very interesting changes in the Doppler broadening of the positron annihilation spectrum. These changes suggested that protons were capable of screening defects created by the cathodic charging from positron detection and that as the protons left the defects with time, the defects once again became detectable by positron annihilation. Earlier still, Alex et al. [2] had, with positron lifetime measurements of cathodically charged 4340 steel, come to similar conclusions about proton screening of defects.

More recently, we have become interested in studying the cathodic charging of the Cu-Al system [3] since the stacking fault energy, γ_{sF}, can be changed greatly with slight Al additions to Cu [4,5] and γ_{sF} is known to be important in both hydrogen embrittlement [6] and positron trapping-annihilation [7] considerations.

Thermal charging of hydrogen into Cu at 1000°C followed by quenching into isopentane at -150°C results in a lower value of the positron Doppler peak parameter than does a similar procedure using an inert Ar atmosphere. The reason for this is that thermally charged protons can produce a screening effect of defects from positron detection. This was also noted for cathodic charging of Ni [1], of Cu and Cu-Al alloys [3] and of steel [2].

For those not that familiar with positron annihilation, it happens that positrons put into a sample from a source such as ^{22}Na will thermalize and eventually annihilate with an electron. If defects are present, a positron will frequently trap at the defect and more often than not annihilate with an electron in that location. If the center of mass of the electron-positron pair were stationary at annihilation, two gamma rays of 511 keV each would be emitted at 180° to one another. But since the center of mass of the annihilating pair is not stationary, the energy of the gamma radiation which accompanies the annihilation is subject to a Doppler shift from the 511 keV value. This shift is larger for an annihilation with a more energetic core electron than with a lower energy conduction electron. Hence, for a positron trapped in a defect, a smaller Doppler shift is a consequence of the higher probability of a conduction electron being involved in such an ion core poor location. Smaller Doppler shifts lead to a sharper annihilation spectrum or a higher value of (P) or (P/W) which are ratios of the number of events in the central or peak region to the total number in the whole spectrum or to the number in the two wing regions of the spectrum. We will use (P/W) for the cathodic studies and (P) for the thermal studies, since they were done by different people at different times.

For hydrogen studies [1-3] it is extremely useful to use positrons to look at defects as a function of their interaction with protons. Thus protons trapped in a vacancy or on a dislocation will repel a subsequently approaching positron which will then annihilate in a more perfect lattice region with a higher momentum core electron.

Experimental

Cathodic charging was performed as described previously [3] using 0.1N H_2SO_4 with 0.25 g/l of As_2O_3 as a hydrogen recombination inhibitor. The current density was 10 mA/cm^2 for three hours. Indentations were used to impose gradients of plastic deformation. These consisted of 500 or 1000 kg loadings with a Brinell machine. For 150 kg or lower, a Rockwell superficial hardness machine was used. Microhardness surveys were made with a Vickers indentor and a 25 g load.

Positrons were emitted from a 10 mm high x 1 mm wide line source of ^{22}Na. Samples containing a gradient of dislocation density were then mechanically traversed across the stationary line source before and after cathodic charging. In some experiments the gradient of plastic deformation was imposed on a sample after cathodic charging. An intrinsic Ge detector, multichannel analyzer, analog to digital converter and computer were utilized to record and analyze the annihilation spectrum from each sample as described elsewhere [3].

Alloys of Cu + 1.83 w/o Al, 3.69 w/o Al and 7.49 w/o Al were prepared by AMAX, Inc. These Al contents will be referred to as 2, 4 and 8%, respectively, for convenience.

Thermal charging consisted of exposure at 1000°C in a hydrogen atmosphere for times between one and four hours followed by a rapid quench into -150°C isopentane as in the work of Wampler et al. [8] and using the same furnace as Panchanadeeswaran and Byrne [9]. An argon atmosphere was used for control experiments. Initial material was either 90% cold rolled Cu or Cu-4 w/o Al.

Results and Discussion

Deformation Studies of Cathodically Charged Cu Samples

Protons in octahedral Cu sites cause a lattice dilation of 0.27 of the Cu atomic volume per atomic percent hydrogen [10]. It is thus more favorable for protons to trap at dislocations if those are present. Either location results in solid solution hardening. We generally find an increase in the entire (P/W) versus distance curve on charging and associate this with an increase in defect density as well as the presence of interstitial hydrogen. Such an increase reflects a predominance of new defect creation over any concurrent proton screening of some of the defects. A similar observation in Vanadium [11] was attributed to positron annihilation with proton shielding electrons in the neighborhood of the proton, i.e., nearest or second nearest neighbor interstitices.

Figures 1 and 2 show typical (P/W) and microhardness trends respectively for indented only, indented and then charged, and charged and then indented Cu (500 kg indentations). Right at the indentation, the percent increase in (P/W) upon charging in Fig. 1 is 1.22%. For a 150 kg indentation, this value was 1.36% and it has been shown [12] that one gets smaller increases in (P/W) upon charging Cu as the prior damage load increases to 1000 kg. No doubt reduced positron trapping at, and thus detection of, these defects is involved at these locations because of the repulsion between previously trapped protons at some of the defects and the similarly charged positrons. A similar finding was made by Alex et al. [2] using positron lifetime measurements of 4340 steel of increasing initial hardness, cathodically charged with hydrogen. Another consideration is that as the loads are increased (or the initial hardness [2]) it would become increasingly difficult for the hydrogen to produce new dislocations in the now harder material.

The highest curve in Fig. 1 is for the charged and later indented sample. Beyond 8 mm, where no influence of indentation exists, the sequence of steps is immaterial as it should be, and we see only the effect of charging on annealed Cu. At 0 mm, the highest values of (P/W) and VHN always result from deformation after charging. One interpretation of the location of these highest curves in Figs. 1 and 2 is that charging results in extra dislocation structure [13], especially dislocation loops, and probably shortens the length of Frank-Read sources, hence subsequent dislocation motion during a final deformation step should produce additional interaction with the dislocation loop structure left by the hydrogen charging. This clearly would raise the

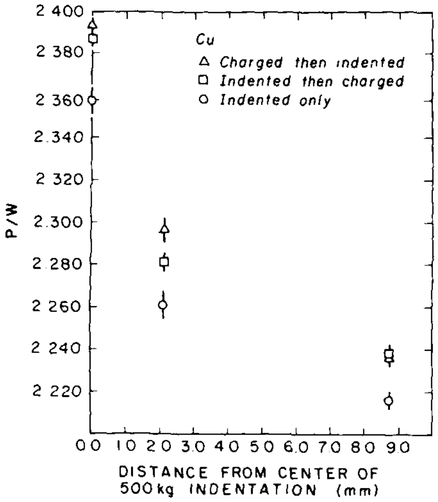

Fig. 1 - (P/W) versus distance from the center of a 500 kg indentation in Cu for each of indented only, indented then charged and charged and then indented.

hardness and also (P/W) if we make the very safe assumption that new dislocation lengths result from the above mentioned interactions during the final deformation step. From Fig. 1, one can show that both the absolute magnitude of the (P/W) increase (0.160) and its percent (7.16) are larger for deforming hydrogen charged Cu than they are (0.142 and 6.4% respectively) for deforming annealed Cu. It is also of interest to note from Fig. 1 that charging already deformed Cu gives larger magnitude and percent increases in (P/W) than if one charges annealed Cu, i.e., 0.03 and 1.27% and 0.019 and 0.86%, respectively. The other reason for the highest position of the curves for charging followed by deformation in Figs. 1 and 2 is solid solution hardening by interstitial hydrogen and this on further perturbation by dislocation motion adds to additional work hardening and more elevated (P/W) values. Qualitatively, the passage of dislocations may "sweep" originally interstitial hydrogen into more effective locations for the generation of new line defects. We will show later

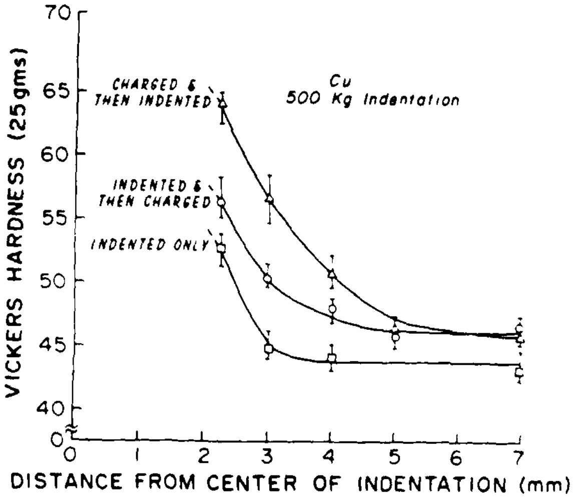

Fig. 2 - VHN (25 g load) versus distance from a 500 kg indentation in Cu for each of indented only, indented then charged and charged and then indented.

in terms of trapping model theory that the calculated dislocation density indeed is highest for the sequence of charge-then-deform. Some experimental evidence will be shown indicating a decrease in X-Ray particle size which is related to an increase in dislocation density and "R" parameter measurements will show that the line defect is the main trapping site for positrons for all current samples.

In Fig. 2, one sees that the hardness increase falls off to zero at about 3 mm for the indented only specimens and does so at about 5 mm for both the charged plus indented specimens and the indented then charged specimens. Since the application of force after charging did not appreciably extend the gradient region any further than did charging alone, one may conclude that the presence of hydrogen did not increase the dislocation mobility as proposed in systems which exhibit solid solution softening [14,15,16]. One is led to conclude that of the two sequences: charging plus deformation and deformation plus charging, the former sequence is more productive of defects.

Figure 3 shows stress-strain curves for all three materials in uncharged and charged conditions. As in the indentation results, we again find a solid solution hardening effect due to charging. At the strain rates of 2.2 x 10^{-4} s^{-1} used, it can be shown via calculation [17] that dislocations do not escape from the hydrogen pinning atmosphere. The fracture strain is reduced about 5% by charging in all three materials. Figure 4 verifies earlier (P/W) indentation results to the effect that deformation after charging exhibits more defect generation than either charging after deformation or deformation alone. It can be seen that charging after deformation in the 4 w/o Al alloy only slightly raises (P/W) relative to no charging and even then only up to strain of 20% elongation. Consistent with earlier results, one finds a negative effect for the Cu-8 w/o Al for charging after straining. The stress-strain curves for each of charged and uncharged Cu-4 w/o Al and Cu-8 w/o Al alloys in Fig. 3 show much higher yield strengths than Cu. The charged curves are again higher at all strains, and in both alloys the elongation loss due to charging, like the Cu case, is never more than 5%.

Both protons and the positrons have an affinity for stacking faults [7]. In the present alloy system, the stacking fault energy is reduced 71% by the 4% Al addition and 96% by the 8% Al addition [4,5]. The positron in addition has a preference for the Al atom over the Cu atom as has been shown by a pseudo-potential treatment by Lock and West [18].

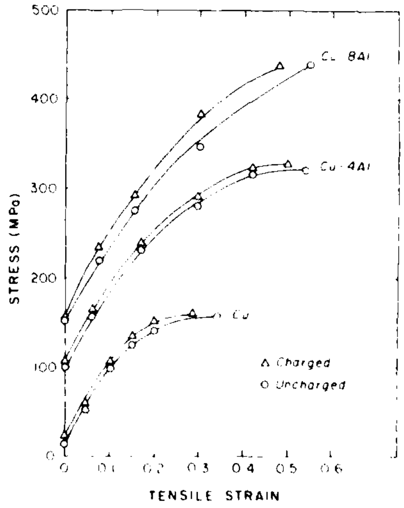

Fig. 3 - Engineering stress-strain curves for annealed (750°C for 1 h) and charged: Cu, Cu-4 w/o Al, and Cu-8 w/o Al, respectively.

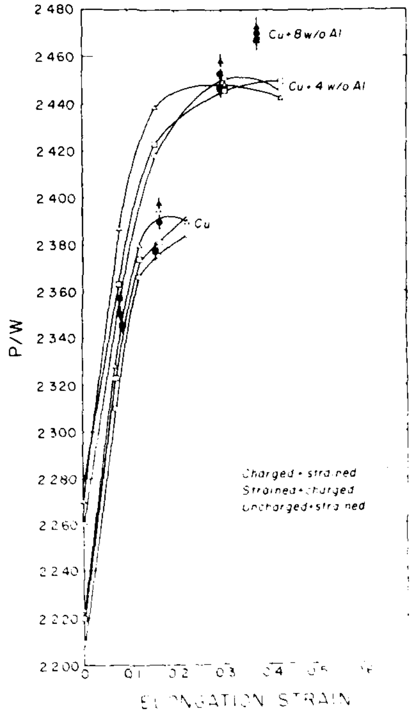

Fig. 4 - (P/W) versus elongation strain for uncharged, charged and strained and then charged Cu, Cu-4 w/o Al, and Cu-8 w/o Al, respectively.

Table I. (P/W) Changes After Charging

	Cu	Cu-4 w/o Al	Cu-8 w/o Al
500 kg Load			
At Indentation Center	+1.23%	0%	-0.38%
Far From Indentation Center	+1.08%	0.75%	+0.40%
1000 kg Load			
At Indentation Center	+0.79%	-0.24%	-0.61%
Far From Indentation Center	+1.13%	+0.50%	+0.41%

Table I shows that the amount of (P/W) increase after charging exactly at the center of the 500 kg indentation is 1.23% for Cu, zero for the 4% Al alloy and -0.38% for the 8% Al alloy. Similar results are seen in Table I for the 1000 kg load. Kim [19] effectively eliminated grain size, solubility differences, and proton-Al atom interactions from possible explanations for these lower (P/W) values with increasing % Al. It is, however, likely that material hardness is involved. In the annealed condition, the VHN hardness numbers for our materials were: 42 for Cu, 61.5 for Cu-4 w/o Al, and 94 for Cu-8 w/o Al. One expects more resistance to new defect generation by hydrogen in initially harder material and hence a lower (P/W) value [3]. At the center of the indentation, a lack of change or a negative change in (P/W) with higher Al content can be explained as before [3], i.e., not only by resistance of stronger materials to new defect generation but also by accentuated proton screening effects in the alloys at the more extended dislocations. Increased planar slip of hydrogen bearing extended dislocations can lead to embrittlement when that hydrogen is liberated at dislocation pileups [6]. This is all consistent with the proton screening argument given earlier. For the 500 kg indentation, Fig. 5 may serve as a summary of the effects of stacking fault energy and sequence of operations. One here can note the "condensing" effect of higher % Al on both the total range of (P/W) and the distance over which a change in (P/W) can be detected. In earlier work [3], the furthest extent of the hardness gradient for a 1000 kg indentation was to about 5 mm for Cu. However, using (P/W) the gradient region for Cu (charged or uncharged) was still easily detected at 9 mm.

Kinetics and Isochronal Annealing Studies

Kinetic studies [3] of annealed and deformed Cu and Cu-4 w/o Al showed that for annealed Cu, Cu-4% Al and 90% cold rolled Cu an initial increase of (P/W) after charging, decayed to some intermediate level in about one day for the alloy and two days for the pure Cu. However, for the deformed 4% Al alloy charging produced an immediate decrease in (P/W). Similarly, more recent results [12] on the Cu-8% Al alloy show that when the 90% cold rolled condition is charged, (P/W) immediately decreases and then remains stable. Yet when the same alloy in the annealed condition is charged, a slight increase occurs followed by a decay due to screening protons reaching the new dislocations again over about a one day period. The immediate decrease and later stability of the (P/W) value upon charging the 90% cold rolled 8% Al alloy is interpreted as were Figs. 5 and 7 of reference [3] for the 4% Al alloy, i.e., the dislocation density is so high and the dislocations are so stable (due to the low stacking fault energy) that few new dislocations are created by hydrogen charging but rather all the hydrogen immediately is partitioned to proton screening of dislocations. The annealed 8% Al alloy [12] when charged shows an increase followed by a decay in (P/W) over about one day to a stable level which is below both the initial and charged values of (P/W) rather than an intermediate level between the two as earlier found for Cu and for Cu-4 w/o Al [3]. Thus again, one sees evidence for extra strong screening as the stacking fault energy decreases. A decrease in (P/W) following an initial increase due to charging could be due to interstitial protons either leaving the sample or detrapping from interstitial positions and retrapping at dislocations. Diffu-

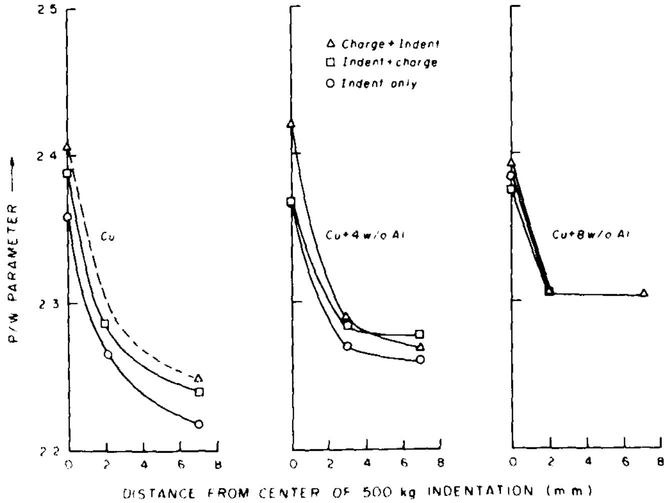

Fig. 5 - Summary of curves of (P/W) versus distance for Cu and the 4% and 8% Al alloys for 500 kg indentations.

sion out of interstices would lower (P/W) since a strain is relieved and, of course, so would retrapping at a dislocation which then becomes screened. A similar observation was made by Lengler et al. [20].

To more closely study trapping/detrapping events, isochronal annealing was applied to annealed samples which were charged for six hours. For all three materials (P/W) started decreasing between 50 and 80°C, minimized between 110 and 140°C, and subsequently increased and leveled off between 250 and 290°C [12]. The initial decrease in (P/W) may be associated with proton trapping at defects. This effect was never observed at room temperature but the enhanced diffusivity at temperatures slightly above room temperature may enable proton trapping. The subsequent rise in (P/W) above 250°C is ascribed to positron detrapping from defects as the thermal energy increases.

Trapping Model Analysis

The trapping model developed by Connors and West [21] and others can be simplified and reformulated [22] to give a defect specific parameter "R" which is independent of defect concentration and changes only where the type of defect causing positron trapping changes [23]. The R value did not statistically differ significantly from its value for dislocations in each material [12]. It was noted, however, that the level of the main R value of 0.85 for the 8% Al alloy was significantly different from about 0.74, the typical value of R for both Cu and Cu-4 w/o Al. This could mean that in the 8% Al alloy, where we have reduced the stacking fault energy by 96% of its original Cu value, we indeed have a different trapping mechanism, i.e., even though the trapping in all three alloys is mainly at dislocations, the dislocations are considerably extended in the 8% Al case and the different R suggests a basically different mechanism. The other fact drawn from R calculations by Kim and Byrne [12] was that there were no reproducible differences in R between the three types of treatment, i.e., strained, strained then charged and charged then strained.

When one type of defect predominates as in the present case, the trapping model equations can be manipulated [24] to calculate the defect density. This was done in the current work with the results shown in Table II for Cu. From Table II one can see that the dislocation density increases for charging after deformation and always is highest for charging followed by deformation. It would seem safe to conclude that defects other than dislocations (such as pressurized voids) do not contribute significantly to the total positron annihilation characteristics.

Some X-Ray line broadening measurements [25] were made in order to determine if any large differences in X-Ray particle size, microstrain or calculated dislocation density resulted from the various time sequences of treatments [12]. Table III shows root mean square (R.M.S.) microstrain, X-Ray particle size and calculated [24] dislocation densities. Charging reduces the particle size and increases both the microstrain and the dislocation density consistently with increasing strain. Charging followed by rolling results in the higher dislocation density of the two 10% rolling procedures.

It is of interest to note that the dislocation densities calculated for 11% strain in Table II compare favorably with those for the first 10% comparison in Table III.

Table II. Dislocation Densities Calculated from the Trapping Model for Cu

	Strained Only	Strained then Charged	Charged then Strained
Strain	(Cm^{-2})	(Cm^{-2})	(Cm^{-2})
0.073	9.09×10^{8}	2.79×10^{9}	3.29×10^{9}
0.11	9.27×10^{9}	1.59×10^{10}	2.00×10^{10}
0.15	2.32×10^{10}	1.20×10^{11}	1.32×10^{11}

Table III. X-Ray Line Broadening Information on Cu

	Rolling Only			Rolled Then Charged			Charged Then Rolled		
Reduction%	D	ε	ρ_d	D	ε	ρ_d	D	ε	ρ_d
10	338	4.6	1.9	380	6.8	2.4			
10	292	3.5	1.6				243	4.9	2.5
17	284	5.0	2.4	472	5.2	1.5			

D(Å); $\varepsilon(10^{-4})$; $\rho_d(10^{10}cm^{-2})$

Deformation After Thermal Charging

Figure 6 displays several important features of deformation after thermal charging of hydrogen relative to Ar. At the left end of the figure, the zero post charging strain values of (P) suggest that the full thermal hydrogen charge (accompanied by recrystallization of the 90% cold rolled condition) apparently results in more dislocation screening by protons than does the partial hydrogen anneal, and, of course, than does the full Ar thermal exposure. 50% rolling deformation after the same three thermal treatments exactly inverts the three curves and one sees that, as for deformation after cathodic charging, the most unscreened damage is associated with hydrogen charging followed by deformation. The (P) value of just over 0.380 for this case in Fig. 6 is very close to the value of about 0.381 found by Pan and Byrne [26] at the center of a 500 kg indentation in identically prepared Cu, and the value of about 0.374 for the undeformed thermal hydrogen charged condition in Fig. 6 is quite similar to the value found [26] far from (over 6 mm) the center of a 500 kg indentation. One also sees in Fig. 6 that after a strain of 15 to 20%, the initial screening of defects gives way to evident new defect generation over and above that for Ar treated Cu. Evidently, 30% rolling deformation about saturates the situation in hydrogen charged Cu, but in Ar treated Cu, (P) continues to increase to a strain of 50% although it remains significantly lower than for hydrogen charging.

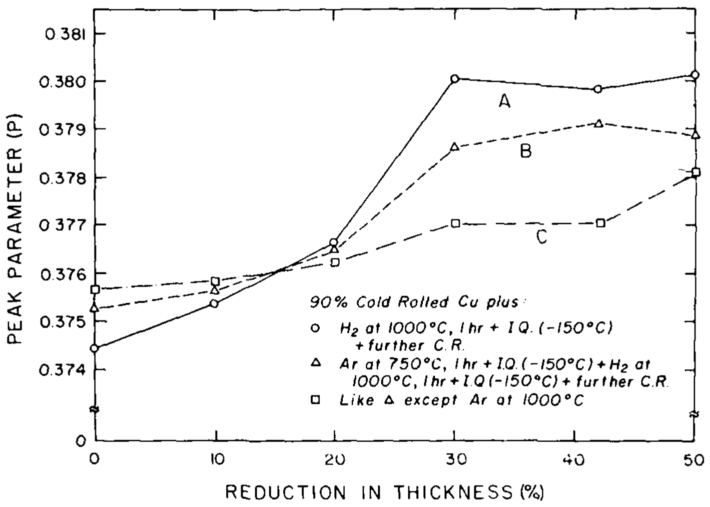

Fig. 6 - (P) versus % final thickness reduction for 90% cold rolled Cu plus the sequences: A) H_2 at 1000°C + I.Q. (-150°C) + further cold rolling; B) Ar at 750°C + I.Q. (-150°C) + H_2 at 1000°C + I.Q. (-150°C) + further cold rolling; C) like previous but with Ar at 1000°C. (I.Q. = isopentane quench).

Microhardness measurements as a function of distance from a 500 kg indentation are shown in Fig. 7 and indicate that thermal hydrogen exposure not only raises the Ar curve far from the indentation but does so to an increasing extent as one approaches (within 4 mm of) the highest dislocation density region (i.e., the H_2 curve steepens relative to the Ar curve as 1.5 mm is approached). This suggests, in the region unaffected by the indentation, that interstitial hydrogen solid solution hardening is predominant and, that from 1.5 to 4 mm, the motion of the newly introduced dislocations results in some new form of damage as suggested earlier. For example, if as for cathodic charging, dislocation loops [13] and strained interstitial sites are created, these would be expected to interact with the moving dislocations (from the indentation) to generate even more defects. R parameter [22,23] determinations and TEM should help clarify the nature of this extra damage. An Ar anneal at 750°C prior to hydrogen charging at 1000°C, changes the dislocation structure seen by the thermal charging so that one finds less interaction with the newly inserted dislocations from the indentation than was seen in Fig. 7 inside of 4 mm, however, the hardness beyond 4 mm is identical to that in Fig. 7 [26].

Figure 8 shows that a large difference in behavior is found when exactly similar experiments to those described by Fig. 7 are applied to the Cu-4 w/o Al alloy. Between about 4 and 7 mm, where no new dislocations from the indentation reach, a hydrogen hardening is seen which is about six times larger than that produced by H_2 in pure Cu. As one approaches 1 mm, the new dislocations from the indentation produce new hardening, but the slopes in this region are about equal for both H_2 and Ar exposures suggesting that the strong affiliation between the "old" extended dislocations and the hydrogen precludes the newly introduced dislocations from interacting at all with the hydrogen [3].

Pan and Byrne [26] found that (P) versus distance plots for Cu-4 w/o Al initially 90% cold rolled were essentially indistinguishable among full H_2 charging, partial H_2 charging and the Ar control. Evidently far from the indentation where the large hardening effect occurred via hydrogen (Fig. 8), the protons must indeed pin the extended dislocations very effectively, but

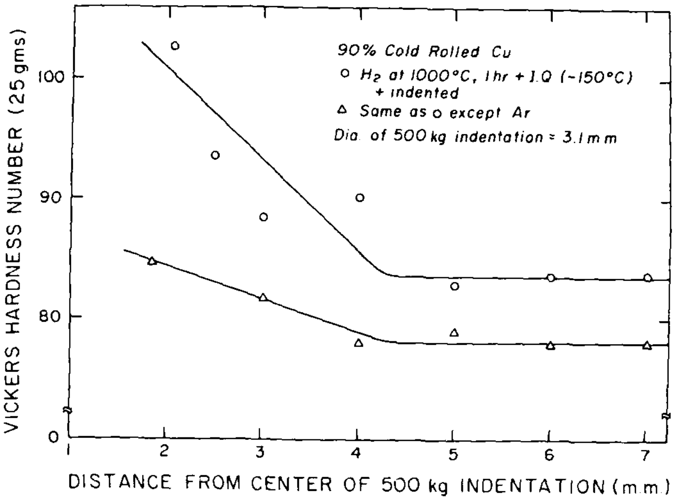

Fig. 7 - VHN versus distance from the center of a 500 kg indentation in 90% cold rolled Cu: thermally charged one hour at 1000°C in H_2 + I.Q. (-150°C) + indented; the same except for Ar.

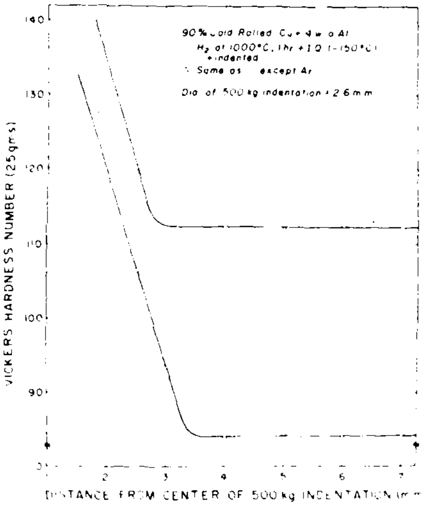

Fig. 8 - VHN versus distance from the center of a 500 kg indentation in 90% cold rolled Cu-4 w/o Al alloy: thermally charged one hour at 1000°C in H_2 + I.Q. (-150°C) + indented; the same except for Ar.

this is not detected by the subsequently introduced positrons. This could simply be a matter of the fully relaxed extended dislocations in a low dislocation density region presenting such large areas for both proton and positron trapping that the faults are indistinguishable from faults in Ar treated samples as far as the positrons are concerned.

In the region nearer the indentation, where in pure Cu the extra interaction of new dislocations with thermal hydrogen damage could barely be seen by positrons, in the 4 w/o Al alloy no extra interaction of new dislocations with hydrogen related defects is seen [26]. Protons probably strongly attach themselves to extended dislocations rather than produce hydrogen damage such as dislocation loops with which new dislocations from the indentation could react.

Kinetics and Isochronal Annealing Studies of Thermal Charging

Figure 9 shows that hydrogen charging at 1000°C followed by a rapid quench into isopentane at -150°C results in progressive hardening of Cu with exposure time relative to the same treatment in Ar. Figure 10 shows the counterpart measurements of the positron peak (P) parameter. It is interesting that after about 45 minutes, the hydrogen seems to show a predominance of proton screening over new defect generation which decreases (P) slightly below the value for equivalent time in Ar.

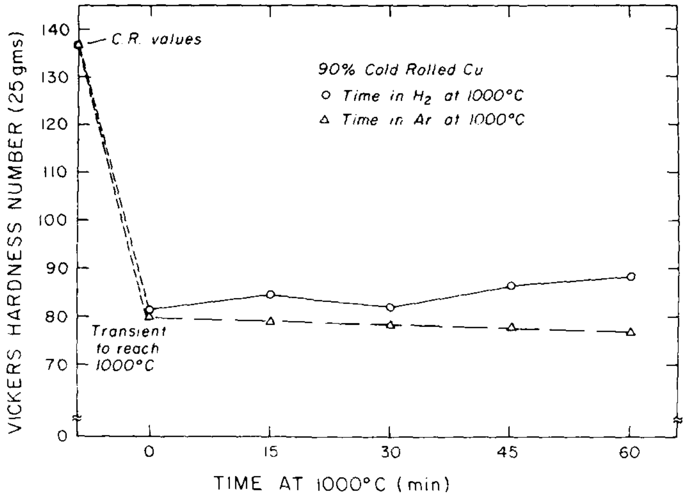

Fig. 9 - VHN versus time of holding 90% cold rolled Cu in each of H_2 and Ar at 1000°C. The transient to reach 1000°C is about 20 minutes. An I.Q. (-150°C) followed.

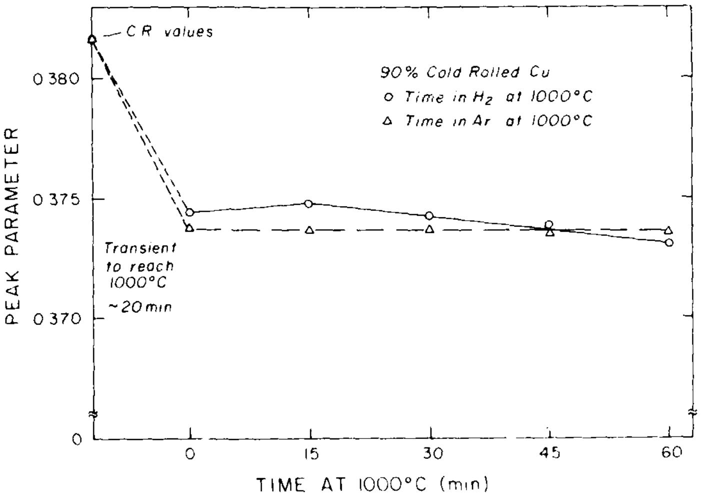

Fig. 10 - (P) versus time of holding 90% cold rolled Cu in each of H_2 and Ar at 1000°C as in Fig. 8.

Charging time was examined in terms of relaxation in (P) value after various times at ambient. Samples were held in liquid nitrogen prior to exposure at ambient temperature. It was found [26] that thermal charging times of 1, 2, and 3 hours continued to depress the value of (P) but more than three hours did not. This suggests that thermal charging at 1000°C takes three hours to saturate Cu as far as positron measurements are concerned. In four hours of relaxation at ambient temperature, all of these charging effects had dissipated, i.e., an increase in (P) to a stable value was observed for each sample within four hours with no significant change up to eight hours.

Conclusions

Cathodic Charging

1) The hydrogen-defect interaction depends strongly on stacking fault energy.

2) Hydrogen charging previously indented Cu increases (P/W) and VHN for indentation loads less than 500 kg. New defect generation on charging predominates over proton screening of existing and new defects.

3) For more severe indentation loads (500 and 1000 kg) (P/W) in the damage center can actually decrease due to predominance of proton screening of existing defects over generation of new defects.

4) Hydrogen charging of indented Cu-4 w/o Al alloy increases (P/W) in lightly or undamaged regions but causes little or no increase in (P/W) at the damage center.

5) All the materials, deformed after charging of hydrogen, show higher (P/W) and microhardness values than for uncharged and deformed material. This is attributed to a dislocation mobility decrease and/or a dislocation density increase. All of the effects observed in indented samples also appear in materials deformed in tension.

6) The kinetic and isochronal annealing studies have shown evidence of proton trapping and detrapping. At room temperature, the trapping effect was seen in materials of both lower and higher stacking fault energy as a decrease in (P/W) with time. The effect was larger in material of higher stacking fault energy. This implies that the decaying process is mainly controlled by hydrogen trapping into the newly created defects. Proton detrapping effects in all materials were shown to appear in the same temperature range of 100 to 280°C. This is interpreted as being due to there being a similar binding energy of hydrogen to defects in all three materials.

7) The R parameter analysis showed that the generated defects are of dislocation type.

8) Dislocation densities calculated from the trapping model and a few calculated for X-ray line broadening measurements were in reasonable agreement. Both were higher after cathodic charging than after deformation and the former were highest for charging followed by deformation.

Thermal Charging

9) Thermal hydrogen charging at 1000°C followed by quenching slightly lowers the positron peak parameter (P) of annealed Cu relative to an Ar exposure at 1000°C.

10) For deformation after thermal charging of Cu, the above trend of conclusion #9 reverses and (P) is higher for a hydrogen containing sample than for one quenched from an Ar atmosphere and similarly deformed.

11) Microhardness is increased by hydrogen charging of Cu at 1000°C. 500 kg indentation damage after charging increases the microhardness in the indentation neighborhood more so than a similar indentation after exposure at 1000° C in Ar.

12) Thermal charging of Cu-4 w/o Al increases the microhardness of annealed material by a factor of three relative to the extra hardening it causes in a more deformed region. Evidently, proton pinning of the extended dislocations [4,5] in the annealed material is very effective so that subsequently introduced dislocations have much less hardening effect.

13) When (P) is measured for the above experiment, little change in (P) is discernable either in annealed or subsequently deformed Cu-4 w/o Al. It is believed that the pinning protons are not detected in the widely extended stacking faults to which the positrons also are attracted. Thus Ar treated samples would have similar (P) values.

14) It takes about 60 minutes for hardening to be produced for Cu in H_2 at 1000°C. This also slightly lowers (P) relative to Ar due to proton screening.

15) Three hours in H_2 at 1000°C produce in Cu saturation in terms of positron annihilation. All charging times up to and including three hours decreased (P) progressively and all these decreases relax within four hours at room temperature.

Acknowledgement

The author wishes to thank the Office of Naval Research and Dr. Philip Clarkin for the support under Grant N00014-81-K-0331 which made this work possible. These results are taken from the Ph.D. studies of J. J. Kim and Y. Pan. The invaluable assistance of Dr. Bob DeAngelis on the X-Ray work is much appreciated.

References

1. Po-We Kao, R. W. Ure and J. G. Byrne, "A Study of Hydrogen Charging of Ni by Positron Doppler Broadening," Phil. Mag., A39 (1979) p. 517.

2. F. Alex, T. D. Hadnagy, K. G. Lynn and J. G. Byrne, "Positron Annihilation Studies of Hydrogen Embrittlement," Int. Conf. on the Effect of Hydrogen on the Behavior of Materials, Met. Soc. AIME,, eds. A. W. Thompson and I. M. Bernstein, (1976) p. 642.

3. J. J. Kim and J. G. Byrne, "Hydrogen/Dislocation Studies by Positrons in Thermally Charged Cu", Scripta Met., 17 (1983) p. 773.

4. P. R. Thornton, T. E. Mitchell and P. B. Hirsch, "Dependence of Cross-Slip on Stacking-Fault Energy in Face Centered Cubic Metals and Alloys," Phil. Mag., 7 (1962) p. 1349.

5. G. A. Miller, D. H. Avery, and W. A. Backofen, "Fatigue Crack Growth in Some Copper-Base Alloys," T.M.S. of AIME, 236 (1966) p. 1667.

6. M. R. Louthan, Jr., G. R. Caskey, Jr., J. A. Donovan, and D. E. Rawl, Jr., "Hydrogen Embrittlement in Metals," Mater. Sci. Engr., 10 (1972) p. 357.

7. K. G. Lynn, R. W. Ure and J. G. Byrne, " Positron Trapping at Stacking Faults in Metals," Phys. Stat. Solidi., A60 (1973) p. 177.

8. W. R. Wampler, T. Schober and B. Lengler, "Precipitation and Trapping of Hydrogen in Copper," Phil. Mag., 34 (1976) #1 p. 129.

9. S. Panchanadeeswaran and J. G. Byrne, "Hydrogen/Dislocation Studies by Positrons in Thermally Charged Cu," Scripta Met., 17 (1983) p. 1329.

10. L. Katz, M. Guinan, and R. J. Borg, "Diffusion of H_2 D_2 and T_2 in Single-Crystal Ni and Cu," Phys. Rev., B4 (1971) p. 330.

11. M. Hasegawa, Y. Abe, T. Suzuki, H. Asano and M. Hirabayashi, "Positron Annihilation in the V-D (H) Alloys," 4th Intl. Conf. on Positron Annihilation, Helsingor, Denmark, 1976, Vol. D12.

12. J. J. Kim and J. G. Byrne, "Mechanical and Kinetic Effects of Cathodic Charging of Cu and Cu-Al Alloys," in press, Materials Science and Engineering (1985).

13. J. J. Kim and J. G. Byrne, "T.E.M. and S.E.M. Studies of Hydrogen Effects in Cu and Cu-Al Alloys," to be published in Materials Science and Engineering (1985).

14. M. Matsui, S. Moriyama, and H. Kimura, Proc. 4th Intl. Conf on Strength of Metals and Alloys, 1976, p. 291.

15. J. Eastman, F. Heubaum, T. Matsumoto, and H. K. Birnbaum, "The Effect of Hydrogen on the Solid Solution Strengthening and Softening of Nickel," Acta Met., 30 (1982) p. 1579.

16. H. Kimura and H. Matsui, Hydrogen Effects in Metals, ed. by I. M. Bernstein and A. W. Thompson, AIME, 1980, p. 191.

17. A. H. Cottrell, "Dislocations and Plastic Flow in Crystals," Clarendon Press, Oxford, 1956.

18. D. G. Lock and R. N. West, "Positron Annihilation in Disordered Binary Alloys," J. Physics F, 4 (1974) p. 2179.

19. J. J. Kim, "Hydrogen Effect in Casual Cu-Al Alloys," Ph.D. Thesis, University of Utah (1984).

20. B. Lengler, S. Mantl, and W. Triftshaüser , "Interaction of Hydrogen and Vacancies Investigated by Positron Annihilation," J. Phys. F, 8 (1978) p. 1691.

21. D. C. Connors and R. N. West, "Positron Annihilation and Defects in Metals," Phys. Lett., 30A (1969) p. 24.

22. W. Triftshaüser , "Positron Trapping in Solid and Liquid Metals," Phys. Rev., B12 (1975) p. 4634.

23. R. Duffin and J. G. Byrne, "Positron Measurements in Steels," Mat. Res. Bull., 15 (1980) p. 635.

24. M. L. Johnson, S. R. Saterlie and J. G. Byrne, "The Trapping of Positrons by Dislocations Produced in Single Crystal Bending," Met. Trans., 9A (1978) p. 841.

25. A. Kidron and R. De Angelis, "Direct Evaluation of Kα_1 Fourier Coefficients in X-ray Profile Analysis," Acta Cryst., A27 (1971) p. 596.

26. Y. Pan and J. G. Byrne, "Thermal Charging Effects of Hydrogen in Cu and Cu-Al Alloys," to be published, Materials Science and Engineering (1985).

APPENDIX

ONR WORKSHOP
ON
ENVIRONMENT-SENSITIVE FRACTURE OF METALS AND ALLOYS

Monday-Tuesday, 3-4 June 1985
U. S. Naval Research Laboratory
Washington, DC

0800 Registration

Monday A. M. (0830-1200)

CORROSION FATIGUE

(Session Chairman: Dr. B. B. Rath, NRL)

0830 WELCOME: Captain J. P. O'Donovan, Commanding Officer, Naval Research Laboratory

0840 OPENING REMARKS: A. M. Diness, Office of Naval Research

0900 "Corrosion Fatigue of Aluminum Alloys", David J. Duquette, Materials Engineering Department, Rensselaer Polytechnic Institute.

0940 "Role of Surface Layers in Fatigue", Edgar A. Starke, University of Virginia.

1020 Coffee Break

1040 "Environmental Alteration of Fatigue Crack Tip Plasticity", David L. Davidson, Southwest Research Institute.

1120 "Fatigue Crack Propagation in HY80 and HY130 Steels With Various Heat Treatments", Morris E. Fine, Technological Institute, Northwestern University.

1200 End of morning session.

1200-1330 Lunch

Monday P. M. (1330-1710)

STRESS CORROSION CRACKING & HYDROGEN EMBRITTLEMENT

(Session Chairman: Dr. R. P. Wei, Lehigh Univ.)

1330 "Overview of Hydrogen Embrittlement", John P. Hirth, Department of Metallurgical Engineering, Ohio State University.

1410 "Microstructural Effects and Control of Environmental Embrittlement", Mel Bernstein, Department of Metallurgical Engineering & Materials Science, Carnegie Mellon University.

1450 "The Electrochemistry and Solid State Chemistry of Intergranular Hydrogen Embrittlement", Ronald M. Latanision and M. E. Eberhnart, The H. H. Uhlig Corrosion Laboratory, Massachusetts Institute of Technology.

1530 Coffee Break

1550 "High Resolution Studies of Mechanical and Chemical Processes at Crack Tips", Howard K. Birnbaum, Department of Metallurgy, University of Illinois.

1630 "Mechanisms of SCC in Al-Zn-Mg Alloys", Joseph R. Pickens, Martin Marietta Laboratories.

1710 End of afternoon session.

Monday Eve.

RECEPTION AND DINNER IN HONOR OF DR. PHILIP A. CLARKIN

1800 Reception - Hogate's Restaurant

1900 Dinner - Hogate's Restaurant

Tuesday A. M. (0830-1130)

MODELING

(Session Chairman: Dr. D. J. Duquette, RPI)

0830 "Chemical Processes Important to Environmentally Sensitive Fracture", Jerome Kruger, Department of Materials Science and Engineering, The Johns Hopkins University.

0910 "Effect of Grain Boundary Structure on Segregation, Precipitation, Embrittlement and Corrosion at Grain Boundaries", Howard W. Pickering, Department of Materials Science & Engineering, Pennsylvania State University.

0950 "Positron Studies of Hydrogen Effects in Alloys", J. G. Byrne, Department of Materials Science & Engineering, University of Utah.

1030 "Modeling of Environmentally Assisted Crack Growth", R. P. Wei and G. W. Simmons, Department of Mechanical Engineering and Mechanics and Department of Chemistry, Lehigh University.

1110 CLOSING REMARKS: John Sedriks, Office of Naval Research

1130 Adjournment.

* * * * *

A. M. Sessions 0830-1200

P. M. Session 1330-1700

Monday Evening

1800-2100 Social and Dinner in Honor of Dr. Philip A. Clarkin
Hogate's Restaurant, Washington

Publication of Proceedings by ONR through Government Printing Office; hard cover, camera ready manuscripts, mats to be furnished to authors. (Editors: Wei, Duquette, Sedriks, Crooker; in some order).

ONR Liaison: John Sedriks

NRL Liaison: Tom Crooker

MASTER OF CEREMONY: Dave Duquette